

**Metal Impurities in *n*-type Crystalline Silicon for  
Photovoltaics: Simulation, Synchrotron-Based  
Characterization, and Mitigation**

by

Ashley E. Morishige

S.M., Mechanical Engineering

Massachusetts Institute of Technology (2013)

Bachelor of Engineering

Thayer School of Engineering at Dartmouth College (2011)

A.B., Engineering Sciences

Dartmouth College (2011)

Submitted to the Department of Mechanical Engineering  
in partial fulfillment of the requirements for the degree of

Doctor of Philosophy in Mechanical Engineering

at the

MASSACHUSETTS INSTITUTE OF TECHNOLOGY

June 2016

© Massachusetts Institute of Technology 2016. All rights reserved.

Author .....

Department of Mechanical Engineering

May 2, 2016

Certified by .....

Tonio Buonassisi

Associate Professor of Mechanical Engineering

Thesis Supervisor

Accepted by .....

Rohan Abeyaratne, Professor of Mechanical Engineering

Chairman, Department Committee on Graduate Theses



# Metal Impurities in $n$ -type Crystalline Silicon for Photovoltaics: Simulation, Synchrotron-Based Characterization, and Mitigation

by

Ashley E. Morishige

Submitted to the Department of Mechanical Engineering  
on May 2, 2016, in partial fulfillment of the  
requirements for the degree of  
Doctor of Philosophy in Mechanical Engineering

## Abstract

Crystalline silicon is the dominant technology in the rapidly-growing photovoltaics (PV) industry, but significant cost reduction is still required before widespread grid parity is achieved. One-quarter of the cost of a PV module is the Si wafer. One way to reduce the cost/kWh of PV is to identify a higher-efficiency “drop-in” substitute for the currently dominant  $p$ -type multicrystalline silicon (mc-Si) wafer. This thesis explores one class of wafer substitute:  $n$ -type silicon. This material is thought to have higher defect tolerance than  $p$ -type, but practical mc-Si cell efficiencies have remained lower than in  $p$ -type. This thesis explores why, using a combination of simulation and experiment. In particular, synchrotron-based micro-X-ray fluorescence mapping is used to non-destructively evaluate metal impurity evolution during processing.

This thesis demonstrates that metal impurity redistribution during solar cell processing is similar in  $n$ - and  $p$ -type mc-Si but the relative electrical impact of point defect and precipitated impurities is different, requiring different approaches to processing.

It has been hypothesized and shown indirectly that metal impurities redistribute similarly in  $n$ - and  $p$ -type mc-Si during processing. To confirm this hypothesis, I combined Fermi-level analysis with direct measurements of the metal distribution before and after an industrially-relevant range of gettering processes. This study confirmed that the understanding of metal redistribution developed for  $p$ -type mc-Si is directly applicable to  $n$ -type mc-Si.

To improve the understanding of metal impurity movement during solar cell processing, I developed a tool using Sentaurus TCAD software to visualize in 2D metal redistribution and the resulting recombination activity. I also performed an analytical review of the state of the art of crystalline silicon solar cell process simulation tools. The analysis elucidated the key physics of impurity gettering during solar cell processing and enabled guidelines for efficient, yet accurate, solar cell process simulations.

To quantify the recombination activity of precipitated iron in  $n$ -type crystalline silicon, I directly measured the iron content and recombination strength of iron precipitates in  $n$ -type crystalline silicon using a suite of micro-characterization tools. I found that iron-containing precipitates are highly recombination active in  $n$ -type Si and that the precipitate size is correlated with its recombination strength. To enable this study, I benchmarked the use of a new high-throughput synchrotron-based data collection mode called on-the-fly scanning.

To bring the level of sophistication of predictive simulation for  $p$ -type mc-Si to that of  $n$ -type mc-Si, I developed a simulation tool that calculates the redistribution of iron throughout the solar cell process and the resulting injection-dependent electrical performance of the wafer for both  $p$ - and  $n$ -type Si. Analysis using this tool indicates that  $p$ -type mc-Si usually requires point defect remediation during a slow cooling process, but for  $n$ -type mc-Si, dissolving iron-rich precipitates during shorter, higher temperature processing is often sufficient. Efficiency entitlement curves predict that  $n$ -type mc-Si can support 20% efficient solar cells.

Finally, knowledge of defects developed for Si wafers was applied to a key challenge facing the PV industry at the PV system level. In the field, degradation of next-generation industrial  $p$ -type mc-Si PV modules has been observed. Leveraging the fundamental understanding of the physics of impurities in Si wafers, the recombination parameters of the root-cause defect were quantified.

Building on the rich literature of  $p$ -type multicrystalline silicon, this thesis enables predictive engineering of all crystalline silicon materials from wafer growth to module performance in the field.

Thesis Supervisor: Tonio Buonassisi

Title: Associate Professor of Mechanical Engineering

## Acknowledgments

Thank you to my advisor, Professor Tonio Buonassisi, for the opportunity to do research in such an exciting and relevant field. Thank you for sharing your enthusiasm, guidance, and broad and deep perspective, for enabling access to essential tools and financial support, and for introducing me to the PV community. Thank you to my committee members, Professor Jesús del Alamo and Professor Jeff Grossman, for their encouragement and thoughtful feedback that strengthened the research.

Thank you to my wonderful colleagues in the PVLab. Thank you, Jasmin Hofstetter and David Fenning, for introducing me to the experimental techniques, simulation tools, and fundamentals that are the building blocks of our research. Thank you, Mallory Jensen, David Berney Needleman, Sergio Castellanos, Niall Mangan, Rafael Jaramillo, Austin Akey, Doug Powell, Joe Sullivan, Erin Looney, Alex Polizzotti, Patricia Yen, and Amanda Youssef, for your intellectual contributions, for being examples of outstanding researchers and professionals, and for essential hands-on assistance, especially during beamtimes. Thank you, Mariela Castillo, for providing support as lab manager.

I had the opportunity to work with and learn from several industry collaborators. Ibrahim Avci and Pratheep Balasingham of Synopsys Inc. taught me how to add models to Sentaurus TCAD software. Saptharishi Ramanatham and Chenlei Wang of Supreme Inc. supplied invaluable industrially-produced  $n$ -type mc-Si wafers. Kenta Nakayashiki of Renewable Energy Corporation generously contributed samples, essential data, and insight for the module degradation work.

I also had the opportunity to collaborate with and learn from colleagues from several research institutes, including Hannu Laine, Antti Haarahiltunen, and Prof. Hele Savin of Aalto University, Friedemann Heinz, Jonas Schön, and Dr. Martin Schubert of Fraunhofer ISE, and Prof. Carlos del Cañizo of the Institute for Solar Energy at the Polytechnic University of Madrid. Barry Lai enabled the synchrotron work at Argonne National Laboratory's Advanced Photon Source.

I am grateful for financial support of the U.S. Department of Defense's National

Defense Science and Engineering Graduate Fellowship, the MIT School of Engineering SMA2 Fellowship, and the National Science Foundation and the U.S. Department of Energy through the QESST Engineering Research Center under NSF CA No. EEC-1041895.  $\mu$ -XRF was performed at the Advanced Photon Source, a U.S. DOE Office of Science User Facility operated for the DOE Office of Science by Argonne National Laboratory under Contract No. DE-AC02-06CH11357. EBSD and ALD were performed at the Center for Nanoscale Systems (CNS), a member of the National Nanotechnology Infrastructure Network, which is supported by NSF award no. ECS-0335765.

Thank you to the faculty and my classmates at Dartmouth College, especially Thayer School of Engineering, and The Harker School for teaching me the fundamentals that enabled this research.

Thank you to Kari Jo, Thea, neighbors, friends, and family for their love and support. Thank you, Kellie.

# Contents

<b>Acknowledgements</b>	<b>5</b>
<b>List of Figures</b>	<b>12</b>
<b>List of Tables</b>	<b>18</b>
<b>References to published work</b>	<b>20</b>
<b>1 Why Crystalline Silicon Photovoltaics?</b>	<b>23</b>
1.1 Thesis Overview . . . . .	26
<b>2 Silicon PV: Crystallinity, Doping Type, Impurities, and Injection Level</b>	<b>29</b>
2.1 Monocrystalline and Multicrystalline Silicon for Solar Cells . . . . .	29
2.2 <i>n</i> -type vs. <i>p</i> -type mc-Si Wafers for PV . . . . .	29
2.2.1 Definitions . . . . .	29
2.2.2 Current Status . . . . .	30
2.3 <i>n</i> - and <i>p</i> -type mc-Si: Impurity Content, Electrical Impact, Characterization, Mitigation, and Simulation . . . . .	31
2.3.1 Impurity Content . . . . .	31
2.3.2 Electrical Impact of Impurities . . . . .	33
2.3.3 Impurity Characterization . . . . .	35
2.3.4 Impurity Mitigation . . . . .	36
2.3.5 Impurity Simulation . . . . .	37

2.4	Injection Level as a Constraint and a Tool . . . . .	37
2.4.1	The Role of Injection Level in Solar Cells . . . . .	37
2.4.2	Injection Level Dependence as a Characterization Tool . . . . .	40
<b>3</b>	<b>Visualizing Metal Redistribution and Lifetime Distribution after Phosphorus Diffusion Gettering in <i>p</i>-type Multicrystalline Silicon Solar Cells</b>	<b>43</b>
3.1	Tailoring Processing to Crystalline Silicon Wafer Quality . . . . .	44
3.2	Coupled 2D Process and Device Models . . . . .	45
3.3	Simulating the Effect of Varying Total Iron Concentration and Area Fraction of Defective Regions . . . . .	45
3.4	Simulated Solar Cell Efficiencies . . . . .	47
3.5	Visualizing the Post-Gettering Iron and Recombination Distributions in mc-Si . . . . .	48
3.6	Conclusions . . . . .	58
<b>4</b>	<b>Building Intuition of Iron Evolution during Solar Cell Processing through Analysis of Different Process Models</b>	<b>61</b>
4.1	State-of-the-Art of Technical Computer Aided Design (TCAD) for Crystalline Silicon PV . . . . .	61
4.2	Description of 8 Silicon PV Process Models . . . . .	64
4.2.1	Systematic variation of model elements . . . . .	64
4.2.2	Four structural defect distributions . . . . .	66
4.2.3	Two sets of iron-precipitation equations . . . . .	67
4.3	Simulated solar cell fabrication processes . . . . .	69
4.3.1	Crystallization and re-heating: processes without a phosphorus-rich boundary layer . . . . .	70
4.3.2	Phosphorus diffusion gettering and contact firing: processes with a phosphorus-rich boundary layer . . . . .	81
4.4	Conclusions . . . . .	100
4.5	Detailed description of precipitation equations Model Element . . . . .	101



<b>5</b>	<b>Synchrotron-based investigation of transition-metal getterability in <i>n</i>-type multicrystalline silicon</b>	<b>105</b>
5.1	Overview of Impurity Gettering and Process Simulations for <i>n</i> - and <i>p</i> -type mc-Si . . . . .	106
5.2	Samples, Gettering Processes, and Impurity and Lifetime Characterization Methods . . . . .	106
5.3	$\mu$ -XRF Maps of Metals and Calibrated Lifetime Maps Before and After a Wide Range of PDG Temperatures . . . . .	109
5.4	Discussion: metal redistribution is similar in <i>n</i> -type and <i>p</i> -type mc-Si during phosphorus diffusion gettering . . . . .	118
5.5	Conclusions . . . . .	122
<b>6</b>	<b>Direct measurement of Iron Content and Lifetime of individual Fe-rich precipitates in <i>n</i>-type crystalline silicon using <math>\mu</math>-XRF in on-the-fly scanning mode and <math>\mu</math>-photoluminescence</b>	<b>123</b>
6.1	Development of Flyscan Capability at Advanced Photon Source's Synchrotron Beamline 2-ID-D . . . . .	124
6.1.1	$\mu$ -XRF at Beamline 2-ID-D: Step-by-Step and On-the-Fly Scanning Modes . . . . .	124
6.1.2	Benchmarking Flyscan Mode . . . . .	126
6.1.3	Impact and Applications of Flyscan Mode . . . . .	130
6.2	Analysis of $\mu$ -XRF and $\mu$ -PL maps of Fe-rich particles in <i>n</i> -type crystalline silicon . . . . .	131
6.3	Modeling the Recombination Strength of Fe-rich Particles in <i>n</i> -type Crystalline Silicon . . . . .	131
<b>7</b>	<b>A Comparative Predictive Simulation Tool for <i>n</i>-type and <i>p</i>-type Crystalline Silicon for Photovoltaics</b>	<b>139</b>
7.1	Tool Description . . . . .	139
7.2	Quantifying the Electrical Impact of Iron Point Defects and Precipitates in <i>n</i> -type and <i>p</i> -type mc-Si . . . . .	141

7.2.1	Comparing Injection-Dependent and Injection-Independent Lifetime Models . . . . .	142
7.2.2	Quantifying the Relative Impact of Iron Point Defects and Precipitates in <i>n</i> - and <i>p</i> -type mc-Si . . . . .	147
7.3	Comparing Simulation Predictions and Experimental Results for <i>n</i> -type mc-Si . . . . .	150
7.3.1	Accounting for Enhanced Precipitation due to Co-Location of Multiple Metals . . . . .	153
<b>8</b>	<b>Sensitivity analysis to guide PDG processing for <i>n</i>-type mc-Si and <i>p</i>-type mc-Si</b>	<b>157</b>
8.1	Defining Test Processes and Initial Total Iron Concentrations . . . . .	157
8.2	Base Cases: Iron Distributions and Injection-Dependent Minority Carrier Diffusion Lengths . . . . .	159
8.3	Minority Carrier Diffusion Length Sensitivity Plots for <i>n</i> - and <i>p</i> -type Si	163
<b>9</b>	<b>Injection-Dependent Efficiency Entitlement of Various <i>n</i>-type Si Materials</b>	<b>169</b>
9.1	Efficiency Depends on Lifetime and Injection Level . . . . .	169
9.2	Efficiency entitlement of <i>n</i> -type materials . . . . .	170
<b>10</b>	<b>Root-Cause Analysis of Light-Induced Degradation in <i>p</i>-type Multicrystalline Silicon PERC Modules</b>	<b>177</b>
10.1	Overview of <i>p</i> -type mc-Si PERC LID . . . . .	177
10.2	Root-cause analysis for PERC LID . . . . .	179
10.2.1	The case for a ubiquitous, bulk point defect . . . . .	179
10.2.2	Defect Identification Using Injection-Dependent Lifetime Spectroscopy . . . . .	180
10.3	Discussion . . . . .	182
10.3.1	The case for a metastable deep-level donor . . . . .	184
10.3.2	Possible root causes for LID . . . . .	184

10.4 Conclusions . . . . .	185
<b>11 Outlook and Implications: Vertically-Integrated Defect Engineering in Crystalline Silicon PV</b>	<b>187</b>
<b>Bibliography</b>	<b>193</b>



# List of Figures

1-1	Learning Curve for PV Module Price as a Function of Cumulative PV Module Shipments . . . . .	24
1-2	Historical PV Module Production by Technology . . . . .	25
2-1	Cell Efficiencies of Mono- and Mc-Si Over Time . . . . .	30
2-2	Predicted and actual market share of <i>p</i> -type and <i>n</i> -type mc-Si. . . . .	32
2-3	Iron Point Defect Lifetime for <i>n</i> - and <i>p</i> -type Si . . . . .	35
2-4	Efficiency vs. Lifetime for Four Simulated Cell Architectures . . . . .	38
2-5	Injection Level and Lifetime-Dependent Efficiency for Four Simulated Cell Architectures . . . . .	39
2-6	Converting between Minority Carrier Diffusion Length and Minority Carrier Lifetime . . . . .	41
3-1	Simulated PERC Wafer Structures . . . . .	47
3-2	Cell efficiency vs. % ingot height and as-grown total Fe <sub>0</sub> for different PDG t-T profiles . . . . .	48
3-3	Scenario B – Cell efficiency vs. area fraction of “cleaner” grain for different PDG t-T profiles . . . . .	49
3-4	Total Recombination Rate Across the Wafer at V <sub>oc</sub> . . . . .	50
3-5	Total Recombination Rate Across the Wafer at MPP . . . . .	51
3-6	Scenario A: Point Defect and Precipitate Lifetime . . . . .	53
3-7	Scenario B: Point Defect and Precipitate Lifetime . . . . .	53
3-8	Scenario A: Cross-Section Maps of Fe <sub>i</sub> and Precipitate Radius . . . . .	55
3-9	Scenario B: Cross-Section Maps of Fe <sub>i</sub> and Precipitate Radius . . . . .	57

4-1	Summary of the 8 Process Simulation Models . . . . .	65
4-2	Precipitate Growth Rates . . . . .	70
4-3	Spatially-Resolved Precipitation Site Density and Point Defect Distribution . . . . .	72
4-4	Crystallization Temperature and Iron Distribution as a Function of Time	74
4-5	Crystallization Temperature, Solubility, and Diffusivity . . . . .	75
4-6	Crystallization Temperature and Iron Distribution as a Function of Time for two Different Fe Concentrations . . . . .	76
4-7	Heating Temperature and Iron Distribution as a Function of Time . .	78
4-8	Heating Temperature, Solubility, and Diffusivity . . . . .	79
4-9	Heating Temperature and Iron Distribution as a Function of Time for Two Different Iron Concentrations . . . . .	80
4-10	Cooling Temperature and Iron Distribution as a Function of Time for Two Different Iron Concentrations . . . . .	82
4-11	3 Different Typical PDG Time-Temperature Profiles . . . . .	83
4-12	Evolution of Iron Distribution during PDG for Select Profiles . . . . .	84
4-13	Evolution of Iron Distribution during PDG for High and Low Temperatures and Iron Concentrations . . . . .	85
4-14	Summary of $Fe_i$ Concentration Before and After Gettering . . . . .	87
4-15	Post-Gettering $Fe_i$ Concentration as a Function of Initial Total Fe Concentration with Regimes Labeled . . . . .	88
4-16	4 Different Shapes of PDG Time-Temperature Profile . . . . .	91
4-17	Evolution of Temperature and Iron Distribution Over Time during Peak + PD + Cool + Anneal . . . . .	92
4-18	Evolution of Temperature and Iron Distribution Over Time during Peak + PD + Cool + Anneal for Low and High Initial Iron Concentration	93
4-19	Summary of $Fe_i$ Concentration Before and After Different Gettering Profile Shapes . . . . .	95
4-20	Evolution of Temperature and Fe Distribution Over Time After Firing	97
4-21	Summary of Average $Fe_i$ Concentration Before and After Firing . . .	98

5-1	PDG Time-Temperature Profiles . . . . .	108
5-2	ICP-MS Results: Red Zone . . . . .	109
5-3	ICP-MS Results: Red Zone and Bulk . . . . .	110
5-4	As-Grown $\mu$ -XRF Maps of Fe, Co, Ni, and Cu . . . . .	111
5-5	$\mu$ -XRF maps for 820° for 30 and 60 min . . . . .	112
5-6	$\mu$ -XRF maps of Fe channel for 3 Different PDG Processes . . . . .	112
5-7	Histograms of Fe Precipitate Distribution for 820° Processes . . . . .	113
5-8	Quantified Fe Precipitate Sizes Before and After PDG . . . . .	114
5-9	Histogram of Fe Reduction in Precipitate Sizes Before and After PDG for 820°C and 880°C . . . . .	115
5-10	All Measured Data: Fe $\mu$ -XRF maps measured before and after PDG at 820, 880, and 920°C . . . . .	116
5-11	Quantified Precipitate Sizes Before and After PDG at 820°C of two Different Lengths and 880 and 920°C . . . . .	117
5-12	PC-PL-Based Lifetime Improvement Ratios for Three Different PDG Processes . . . . .	118
5-13	PC-PL Lifetime Images for Three Different PDG Processes . . . . .	119
5-14	Energy Band Diagram of <i>n</i> - and <i>p</i> -type Doped Si as a Function of Temperature . . . . .	120
6-1	Flyscan mode $\mu$ -XRF maps of Fe for dwell times of 50, 250, and 1000 ms	127
6-2	Precipitate Sizes and Detection Limits for Several Dwell Times . . . . .	128
6-3	New Parameter Space Made Practical with 50 ms Flyscans . . . . .	129
6-4	Large-Area Correlative Microscopy Enabled by Flyscan . . . . .	130
6-5	$\mu$ -XRF and $\mu$ -PL maps of an intentionally Fe-contaminated wafer- bonded dislocation network <i>n</i> -type Si sample . . . . .	132
6-6	Cropped $\mu$ -XRF and $\mu$ -PL maps of an intentionally Fe-contaminated <i>n</i> -type Si sample . . . . .	133
6-7	Registered $\mu$ -XRF and $\mu$ -PL maps of Fe-contaminated <i>n</i> -type Si sample	134

6-8	Further cropped $\mu$ -XRF and $\mu$ -PL maps of an Fe-contaminated $n$ -type Si sample . . . . .	135
6-9	$\mu$ -XRF with individual Fe precipitates identified and numbered . . .	135
6-10	$\mu$ -XRF and $\mu$ -PL maps of Fe-contaminated $n$ -type Si sample masked for recombination activity model . . . . .	136
6-11	Recombination Strength vs. Fe Atoms/ Precipitate . . . . .	138
7-1	Comparative Simulation Tool Components . . . . .	140
7-2	Fe Distributions for Testing Simulation Tool . . . . .	141
7-3	Diffusion lengths for initial Fe concentration of $10^{12} \text{ cm}^{-3}$ . . . . .	143
7-4	Diffusion lengths for initial Fe concentration of $10^{13} \text{ cm}^{-3}$ . . . . .	144
7-5	Diffusion lengths for initial Fe concentration of $10^{14} \text{ cm}^{-3}$ . . . . .	145
7-6	Diffusion lengths for initial Fe concentration of $10^{15} \text{ cm}^{-3}$ . . . . .	146
7-7	Percent Difference in Diffusion Lengths Due to Point Defects and Precipitates in $p$ - and $n$ -type Si . . . . .	148
7-8	Percent of Diffusion Lengths Limited by Precipitates . . . . .	149
7-9	Comparison with Experimental Values: Post-Gettering Diffusion Lengths	152
7-10	Accounting for Enhanced Precipitation and Dissolution: Fe Distribution	155
7-11	Accounting for Enhanced Precipitation and Dissolution: As-Grown Diffusion Lengths . . . . .	156
8-1	Time-temperature profiles used in sensitivity study . . . . .	158
8-2	Base Case Iron Distributions for Total Fe of $10^{13}$ , $10^{14}$ , and $10^{15} \text{ cm}^{-3}$	160
8-3	Base Case Minority Carrier Diffusion Lengths for Total Fe of $10^{13}$ , $10^{14}$ , and $10^{15} \text{ cm}^{-3}$ . . . . .	161
8-4	Sensitivity of Diffusion Length to PDG Parameters for $10^{13} \text{ cm}^{-3}$ of Fe	164
8-5	Sensitivity of Diffusion Length to PDG Parameters for $10^{14} \text{ cm}^{-3}$ of Fe	165
8-6	Sensitivity of Diffusion Length to PDG Parameters for $10^{15} \text{ cm}^{-3}$ of Fe	167
8-7	Manufacturing benefits of $n$ -type Si . . . . .	168
9-1	Efficiency as a Function of Lifetime for $n$ - and $p$ -type Si . . . . .	170



9-2	Efficiency as a Function of Lifetime and Injection Level during Operation for $n$ - and $p$ -type Si . . . . .	171
9-3	Comparisons of Efficiency as a Function of Lifetime and Injection Level during Operation for $n$ - and $p$ -type Si . . . . .	172
9-4	Efficiency Entitlement for Various $n$ -type Si Materials . . . . .	173
10-1	Linearized SRH Lifetime Curves for Undegraded and Degraded States	181
10-2	Extracted Defect Parameters for the Dominant Defects in the Undegraded and Degraded States . . . . .	183
11-1	Vertically Integrated Defect Engineering . . . . .	191



# List of Tables

4.1	Equations for Precipitation Behavior Model Element . . . . .	104
6.1	Surface Area Calculations for Different Shape Precipitates . . . . .	137

# References to Published Work

Chapters 3, 4, and 5 largely appear in the following three publications:

A. E. Morishige, H. Wagner, J. Hofstetter, I. Avci, C. del Cañizo, T. Buonassisi, “Combined impact of heterogeneous lifetime and gettering on solar cell performance,” *Energy Procedia* **77**, 119-128 (2015).

A. E. Morishige, H. S. Laine, J. Schön, A. Haarahiltunen, J. Hofstetter, C. del Cañizo, M. C. Schubert, H. Savin, T. Buonassisi, “Building Intuition of Iron Evolution during Solar Cell Processing through Analysis of Different Process Models,” *Applied Physics A* **120**, 1357 (2015).

A.E. Morishige, M.A. Jensen, J. Hofstetter, P. X. T. Yen, B. Lai, D. P. Fenning, T. Buonassisi, “Synchrotron-based investigation of transition-metal getterability in *n*-type multicrystalline silicon,” *Applied Physics Letters* **108**, 202104 (2016).

Development of the flyscan capability at APS’s Synchrotron Beamline 2-ID-D described in Chapter 6 is described in the following proceeding and oral presentation:

A. E. Morishige, H. S. Laine, M. A. Jensen, P. X. T. Yen, E. E. Looney, S. Vogt, B. Lai, T. Buonassisi, “Accelerating Synchrotron-Based Characterization of Solar Materials: Development of Flyscan Capability,” 43rd IEEE Photovoltaic Specialists Conference, Portland, OR June, 2016.

In Chapter 6, measurement of iron content using  $\mu$ -XRF was performed by Ashley Morishige, Hannu Laine, and Mallory Jensen. Mapping of lifetime using  $\mu$ -PL was developed, performed, and quantified by Friedemann Heinz. Further analysis and quantification was carried out by Ashley Morishige and Hannu Laine.

Development of the simulation tool described in Chapter 7 was led by Ashley Morishige with contributions from Hannu Laine and Erin Looney.

The sensitivity analysis of Chapter 8 and the efficiency entitlement analysis of Chapter 9 were carried out by Ashley Morishige.

The module degradation study of Chapter 10 was enabled by samples, data, and insight from Kenta Nakayashiki and Andrew Li of REC and experimental design and lifetime measurements by Jasmin Hofstetter. Ashley Morishige led the writing of the manuscript in collaboration with Mallory Jensen, who contributed the lifetime spectroscopy method, and David Berney Needleman and Tonio Buonassisi, who contributed to writing the manuscript, data analysis, and interpretation.

K. Nakayashiki, J. Hofstetter, A. E. Morishige, T. A. Li, D. Berney Needleman, M. A. Jensen, T. Buonassisi, “Engineering Solutions for and Root-Cause Analysis of Light-Induced Degradation in *p*-type Multicrystalline Silicon PERC Modules,” IEEE Journal of Photovoltaics (2016). Accepted.

A. E. Morishige, M. A. Jensen, D. Berney Needleman, K. Nakayashiki, J. Hofstetter, T.A. Li, T. Buonassisi, “Lifetime Spectroscopy Investigation of Light-Induced Degradation in *p*-Type Multicrystalline Silicon PERC,” 43rd IEEE Photovoltaic Specialists Conference, Portland, OR June, 2016. Oral Presentation.



# Chapter 1

## Why Crystalline Silicon Photovoltaics?

In light of the simultaneous global challenges of climate change and the increasing demand for energy, there is a clear and urgent need to increase the adoption of renewable, cost-effective utility scale energy. Solar energy is clean and abundant: “The Sun provides Earth with as much energy every hour as human civilization uses every year” [1].

With over 100 gigawatts (GW) of photovoltaic (PV) power installed and a cumulative annual growth rate of global installed PV capacity of 55% from 2002 to 2012 [2], the global PV industry is rapidly growing, and PV is at grid parity in a rapidly increasing number of locations. In the year 2015, the average PV module sales price was  $\$0.60/W_p$ , significantly below the long-standing target of  $\$1.00/W_p$ . Figure 1-1 shows the learning curve for PV up to the year 2015 [3].

Crystalline silicon is an ideal material for PV because its 1.1 eV energy band gap efficiently absorbs the solar spectrum [4], and silicon is the second most common terrestrial element after oxygen [5], so silicon supply is unlikely to limit mass production of solar cells. Crystalline silicon PV is a proven technology with a single-junction solar cell record efficiency of 25.6% and commercially available modules with efficiencies exceeding 22% [6].

Today’s crystalline silicon solar cell research and manufacturing benefits from and

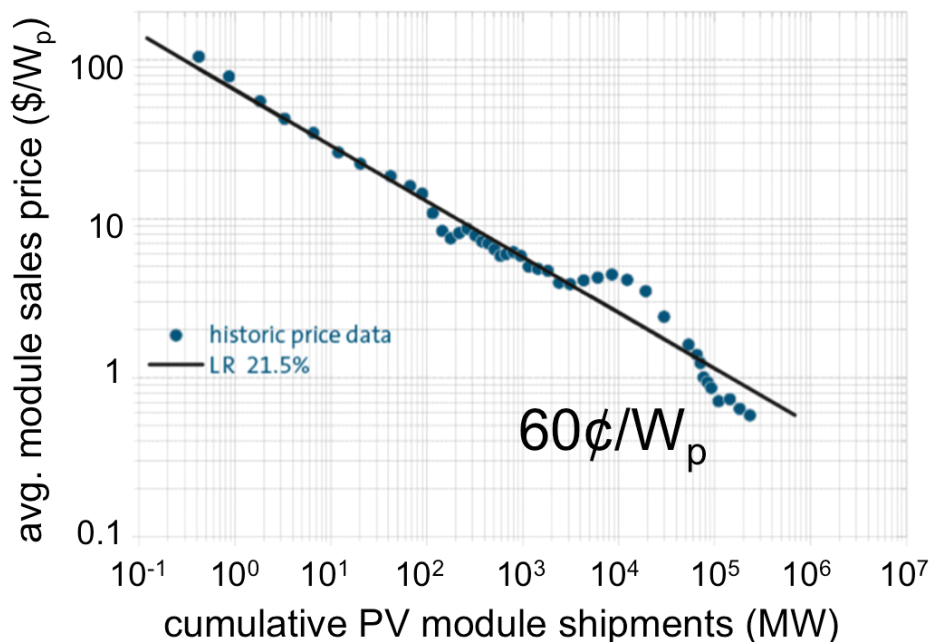
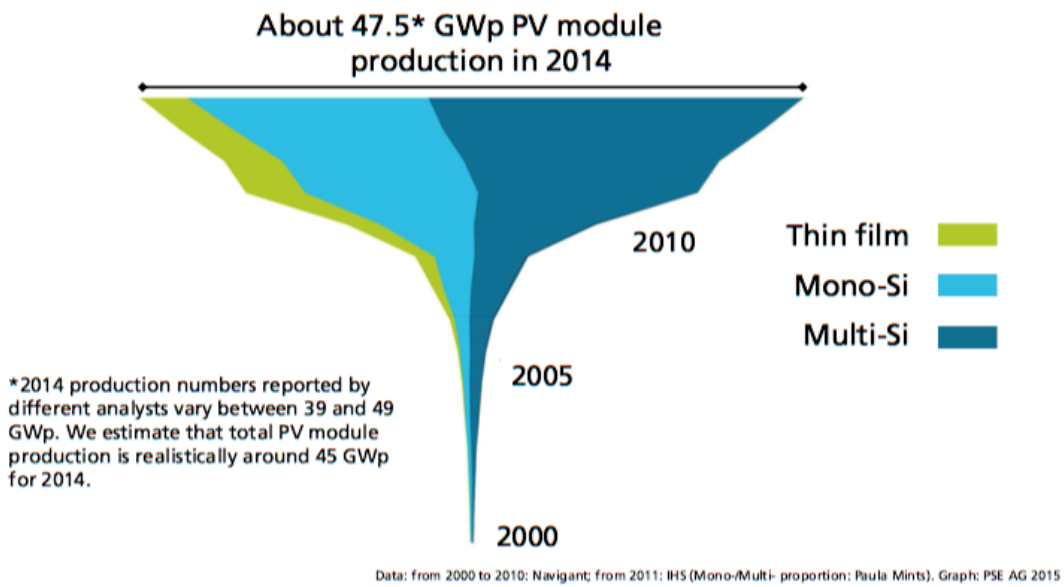


Figure 1-1: Learning curve for PV module price as a function of cumulative PV module shipments [2].

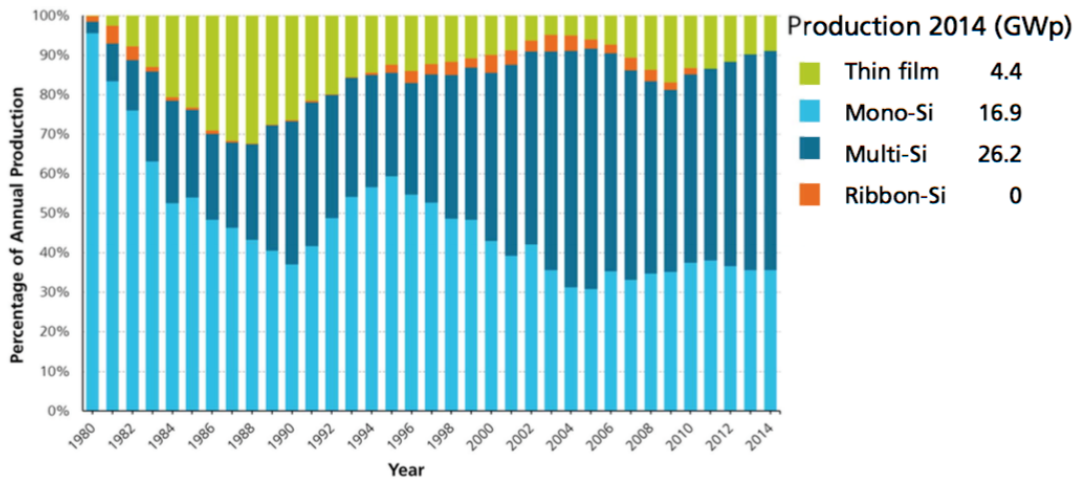
builds on over sixty years of scientific, processing, equipment, and device knowledge and investment from the integrated circuit industry [8]. Due to these strengths, crystalline silicon comprises over 90% of today’s PV market [9] (Fig. 1-2). However, PV has much more room to grow. In 2012 in the United States, just 1% of electricity was generated from solar energy, and between 2000 and 2011, the amount of electricity generated from solar energy in the United States more than doubled [10, 11]. The U.S. Department of Energy’s SunShot Initiative was launched in 2011 to accelerate the adoption of solar energy in the U.S with the goal of 14% of electricity from solar by 2030. Its SunShot Vision Study projects that solar energy will reach grid parity “when the price of solar electricity reaches about \$0.06 per kilowatt-hour over its lifetime” [12].

To realize the possibility of widespread PV use, the cost of the technology must be reduced to that of current fossil fuel energy sources. The cost of crystalline silicon PV modules is most sensitive to solar cell efficiency due to the area-dependence of the cost of module materials and installation, and the largest single contributor to the





(a) Annual PV production from 2000 to 2014 for thin film, monocrystalline Si, and multicrystalline Si.



(b) Percentage of annual PV production from 1990 to 2014 for thin films, monocrystalline Si, multicrystalline Si, and ribbon Si.

Figure 1-2: Historical PV Module Production by Technology. Crystalline silicon has dominated the market for over 25 years, and multicrystalline silicon has dominated for the last 15 years. Figures from [7].

cost of a module is the silicon wafer [13]. Reflected by its market dominance today, multicrystalline silicon (mc-Si) is the technology that balances cost and performance and has been successfully scaled to industrial manufacturing level.

Solar cells were first developed in the 1960s for space applications. It was found that *p*-type crystalline silicon cells were less prone to irradiation-induced degradation than *n*-type silicon, so *p*-type silicon became the standard and still dominates today [14]. In *p*-type silicon, recombination-active metal point defects often limit the minority carrier diffusion length of the material, reducing cell efficiency.

In a typical diffused-junction *p*-type silicon solar cell process, in addition to being the *p-n* junction formation step, the phosphorus diffusion step is the key opportunity to redistribute iron impurities because it is the longest high temperature step. Extensive research has enabled the development of metal defect process simulations and engineering guidelines for *p*-type mc-Si, pushing the material performance close to its intrinsic limit.

Phosphorus-doped, *n*-type crystalline silicon ostensibly has a higher intrinsic performance potential, because many common metal point defects are less recombination active. In *n*-type solar cells, phosphorus in-diffusion cannot be used to form the emitter region, but it can be used as a back-surface field or as a sacrificial impurity gettering step. However, the roles of other defects (*e.g.*, metal-silicide precipitates and structural defects) in *n*-type mc-Si are not well known. Thus, optimal processing conditions for *n*-type mc-Si have not been identified, and *n*-type mc-Si today remains far from its intrinsic material potential.

## 1.1 Thesis Overview

This thesis aims to enable optimized processing that improves the performance of *n*-type mc-Si, maintaining crystalline silicon wafer cost while increasing cell efficiency compared to *p*-type mc-Si. I leverage the material characterization techniques, processing approaches, and simulation tools that have been enabled the long-standing dominance and steady improvement of *p*-type mc-Si. This thesis demonstrates that

metal impurity redistribution during solar cell processing is similar in  $n$ - and  $p$ -type mc-Si but the relative electrical impact of point defect and precipitated impurities is different, requiring different approaches to processing.

In Chapter 2, I provide background information about key aspects of crystalline silicon PV, including the advantages and potential of mc-Si, key differences between and similarities of  $n$ - and  $p$ -type silicon for PV, impurities in silicon, and the importance of the injection level as a constraint and a tool.

In Chapters 3 and 4, I describe the development of new simulation tools that are applicable to  $n$ -type and  $p$ -type mc-Si. I developed a tool to visualize in 2D metal redistribution due to solar cell processing and the resulting recombination activity through the wafer cross-section. Simulating metal precipitation behavior quickly and accurately is essential to developing process simulations. Through a side-by-side review and analysis of several state-of-the-art models of varying complexity, I determined what levels of model complexity are essential to accurately capture precipitate behavior for different varieties of mc-Si material subjected to different processing conditions. The analysis also elucidated the key physics of gettering during processing.

In Chapter 5, to show that and explain why metals redistribute similarly in  $n$ -type and  $p$ -type mc-Si, I combined Fermi-level analysis with direct measurements of the metal distribution before and after a wide range of gettering processes. For both  $n$ - and  $p$ -type mc-Si, fast-diffusing species such as Cu, Ni, and Co are readily gettered while Fe persists and is removed to below detection limits only after a high-temperature gettering step. These results show that the deep understanding of metal redistribution and thus the simulation tools developed for  $p$ -type mc-Si can be directly applied to  $n$ -type mc-Si, significantly shortening the learning time for  $n$ -type mc-Si.

In Chapter 6, to answer the open question of the recombination activity of precipitated iron in  $n$ -type crystalline silicon, I directly measured the iron content and carrier distribution in the vicinity of precipitates in an intentionally iron-contaminated  $n$ -type crystalline silicon sample using  $\mu$ -XRF (elemental mapping) and  $\mu$ -photoluminescence (carrier distribution map). To carry out this relatively large-area  $\mu$ -XRF measurement, I benchmarked the use of a new scanning mode called on-the-fly scanning.

In Chapters 7–9, I introduce and perform analyses with a predictive simulation tool that compares the impact of metal impurities in  $n$ - and  $p$ -type Si. To bring the level of sophistication of modeling in  $n$ -type to that of  $p$ -type, I developed a simulation tool that calculates the redistribution of iron throughout the solar cell process and the resulting injection-dependent electrical performance of the wafer for wafers of both doping types. This tool development then enabled a one-factor-at-a-time sensitivity analysis that revealed that mitigating the negative impact of Fe-rich precipitates by dissolving them during high temperature processing is often important to maximize the performance of  $n$ -type mc-Si. This is in strong contrast to  $p$ -type mc-Si, for which Fe point defect removal during a slow cooling or low-temperature annealing step is typically critical. Overlaying injection-dependent minority carrier lifetime curves on efficiency entitlement curves predicts that even relatively impure upgraded metallurgical grade  $n$ -type mc-Si can support  $>20\%$  efficient solar cells.

Finally, in Chapter 10, I leverage the injection-dependence of the minority carrier lifetime associated with trace impurities in crystalline silicon to identify candidate defects that cause light-induced degradation in industrial  $p$ -type mc-Si PERC modules.

Building on the rich literature of  $p$ -type multicrystalline silicon, this thesis enables predictive engineering of all crystalline silicon materials from wafer growth to module performance in the field.

# Chapter 2

## Silicon PV: Crystallinity, Doping Type, Impurities, and Injection Level

### 2.1 Monocrystalline and Multicrystalline Silicon for Solar Cells

Silicon for photovoltaics is manufactured in amorphous, single-crystalline, and multicrystalline forms. Single-crystal Czochralski-grown (Cz-Si) wafers and cast multicrystalline (mc-Si) wafers continue to be the dominant PV technologies today (Fig. 1-2). Multicrystalline and monocrystalline silicon solar cell efficiencies continue to increase at a similar rate with Cz-Si at higher absolute efficiencies (Fig. 2-1) [9, 15–17]. In 2014, average industrial *p*-type Cz-Si cells were about 20% efficient while mc-Si cells were about 18.5%. The polysilicon-to-module capital expenditure for mc-Si is 10% less than that of Cz-Si, contributing to the dominance of mc-Si [18].

### 2.2 *n*-type vs. *p*-type mc-Si Wafers for PV

#### 2.2.1 Definitions

Throughout this thesis, I will refer to *n*-type and *p*-type silicon. These terms denote crystalline silicon that has substitutional impurities, called “dopants”, that are

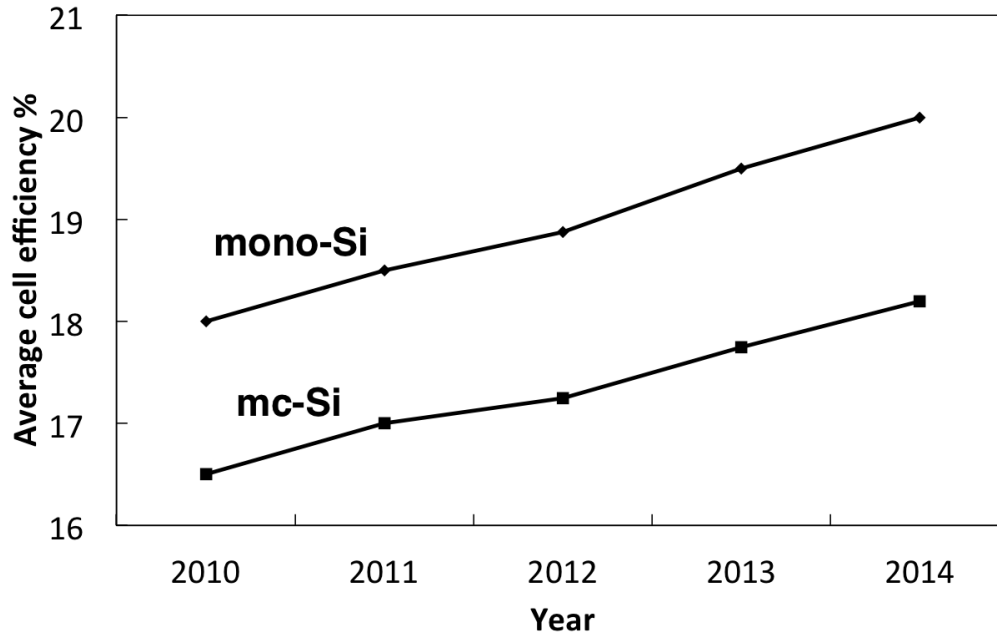


Figure 2-1: Average industry solar cell efficiencies of mono- and mc-Si from 2010 to 2014. The efficiencies steadily increase over time at a similar rate with mono-Si having higher efficiencies than mc-Si. Data from [9, 15–17].

intentionally introduced into the crystal lattice to perturb the ratio of free charge carriers in the material. *n*-type refers to a condition in which the silicon has extra free negatively charged electrons, while *p*-type refers to having extra free positively charged holes. Wafers are typically doped by introducing the dopant into the melt during ingot growth. Typical dopant elements are boron for *p*-type and phosphorus for *n*-type, both at concentrations of approximately 1 part per million, depending on the desired bulk resistivity. Silicon can be doped by many other elements as well, including aluminum and gallium for *p*-type and arsenic and antimony for *n*-type. In addition to the base doping, which is fairly uniform throughout a wafer, dopants can be introduced locally during the solar cell process by diffusion or ion implantation.

### 2.2.2 Current Status

Today, *p*-type mc-Si has outlived its predicted market share and continues to gain market share (Fig. 2-2a) [9, 15–17]. Historically, it has been predicted that *p*-type mc-

Si will lose market share, but it continues to dominate the market. This persistence is due in part to the invention of high-performance multicrystalline silicon [19]. In contrast, the quantity of *n*-type mc-Si that is commercially produced is negligible. *n*-type mc-Si was predicted in 2013 and 2014 to eventually achieve single-digits market share, but those predictions were revised to 0% in 2015 (Fig. 2-2b) [9, 15–17].

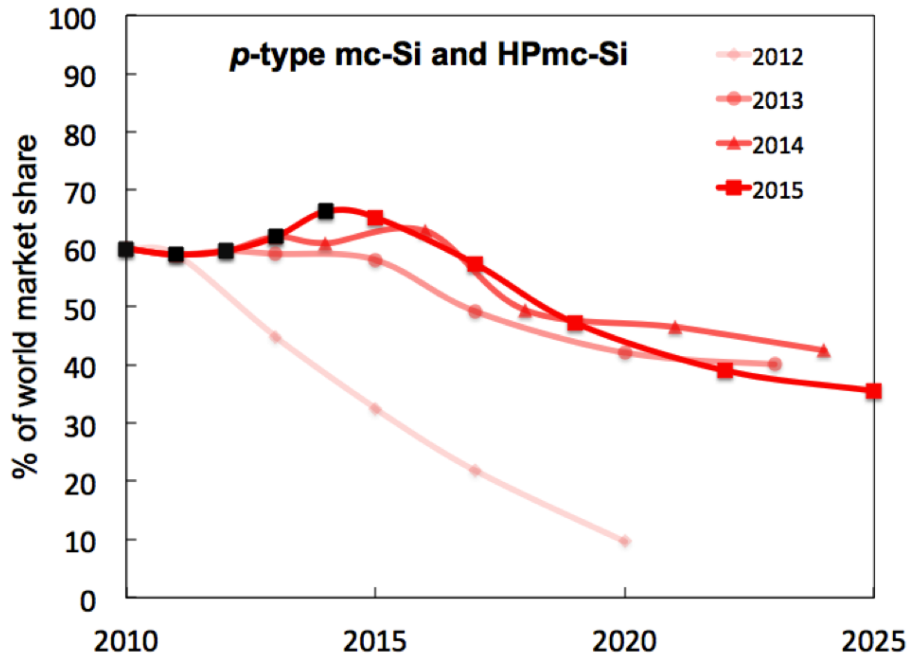
*n*-type mono-Si has been a growing percentage of the PV market and is projected to continue [9]. As of 2013, the record efficiency crystalline silicon large-area solar cell module is based on an *n*-type single-crystal wafer [20]. While there is a clear efficiency advantage of *n*-type Cz-Si over *p*-type Cz-Si, the advantage of *n*-type has not yet been realized in mc-Si. Previous studies of *n*-type mc-Si have shown that minority carrier diffusion lengths do not consistently exceed those of *p*-type mc-Si [21] and have revealed recombination-active regions that persist even after standard solar cell processing [22]. The distribution, electrical effect, and response to processing of metal impurities in mc-Si, are still open questions, especially in *n*-type Si.

## 2.3 *n*- and *p*-type mc-Si: Impurity Content, Electrical Impact, Characterization, Mitigation, and Simulation

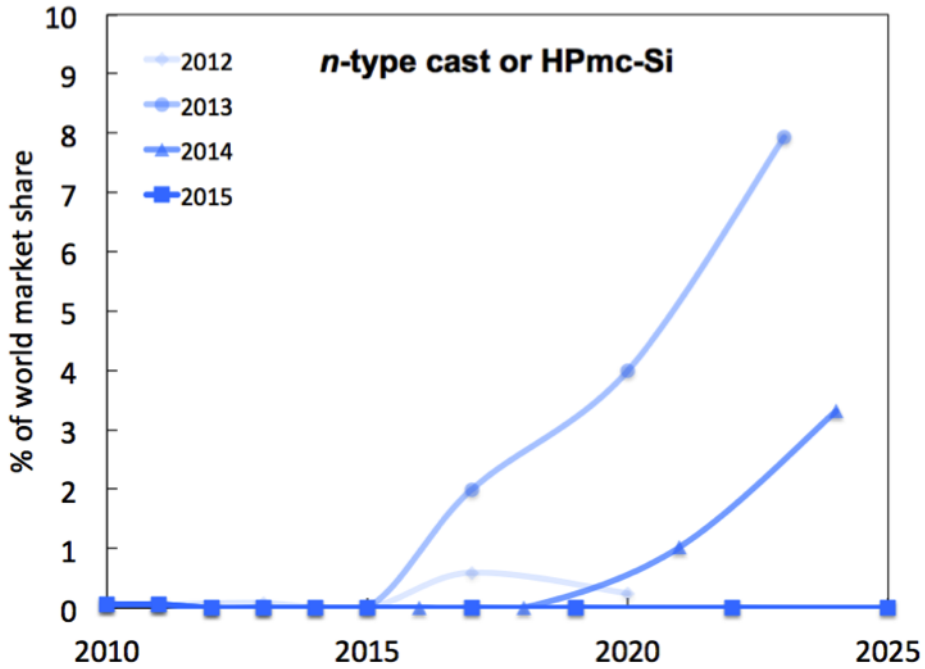
### 2.3.1 Impurity Content

Impurities, including iron, nickel, copper, zinc, and titanium, and light elements, continue to be of concern in solar cell manufacturing because they are abundant in industrial environments and can be incorporated into the ingot and wafers [23–25].

Multicrystalline silicon (mc-Si) ingots are typically cast using a directional solidification process in which molten silicon in a crucible is solidified from bottom to top. As the solid-liquid interface moves upward, metal impurities, which are more soluble in the liquid than in the solid silicon, partially segregate into the liquid fraction [26–30]. In parallel, impurities from the crucible and crucible lining diffuse into the



(a) Predicted and actual market share of *p*-type mc-Si. *p*-type mc-Si has persisted in spite of predictions that it will lose market share.



(b) Predicted and actual market share of *n*-type mc-Si. *n*-type mc-Si was predicted in 2013 and 2014 to eventually achieve single-digits market share, but those predictions were revised to 0% in 2015.

Figure 2-2: Predicted and actual market share of *p*-type and *n*-type mc-Si. Data from [9, 15–17].



solidifying ingot and also segregate into the liquid fraction. Thus, the solidification process results in a heterogeneous mc-Si ingot with a core of material with significantly reduced impurity concentrations and a shell of highly-contaminated “red zone” material.

As a result of the ingot growth process, metal impurities in as-grown mc-Si wafers are found in three forms: homogeneously-distributed atomic point defects, metal-silicide precipitates typically 10-30 nm in radius but as large as 800 nm, and rare large inclusions that are  $>1 \mu\text{m}$  in diameter. For the case of iron, the majority of the iron atoms are in precipitates that are typically distributed along structural defects in much lower densities than atomic point defects [23]. The precipitated and atomic point defect distribution of a given impurity depends on the time-temperature profile of the ingot formation, the concentration of the impurity, and the diffusivity and solubility of the impurity of interest [31, 32].

### 2.3.2 Electrical Impact of Impurities

At even parts per billion, metal impurities can be detrimental to solar cell efficiency because they introduce energy levels into the Si energy band gap [14, 33, 34]. Electron-hole pairs can readily recombine at these sites, interrupting charge carrier flow, reducing minority carrier diffusion length or lifetime and ultimately, solar cell efficiency.

Outside of thermal equilibrium the concentrations of charge carriers, electrons and holes, are perturbed from their equilibrium values. For example during illumination, photons with energy equal to or larger than that of the bandgap excite electron-hole pairs, increasing the total electron and total hole concentrations. The excess carrier density at steady-state during operation depends on the balance between carrier generation due to light and heat, carrier recombination in the cell due to radiative recombination, impurity levels, etc., and extraction of excited carriers from the metal contacts to the circuit the cell is powering. The terms “excess carrier density” and “injection level” are used interchangeably in this thesis. Because recombination-active sites are all parallel pathways for electron-hole pair recombination, the effective lifetimes is the harmonic sum of the lifetime associated with each

individual recombination pathway [35]. The minority carrier lifetime can be reduced by Shockley-Read-Hall (SRH), surface, Auger, and radiative recombination as shown in Eq. 2.1.

$$\frac{1}{\tau_{eff}} = \frac{1}{\tau_{SRH}} + \frac{1}{\tau_{surf}} + \frac{1}{\tau_{Auger}} + \frac{1}{\tau_{rad}} + \frac{1}{\tau_{other}} \quad (2.1)$$

The SRH model quantifies the recombination rate and the associated lifetime of charge carriers as a function of the energy level of an impurity relative to the energy band structure, the thermal velocities and capture cross sections of charge carriers, the excess carrier density, and the impurity concentration [36, 37]. A thorough discussion of the SRH model can be found in [38].

The energy levels and capture cross sections of common metal point defects in both *p*- and *n*-type crystalline silicon have been established [33, 39]. Notably, for iron, the capture cross section for electrons,  $1.3 \times 10^{-14}$  cm<sup>2</sup>, is 186 times greater than that for holes,  $7 \times 10^{-17}$  cm<sup>2</sup>, so iron point defects are less recombination-active in *n*-type than in *p*-type silicon [33] – one of the major benefits of *n*-type silicon. The minority carrier lifetime as a function of the iron point defect concentration calculated with the SRH equations for both *n*- and *p*-type Si is shown in Figure 2-3. Compared to *p*-type Si, for a given minority carrier lifetime, *n*-type Si can tolerate more than ten times the iron point defect concentration.

Quantifying and modeling the recombination activity of metal-silicide precipitates in both *p*-type and *n*-type silicon is an active area of research. In model systems, metal-silicide precipitates have been shown to be recombination active in both *p*- and *n*-type mc-Si [22, 40–43], but they are typically present in much lower spatial concentration than point defects. For *p*-type silicon, because iron point defects are highly recombination active, the detrimental impact of precipitates is mostly as a source of highly recombination-active point defects. A combination of simulations and experiments indicates that precipitated iron limits the border region of high-performance *n*-type mc-Si, but no direct measurements of metal-rich precipitates were performed [44]. Due to iron’s abundance in the PV manufacturing environment and

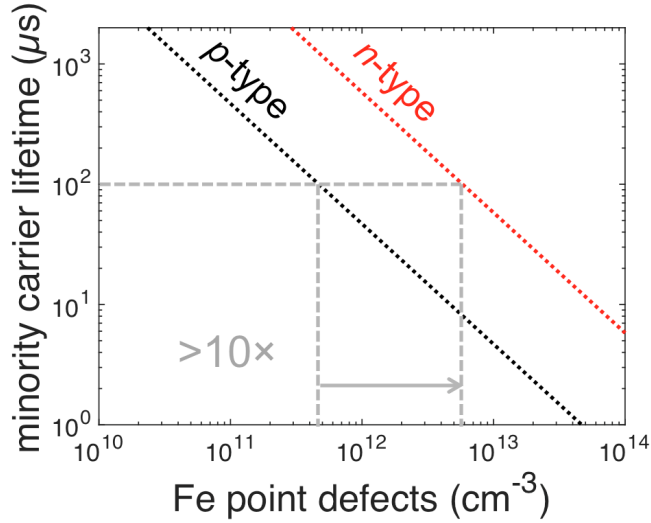


Figure 2-3: Iron point defect-related minority carrier lifetime for  $n$ - and  $p$ -type Si.

its likely still important impact in  $n$ -type mc-Si, this thesis will focus on comparing the effect of iron impurities in  $n$ - and  $p$ -type mc-Si.

### 2.3.3 Impurity Characterization

Measuring the concentration, distribution, chemical nature, and electrical effect of metals in  $n$ -type mc-Si is central to this work. Total metal concentrations can be measured with readily available mass spectrometry methods, including inductively coupled plasma mass spectrometry (ICP-MS) and secondary ion mass spectrometry (SIMS). However, these methods are destructive, and they are not suited to characterizing the heterogeneous spatial distribution of metals. Synchrotron-based micro-X-ray fluorescence spectroscopy ( $\mu$ -XRF) has been used to identify the elemental and spatial distribution of metals in  $p$ -type crystalline silicon solar cell materials and the effect of processing on those distributions [45–50]. State-of-the-art nanoprobe produce high-energy, tunable-wavelength, collimated, and high-flux photon beams with spot sizes of  $\sim 200$  nm or less, enabling the detection of down to  $\sim 10^{14}$  atoms/cm<sup>3</sup> in crystalline silicon [49]. Minority carrier lifetime can be mapped by microwave photoconductance decay ( $\mu$ -PCD) or averaged and quantified as a function of excess carrier density by quasi-steady-state photoconductance (QSSPC) or transient photoconductance decay

(PCD) [51]. Spatially-resolved recombination activity can be measured by photoluminescence imaging (PLI) [52] or at sub-micron resolution using electron beam-induced current (EBIC) [53]. In  $p$ -type mc-Si, the concentration of interstitial iron can be measured using lifetime measurements because iron pairs and unpaired with boron, and the difference in minority carrier lifetime in the two states is proportional to the iron concentration [54, 55]. However, there are no known metastable defects that one can leverage in  $n$ -type to easily measure point defect concentrations.

### 2.3.4 Impurity Mitigation

For  $p$ -type silicon, the formation of the  $p$ - $n$  junction by phosphorus in-diffusion, which enables charge carrier separation, is the longest high-temperature ( $>25$  min,  $>830^\circ\text{C}$ ) step of the solar cell process, making it the key opportunity to getter, or re-distribute and remove, metals because the solubilities and diffusivities of metals in silicon both increase exponentially with temperature [56]. The solubility of metals in the phosphorus-rich layer is much higher than that in the boron-doped bulk of the wafer because the solubility tends to increase as the Fermi level nears the conduction band [57, 58]. For  $p$ -type mc-Si, because point defects are highly recombination active, reducing point defect concentration by either relaxation gettering to precipitates and structural defects or external gettering, for example to a phosphorus-rich layer, is essential to achieving high minority carrier lifetime. Generally, higher temperatures and longer times more effectively dissolve precipitated metals, and low-temperature annealing or slow cooling drives the segregation of metal point defects to the phosphorus-rich layer [45, 59, 60]. If done effectively, phosphorus diffusion results in a purer, higher-lifetime region in the bulk of the  $p$ -type wafer.

For  $n$ -type mc-Si, there are similar benefits to gettering. Phosphorus diffusion gettering has been shown to increase minority carrier lifetime in  $n$ -type mc-Si [22, 61] because metals are more soluble in the heavily phosphorus-diffused region than the more lightly phosphorus-doped bulk of the wafer [62]. Additionally, relaxation gettering, which involves collecting metal point defects at metal-silicide precipitates, is not expected to be weaker than in  $p$ -type mc-Si [62]. While a standard solar cell

with an  $n$ -type substrate wafer has a boron-diffused emitter, phosphorus diffusion gettering of  $n$ -type wafers to increase minority carrier lifetimes is compatible with increasingly common, high-efficiency cell architectures, such as passivated emitter and rear contact devices [63]. However, the guidelines for gettering of  $n$ -type silicon are not yet clear because the relative impact of metal point defects and metal-rich precipitates and their interaction with structural defects are not well known.

### 2.3.5 Impurity Simulation

Simulation of the thermodynamics, kinetics, and lifetime impact of metals during phosphorus in-diffusion and thermal annealing provides insight about the cause of experimentally observed changes in metal impurity distribution and lifetime due to processing. A thorough review of the state-of-the-art is provided in Chapter 4.

## 2.4 Injection Level as a Constraint and a Tool

### 2.4.1 The Role of Injection Level in Solar Cells

The injection level plays a key role in determining the efficiency of a solar cell. Given the same illumination and temperature conditions and the same power demand, a higher efficiency cell tends to operate at higher injection level or excess carrier density. This effect is captured implicitly in a graph of efficiency as a function of bulk lifetime as shown in Fig. 2-4 [64]. For several different simulated solar cell device architectures, including today's typical standard back surface field (BSF) and the newer passivated emitter and rear contact (PERC), and advanced concept GaP/Si and thin GaP/Si, the efficiency tends to increase as the bulk lifetime increases up to a point. To explicitly account for the injection level dependence of the efficiency and the minority carrier lifetime, the graph can be plotted as in Fig. 2-5 [64]. In this case, the excess carrier density plotted on the  $x$ -axis is the average excess carrier density in the bulk of the wafer while the cell is operating at its maximum power point. As the excess carrier density increases, the lifetimes and the cell efficiencies increase. This method of

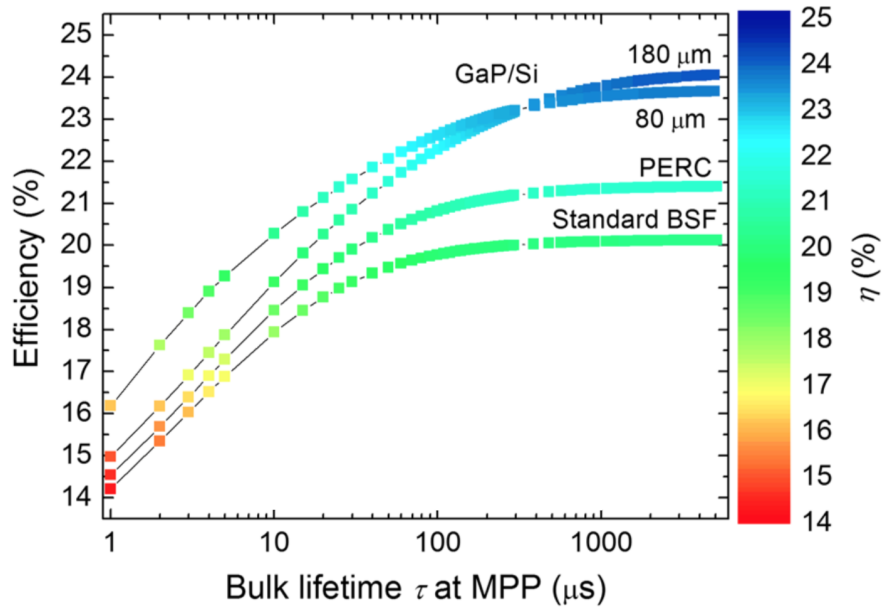


Figure 2-4: Simulated dependence of solar cell efficiency on minority carrier lifetime for four simulated *p*-type solar cell architectures. As the lifetime increases, the solar cell efficiency tends to increase. Above 100  $\mu\text{s}$ , the cell efficiency is less sensitive to the lifetime. Achieving the highest efficiencies requires  $>1$  ms lifetimes. Adapted from [64].

plotting also shows that as cell architectures improve from, for example, the Standard BSF to the PERC, the injection level at which it is important to have high lifetimes increases. Further details about the solar cell architectures mentioned here can be found in [63, 65, 66].

Also overlaid in Fig. 2-5 are measured injection-dependent lifetime curves for several different Si materials. The intersection between injection-dependent lifetime curves and the efficiency curves allows for the definition of the efficiency entitlement or maximum potential efficiency of the material assuming only the bulk lifetime limits the efficiency. For example, if one linearly extrapolates the lifetime curve of the material labelled “Gen II - Std.” is predicted to be able to support 20% Standard BSF and 21% PERC devices.

These graphs also make it clear that 1) high bulk lifetimes are required to achieve high efficiency devices, and 2) often the bulk lifetime is not constant with injection level.

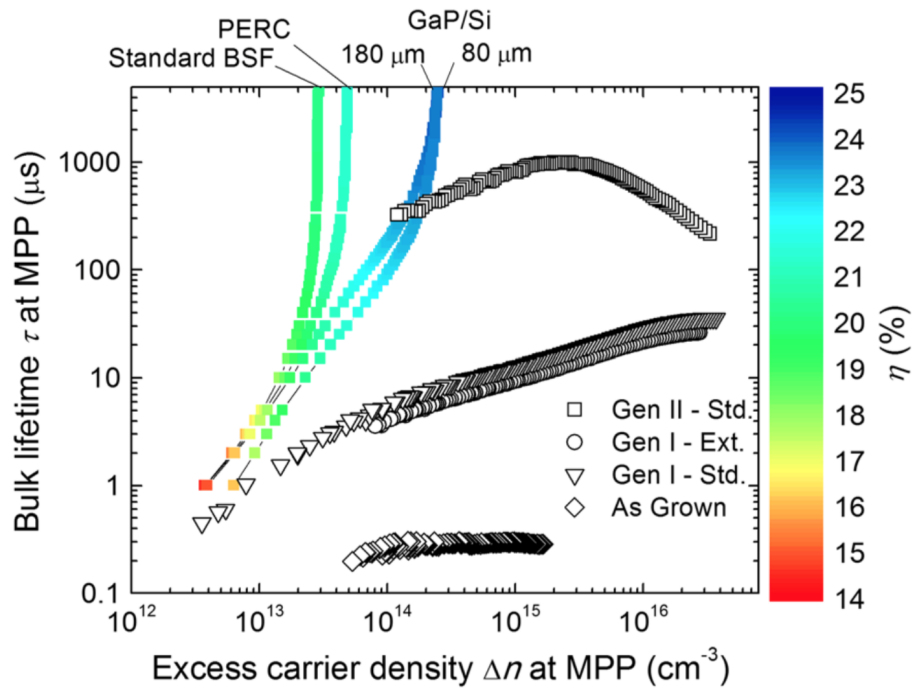


Figure 2-5: Solar cell efficiency as a function of injection level and bulk minority carrier lifetime at maximum power point for four simulated solar cell architectures. Higher efficiency architectures operate at higher injection level and require higher minority carrier lifetimes to achieve those high efficiencies. The potential solar cell efficiency is defined by the intersection between measured injection-dependent minority carrier lifetime curves and the simulated solar cell efficiency curves. Adapted from [64].

For precipitated metals in silicon, recently, an injection-dependent numerical model [67] and a parameterized analytical version of that injection level dependent lifetime model [68] was developed. The model treats the interface between metal-rich precipitates and the silicon lattice as a Schottky junction over which carriers can recombine via thermionic emission. It has been experimentally validated for both *p*-type and *n*-type samples [68].

In addition to the minority carrier lifetime, wafers can be described by their minority carrier diffusion length, which is the average distance that an excited carrier travels before it recombines. The diffusion length,  $L$ , and the minority carrier lifetime,  $\tau$ , are related by the diffusivity of the minority carrier,  $D$ , as shown in Eq. 2.2.

$$L = \sqrt{D \times \tau} \quad (2.2)$$

In this thesis, comparisons of *n*-type and *p*-type material will typically be expressed in terms of diffusion lengths while cell efficiency will typically be expressed in terms of lifetime. The diffusivity of electrons used throughout this thesis is 29 cm<sup>2</sup>/s, and the diffusivity of holes used throughout this thesis is 11.7 cm<sup>2</sup>/s. Using these values the equivalence between minority carrier diffusion length and minority carrier lifetime in *n*- and *p*-type Si is shown in Fig. 2-6.

### 2.4.2 Injection Level Dependence as a Characterization Tool

In the previous section, the injection-dependent minority carrier lifetime was calculated given a certain impurity species, chemical composition, and concentration. One can also do the analysis the other direction. The injection level dependence of the minority carrier lifetime can be leveraged to identify and quantify unknown defects in a material. This approach is referred to as lifetime spectroscopy and the theory and limitations of the approach are described in detail in [38]. Parameterizing the Shockley-Read-Hall expression for lifetime enables the extraction from a measured injection-dependent lifetime curve of 1) the energy levels and 2) the ratio of the capture cross section for electrons to the capture cross section of holes [69]. The procedure



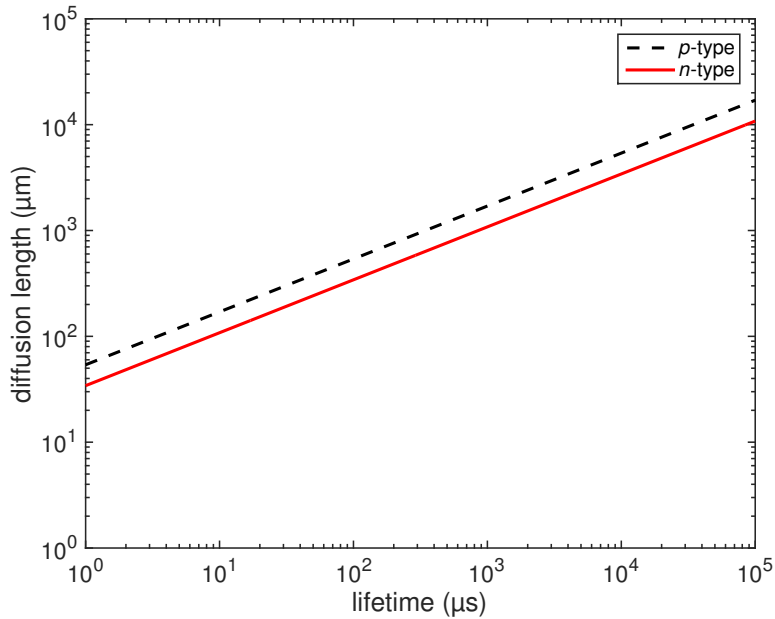


Figure 2-6: Relationship between minority carrier diffusion length and minority carrier lifetime for *p*-type Si (black dotted line) and *n*-type Si (red solid line).

followed in the module degradation study described in Chapter 10 is as follows:

- Calculate the Auger and radiative recombination components [70]
- Quantify the surface-related lifetime either through  $J_{0e}$  or through a calculation of the surface recombination velocity
- Extract the Shockley-Read-Hall-related lifetime from the measured lifetime by subtracting out the Auger, radiative, and surface components
- Plot the SRH lifetime as a function of the parameterized carrier concentration. For *p*-type Si, use  $X$ , the ratio of electrons to holes. For *n*-type Si, use  $Y$ , the ratio of holes to electrons.
- Fit the lifetime vs.  $X$  curve with one or more lines, depending on how many distinct slope values the parameterized lifetime curve has.
- From the slope and  $y$ -intercept of the lines, calculate the relationship between the capture cross section ratio and the energy level within the bandgap.



## Chapter 3

# Visualizing Metal Redistribution and Lifetime Distribution after Phosphorus Diffusion Gettering in *p*-type Multicrystalline Silicon Solar Cells

The material in this Chapter is adapted from [71].

We couple numerical process and device simulations to provide a framework for understanding the combined effects of as-grown wafer impurity distribution, processing parameters, and solar cell architecture. For this study, we added the Impurity-to-Efficiency simulator to Synopsys' Sentaurus Process software using the Alagator Scripting Language. Our results quantify how advanced processing can eliminate differences in efficiency due to different as-grown impurity concentrations and due to different area fractions of defective wafer regions. We identify combinations of as-grown impurity distributions and process parameters that produce solar cells limited by point defects and those that are limited by precipitated impurities. Gettering targeted at either point defect or precipitate reduction can then be designed and ap-

plied to increase cell efficiency. We also visualize the post-processing iron and total recombination distributions in 2D maps of the wafer cross-section. PV researchers and companies can input their initial iron distributions and processing parameters into our software and couple the resulting process simulation results with a solar cell device design of interest to conduct their own analyses. The Alagator scripts we developed are freely available online at <http://pv.mit.edu/impurity-to-efficiency-i2e-simulator-for-sentaurus-tcad/>.

### 3.1 Tailoring Processing to Crystalline Silicon Wafer Quality

Multicrystalline silicon (mc-Si) wafer quality varies widely. Total impurity concentrations and the area fraction of high defect density [72–74] both impact solar cell performance. Poorly performing areas are disproportionately detrimental [75], and wafers with higher defect concentrations are not sufficiently remediated by standard gettering [76]. Thus, treating all mc-Si wafers with the same process results in lower average efficiencies with a wider standard deviation [77]. Sorting wafers by quality, defined by the area fraction of high dislocation density, with inline photoluminescence imaging can enable better statistical process control and smaller standard deviations in cell performance [72–74]. A fast, 1D gettering model, the Impurity-to-Efficiency (I2E) Simulator [59] is a powerful tool for process optimization [60, 78], but it does not capture 2D effects. Additionally, 2D simulations enable analysis of gettering in advanced cell architectures including Passivated Emitter and Rear Cell (PERC) and Interdigitated Back Contact. For this study, we developed a 2D version of the I2E Simulator for use with Synopsys, Inc.’s Sentaurus TCAD simulation software. We couple 2D phosphorus diffusion gettering (PDG) and solar cell device simulations to define effective gettering of mc-Si wafers for two different wafer sets. Wafers in Scenario A have different total iron concentrations [ $Fe_0$ ] but the same area fraction of dislocation-rich grains (*e.g.* from different ingot heights but similar crystal structure).

Wafers in Scenario B have different area fractions of dislocation-rich grains but the same  $[\text{Fe}_0]$  (e.g. same ingot height but from different bricks). Our results present a pathway for manufacturers to identify optimal processing for wafers sorted by total impurity content and by the area fraction of defective regions.

## 3.2 Coupled 2D Process and Device Models

To simulate in 2D the redistribution of iron impurities during solar cell processing, we added the kinetics and thermodynamics of precipitates, interstitials, and their redistribution during phosphorus diffusion gettering as defined in the Impurity-to-Efficiency Simulator [59, 79] to Synopsys' Sentaurus Process via the Alagator Scripting Language [80]. The process simulation results are passed to Sentaurus Device [81] to simulate the performance of a PERC solar cell architecture. The wafer is  $p$ -type, with a resistivity of 2  $\Omega\text{-cm}$  and a thickness of 180  $\mu\text{m}$ . A distance of 1.2 mm is assumed between two front grid finger contacts, while local rear contacts are 600  $\mu\text{m}$  apart. Further details of the device architecture and simulation input parameters can be found in [66, 82]. We explicitly calculate recombination due to interstitial iron ( $\text{Fe}_i$ ) and the carrier lifetimes associated with iron-silicide precipitates ( $\text{Fe}_p$ ), and we assume a uniform 2 ms background lifetime to account for other homogeneously distributed recombination sources. The rest of the model parameters are taken from well-known physical models or fitting to experimental values.

## 3.3 Simulating the Effect of Varying Total Iron Concentration and Area Fraction of Defective Regions

We simulated three PDG time-temperature ( $t$ - $T$ ) profiles, each tailored to optimize iron removal for different  $[\text{Fe}_0]$ . All three profiles consisted of a 30-minute isothermal phosphorus diffusion step at 840°C followed by a linear cool to 500°C. The cooling

rate was varied such that the cool took 5, 20, or 100 minutes, with longer cooling times tailored to higher impurity contents. To analyse the effect of different post-processing iron distributions on efficiency, we simulated two different material Scenarios. In both Scenarios, we simulate a 600  $\mu\text{m}$ -wide simulation domain with three wafer regions: (1) a lower impurity content “cleaner” grain, consistent with low dislocation density; (2) a 6  $\mu\text{m}$ -wide grain boundary (GB); and (3) a higher impurity content “dirtier” grain, consistent with high dislocation density. We assumed spherical iron-silicide precipitates with an initial radius of 30 nm [78]. From the initial precipitate radius and the initial  $[\text{Fe}_p]$  in each wafer region, we calculated a spatial precipitate density, which remains constant as the simulated process proceeds. The precipitate densities vary several orders of magnitude across the three wafer regions.

In Scenario A (Fig. 3-1 (left)), the fraction of the wafer that was “cleaner” (low dislocation density) was fixed at 70%, and the as-grown total wafer-level iron concentration,  $[\text{Fe}_0]$ , was varied between  $4 \times 10^{12} \text{ cm}^{-3}$  (middle of a mc-Si ingot) and  $1 \times 10^{15} \text{ cm}^{-3}$  (top of a mc-Si ingot).  $[\text{Fe}_0]$  as a function ingot height was calculated as in [78], and these Fe concentrations are typical for a cast mc-Si ingot [78]. The average  $[\text{Fe}_i]$  for the chosen impurity levels varies between  $5 \times 10^{10} \text{ cm}^{-3}$  and  $7.5 \times 10^{12} \text{ cm}^{-3}$  [78], so we defined the “cleaner” grain as having  $[\text{Fe}_i]$  equal to half the average while the “dirtier” grain has twice as much  $[\text{Fe}_i]$  as the average. The “cleaner” grain was defined as having  $[\text{Fe}_p] = [\text{Fe}_i]/10$ . The “dirtier” grain (high dislocation density) had  $[\text{Fe}_p] = 50 \times [\text{Fe}_i]$ . The “cleaner” grain  $[\text{Fe}_p]$  thus varies between  $5 \times 10^9 \text{ cm}^{-3}$  and  $7.5 \times 10^{11} \text{ cm}^{-3}$ , and the dirtier grain  $[\text{Fe}_p]$  ranged from  $1 \times 10^{13} \text{ cm}^{-3}$  to  $1.5 \times 10^{15} \text{ cm}^{-3}$ , consistent with experimentally observed impurity variations within an ingot [83]. The GB was modeled with a low  $[\text{Fe}_i] = 10^{10} \text{ cm}^{-3}$  because the high spatial density of precipitates facilitates precipitation. Finally, the  $[\text{Fe}_p]$  in the grain boundary was calculated to achieve the target wafer-level  $[\text{Fe}_0]$ . The GB  $[\text{Fe}_p]$  varied from  $9.5 \times 10^{13} \text{ cm}^{-3}$  to  $5.4 \times 10^{16} \text{ cm}^{-3}$ , consistent with experimental and simulated values [84].

In Scenario B (Fig. 3-1 (right)), the as-grown wafer-level  $[\text{Fe}_0]$  was fixed, and the area fraction of the cleaner grain was varied between 67% and 87%. Two cases with different total  $[\text{Fe}_0]$  were simulated: 1)  $2 \times 10^{13} \text{ cm}^{-3}$  representing wafers in the middle

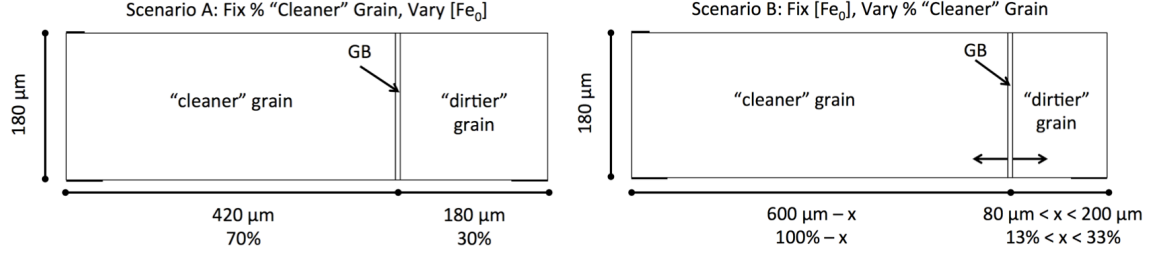


Figure 3-1: Simulated PERC wafer structure cross-section views for Scenarios A (left) and B (right). The thick, short black horizontal lines at the upper left and bottom corners of the structure are metal contacts.

of a typical mc-Si ingot, and 2)  $1.65 \times 10^{14} \text{ cm}^{-3}$  representing wafers from near the top of the ingot [78]. The  $[\text{Fe}_i]$  in each part of the wafer was selected as in Scenario A. The  $[\text{Fe}_p]$  values for the  $[\text{Fe}_0] = 2 \times 10^{13} \text{ cm}^{-3}$  and  $1.65 \times 10^{14} \text{ cm}^{-3}$  from Scenario A were used in the 70% “cleaner” grain simulations in Scenario B. Then, as the area fraction of the “cleaner” grain was increased, the  $[\text{Fe}_p]$  in the “cleaner” grain was decreased while that in the “dirtier” grain was increased to maintain a constant wafer-level average  $[\text{Fe}_0]$ . Precipitated iron in the “cleaner” grain thus ranged from  $4 \times 10^{11} \text{ cm}^{-3}$  down to  $1 \times 10^{10} \text{ cm}^{-3}$  while that in the “dirtier” grain ranged from  $3.5 \times 10^{14}$  up to  $9.3 \times 10^{14} \text{ cm}^{-3}$ .

### 3.4 Simulated Solar Cell Efficiencies

The solar cell efficiencies for each of the above-described scenarios were simulated. For both scenarios, the combination of initial iron distribution and gettering time-temperature (t-T) profile influences device efficiency. For Scenario A (Fig. 3-2), as the total as-grown  $[\text{Fe}_0]$  increases, the efficiency decreases. The 5 min cool results in a wide efficiency range of 3.5% absolute. A process that is just 15 min longer results in significant increase in efficiency and decrease in variation. For a 5 min cool, only wafers from near the middle of the ingot reach an efficiency  $\geq 20\%$ , while for a 20 min cool, all wafers up to 85% ingot height reach an efficiency  $\geq 20\%$ , increasing the yield of high-performance wafers. For example, for a specific ingot height of 90% (as-grown  $[\text{Fe}_0] = 10^{13} \text{ cm}^{-3}$ ), the 20 min cool achieves a 2% absolute gain in efficiency

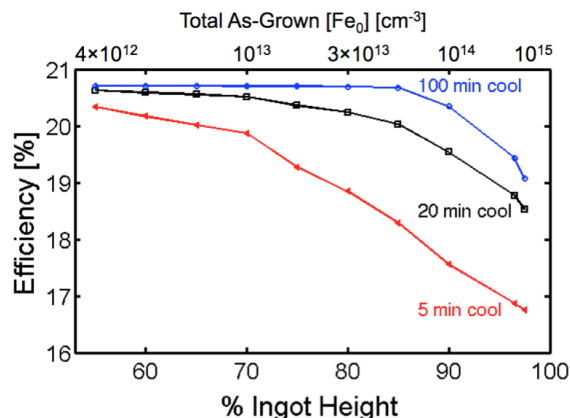


Figure 3-2: Scenario A – Cell efficiency vs. % ingot height and as-grown total  $[\text{Fe}_0]$  for different PDG t-T profiles. As the  $[\text{Fe}_0]$  increases, cell efficiency decreases significantly. As the cooling time from  $840^\circ\text{C}$  to  $500^\circ\text{C}$  increases, the cell efficiency noticeably increases.

compared to the 5 min cool. The 100 min cool achieves another 1% absolute, but at the expense of a significantly longer process. These results are consistent with those in [78], with the results updated to explicitly include the effect of recombination due to iron-silicide precipitates, an effect that is especially important for high  $[\text{Fe}_0]$  found at high ingot heights. For Scenario B (Fig. 3-3), for a given cooling time, as the area fraction of “cleaner” grain area increases, efficiency is unchanged except for the 5 min cool for the higher  $[\text{Fe}_0] = 1.65 \times 10^{14} \text{ cm}^{-3}$ . For the lower  $[\text{Fe}_0] = 2 \times 10^{13} \text{ cm}^{-3}$ , as cooling time increases, the efficiency increases, but the area fraction of “cleaner” grain appears to have no effect. For the higher  $[\text{Fe}_0] = 1.65 \times 10^{14} \text{ cm}^{-3}$ , as the area fraction of “cleaner” grain increases, the efficiency increases by 0.4% absolute for the 5 min cool and 0.16% absolute for the 20 min cool. The slow 100 min cool shows no visible difference as the area fraction of “cleaner” grain increases.

### 3.5 Visualizing the Post-Gettering Iron and Recombination Distributions in mc-Si

Solar cell efficiency depends on both the initial Fe distribution and the applied gettering process. For all the scenarios considered here, two important trends hold: 1) The



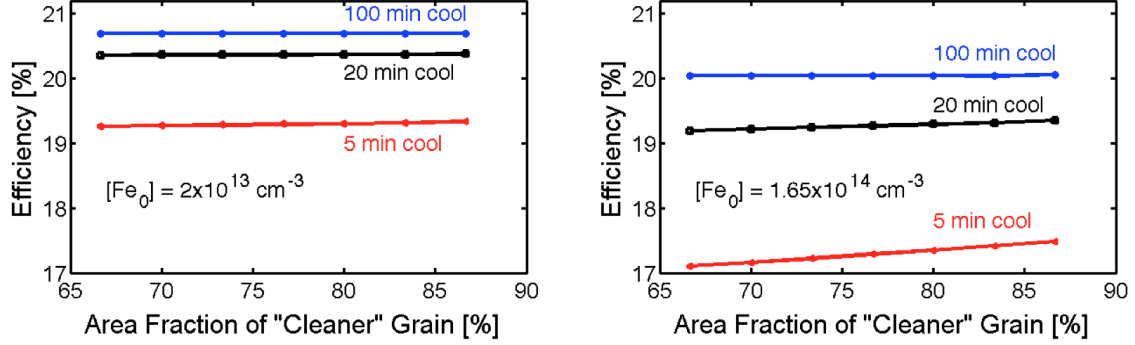


Figure 3-3: Scenario B – Cell efficiency vs. area fraction of “cleaner” grain for different PDG t-T profiles. For lower  $[Fe_0] = 2 \times 10^{13} \text{ cm}^{-3}$ , efficiency does not change with area fraction of “cleaner” grain, but a longer cooling time does increase efficiency. For the higher  $[Fe_0] = 1.65 \times 10^{14} \text{ cm}^{-3}$ , a larger area of “cleaner” grain is predicted to increase efficiency, but the length of the cool down has a much larger effect.

“dirtier” grain (on the right) is highly recombination active and 2) as the cooling time increases, the fraction of the cell that is significantly recombination active decreases. These trends are illustrated by a representative example at open-circuit voltage in Fig. 3-4 and at maximum power point in Fig. 3-5.

We observe that there are two main lifetime-limiting components after processing: one related to point defects and one related to precipitates. Once we identify which of these dominate after a given process, we can design gettering that is targeted at either point defect or precipitate reduction to increase solar cell efficiency [60]. Recombination at precipitates increases with precipitate size and spatial density [59]. The precipitate spatial density is high in the “dirtier” grain and the area fraction of the “dirtier” grain is at least an order of magnitude greater than that of the GB, so the precipitate-limited lifetime in the “dirtier” grain can limit efficiency. Fe point defects are highly recombination active in p-type Si [8], and they are more continuously distributed throughout the bulk of the wafer. To understand the overall lifetime trends, we consider an average bulk  $[Fe_i]$  to represent this distribution. Our simulations model  $Fe_i$  atoms as single defect with an energy level at 0.38 eV with capture cross sections of  $1.3 \times 10^{-14} \text{ cm}^2$  (electrons) and  $7 \times 10^{-17} \text{ cm}^2$  (holes) [85, 86]. In Sentaurus Device, the trap models explicitly account for the occupation and the space charge stored on traps while SRH lifetime models neglect these effects [81]. Nonetheless, we compare

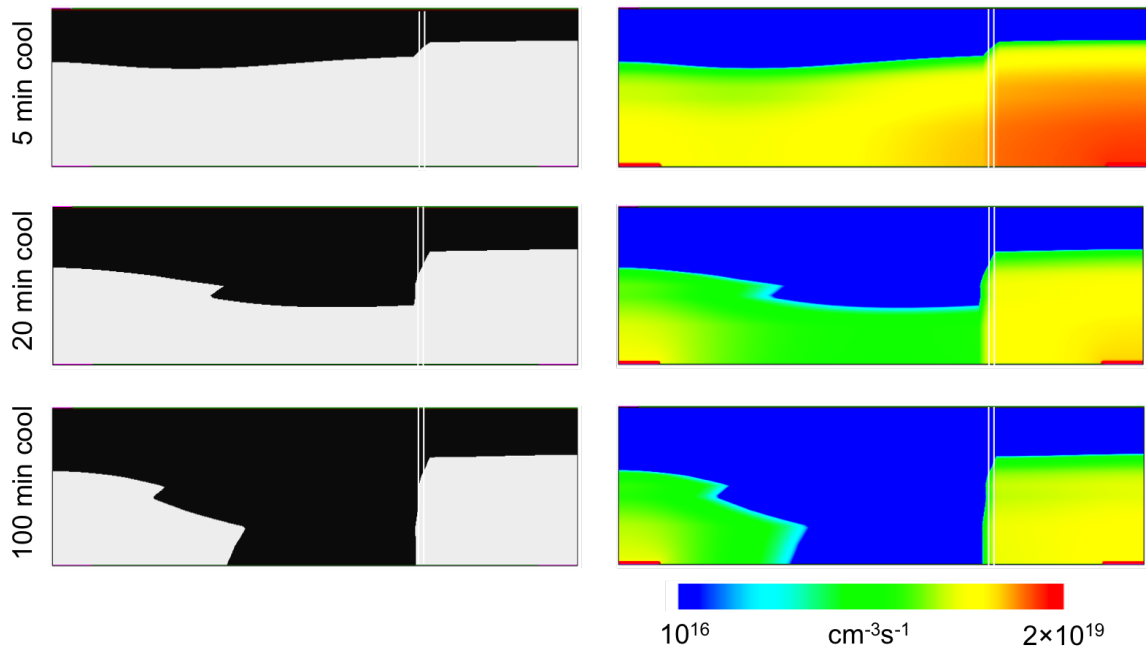


Figure 3-4: Total Recombination Rate across the wafer cross-section at open-circuit voltage – Scenario A, 75% ingot height after each gettering process. For the 5 min cool, much of the bulk is highly recombination active. For the 100 min cool, the back contacts (lower corners) and the “dirtier” grain (right quarter of image) remain recombination active. The pairs of white lines delineate the grain boundary. The wafer structure details are shown in Fig. 3-1.

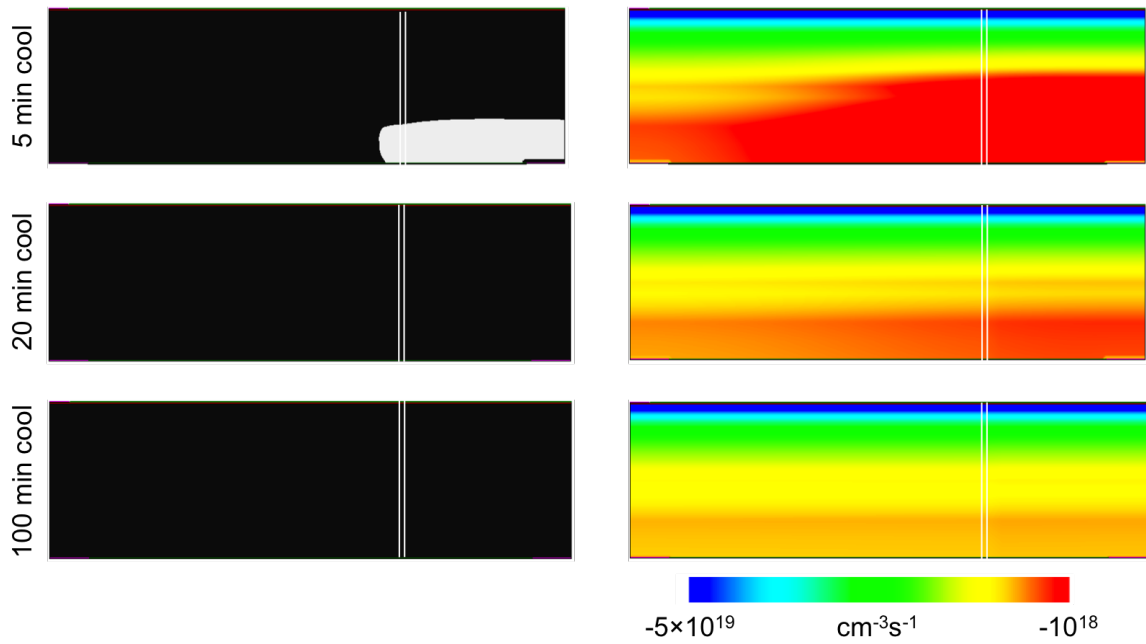


Figure 3-5: Total Recombination Rate across the wafer cross-section at maximum power point – Scenario A, 75% ingot height after each gettering process. For the 5 min cool, much of the bulk is highly recombination active. For the 100 min cool, the back contacts (lower corners) and the “dirtier” grain (right quarter of image) remain recombination active. The pairs of white lines delineate the grain boundary. The wafer structure details are shown in Fig. 3-1.

the electron lifetime due to precipitates in the “dirtier” grain and Shockley-Read-Hall (SRH) recombination due to the average  $[\text{Fe}_i]$  in the bulk. The precipitate lifetime model is from [59], and we assume a homogenous injection level of  $4 \times 10^{13} \text{ cm}^{-3}$  in the device at maximum power point and capture cross-sections of  $\text{Fe}_i$  as stated above for the SRH lifetime. Differences in the trap recombination and SRH lifetime models may account for any discrepancies between the efficiency trends in Fig. 3-2 and 3-3 and the lifetime trends in Fig. 3-6 and 3-7. For a given combination of initial Fe distribution and gettering process, the defect lifetime that is lower (point defects or precipitates) limits the effective lifetime. The point defect-related and precipitate-related minority carrier lifetimes and the effective lifetime given by the inverse of the harmonic sum of the precipitate, point defect, and background lifetimes are shown in Figs. 3-6 and 3-7. For Scenario A (Fig. 3-6),  $\text{Fe}_i$  limits the lifetime when external gettering of point defects to the phosphorus-rich layer is insufficient. For the 5 min cool,  $\text{Fe}_i$  limits lifetime with the exception of the most impure wafer at 97.5% ingot height with a total  $[\text{Fe}_0] = 10^{14} \text{ cm}^{-3}$ . The effective lifetimes for the 5 min cool range from 124  $\mu\text{s}$  to 3  $\mu\text{s}$ . For the 20 min cool,  $\text{Fe}_i$  limits lifetime up to 90% ingot height with a total  $[\text{Fe}_0] = 10^{14} \text{ cm}^{-3}$ . The effective lifetimes for the 20 min cool are higher and range from 343  $\mu\text{s}$  to 5  $\mu\text{s}$ . Finally, for the 100 min cool,  $\text{Fe}_p$  is predicted to always limit the lifetime because the slow cool effectively decreases the point defect concentration. The effective lifetimes are the highest of the three processes, ranging from 655  $\mu\text{s}$  to 5  $\mu\text{s}$ . For all three processes, above 80% ingot height ( $[\text{Fe}_0] = 10^{14} \text{ cm}^{-3}$ ), the precipitate lifetime starts to sharply decrease because the post-processing  $[\text{Fe}_p]$  is significant.

For Scenario B, the lifetime values vary less because the wafer-level  $[\text{Fe}_0]$  is held constant. For the lower  $[\text{Fe}_0] = 2 \times 10^{13} \text{ cm}^{-3}$ ,  $\text{Fe}_i$  limits for the 5 min and 20 min cools, and, due to effective point defect gettering,  $\text{Fe}_p$  limits the 100 min cool. As the cooling time increases, the effective lifetime increases from several  $\mu\text{s}$  to 500–600  $\mu\text{s}$ . For the higher  $[\text{Fe}_0] = 1.65 \times 10^{14} \text{ cm}^{-3}$ , point defects limit the 5 min cool, and precipitates limit the 20 min and 100 min cools. Additionally, the lifetimes for both  $[\text{Fe}_0]$  levels follow similar trends, but the high  $[\text{Fe}_0]$  lifetimes are much lower than

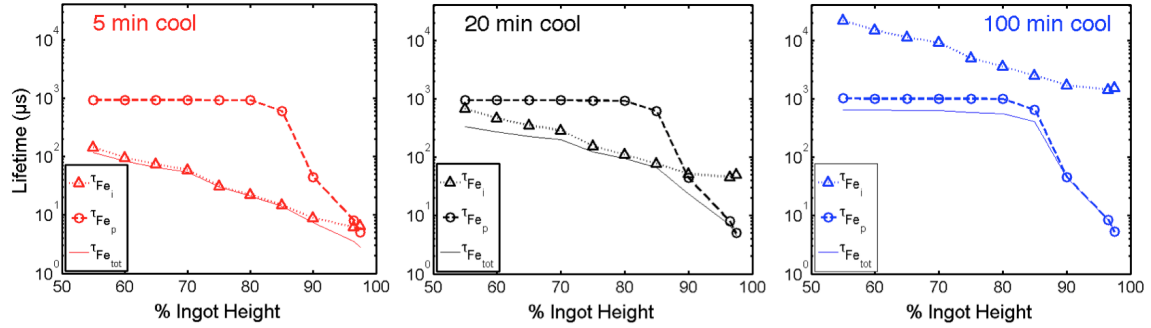


Figure 3-6: Scenario A – Minority carrier lifetimes associated with the average bulk  $[\text{Fe}_i]$  (triangles), the average “dirtier” grain  $[\text{Fe}_p]$  (circles), and the two Fe species together (solid line) after each gettering process as a function of ingot height and total  $[\text{Fe}_0]$ .

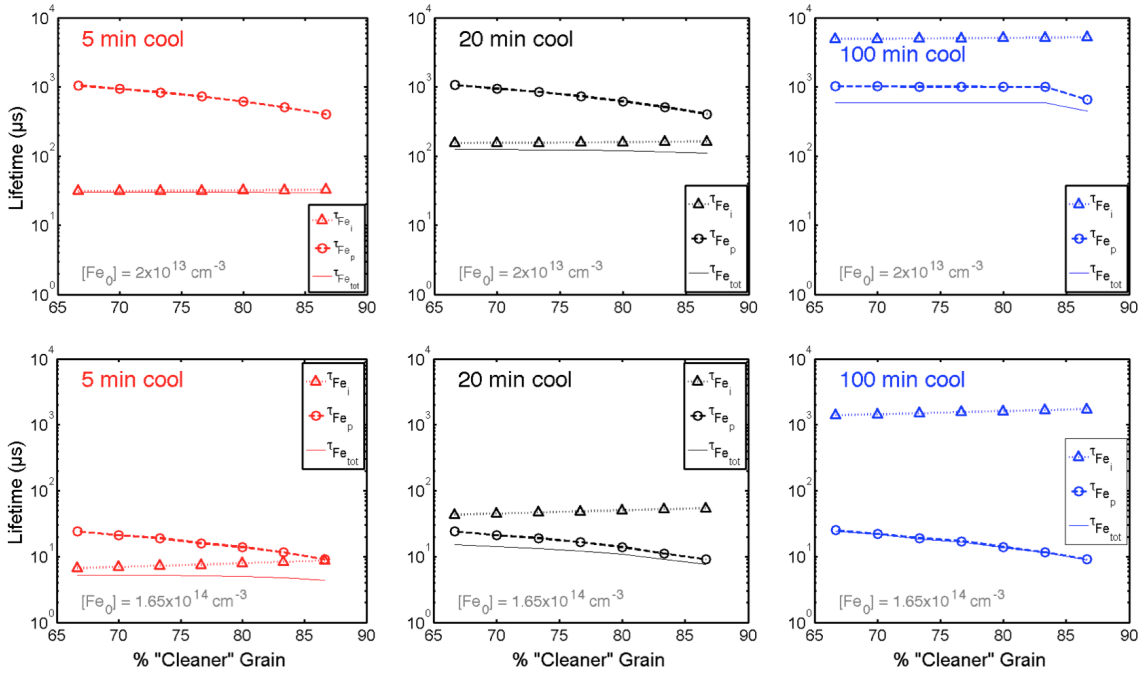


Figure 3-7: Scenario B – Minority carrier lifetimes associated with the average bulk  $[\text{Fe}_i]$  (triangles), the average “dirtier” grain  $[\text{Fe}_p]$  (circles), and the two Fe species together (solid line) after each gettering process as a function of different area fractions of “cleaner” grain for “middle” and “top”  $[\text{Fe}_0]$ .

those of the low  $[\text{Fe}_0]$ .

In both simulation Scenarios, the simulation results likely overestimate the effect of gettering on dirtier grains because the simulations do not explicitly account for the difficulty of gettering impurities from structural defects. Thus, the efficiency may be more strongly affected by the total  $[\text{Fe}_0]$  and the area fraction of dislocation-rich grains than these results indicate. Nonetheless, there are clear benefits to combining tailored phosphorus diffusion gettering with sorting wafers by  $[\text{Fe}_0]$ , and there may also be benefits to sorting by area fraction of defective regions. To elucidate the Fe distribution underlying the lifetime trends discussed above, we visualize the redistribution of Fe during processing in 2D maps (Figs. 3-8 and 3-9). We focus on the post-gettering  $[\text{Fe}_i]$  and the iron-silicide precipitate radii because the radius illustrates the precipitated iron distribution in a continuous manner. In Figs. 3-7 and 3-8, we show the post-gettering  $[\text{Fe}_i]$  and precipitate radius for four extreme cases. We show the highest and lowest  $[\text{Fe}_0]$  (% ingot heights) considered in Scenario A and the distributions for the smallest (67%) and largest (87%) area fraction of “cleaner” grain for the higher  $[\text{Fe}_0] = 1.65 \times 10^{14} \text{ cm}^{-3}$  in Scenario B. Three forces simultaneously drive redistribution of iron during phosphorus diffusion gettering of mc-Si. 1) External gettering to the phosphorus-rich layer has a “flattening” effect on the initially discrete step-function Fe distributions, leading to generally horizontal contours. 2)  $\text{Fe}_i$  diffuses down concentration gradients toward the phosphorus-rich layer and toward regions of lower  $[\text{Fe}_i]$ , including the grain boundary during initial stages of gettering and the “clean” grain during advanced stages of gettering. For these simulations, both of the grains always have an initial  $[\text{Fe}_i]$  greater than that at the grain boundary. 3) Precipitates dissolve, smoothing the  $[\text{Fe}_i]$  distribution and increasing  $[\text{Fe}_i]$ . The temperature is uniform across the wafer, so when the wafer is at high processing temperature, precipitates throughout the wafer can partially dissolve if the local  $[\text{Fe}_i]$  is lower than the solid solubility ( $1.45 \times 10^{13} \text{ cm}^{-3}$  at  $840^\circ\text{C}$ ).

The relative effects of each of these three factors depend on the processing temperatures, the amount of time spent at each temperature, and the initial concentration differences. For example, overall, the  $[\text{Fe}_i]$  decreases as the cooling time increases

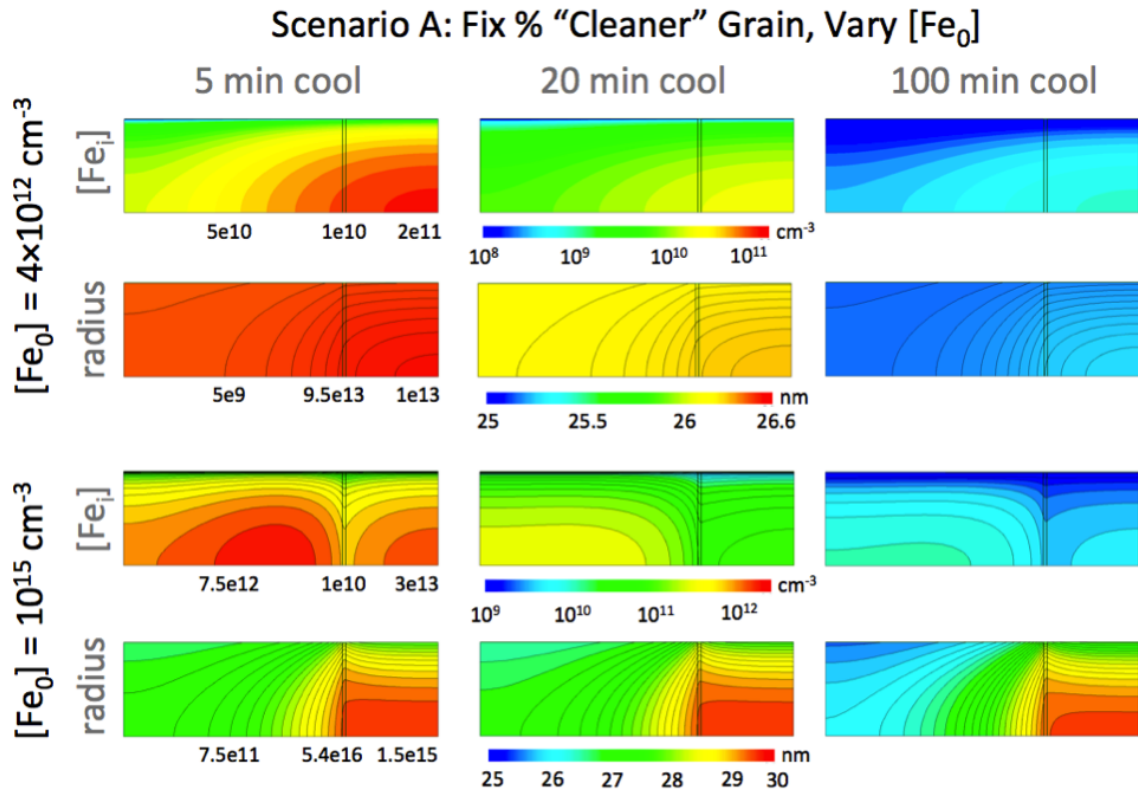


Figure 3-8: Wafer cross-section maps of the post-gettering  $[Fe_i]$  and precipitate radius for the highest and lowest  $[Fe_0]$  (% ingot height) in Scenario A. Initial  $[Fe_i]$  and  $[Fe_p]$  values in units of  $\text{cm}^{-3}$  for each wafer region are below the 5 min cool maps. Note that the color bars represent a different range of values in each of the four rows.

because point defects have more time to segregate to the phosphorus-rich layer at the wafer surface, consistent with many experimental findings [59, 60, 78, 87]. The precipitate radius slightly decreases as the cooling time increases because more time is spent at temperatures that are high enough to noticeably dissolve precipitates, and the stronger concentration gradient created by point defect segregation to the phosphorus-rich region allows for further precipitate dissolution. In the Scenario A simulations, for the low  $[\text{Fe}_0]$ , the  $[\text{Fe}_i]$  concentration remains highest in the “dirtier” grain, but for the high  $[\text{Fe}_0]$ , the  $[\text{Fe}_i]$  ends up highest in the “cleaner” grain with a spatial bias toward to grain boundary. This pattern occurs because in the low  $[\text{Fe}_0]$  case, the initial  $[\text{Fe}_i]$  are fairly similar while in the high  $[\text{Fe}_0]$  case the initial  $[\text{Fe}_i]$  range over three orders of magnitude with the GB as the minimum. Thus, in the low  $[\text{Fe}_0]$  case,  $[\text{Fe}_i]$  diffuses from the “dirtier” grain to the “cleaner” grain with minimal disruption by the GB, and simultaneously, phosphorus diffusion gettering is removing  $[\text{Fe}_i]$  from the bulk. In the high  $[\text{Fe}_0]$  case,  $[\text{Fe}_i]$  that starts in the “cleaner” and the “dirtier” grains diffuses to the grain boundary, which ends up with 1.5–2 orders of magnitude more  $[\text{Fe}_i]$  than it starts with. The superposition of the external phosphorus diffusion gettering and the flow from both grains to the GB results in two areas of high  $[\text{Fe}_i]$  after gettering. For both simulated cases, the precipitate radius remains high in the grain boundary and the “dirtier” grain because precipitates do not diffuse, so they grow and shrink in their initial locations.

In the Scenario B simulations, the same forces are at work and thus patterns similar to those in Scenario A are observed. One perhaps counterintuitive phenomenon is that the “dirtier” grain in the 67% area fraction of “cleaner” grain case has a higher post-gettering  $[\text{Fe}_i]$  than that in the 87% area fraction of “cleaner” grain case. As the “dirtier” grain in the 87% case starts with a higher  $[\text{Fe}_p]$ , one might assume that it should end up with a higher  $[\text{Fe}_i]$ . The pattern shown by the simulations occurs because a smaller impure grain has a smaller volume from which to diffuse a given impurity concentration. A smaller volume can be “cleaned up” and smooth the concentration gradient more quickly than a larger volume. The  $[\text{Fe}_i]$  conditions considered here are the same initially for each  $[\text{Fe}_0]$  in Scenario B, so the initial total



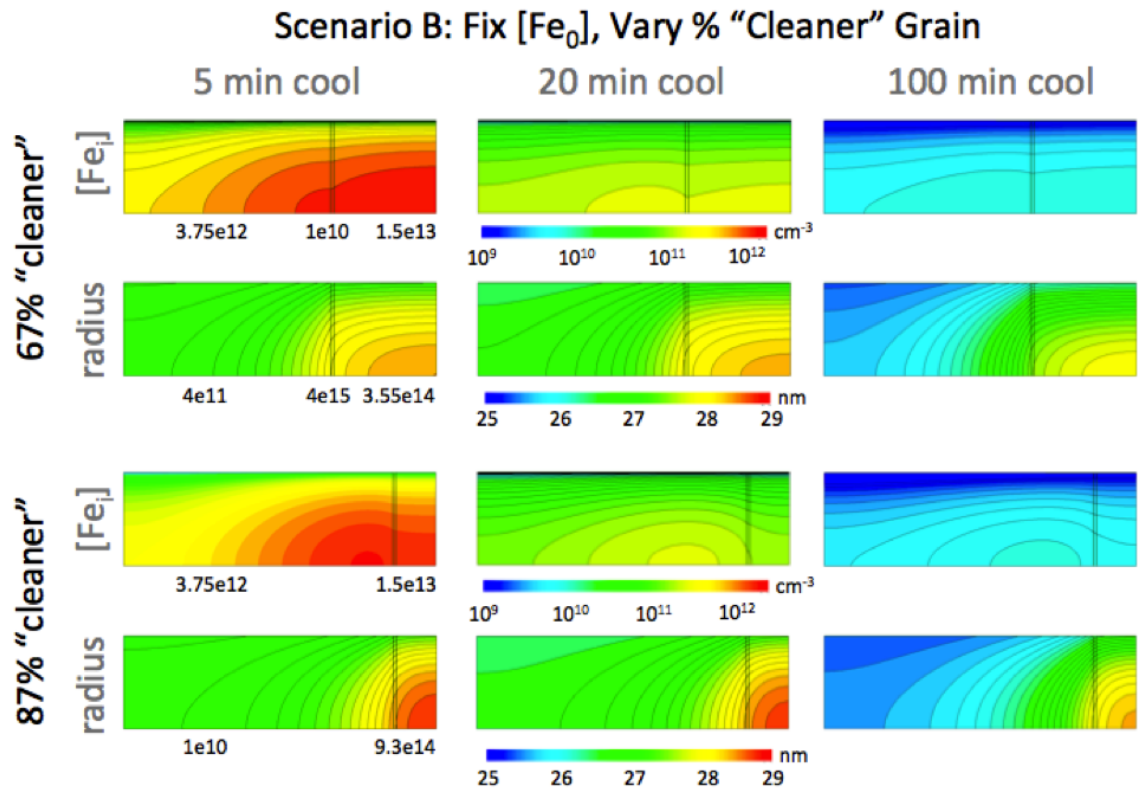


Figure 3-9: Wafer cross-section maps of the post-gettering  $[Fe_i]$  and precipitate radius for smallest and largest area fraction of “cleaner” grain in Scenario B for  $[Fe_0] = 1.65 \times 10^{14} \text{ cm}^{-3}$ . Initial  $[Fe_i]$  and  $[Fe_p]$  values in units of  $\text{cm}^{-3}$  for each wafer region are below the 5 min cool maps. The GB initial conditions are the same for the 67% and 87% “cleaner” simulations. Note that the color bars represent a different range of values in each of the four rows.

wafer-level average  $[\text{Fe}_i]$  is lower for the 87% than the 67% area fraction of “cleaner” grain. This pattern in the initial  $[\text{Fe}_i]$  may account for the increase in efficiency observed in the  $[\text{Fe}_0] = 1.65 \times 10^{14} \text{ cm}^{-3}$  simulations. In contrast to the  $[\text{Fe}_i]$ , the  $[\text{Fe}_p]$  is initially higher in the 87% “cleaner” case than in the 67% cleaner case and remains higher after processing. The relative recombination activity of point defects and precipitates determines which species limits device performance. For example, the lifetime patterns seen here may be different for *n*-type Si, in which  $[\text{Fe}_i]$  is less recombination active than in *p*-type Si.

### 3.6 Conclusions

We coupled 2D process and device simulations by adding the Impurity-to-Efficiency simulator to Synopsys’ Sentaurus Process software using the Alagator Scripting Language to understand and visualize the combined effect of as-grown wafer impurity distribution, processing parameters, and solar cell device architecture on device performance for two different sets of mc-Si wafers. In Scenario A, we varied total iron concentration ( $[\text{Fe}_0]$ ) and maintained the same area fraction of “dirtier” grains (e.g., different ingot height from the same brick). In Scenario B, we varied the area fraction of “dirtier” grains but maintained the same  $[\text{Fe}_0]$  (e.g., same ingot height but from different bricks). From Scenario A, we confirm that increasing  $[\text{Fe}_0]$  results in decreasing solar cell efficiency, and that slower cooling after phosphorus diffusion gettering can confer significant efficiency increases (a few % absolute) by gettering  $\text{Fe}_i$ . The updated efficiency calculations shown herein explicitly account for the detrimental effect of precipitated and interstitial iron, especially for high iron concentrations. From Scenario B, we conclude that the spatial distribution of the same total amount of iron can affect solar cell device performance with a large area fraction of “cleaner” grains increasing efficiency for the parameters considered here. However, the cooling rate after gettering is a much more important factor. The 2D maps of the post-gettering Fe distribution allow us to visualize the superposition of 1)  $\text{Fe}_i$  segregation to a gettering layer, 2)  $\text{Fe}_i$  diffusion down concentration gradients to a phosphorus-rich layer and the

grain boundary, and 3) iron-silicide precipitate dissolution, which increases  $[\text{Fe}_i]$ . We identify combinations of as-grown impurity distribution and process parameters that produce solar cells limited by point defects and those that are limited by precipitated impurities. Gettering targeted at either point defect or precipitate reduction can then be designed and applied to increase cell efficiency. There are clear benefits to combining tailored phosphorus diffusion gettering with sorting wafers by  $[\text{Fe}_0]$ , and there may also be benefits to sorting by area fraction of defective regions. The Alagator scripts developed for this paper are freely available online at <http://pv.mit.edu/impurity-to-efficiency-i2e-simulator-for-sentaurus-tcad/>. PV researchers and companies can use these scripts to carry out analyses similar to the ones we demonstrate here using their own initial iron distributions, processing parameters, and solar cell device design.



## Chapter 4

# Building Intuition of Iron Evolution during Solar Cell Processing through Analysis of Different Process Models

The material in this Chapter is adapted from [32].

### 4.1 State-of-the-Art of Technical Computer Aided Design (TCAD) for Crystalline Silicon PV

Technical computer-aided design has accelerated optimization of semiconductor design and processing for the last few decades. Photovoltaic (PV) device simulators, which compute device performance on the basis of material properties and geometry inputs, are mature and ubiquitous in industry [81, 88–92]. In contrast, Process Simulations are less developed. An important use of Process Simulators is to simulate the evolution of performance-limiting bulk defects in response to varying time-temperature profiles and wafer-surface conditions. As PV devices become increasingly bulk-limited [93], as new wafer materials are developed, and as PV manufacturing becomes even more cost competitive, there is an increasing need for accurate and fast Process Simulations to maximize the potential of each substrate.

A common focus of defect-related Process Simulators is iron, one of the most ubiquitous, detrimental [94] and easily detected [54, 55] impurities in *p*-type PV-grade silicon. Iron can take different forms in silicon: point defects (including interstitials, interstitial-acceptor pairs, and substitutional atoms), iron-silicide precipitates (including the similar  $\alpha$ - and  $\beta$ - phase precipitates, and early-stage  $\gamma$ -phase platelets), and inclusions. Interstitial iron and  $\beta$ -phase precipitates are the most relevant for crystalline silicon photovoltaics. See [23, 24, 28, 56, 94, 95] for further detail. The chemical state and distribution of iron impurities evolve during high-temperature solar cell processing steps [45, 60, 94, 96, 97] because of the exponential dependence of iron-point defect solubility and diffusivity on temperature. As the different states of iron exert varying impacts on minority-carrier lifetime [98], accurate modeling of iron evolution is critical to determining its impact on the finished device.

At least eight research groups have developed tools to simulate the evolution of iron during solar cell processing [59, 99–105]. These Simulators differ in two significant ways: (1) physics: they make different assumptions regarding the governing physics of nucleation, precipitation, growth, and dissolution of iron-silicide precipitates; (2) implementation: they use different coding environments, with unique mesh assumptions and numerical solvers. Most Simulators have been validated by experimental results, albeit for different processing conditions and input wafer impurity types and concentrations [59, 103, 104]. Because of differences in coding and validation, it can be difficult for a third party to compare models and determine the most relevant underlying physics for a wider range of industrially relevant processing and material conditions.

In this study, we combine into one coding environment the salient features of iron process simulators developed at Aalto University [103], Fraunhofer Institute for Solar Energy Systems [104], and Massachusetts Institute of Technology jointly with Universidad Politécnica de Madrid [59]. Our goals are: (1) to elucidate the essential physics at each process step, (2) to determine the necessary Model complexity to accurately simulate today’s materials and processes, and (3) to guide future materials, device, and process simulation development by building intuition for the behavior of

iron.

The intuition developed here for iron in  $p$ -type Si can be generalized to other metal impurities and to  $n$ -type Si. We evaluate ingot crystallization, thermal annealing, phosphorus diffusion, and contact-metallization firing. We systematically vary structural defect distribution and iron precipitation equations to create eight distinct Models, which we describe in detail with self-consistent terminology and with emphasis on the aspects that are most important for iron evolution. As simulation outputs, we report the concentration of interstitial iron ( $[Fe_i]$ ), the state with the greatest lifetime impact on  $p$ -type silicon [8, 39, 106]. We also report iron-silicide precipitate spatial density and size, as precipitates have a secondary lifetime impact [24, 95, 98], and they may be the more dominant recombination center in  $n$ -type silicon [22, 41–43, 106–109].

Notably, we identify two regimes of iron behavior, and we describe how they map onto the different Models, process conditions, and crystalline silicon wafer materials of varying type and quality:

(1) *Diffusivity-limited*: When the availability of heterogeneous nucleation sites is low, iron diffusion to precipitation sites limits precipitation. In this regime, physical assumptions regarding bulk-iron transport and precipitate nucleation can lead to variations of simulated residual interstitial iron point-defect concentrations up to an order of magnitude. This condition describes processing steps during which the annealing temperature is insufficient to dissolve all iron-silicide precipitates and iron gettering is kinetically limited.

(2) *Solubility-limited*: In this regime, the iron point-defect concentration is governed primarily by either bulk solubility, precipitate dissolution, or segregation to the emitter, which is governed by the difference between the solubility in the bulk and in the emitter. Variation between different Models tends to be small. This condition describes iron contamination levels either close to the solid solubility at the annealing temperature (e.g., the early stages of crystallization) or below the solid solubility when there is a high density of precipitation sites or strong segregation to the emitter occurs. In this regime, iron behavior can be considered at or near thermodynamic

equilibrium.

## 4.2 Description of 8 Silicon PV Process Models

We employ the following definitions consistently throughout our manuscript. Because these definitions are not universal, we capitalize them.

*Simulator*: A computer-based software tool designed to complement and accelerate trial-and-error experimentation.

*Process Simulation*: A Simulation that is carried out by a Simulator which is designed to predict defect evolution during solar cell processing, in response to varying time-temperature profiles and surface chemistry.

*Model*: The set of physics-based assumptions that drive the Simulation. In Process Simulations, the Model consists of coupled kinetic and thermodynamic equations, with both geometric and chemical boundary conditions.

*Model Element*: One of the physics-based assumptions coupled into the Simulation. Model Elements include, among others, the definition of the structural defect distributions (grain boundaries, dislocations) and the equations governing precipitation behavior (Ham's Law [110], Fokker-Planck equation [103]).

### 4.2.1 Systematic variation of model elements

To determine the Model Elements with greatest impact on predicted final iron distribution, we explore four variations of precipitation site distribution (see Sect. 4.2.2) and two iron precipitation equations (see Sect. 4.2.3), resulting in a  $4 \times 2$  matrix of eight unique Models (Fig. 4-1). This selection of Model Elements is informed by industrial relevance, and the nearly decade-long experience of iron simulation at each institution. With these eight Models we simulate the entire silicon solar cell processing sequence, with associated time-temperature profiles and changing boundary conditions (e.g., presence or absence of phosphorus in-diffusion).

The following parameters are invariant among the eight Models: The crystal grain is 3 mm wide, the wafer is 180  $\mu\text{m}$  thick, and the boron doping concentration is  $3 \times 10^{16}$



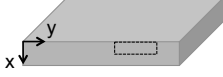
Wafer Cross-Section								
Structural Defect Distribution	Homogeneous (0D/1D)		2D Dislocations (DL)		2D Dislocations + Grain Boundary (DL+GB)		2D Grain Boundary (GB)	
Precipitate Distribution at Defects	Fokker-Planck	Ham's Law	Fokker-Planck	Ham's Law	Fokker-Planck	Ham's Law	Fokker-Planck	Ham's Law
Model Name	0D/1D FPE	0D/1D Ham	2D DL FPE	2D DL Ham	2D DL + GB FPE	2D DL + GB Ham	2D GB FPE	2D GB Ham

Figure 4-1: Summary of the 8 Models. First row: Crystalline silicon wafer cross-section schematic with simulation domain outlined. Second row: Schematics of the 4 structural defect distributions include a 0D/1D homogeneous distribution and three 2D heterogeneous distributions, including only dislocations (DL), dislocations and a grain boundary (DL+GB), and only a grain boundary (GB). The DL density colorbar is a log scale with range  $0-2 \times 10^8 \text{ cm}^{-2}$ . The phosphorus colorbar is a qualitative illustration. Third row: For each structural defect distribution, 2 sets of precipitation equations are analyzed, including Fokker-Planck equation and Ham's Law. Precipitation occurs at the structural defects. Bottom row: The shorthand Model names used in the rest of the paper

$\text{cm}^{-3}$ . We simulate phosphorus in-diffusion and gettering from both wafer surfaces. The local iron solid solubility in silicon,  $C_s$ , is provided by Aoki et al. [111]. Although strain in the silicon lattice at structural defects can enhance the solid solubility of iron [104, 112], we neglect this enhancement because it has only a minor effect on the iron distribution. Additionally, most of the solar cell processes that we simulate occur at higher temperatures where this solubility enhancement becomes negligible. The solubility and concentration gradient diffusion equations are solved by the algorithm suggested by Hieslmair et al. [113], and the diffusivity of iron,  $D_{\text{Fe}}$ , is described by Istratov et al. [56, 114]. Phosphorus diffusion is simulated as described in Bentzen et al. [115]. The phosphorus diffusion gettering model, (*i.e.*, the diffusion-segregation equation) was taken from Tan et al. [116, 117], the iron segregation coefficient as a function of phosphorus doping concentration is taken from Haarahiltunen et al. [58]. During heating, we assume a negligible precipitate dissolution energy barrier in all models – precipitates can start to dissolve the instant the solid solubility exceeds  $[\text{Fe}_i]$  [104, 118]. Lastly, we assume that structural defects are stationary and neither

generated nor annihilated by processing, as the used temperature ranges are not high enough to allow significant dislocation movement [119–121].

## 4.2.2 Four structural defect distributions

In this section, we describe the four variations of precipitation sites used in our eight Models (Fig.4-1). Precipitation sites are locations along structural defects where precipitates can, but are not required to, nucleate. The number of precipitation sites is the maximum number of precipitates allowed. While the density and distribution of precipitation sites can be varied, their nature cannot: all nucleation sites are modeled as sites along dislocations and precipitation is equally favorable at each site.

In all eight Models, including those with grain boundaries, iron-silicide precipitates are assumed to nucleate at precipitation sites along dislocations. In the 2D Models, the heterogeneously distributed intra-grain dislocations are in clusters, each of which has a dislocation density  $N_{DL}(x, y) = C \exp(-\frac{1}{2}(\frac{(y-y_0)^2}{L})^3 - \frac{1}{2}(\frac{(x-x_0)^2}{L})^3)$  where  $C$  is the peak precipitation site density in the dislocation, parameter  $L = 15 \mu\text{m}$  adjusts how fast the dislocation density is reduced from the center of the cluster, and  $x_0$  and  $y_0$  are randomly chosen coordinates that determine the location of the centrum of the dislocation cluster.  $C$  is scaled so that the average dislocation density per area is  $N_{\text{avg}} = 8 \times 10^3 \text{ cm}^{-2}$  within the grain. Then, the dislocation density of node points with dislocation density  $< 10 \text{ cm}^{-2}$  is set to zero. The grain boundary is modeled as a dense band of dislocations with an areal density of  $2 \times 10^8 \text{ cm}^{-2}$ . The simulated grain boundary width is  $10 \mu\text{m}$ , which is unrealistically wide, but it is still less than 1% of the grain width, and for computational reasons we use this value. Most importantly, this grain boundary width paired with the dislocation density in the grain boundary preserves an accurate number of total dislocations and thereby precipitation sites at the grain boundary [84]. The precipitation site density,  $N_{\text{site}}$ , is proportional to the dislocation density,  $N_{DL}$ , as in  $N_{\text{site}} = 3.3 \times 10^5 \text{ cm}^{-1} \times N_{DL}$  [104].

The simplest precipitation site (defect) distribution is a homogeneous distribution. This is equivalent to a wafer with a constant dislocation density and no grain boundaries. This precipitation site distribution has the lowest computational com-

plexity: Without the presence of the phosphorus layer, only relaxation gettering, *i.e.*, the nucleation and precipitation of impurities driven by supersaturation during cooling, occurs, and it proceeds similarly in every point of the wafer. Thus, only a single simulation point is needed to fully account for the changes in the iron distribution and chemical state. If a phosphorus layer is present on either surface of the wafer, segregation gettering causes changes in the iron distribution along the wafer depth, requiring a 1D finite-element simulation. This homogeneous defect distribution is referred to as “0D/1D.”

To account for heterogeneous precipitation site distributions, we add a second dimension to our Models. The first 2D Model consists of heterogeneously distributed dislocations and no grain boundaries, representing mono-like [122–129] and epitaxial silicon [130–133]. The second 2D Model adds a grain boundary to the dislocations, simulating conventional multicrystalline silicon (mc-Si). The grain boundary is modeled as a dense network of dislocations. The third 2D Model comprises a grain boundary but no dislocations representing regions of high-performance mc-Si [19] or ribbon growth on silicon (RGS) material [134, 135], where the relative effect of the intra-grain regions are small relative to the effect of the grain boundaries. These 2D Models are referred to as the “2D DL”, “2D DL+GB”, and “2D GB”, respectively.

### 4.2.3 Two sets of iron-precipitation equations

For the Model Element to describe iron-silicide precipitate formation, either of two sets of equations can be used: one based on Ham’s law [110], and the other using the Fokker-Planck equation [103]. A rigorous mathematical description of both appears in Section 4.5. Here, we provide qualitative descriptions that are sufficiently detailed to infer differences between resulting iron distributions in subsequent sections.

Iron supersaturation is the driving force for precipitation in both sets of equations. Thus, to initiate precipitation of interstitial iron, the dissolved concentration must be sufficiently greater than the equilibrium solid solubility (*i.e.*, typically, the wafer must be cooling down).

Ham’s law assumes a density of precipitation sites that does not vary over time,

with all precipitates modeled as spheres. Mathematically, at each grid point, this is equivalent to the precipitate density being constant and the precipitate size distribution being a time-dependent delta function. Precipitate growth begins the instant iron supersaturation is achieved. This simplicity makes Ham's law computationally straightforward, yet there are certain disadvantages. The precipitate size delta function means that Ostwald ripening (*i.e.* the dissolution of small precipitates to favor the growth of large ones) cannot be modeled. The constant precipitate density implies that complete precipitate dissolution is not accurately modeled. Precipitate nucleation is also not simulated with Ham's law. For these two reasons, crystallization is not simulated with the Ham's law precipitation Model. For process steps after crystallization, including phosphorus diffusion gettering, the average density of precipitates used in Ham's law is calculated from the results of the Fokker-Planck equation-based simulation of ingot crystallization.

The Fokker-Planck equation (FPE) Model Element describes precipitate size by a distribution function, not a delta function. The time evolution of the distribution is governed by the FPE. Consequently, the precipitate density is time varying, although the precipitation site density is constant (*i.e.*, structural defect concentration is invariant). This set of equations, while computationally complex relative to Ham's law, can describe two important phenomena: (1) explicit inclusion of a precipitation site capture radius and a precipitation nucleation barrier allow for simulation of precipitate nucleation, (2) the Ostwald ripening effect mentioned above, and (3) how faster cooling from high temperature leads to higher densities of smaller precipitates (and vice versa).

It is important to highlight two subtle points about our implementation of the Fokker-Planck equation: First, precipitation does not commence instantaneously with iron supersaturation upon cooling. For a precipitate to nucleate, its radius must be greater than the critical radius determined by the Gibbs free energy. Second, we assume spherical precipitates for Ham's law and platelets for the Fokker-Planck equation Model Element. Precipitate growth depends on the degree of iron point defect supersaturation and on iron point-defect capture, which depends on the precipitate radius.

The precipitate growth rate with Fokker-Planck is higher than that with Ham's law, because the capture radius of platelets (Fokker-Planck) depends on  $n^{1/2}$  (where  $n$  is number of iron atoms per precipitate) while that of spheres (Ham's law) depends on  $n^{1/3}$ .

Both points are visible in Fig. 4-2, which shows the net precipitate growth rates for both Models (see Section 4.5) as a function of precipitate size. The effect of the differences in precipitate growth mechanisms of the two precipitation models can be summarized by comparing the two rates. Fig. 4-2 highlights three stages of iron precipitation. Although the  $x$ - and  $y$ -axis values depend on precise dissolved iron concentration and temperature, these Stages are general. In Stage I, when the degree of iron supersaturation is small, precipitates will grow in Ham's law but not in Fokker-Planck (blue dashed line indicates negative total growth rate) because below the Gibbs critical size, precipitates are unstable and tend to dissolve. In Stage II, the Gibbs free energy is favorable for precipitate formation in Fokker-Planck, leading to explosive precipitate growth at the onset of Stage II. In Stage III, the growth rate of precipitates depends on iron capture, and the subtlety of the  $n^{1/2}$  vs.  $n^{1/3}$  dependence can be observed.

### 4.3 Simulated solar cell fabrication processes

To illustrate the governing physics and to elucidate similarities and differences between the Models during realistic processing conditions, all high-temperature steps during the solar cell fabrication process are simulated, from crystal growth to contact metallization firing. Crystal growth starts from the melting temperature of silicon, when metals are dissolved, and often involves slow temperature ramps (for ingot materials, which comprise 90% of the solar market). During crystal growth, the governing physics is relaxation gettering. In contrast, all other device-fabrication steps involve relatively lower temperatures (often resulting in iron solid solubilities below the total iron concentration), relatively faster temperature ramps, and the presence of a phosphorus-rich surface boundary layer. The governing physics includes both re-

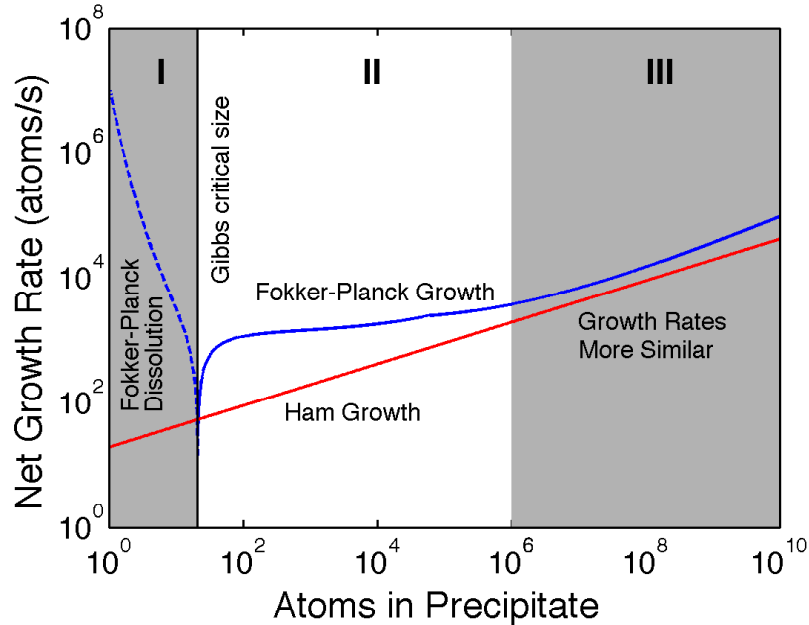


Figure 4-2: Net precipitate growth rate as a function of precipitate size for Ham’s law (red) and Fokker-Planck equation (blue), for a given annealing temperature (815°C) and iron concentration ( $10^{14} \text{ cm}^{-3}$ ). Stages I, II, and III of precipitate growth are delineated. The dashed blue line indicates negative growth (*i.e.* dissolution)

laxation and segregation gettering, the latter of which is responsible for redistributing metals on the basis of solubility differences between the bulk and the phosphorus-rich boundary layer. For each process step, we apply the framework of the *solubility-* and *diffusivity-limited* regimes introduced in Section 4.1.

### 4.3.1 Crystallization and re-heating: processes without a phosphorus-rich boundary layer

#### Crystallization

The solar cell process begins with crystallization (ingot solidification), the step that defines as-grown wafer properties. Crystal cooling starts with fully dissolved iron, and as cooling proceeds, the interstitial iron concentration decreases and the precipitated iron concentration increases. As discussed in Section 4.2.3, crystallization is simulated only with the Fokker-Planck-based Models. The crystallization cooling rate is a key parameter for controlling post-crystallization  $[\text{Fe}_i]$  [103]. For the time-temperature

profile, we assume a linear cool from 1200°C to 200°C at 1.35°C/min. We consider typical mc-Si initial total iron concentrations of  $[\text{Fe}_0] = 3.5 \times 10^{13} \text{ cm}^{-3}$  and  $2 \times 10^{14} \text{ cm}^{-3}$  both for industrial relevance and consistency with previous work [136].

The spatially-resolved precipitation site densities and the interstitial iron distributions after crystal cooling are shown in Fig. 4-3 for the 2D defect distributions with the lower contamination level of  $[\text{Fe}_0] = 3.5 \times 10^{13} \text{ cm}^{-3}$ . A strong correlation is seen between precipitation site density and low  $[\text{Fe}_i]$  because  $\text{Fe}_i$  internally getters to and precipitates at the structural defects as the silicon cools during crystallization. In all Models, regions of higher structural defect density and thus nucleation site density contain more precipitated iron after crystallization, as observed experimentally [23, 83, 137]. During subsequent processing steps, precipitated iron can reduce device performance because precipitates can limit the lifetime [98] and precipitates release iron point defects into the bulk [83, 86, 138].

To understand how the iron distribution evolves during crystallization, we plot the the temperature, solubility, and iron distribution as a function of time for the four Models for the higher  $[\text{Fe}_0] = 2 \times 10^{14} \text{ cm}^{-3}$  (Fig. 4-4). See Fig. 4-5 for the evolution of temperature, solubility, and diffusivity as function of time during the crystallization. Results for both  $[\text{Fe}_0]$  are in Fig. 4-6. For all Models, a monotonic reduction of  $[\text{Fe}_i]$  is observed.  $[\text{Fe}_i]$  is reduced by nucleation of new precipitates and growth of existing ones. At the beginning of crystallization, precipitation is at *Stage I* (see Fig. 4-2). The iron solid solubility is greater than  $[\text{Fe}_0]$  so all of the iron is dissolved as  $\text{Fe}_i$ . The FPE model includes random fluctuations in the precipitate sizes (see  $B(n,t)$  in Section 4.5), which results in a number of precipitates with sizes that oscillate between small precipitates and full dissolution. Thus, immediately, the average precipitate density is non-zero, and the average precipitate size remains at  $\sim 1$  Fe atom until  $\sim 250$  minutes. As the temperature decreases, the solubility decreases exponentially. At  $\sim 250$ -300 minutes, the supersaturation of iron point defects is high enough to favor significant precipitate nucleation, and *Stage II* precipitation begins. Precipitates nucleate and grow. Consistent with other systems undergoing phase transition [139], the growth is very rapid at this point. There is a short period of *Stage*

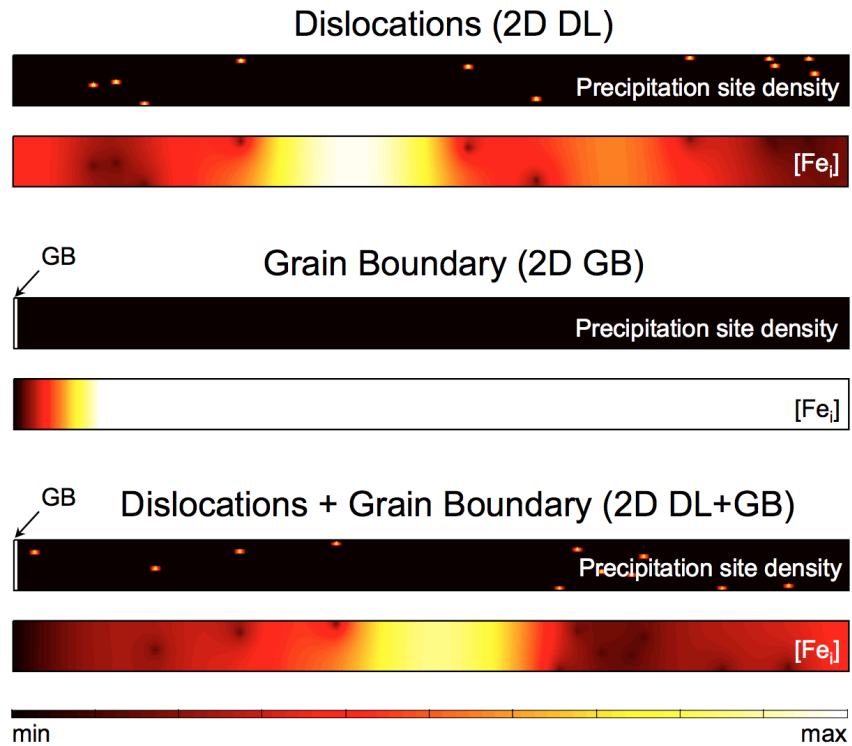


Figure 4-3: Post-crystallization spatially-resolved precipitation site density and  $[Fe_i]$  generated from input parameters for the 2D Models: DL, GB, DL + GB with  $[Fe_0] = 3.5 \times 10^{13} \text{ cm}^{-3}$ . Color scale is linear with precipitation site density range  $0-5 \times 10^{11} \text{ cm}^{-3}$  and  $[Fe_i]$  range  $0-10^{13} \text{ cm}^{-3}$ . Only the Fokker-Planck precipitation equation is used. Precipitation site density and  $[Fe_i]$  are inversely correlated because  $[Fe_i]$  is internally gettered to precipitation sites during ingot cooling



III precipitation at  $\sim 400$  minutes and then the average size slightly decreases due to the formation of new (small) precipitates and saturates as nucleation and diffusivity drop off at low temperatures. Models with higher average precipitate densities have smaller average precipitate size.

The behavior of these four Models during crystallization can be described by two regimes of iron precipitation: *diffusivity-limited* and *solubility-limited*.

Iron precipitation is *solubility-limited* when the availability of precipitation sites is relatively high, and  $Fe_i$  can readily reach precipitation sites.  $[Fe_i]$  more closely follows the equilibrium iron solubility, and is closer to thermodynamic equilibrium. During the crystallization simulated here, the first 500 minutes of the process can be considered *solubility-limited*. Between 250 and 500 minutes,  $[Fe_i]$  follows a certain level of supersaturation that trends with the exponential decrease in solubility.  $[Fe_0]$  plays a more minor role in determining  $[Fe_i]$  in the final crystal. This is the case for any Model with dislocations spread throughout the grain, including 0D/1D, 2D DL, and 2D DL+GB. The 2D DL and 2D DL+GB Models predict similar  $[Fe_i]$  because the grain boundary has a small internal gettering effect relative to the dislocations in the bulk for the parameters used. The 2D DL+GB  $[Fe_i]$  prediction of  $3\text{-}4 \times 10^{12} \text{ cm}^{-3}$  is very close to the measured as-grown  $[Fe_i]$  values for mc-Si in Hofstetter et al. [78]. The 2D GB case is an extreme case, which we show as a point of reference. Note that the 0D/1D Model predicts the largest reduction in  $[Fe_i]$ , because precipitation sites are homogeneously distributed throughout the material and are thus, on average, faster to access for  $Fe_i$  atoms.

Precipitate growth is *diffusivity-limited* when iron must diffuse to either a limited density of precipitation sites or, on average, to the far-away precipitation sites to precipitate out. The latter is the case of the 2D GB Model because the high density of precipitation sites is located in the few microns at the edge of the grain. In this *diffusivity-limited* regime, initial iron concentration  $[Fe_0]$  plays a large role in determining the iron distribution after crystallization: First, a higher  $[Fe_0]$  results in a higher density of precipitates, which translates into a higher density of  $Fe_i$  sinks. Second, if supersaturation (*i.e.*, the onset of precipitation) occurs at higher temperatures,

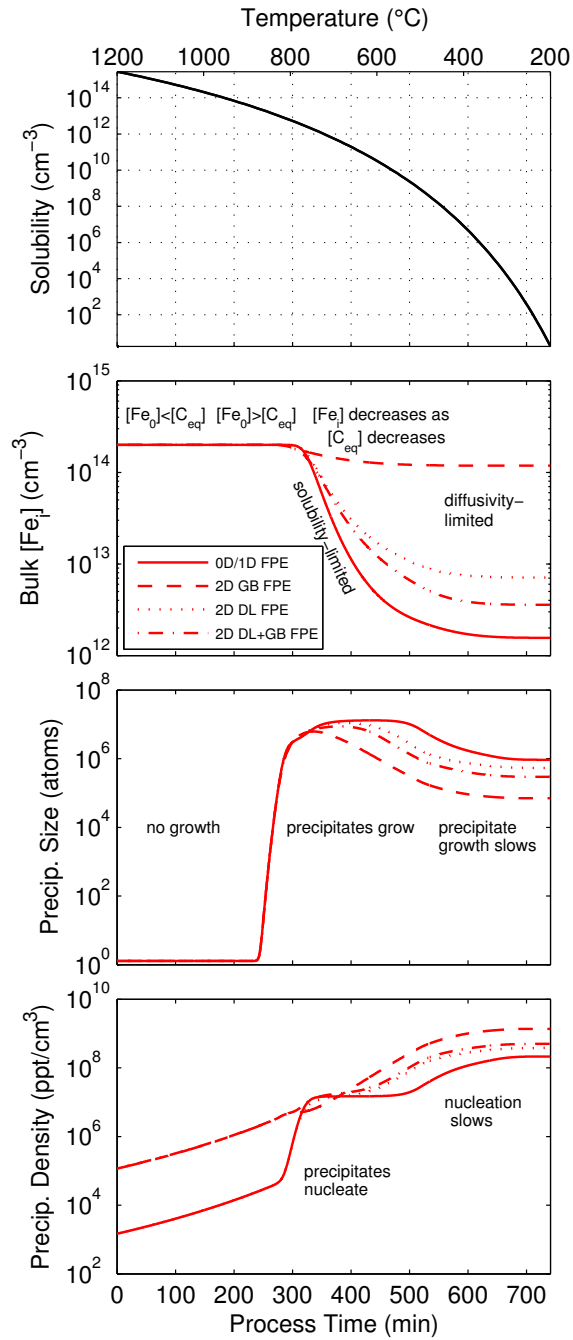


Figure 4-4: Temperature and solubility (panel 1), average bulk  $[Fe_i]$  (panel 2), average precipitate size (panel 3), and average precipitate density (panel 4) as crystallization proceeds for  $[Fe_0] = 2 \times 10^{14} \text{ cm}^{-3}$ . Precipitate nucleation and growth occur simultaneously at  $\sim 250$  minutes. The noticeable increase in precipitate size occurs before the noticeable increase in precipitate density because of the large population of the small unstable precipitates

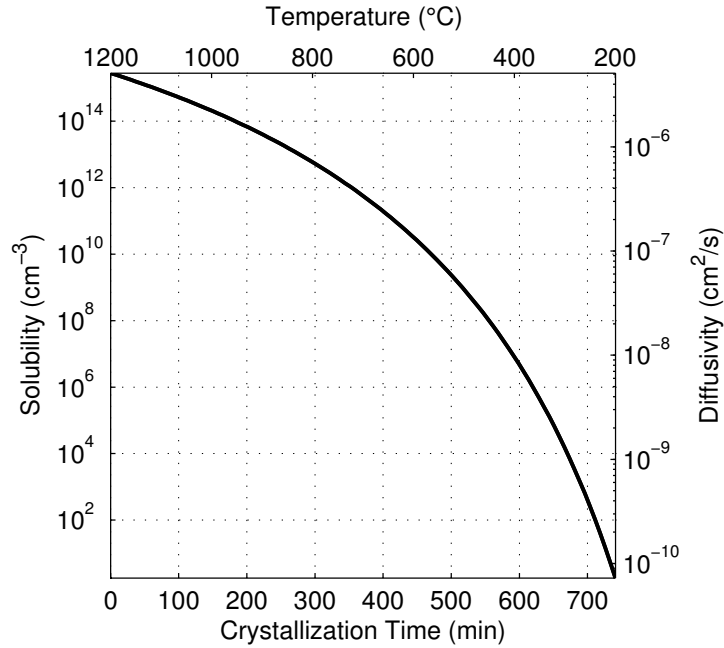


Figure 4-5: Temperature (top), solubility (left), and diffusivity (right) as a function of time (bottom) during crystallization, which is modeled as a linear cool from 1200°C to 200°C.

iron can more easily diffuse to precipitation sites, given the exponential dependence of diffusivity on temperature. Finally, precipitating iron generates a strong  $Fe_i$  concentration gradient, creating a “feedback loop” that drives more iron to precipitate; this concentration gradient is stronger with higher  $[Fe_0]$ . Thus, the effect of higher  $[Fe_0]$  is somewhat compensated at the end of crystallization, and  $[Fe_0]$  and the precipitation site (*i.e.*, structural defect) distribution together determine the resulting  $[Fe_i]$ .

All four of the Models are *diffusivity*-limited for the last ~200 minutes of the crystallization because the diffusivity of iron point defects, and thus the addition of iron to grow precipitates, decreases exponentially with temperature. In this last portion of the crystallization, the diffusivity decreases from  $5 \times 10^{-8}$  down to  $10 \times 10^{-10}$  cm<sup>2</sup>/s. This kinetic limit results in a saturation of the  $[Fe_i]$ , precipitate size, and precipitate density even though  $[Fe_i]$  exceeds the solid solubility during this part of the process.

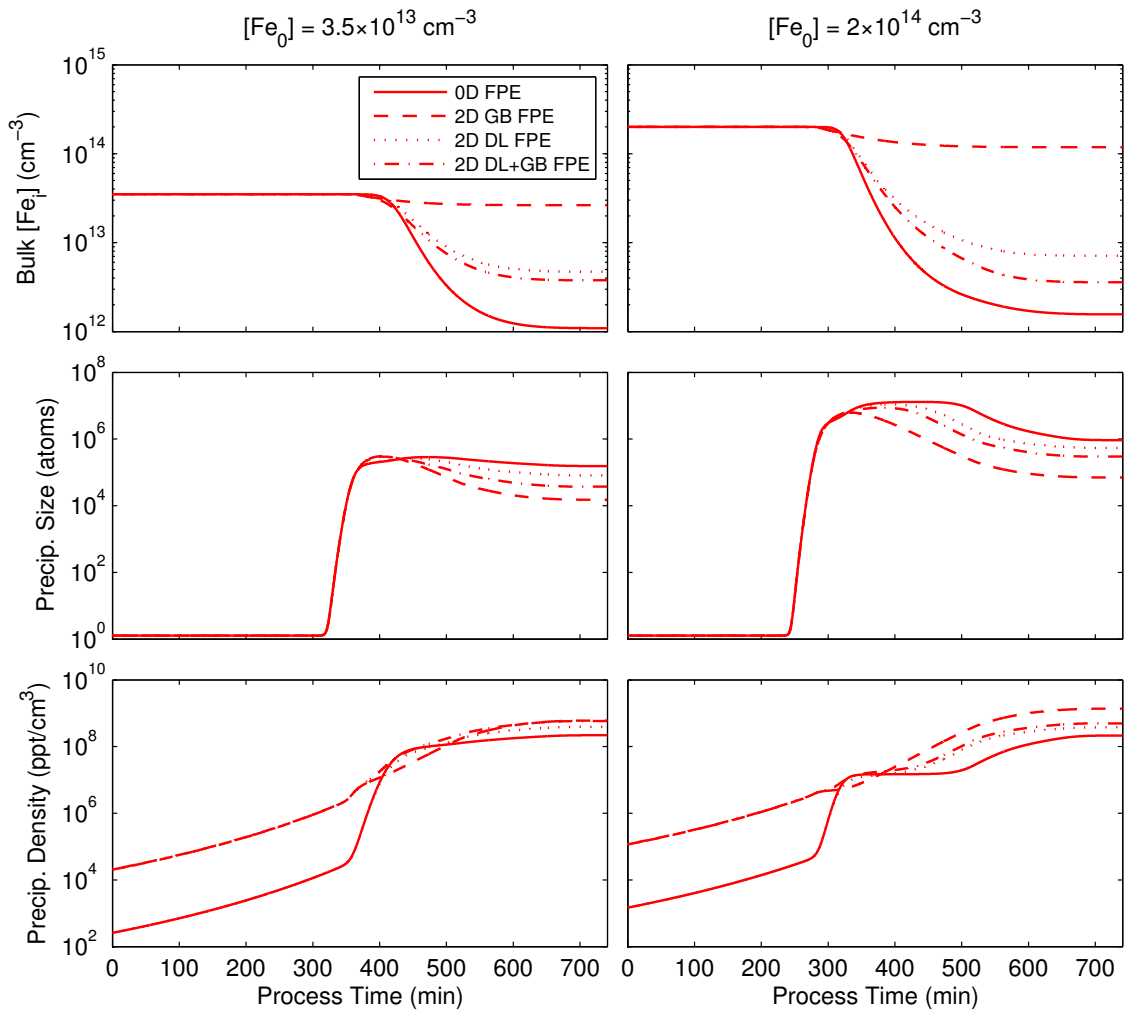


Figure 4-6: Average  $[Fe_i]$  (top), precipitate size (middle), and precipitate density (bottom) as crystallization proceeds for  $[Fe_0] = 3.5 \times 10^{13} \text{ cm}^{-3}$  (left) and  $[Fe_0] = 2 \times 10^{14} \text{ cm}^{-3}$  (right).

## Heating up to full precipitate dissolution

Ingot crystallization (Section 4.3.1) sets the initial wafer conditions and highlights the effect of the differences between the four structural defect distributions. In this section, we explore the effect of a heating step after crystallization or wafering, as has been proposed to maximize gettering efficiency in a subsequent phosphorus diffusion step [97, 104, 136, 140]. The analysis also applies for any thermal step that can be performed in the absence of a phosphorus-rich surface layer. To initialize the Ham's law Models, we use the post-crystallization average precipitate size and spatial density from the FPE Models. When calculating the average precipitate density for Ham's law, we counted only precipitates  $>10^4$  atoms to exclude the very small, but unstable, precipitates that are present due to the random fluctuations of precipitate size in the FPE Models. Thus, we can analyze the iron distribution during heating for all eight Models described in Section 4.2. We simulate heating from 500°C to 1150°C at 0.75 °C/min to examine a wide range of temperatures up through full precipitate dissolution. The temperature, solubility, average  $[\text{Fe}_i]$ , average precipitate size, and average precipitate density as a function of time during heating for  $[\text{Fe}_0] = 2 \times 10^{14} \text{ cm}^{-3}$  are shown in Fig. 4-7. See Fig. 4-8 for the evolution of temperature, solubility, and diffusivity as a function of time during heating. Results for both  $[\text{Fe}_0]$  values are in Fig. 4-9.

For all eight Models, the evolution of  $[\text{Fe}_i]$  has two phases. Early in the heating process,  $[\text{Fe}_i]$  is supersaturated, so iron diffuses to precipitates, and precipitates grow.  $\text{Fe}_i$  is in a *diffusivity-limited* regime, so the precise time at which the minimum in  $[\text{Fe}_i]$  occurs depends on the precipitation site distribution, the set of precipitation equations, and the heating rate. The significant initial change in  $[\text{Fe}_i]$  is accompanied with a barely visible change in average precipitate size and density due to the much higher amount of precipitated iron present. For the 2D GB case, the minimum in  $[\text{Fe}_i]$  occurs much later than the other Models because the high concentration of precipitates within a small volume of material creates a kinetic limitation, as iron dissolving from precipitates must first diffuse into the grain before the next layer

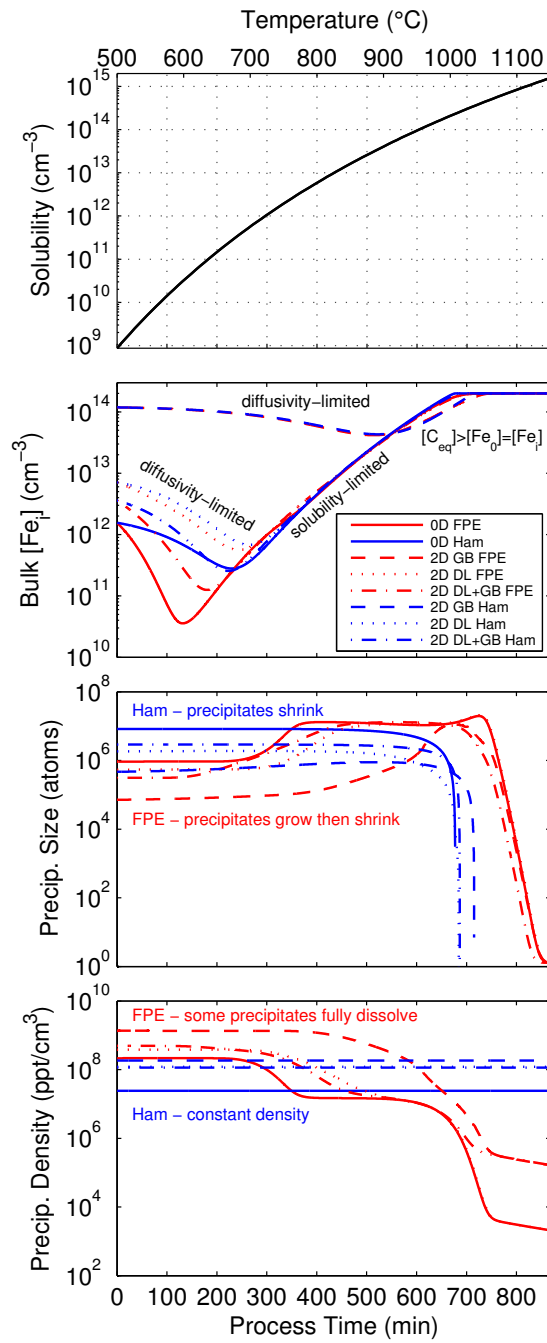


Figure 4-7: Temperature and solubility (panel 1), average bulk  $[Fe_i]$  (panel 2), average precipitate size (panel 3), and average precipitate density (panel 4) during heating linearly from 500°C to 1150°C for  $[Fe_0] = 2 \times 10^{14} \text{ cm}^{-3}$

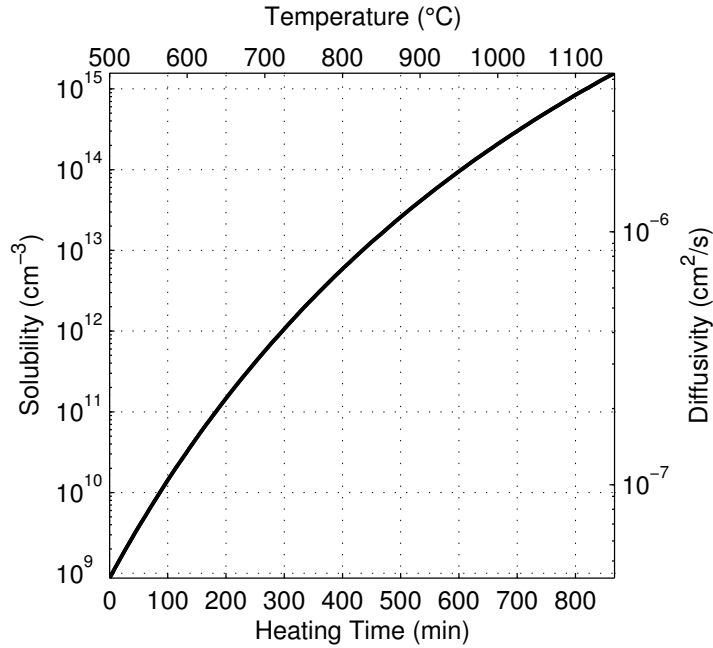


Figure 4-8: Temperature (top), solubility (left), and diffusivity (right) as a function of time (bottom) during heating linearly from 500°C to 1150°C at 0.75°C/min.

of iron can dissolve. Next, at higher temperatures after the minimum in  $[\text{Fe}_i]$ , the Models enter a more *solubility-limited* regime. Precipitates begin to dissolve, and  $[\text{Fe}_i]$  increases uniformly in all Models with most curves overlapping. All eight Models eventually reach the same state in which the solid solubility exceeds the  $[\text{Fe}_0]$ , so the average  $[\text{Fe}_i] = [\text{Fe}_0]$ , with precipitates fully dissolved.

The precipitate evolution depends strongly on the precipitation Model. The Ham's Law and Fokker-Planck precipitation equations treat the precipitate size and precipitate density oppositely; however, they result in similar  $[\text{Fe}_i]$  predictions. With the Fokker-Planck equation Models, during the first 600 min, the average precipitate size increases slightly as small precipitates dissolve, reflected in a slight drop of average precipitate density. Then the precipitate size rapidly decreases as the remaining precipitates dissolve. For Ham's law, there is a slow decrease in average precipitate size because no density change is allowed. Instead, the singular precipitate size decreases negligibly, followed by a precipitous drop as the solubility exceeds the total iron concentration, driving rapid dissolution. For Fokker-Planck, the precipitate densities

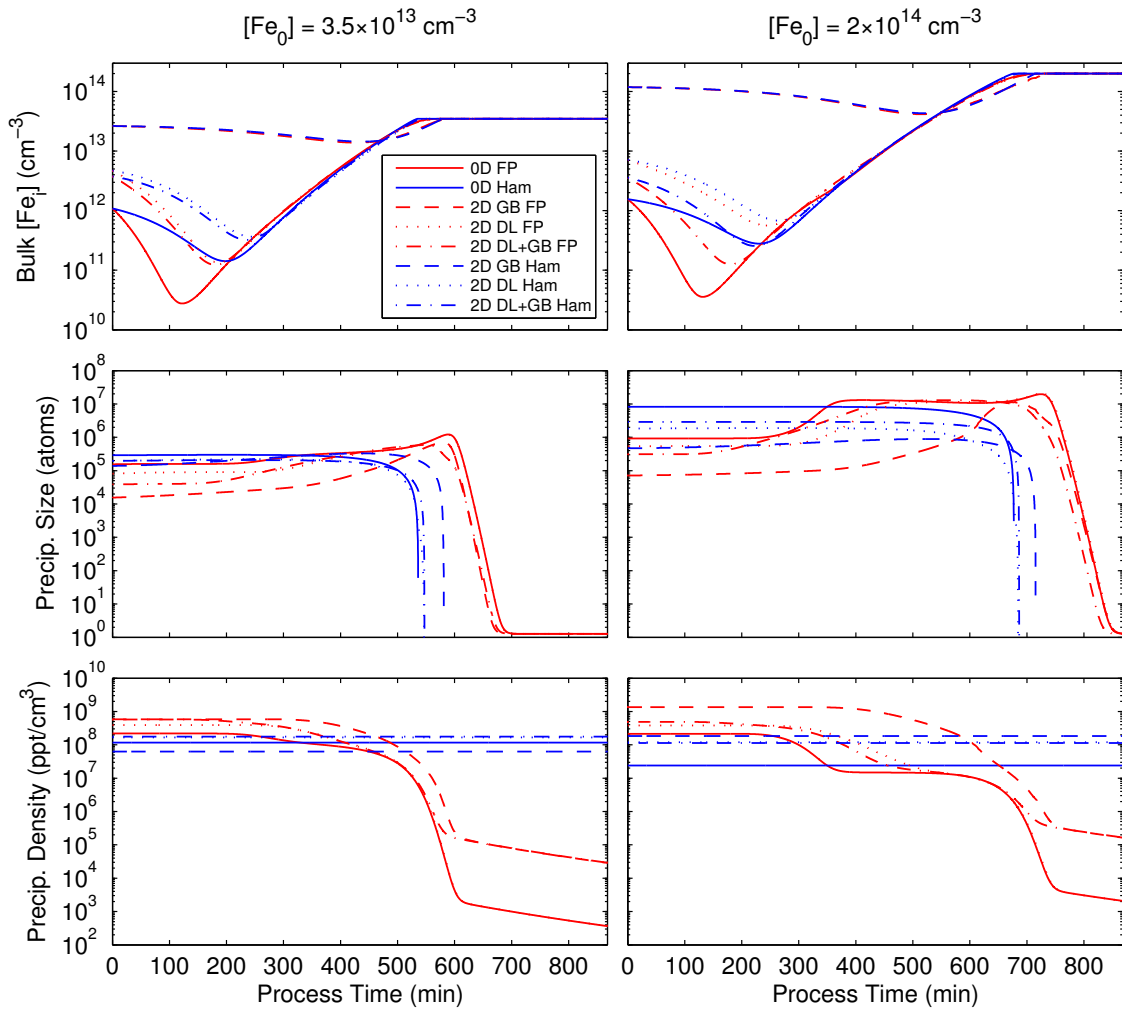


Figure 4-9: Average  $[Fe_i]$  (top), precipitate size (middle), and precipitate density (bottom) during heating for  $[Fe_0] = 3.5 \times 10^{13} \text{ cm}^{-3}$  (left) and  $[Fe_0] = 2 \times 10^{14} \text{ cm}^{-3}$  (right).



decrease monotonically with a similar S-shape as temperature increases, indicating no significant new nucleation at low temperatures, and (near) full dissolution at high temperatures. For Ham's Law, the precipitate density stays at the predetermined value, eventually exceeding the density predicted by Fokker-Planck.

Cooling is an inherent component of solar cell manufacturing processes, and the precise time-temperature profiles are essential for controlling the post-processing iron distribution and solar cell performance [60, 78, 141]. For iron evolution during cooling at 10°C/min from 1150°C to 500°C after the heating step discussed in this section, see Fig. 4-10. The trends of cooling are essentially the reverse of heating, with differences due to the different nucleation behavior and also depending on how *diffusivity-* or *solubility-limited* the impurity and structural defect distributions are. The Ham's law scenarios predict the onset of  $[\text{Fe}_i]$  reduction before the Fokker-Planck Models because they do not assume a nucleation barrier, so the precipitates with their predetermined density can start to grow immediately. For the FPE Models, there is a slight decrease in average precipitate size during the lower temperatures due to the dominance of new nucleation over growth of existing precipitates. The cooling rates used in solar cell processing are typically faster than the solubility-limited 1.35°C/min of crystallization, and they can range from 3°C/min during cooling after phosphorus diffusion up to 100°C/min or more during contact metallization firing. In these faster cooling scenarios, iron behavior is much more *diffusivity-limited*, and the Model predictions differ more strongly, so the choice of Model is more important.

### **4.3.2 Phosphorus diffusion gettering and contact firing: processes with a phosphorus-rich boundary layer**

In typical diffused-junction *p*-type Si solar cells, phosphorus diffusion serves two purposes: *p-n* junction formation and impurity gettering. In *n*-type Si devices, phosphorus can be used to getter impurities [22, 61, 109, 142, 143] and to form a front (or rear) surface field layer [144, 145]. Process Simulations are often used to optimize phosphorus diffusion gettering parameters, and the final spatial and chemical impu-

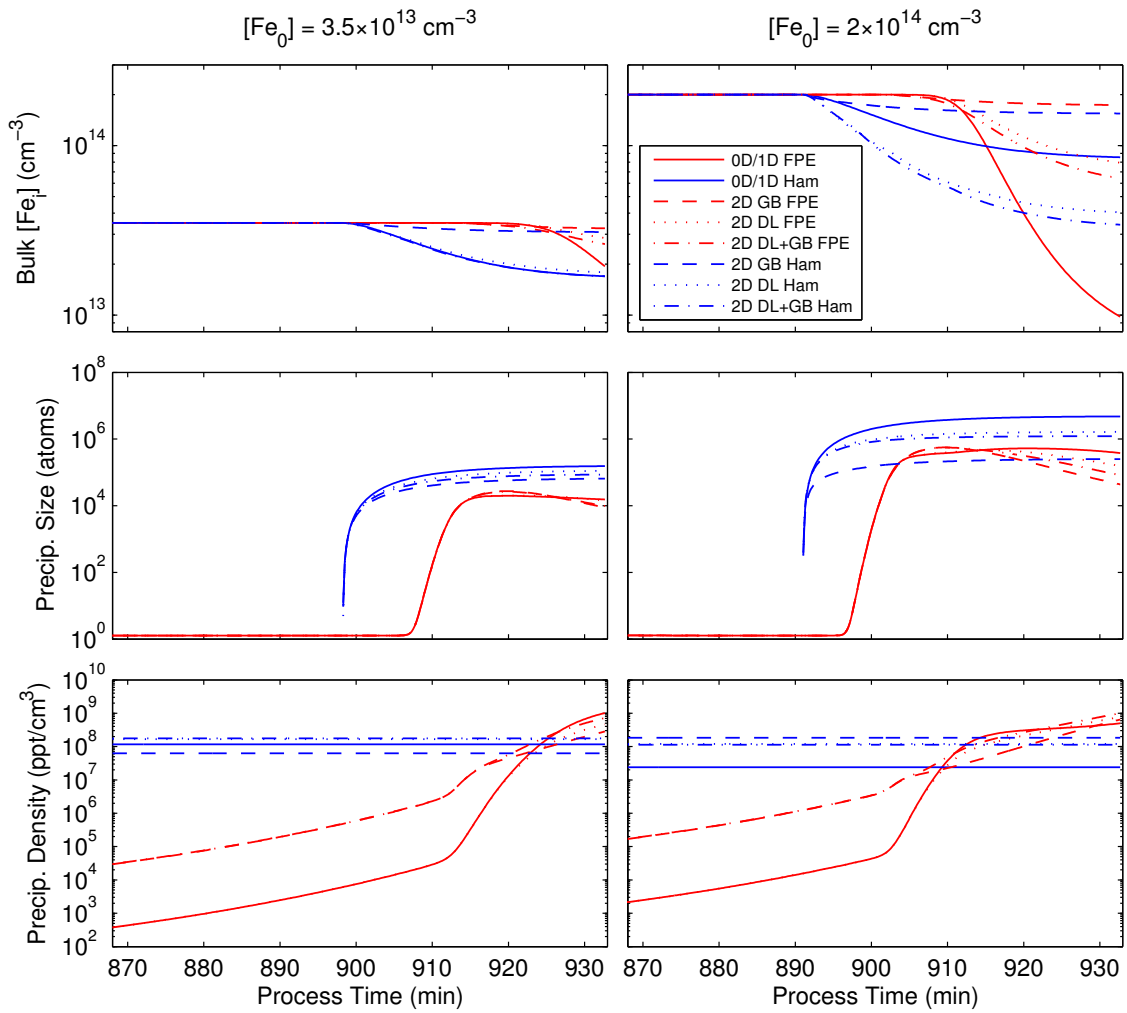


Figure 4-10: Average  $[Fe_i]$  (top), precipitate size (middle), and precipitate density (bottom) during cooling linearly from  $1150^\circ\text{C}$  to  $500^\circ\text{C}$  at  $10^\circ\text{C}/\text{min}$  for  $[Fe_0] = 3.5 \times 10^{13} \text{ cm}^{-3}$  (left) and  $[Fe_0] = 2 \times 10^{14} \text{ cm}^{-3}$  (right).

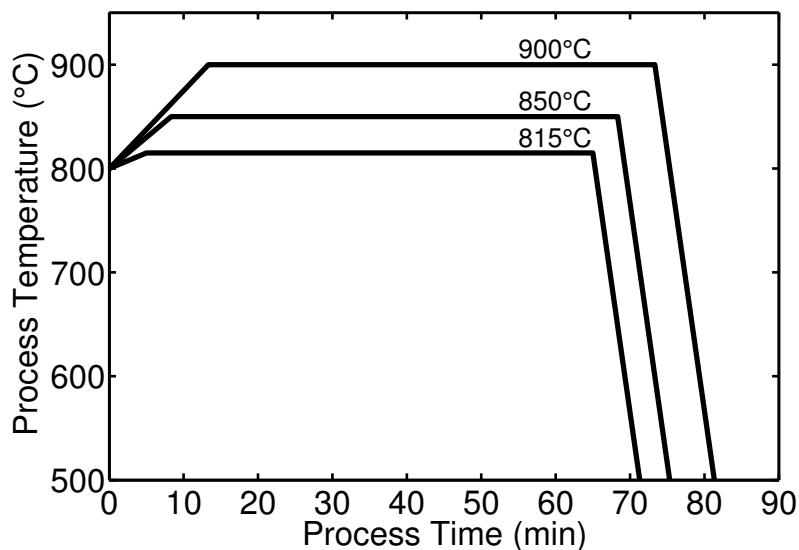


Figure 4-11: Phosphorus diffusion gettering profiles with different 60-minute plateau temperatures

rity distribution determine minority carrier lifetime, so it is essential to understand what the different Models predict under different processing conditions and different material qualities. See [8, 45, 50, 59, 140, 146, 147] for further details about impurity evolution during phosphorus diffusion gettering. The initial conditions are set by the state at the end of the crystallization process described in Section 4.3.1. The average precipitate density and size for the Ham’s law Models are calculated based on the output of the FPE Models after the crystallization step as in Section 4.3.1.

### **Phosphorus diffusion gettering (PDG) at different plateau temperatures**

The phosphorus diffusion plateau temperature is chosen carefully because the junction depth and impurity kinetics and thermodynamics depend exponentially on temperature. Consistent with previous work [136], we simulate phosphorus diffusion with a three-part time-temperature profile shown in Fig. 4-11: heat linearly from 800°C to the diffusion temperature, hold at the in-diffusion temperature for 60 min, then cool linearly to 500°C at 50°C/min. We simulated three different in-diffusion temperatures of 815°C, 850°C, and 900°C, resulting in a wide range of phosphorus profiles suitable for different solar cell architectures. We assume a fixed surface phosphorus concen-

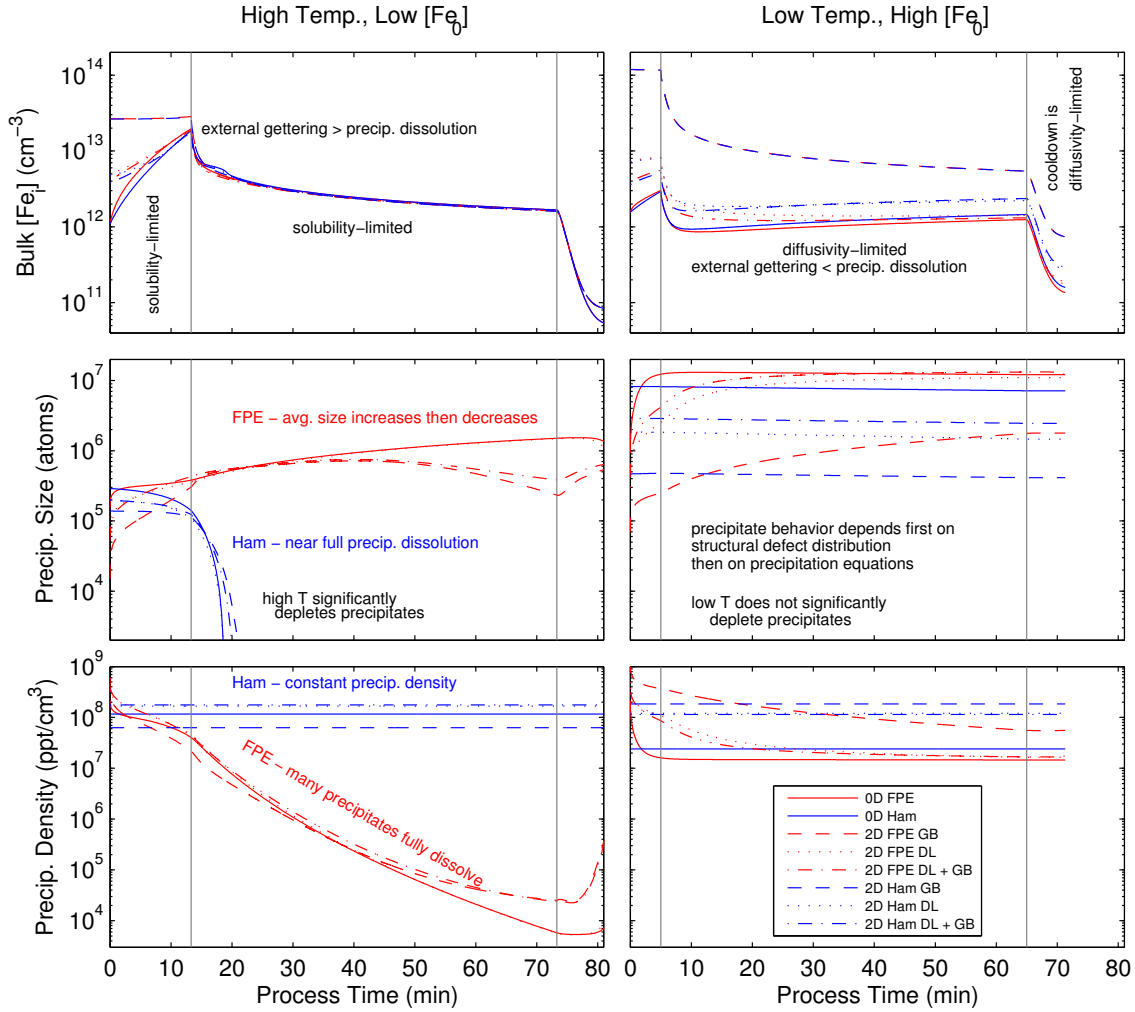


Figure 4-12: Average  $[Fe_i]$  (top), precipitate size (middle), and precipitate density (bottom) during phosphorus diffusion gettering at  $900^\circ\text{C}$  for  $[Fe_0] = 3.5 \times 10^{13} \text{ cm}^{-3}$  (left) and at  $815^\circ\text{C}$  for  $[Fe_0] = 2 \times 10^{14} \text{ cm}^{-3}$  (right). The vertical gray lines delineate the borders between the three sections of the time-temperature profiles

tration of  $4.1 \times 10^{20} \text{ cm}^{-3}$ . We simulated initial total iron concentrations of  $[Fe_0] = 3.5 \times 10^{13} \text{ cm}^{-3}$  and  $2 \times 10^{14} \text{ cm}^{-3}$ . In Fig. 4-12, we show iron evolution during the two extreme cases of high temperature ( $900^\circ\text{C}$ ) for low  $[Fe_0]$  ( $3.5 \times 10^{13} \text{ cm}^{-3}$ ) and low temperature ( $815^\circ\text{C}$ ) for high  $[Fe_0]$  ( $2 \times 10^{14} \text{ cm}^{-3}$ ). The rest of the iron distributions as a function of time for  $815^\circ\text{C}$  and  $900^\circ\text{C}$  are shown in Fig. 4-13. The trends for  $850^\circ\text{C}$  are in between those of the other two temperatures.

For all Models and phosphorus diffusion scenarios, the evolution of the iron distribution follows three phases, corresponding to the three parts of the phosphorus

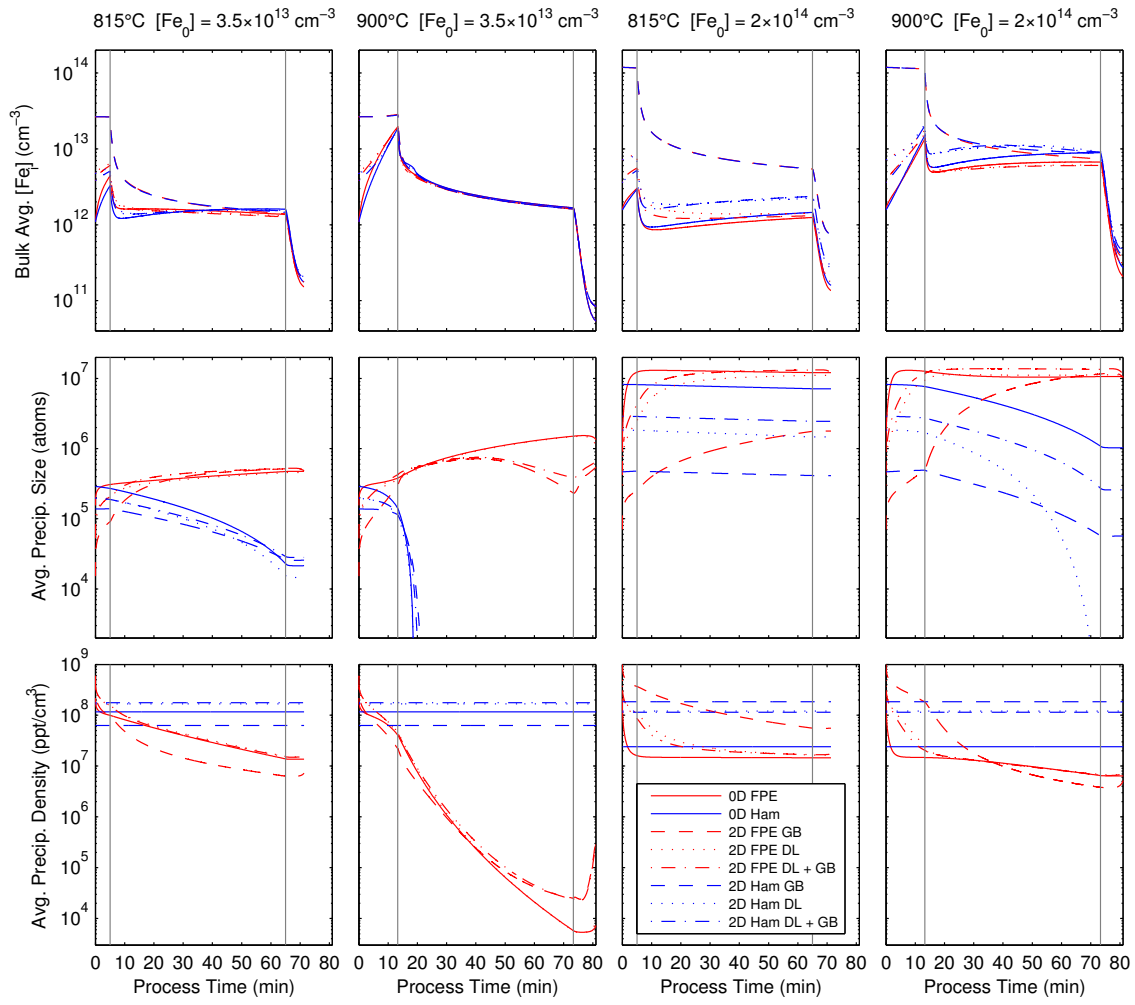


Figure 4-13: Average  $[Fe_i]$  (top), precipitate size (middle), and precipitate density (bottom) during phosphorus diffusion gettering at 815°C and 900°C for  $[Fe_0] = 3.5 \times 10^{13} \text{ cm}^{-3}$  (left two columns) and  $[Fe_0] = 2 \times 10^{14} \text{ cm}^{-3}$  (right two columns). The vertical lines delineate the borders between the three sections of the phosphorus diffusion time-temperature profiles.

diffusion step (separated by vertical gray lines in Fig. 4-12). First,  $[\text{Fe}_i]$  is *solubility-limited* as the wafer is heated from 800°C to the in-diffusion temperature. With the exception of the 2D GB Models, the solid solubility exceeds  $[\text{Fe}_i]$ , dissolving precipitates and increasing  $[\text{Fe}_i]$ . Next, as the wafer is held at the diffusion temperature and phosphorus is introduced, iron behavior can be either *solubility-* or *diffusivity-limited*. During phosphorus diffusion, precipitates are sources of  $\text{Fe}_i$  and the phosphorus-rich layer is a sink for  $\text{Fe}_i$ .  $[\text{Fe}_0]$  and the phosphorus in-diffusion temperature together determine the balance between precipitate dissolution, which increases bulk  $[\text{Fe}_i]$ , and external segregation gettering of point defects, which decreases bulk  $[\text{Fe}_i]$ . The relative rates of these two processes determine the slope of  $[\text{Fe}_i]$  vs. time. Reducing  $[\text{Fe}_i]$  during this part of phosphorus diffusion requires the process to be mainly *solubility-limited*, meaning precipitate dissolution must add  $[\text{Fe}_i]$  to the bulk more slowly than external gettering removes  $[\text{Fe}_i]$ . For low  $[\text{Fe}_0]$  and high temperature, precipitates,  $[\text{Fe}_i]$  sources, are significantly depleted, and external gettering can remove the previously precipitated iron. Although the 2D GB Models are diffusion-limited, they have a negative slope because external gettering of the high post-crystallization  $[\text{Fe}_i]$  levels typically dominates. Finally, in a *diffusivity-limited* process, the wafer is cooled rapidly from the in-diffusion temperature. The decreasing temperature increases the driving force for point defect segregation to the phosphorus-rich region, reducing the bulk  $[\text{Fe}_i]$ . The high supersaturation during cooling can cause some precipitate nucleation as shown in the precipitate density graph for the low  $[\text{Fe}_0]$  scenario in Fig. 4-12. The exponentially decreasing diffusivity opposes the increasing segregation force, eventually slowing the  $\text{Fe}_i$  reduction.

To more easily compare the predicted magnitudes of  $[\text{Fe}_i]$ , the  $[\text{Fe}_i]$  before and after phosphorus diffusion for all the simulated processes are shown in Fig. 4-14. Generally, the most significant factors defining post-phosphorus diffusion  $[\text{Fe}_i]$  are  $[\text{Fe}_0]$  [78] and phosphorus diffusion temperature. Overall, the post-gettering  $[\text{Fe}_i]$  predictions are rather similar. In spite of the wide range of temperatures and Model differences, the range of post-gettering  $[\text{Fe}_i]$  is only 1.5 orders of magnitude. The largest reduction in  $[\text{Fe}_i]$  occurs for the 2D GB Models because they start with the highest  $[\text{Fe}_i]$  post-

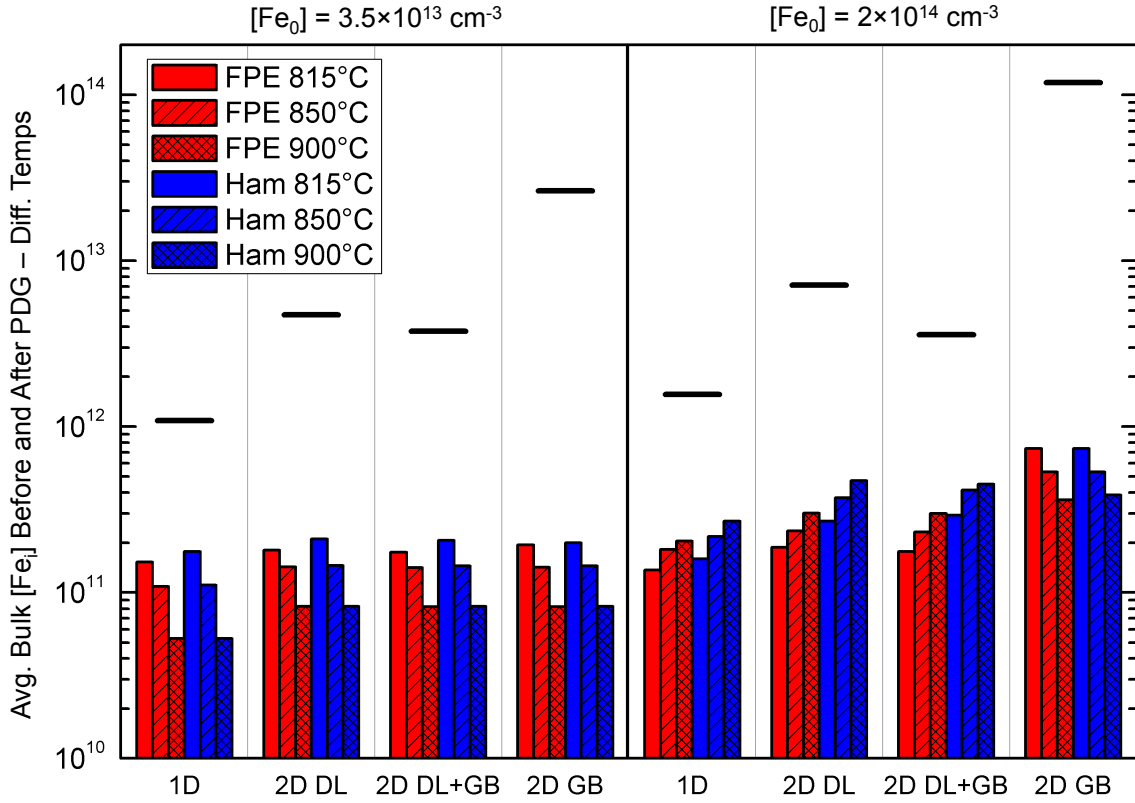


Figure 4-14: Average bulk  $[Fe_i]$  before (horizontal black lines) and after (colored vertical bars) different temperatures of phosphorus diffusion for low  $[Fe_0]$  (left half) and high  $[Fe_0]$  (right half). Predictions are shown for the different structural defect distributions as indicated on the x-axis and the different precipitation equations with the FPE in red (left four bars of each group) and the Ham's law in blue (right four bars of each group).

crystallization. The smallest reduction is for the 1D Models because they start with the lowest  $[Fe_i]$ . Removal of bulk  $[Fe_i]$  in the 2D GB Models are limited only by external gettering and essentially never by precipitate dissolution whereas the 1D Models are limited by both processes.

For the more *solubility-limited* low  $[Fe_0]$ , a higher temperature PDG more effectively reduces  $[Fe_i]$  because precipitates (finite sources) are more completely dissolved at higher temperature and external gettering is fast enough to remove the resulting point defects. For the more *diffusivity-limited* high  $[Fe_0]$ , a lower temperature PDG results in lower  $[Fe_i]$  because the PDG typically does not dissolve a significant fraction of the precipitates, and external gettering can remove the point defects that do dis-

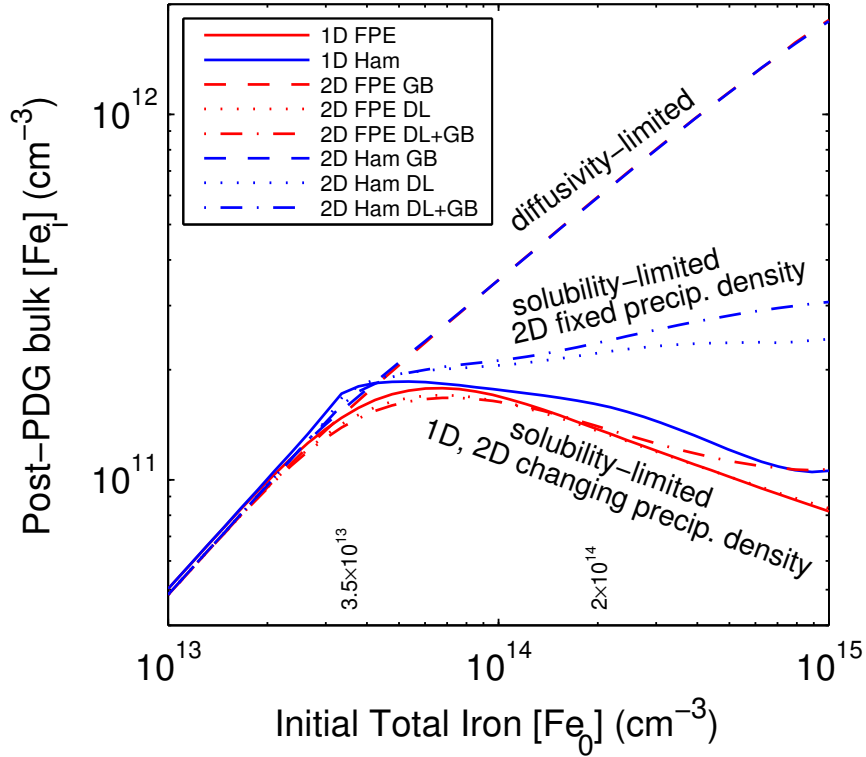


Figure 4-15:  $[\text{Fe}_i]$  after crystallization and PDG at  $815^\circ\text{C}$  as a function of a wide range of  $[\text{Fe}_0]$  for all eight Models. The Models predict very similar  $[\text{Fe}_i]$  for  $[\text{Fe}_0] < \sim 4 \times 10^{13} \text{ cm}^{-3}$ . Above  $[\text{Fe}_0] \sim 4 \times 10^{13} \text{ cm}^{-3}$ , the Models fall into three distinct Groups. The two  $[\text{Fe}_0]$  values that we focus on in this work are indicated along the  $x$ -axis. The low  $[\text{Fe}_0]$  is close to where the Models diverge, and the high  $[\text{Fe}_0]$  is in the regime where there is significant divergence in the Models

solve. As  $[\text{Fe}_0]$  increases,  $[\text{Fe}_i]$  depends more strongly on precipitate size and density, so more variation is observed between the different precipitation models. For the high  $[\text{Fe}_0]$ , the 2D GB Models show a decrease in  $[\text{Fe}_i]$  as temperature increases because they are always *diffusivity-limited*. Longer or even higher temperature gettering may be of interest for materials dominated by precipitated metals at structural defects.

Within each  $[\text{Fe}_0]$  and for each temperature, the differences in  $[\text{Fe}_i]$  predictions are most strongly dependent on the structural defect distribution and secondarily dependent on the precipitation model element because  $[\text{Fe}_i]$  reduction during PDG is typically ultimately limited by diffusion to the emitter, not by precipitate dissolution. The 0D/1D Models and the 2D Models have very similar results. The Ham's law Models predict a higher bulk  $[\text{Fe}_i]$  because they generally model a higher density



of precipitates, which are sources of  $[\text{Fe}_i]$ . However,  $[\text{Fe}_i]$  predictions are similar for a given  $[\text{Fe}_0]$ , despite significant differences in the precipitate evolution. It is important to note that the uncertainty in the Models themselves is likely greater than the differences between the Models shown here.

Finally, to offer a more complete picture of the behavior of the Models as a function of the initial iron concentration, we simulated the crystallization and the 815°C PDG process for a range of  $[\text{Fe}_0]$  values from  $10^{12} \text{ cm}^{-3}$  to  $10^{15} \text{ cm}^{-3}$ . The resulting interstitial iron concentrations for  $[\text{Fe}_0]$  between  $10^{13}$  and  $10^{15} \text{ cm}^{-3}$  are shown in Fig. 4-15. For  $[\text{Fe}_0] < 10^{13} \text{ cm}^{-3}$  the Models are all very similar and as  $[\text{Fe}_0]$  decreases,  $[\text{Fe}_i]$  continues to decrease exponentially. The behavior of the Models falls into three Groups:

- (1) 2D GB,
- (2) 2D Ham DL and 2D Ham DL+GB, and
- (3) 1D FPE, 1D Ham, 2D FPE DL and 2D FPE DL+GB.

For  $[\text{Fe}_0]$  levels below  $\sim 4 \times 10^{13} \text{ cm}^{-3}$ , the Models are *solubility-limited*, where the residual iron concentration is mostly determined by the gettering efficiency of the phosphorus emitter. However, after the contamination level considerably surpasses the solid solubility of iron at 815°C ( $\sim 8 \times 10^{12} \text{ cm}^{-3}$ ), the role of precipitation becomes more important. Further simulations (not shown here) also revealed that with higher PDG temperature, and thus solid solubility, the  $[\text{Fe}_0]$  level where the models begin to differ increases.

After the Models deviate, Group 1 is in the *diffusivity-limited* regime, where post-crystallization  $[\text{Fe}_i]$  is high because the iron does not have time to diffuse to the grain boundary, and hardly any additional gettering effect is gained from precipitation at structural defects. The exponential increase in final  $[\text{Fe}_i]$  as a function of  $[\text{Fe}_0]$  observed in Group 1 Models slows slightly at  $[\text{Fe}_0]$  levels over  $\sim 4 \times 10^{13} \text{ cm}^{-3}$ . This is due to the fact that a higher initial iron concentration results in larger precipitates after crystallization, as can be seen from Fig. 4-4. When iron is distributed in fewer, but larger precipitates, the dissolution of these precipitates during PDG is slower,

which results in a lower  $[\text{Fe}_i]$  after PDG. The rest of the Models (Groups 2 and 3) fall into the *solubility-limited* regime, with slight differences in magnitude. With increasing  $[\text{Fe}_0]$ , Group 2 Models diverge from Group 3 because their precipitate density is fixed, and thus the precipitate density reduction exhibited in the FPE Models during PDG (evident from Fig. 4-12) does not occur. This subsequently leads into more iron sources toward the end of PDG for Group 2 Models, and results in a slightly larger post-PDG  $[\text{Fe}_i]$ . It should be noted, however, that the decrease of the final  $[\text{Fe}_i]$  as a function  $[\text{Fe}_0]$  predicted for the Group 3 Models does not necessarily translate into improved performance of the final solar cell, because of the increased amount of precipitated iron [59].

### **Different PDG approaches (preanneal peak, standard PDG, annealing)**

Variations on the 815°C standard (PD) time-temperature profile shape discussed in Section 4.3.2, including a “preanneal peak” (Peak) and low-temperature anneal (Anneal) have been shown to reduce  $[\text{Fe}_i]$  more effectively [104, 136, 148–151]. In Michl et al., four variations of phosphorus diffusion time-temperature profile shape were analyzed. They are the 815°C reference profile (PD), the reference followed by a post-deposition low-temperature anneal at 600°C (PD+Anneal), the reference preceded by a pre-deposition 900°C precipitate dissolution peak (Peak+PD), and finally all three segments together (Peak+PD+Anneal). Compared to the 71-minute PD profile, the Anneal adds 248 minutes, and the Peak adds 44 minutes. The four profiles are reproduced in Fig. 4-16. As before, we simulate initial total iron concentrations of  $[\text{Fe}_0] = 3.5 \times 10^{13} \text{ cm}^{-3}$  and  $2 \times 10^{14} \text{ cm}^{-3}$ . Here, we focus on comparing the predictions from the different Models. The temperature and iron distributions as a function of time for the Peak+PD+Anneal are shown in Fig. 4-17 with the high  $[\text{Fe}_0]$  shown in 4-18. The PD is shown in Fig. 4-12, and trends for the Peak+PD and the PD+Anneal are a subset of the profiles shown with slight differences in magnitude.

The preanneal peak step is in the *solubility-limited* regime. During the preanneal peak step, no phosphorus is present, so there is no point defect segregation. As the wafer is heated to and annealed at 900°C,  $[\text{Fe}_i]$  approaches the total iron concentra-

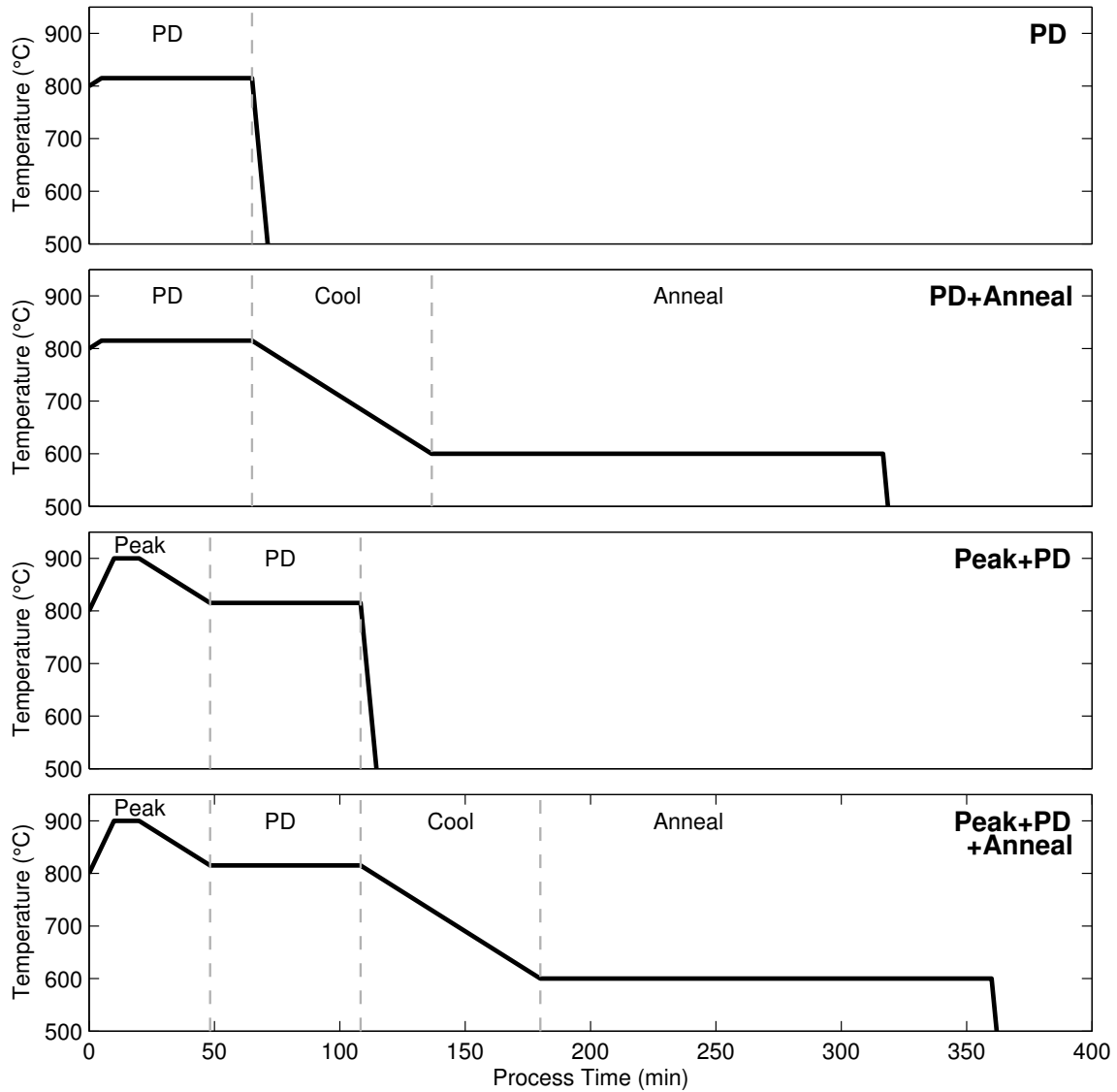


Figure 4-16: Four different shapes of phosphorus diffusion bettering time-temperature profile: standard (PD), standard followed by a slow cool to an anneal (PD+Anneal), a preanneal peak preceding the standard (Peak+PD), and a combination of a preanneal peak, standard isothermal plateau, and cooling followed by an anneal (Peak+PD+Anneal).

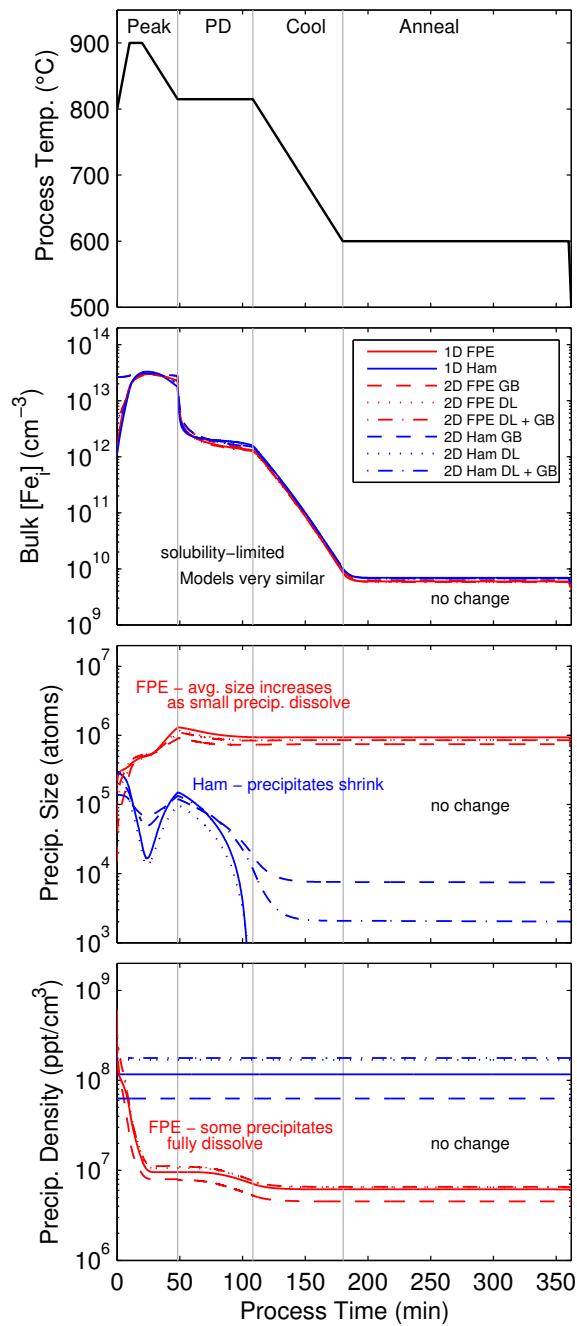


Figure 4-17: Temperature (panel 1) and average  $[Fe_i]$  (panel 2), precipitate size (panel 3), and precipitate density (panel 4) during Peak+PD+Anneal phosphorus diffusion gettering  $[Fe_0] = 3.5 \times 10^{13} \text{ cm}^{-3}$ . The vertical gray lines delineate the borders between the sections of the time-temperature profile

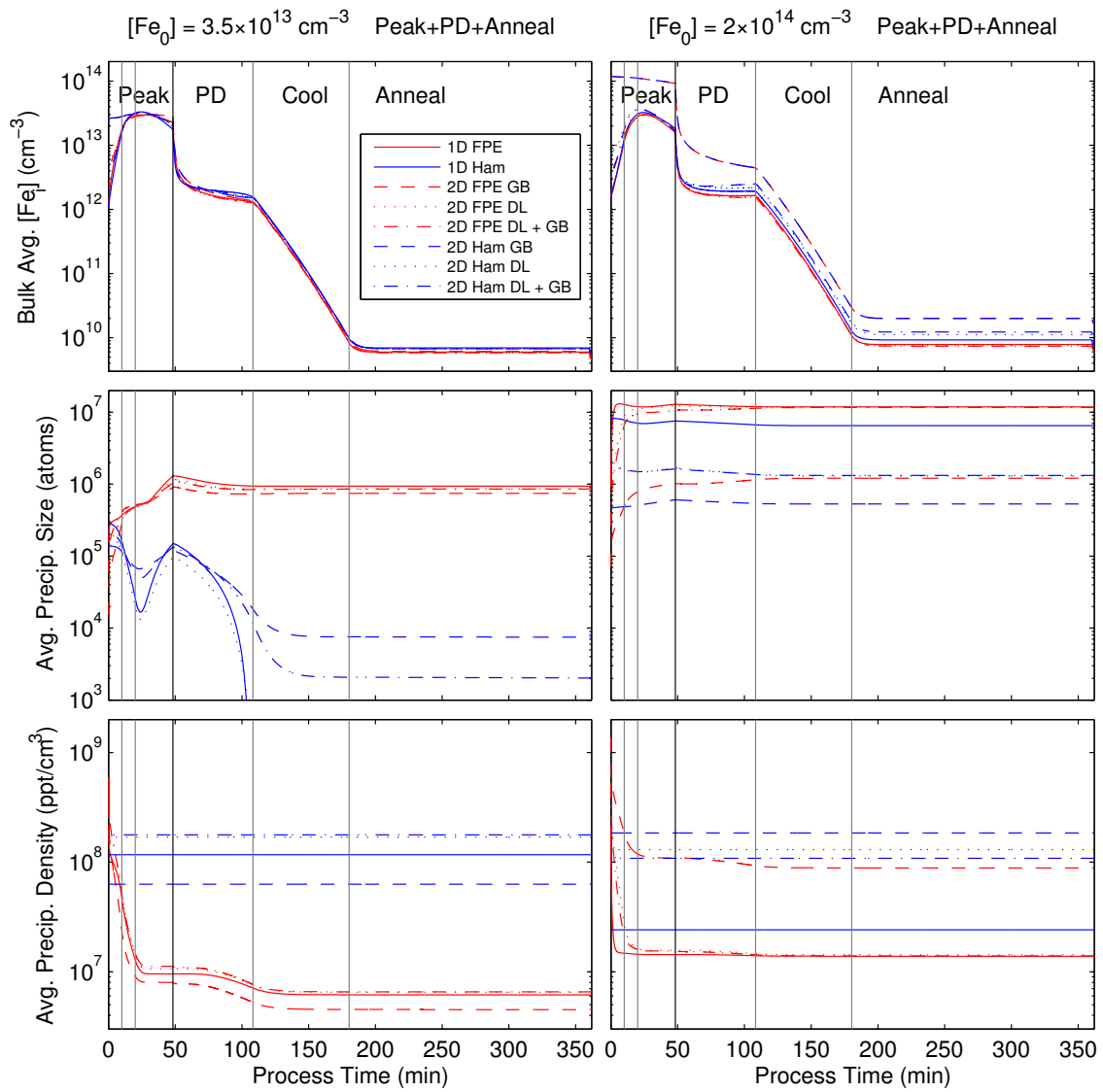


Figure 4-18: Average  $[Fe_i]$  (top), precipitate size (middle), and precipitate density (bottom) during Peak+PD+Anneal phosphorus diffusion for  $[Fe_0] = 3.5 \times 10^{13} \text{ cm}^{-3}$  (left) and  $[Fe_0] = 2 \times 10^{14} \text{ cm}^{-3}$  (right).

tion. As the wafer cools from 900°C to the phosphorus in-diffusion temperature of 815°C, the decreasing solubility drives precipitate growth but no significant precipitate nucleation. The main benefit of the preanneal peak is to reduce the precipitated iron concentration by either size or density reduction ahead of the phosphorus diffusion step so that precipitate dissolution does not limit external gettering of point defects. For example during the 815°C standard process for  $[\text{Fe}_0] = 3.5 \times 10^{13} \text{ cm}^{-3}$  4-13 precipitates do not fully dissolve, but during the PD portion of the Peak+PD+Anneal, nearly full dissolution occurs. As discussed before, the phosphorus diffusion step is typically a mix of *solubility-* and *diffusivity-limited* regimes. The Ham's Law Models account for precipitate behavior with a monotonically decreasing precipitate size and a constant precipitate density. On the other hand, the Fokker-Planck Models account for the behavior with a monotonically decreasing precipitate density and increasing precipitate size. The cooldown from the phosphorus diffusion temperature of 815°C to the post-deposition annealing temperature of 600°C at 3°C/min reduces  $[\text{Fe}_i]$  by over two orders of magnitude without significant change in precipitate size or density. The decreasing temperature increases the difference in bulk and emitter solubility, driving  $\text{Fe}_i$  to the emitter. The transition between phosphorus diffusion temperature and post-deposition anneal is governed by the solubility difference between the bulk and the emitter, and is thus *solubility-limited*, and the similar  $[\text{Fe}_i]$  at the beginning of the cooldown leads to similar  $[\text{Fe}_i]$  Model predictions after the cooldown. For these time-temperature profile parameters, the  $[\text{Fe}_i]$  at the beginning of the 600°C anneal is close to the solid solubility ( $\sim 10^{10} \text{ cm}^{-3}$ ) [111], so no significant change in  $[\text{Fe}_i]$  or precipitates is observed during the low-temperature plateau. The relative invariance of the precipitate distribution during a post-PDG anneal has also been observed experimentally [152].

To more easily compare the predicted magnitudes of  $[\text{Fe}_i]$ , the  $[\text{Fe}_i]$  before and after phosphorus diffusion for all the simulated processes are shown in 4-19. For the low  $[\text{Fe}_0]$ , the Model predictions are nearly identical while for the high  $[\text{Fe}_0]$ , there are some differences with the 2D GB Model as the typical outlier. All the profiles reduce  $[\text{Fe}_i]$  by over 80%, with the most important factor being the presence or absence of the

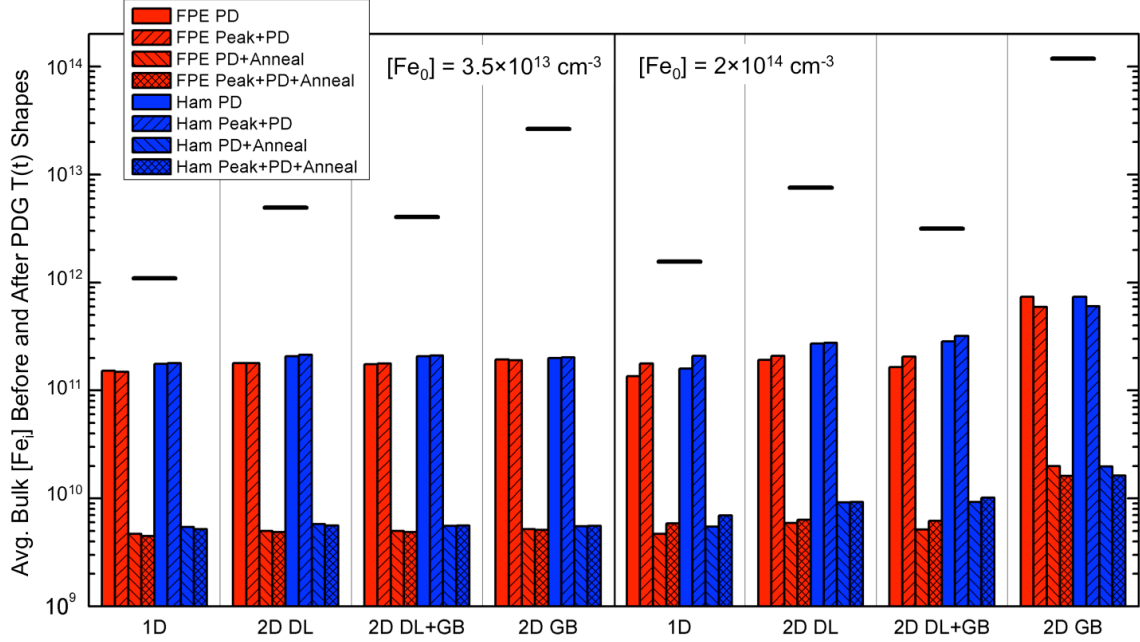


Figure 4-19: Average bulk  $[Fe_i]$  before (horizontal black lines) and after (colored vertical bars) different shapes of phosphorus diffusion time-temperature profile for low  $[Fe_0]$  (left half) and high  $[Fe_0]$  (right half). Predictions are shown for the different structural defect distributions as indicated on the x-axis and the different precipitation equations with the FPE in red (left four bars of each group) and the Ham's law in blue (right four bars of each group).

slow cooling step associated with the low-temperature anneal. The Peak is predicted to make almost no difference in  $[Fe_i]$  for the low  $[Fe_0]$  and a slight increase in  $[Fe_i]$  for the high  $[Fe_0]$  with the exception of the 2D GB Models. The predictions vary more as  $[Fe_0]$  increases because  $[Fe_i]$  more strongly depends on the precipitate distribution, which is determined by the precipitation site distribution and the precipitation Model Element details as discussed previously.

Although the focus of this paper is on the physical trends of the different Models, we can compare the Model predictions to the limited experimental data available for these exact profiles in [136]. Note that the cooling rate of  $50^\circ\text{C}/\text{min}$  from either the PD (if no subsequent anneal) or the Anneal portion was chosen to closely match the experimental data in [136], and the cooling rate has a strong effect on how much time iron has to precipitate and segregate during cooling, thus affecting the final  $[Fe_i]$ . The effect is larger if the wafers are pulled out directly after the PD step

without the Anneal portion. Excluding the 2D GB Models, which are known to not be representative of the mc-Si used in the study, the PD and Peak+PD simulated and experimental  $[\text{Fe}_i]$  are within a factor of two in magnitude. For the high  $[\text{Fe}_0] = 2 \times 10^{14} \text{ cm}^{-3}$ , the Models in this work predict that the Peak+PD results in a slightly higher post-gettering  $[\text{Fe}_i]$  than the PD alone. For both  $[\text{Fe}_0]$ , the Models overestimate the  $[\text{Fe}_i]$  reduction due to the Anneal step by about an order of magnitude. Overall, although there are discrepancies, all of the Models considered here simulate the main trends and magnitudes of post-gettering  $[\text{Fe}_i]$  fairly well.

### **Firing in the presence of a phosphorus-rich layer**

In a typical solar cell, using a rapid ( $< 1 \text{ min}$ ), high-temperature ( $\sim 800\text{-}900^\circ\text{C}$ ) spike, the screen-printed metal pastes are fired through a  $\text{SiN}_x$  layer to form a good Ohmic contact with the silicon substrate. The exact profile shape depends on the metal paste being used, and here we use a typical profile, which is the same as that used in [136]. We focus on the effect of the thermal step in the iron dynamics in the presence of the phosphorus-rich layer, and do not include in our analysis other aspects that may have a secondary effect (such as the potential hydrogenation due to the silicon nitride layer [153] or gettering if an Aluminum Back Surface Field is present [154, 155]). We use a no-flux boundary condition for the phosphorus in these firing simulations to describe the fact that there is no additional phosphorus source present at the surface during firing, and we simulate a phosphorus-rich emitter on only one side of the wafer.

For low and high  $[\text{Fe}_0]$  and for firing after the four different PDG approaches discussed in Section 4.3.2, we simulated the iron distribution as a function of time using all eight Models. The evolution of iron as a function of time during firing for the Peak+PD+Anneal phosphorus diffusion process for the high  $[\text{Fe}_0] = 2 \times 10^{14} \text{ cm}^{-3}$  is shown in Fig. 4-20. The trends are similar for the other scenarios, and  $[\text{Fe}_i]$  before and after Firing for all the simulated scenarios are summarized in Fig. 4-21.

The rapid temperature change during Firing is a strongly *diffusivity-limited* process. The trends in Model predictions of post-phosphorus diffusion gettering  $[\text{Fe}_i]$  persist after firing. During Firing, the precipitated iron distribution does not un-



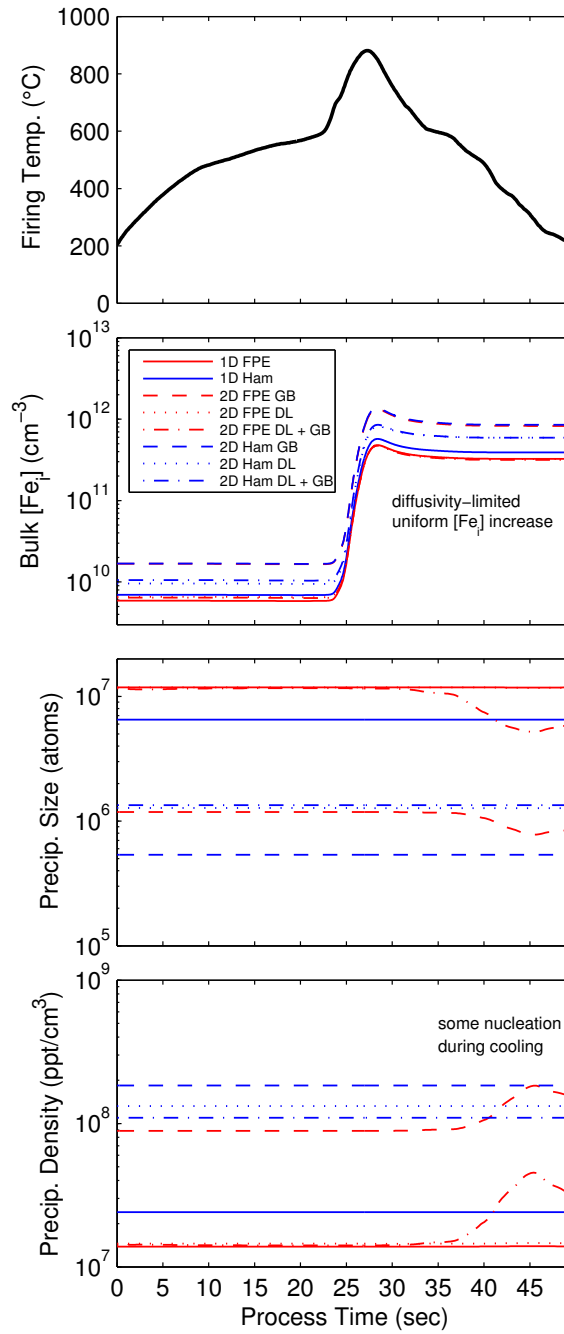


Figure 4-20: Evolution of temperature,  $[Fe_i]$ , Precipitate size, precipitate density during Firing after Peak+PD+Anneal phosphorus diffusion for  $[Fe_0] = 2 \times 10^{14} \text{ cm}^{-3}$

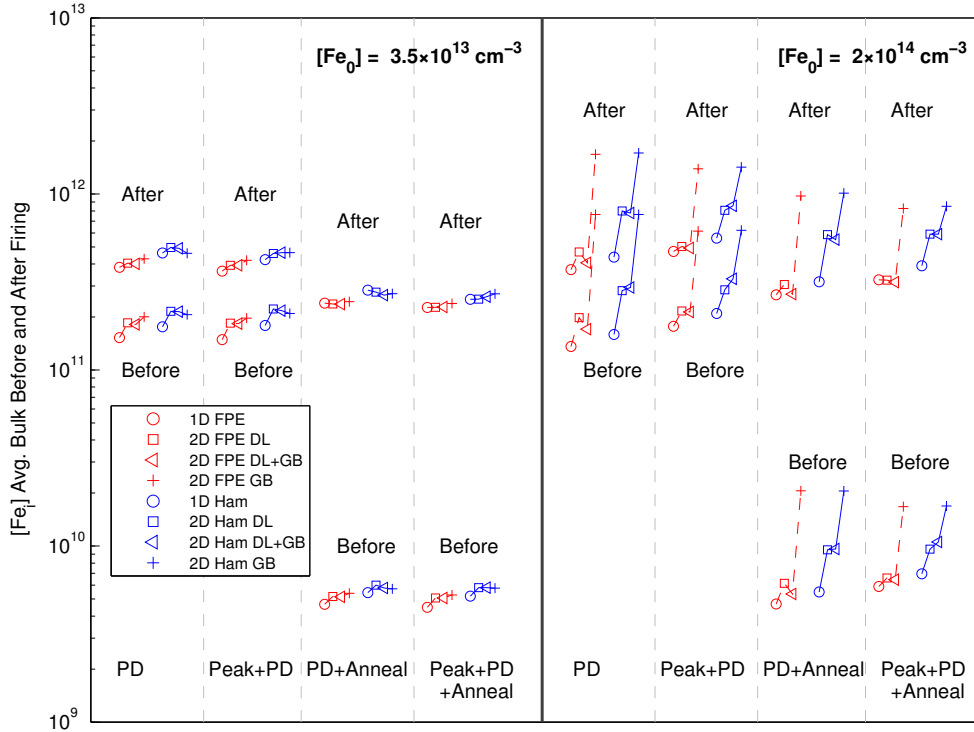


Figure 4-21: Average bulk  $[Fe_i]$  before and after Firing for low  $[Fe_0]$  (left half) and high  $[Fe_0]$  (right half). Predictions are shown for the different shapes of phosphorus diffusion time-temperature profile as labelled along the x-axis and the different precipitation equations with the FPE in red (on the left in each pair) and the Ham's law in blue (on the right in each pair). The structural defect distributions are differentiated by the marker shape.

dergo major changes and correspondingly, the differences between the models are small. However, there is a two orders of magnitude increase in  $[\text{Fe}_i]$  when the temperature peaks. In our simulations, the  $[\text{Fe}_i]$  increase mostly due to iron out-diffusion from the emitter as observed in [156], with precipitate dissolution also playing a minor role. The out-diffusion is caused by a strong decrease of the segregation coefficient as a function of temperature, which releases iron point defects from the emitter into the bulk. Also, due to the no-flux phosphorus boundary condition the phosphorus profile diffuses deeper into the bulk and the surface concentration decreases, slightly reducing the total segregation effect. Toward the end of the firing, around 30-45 seconds, some of these released iron point defects precipitate out, and a part of the released iron is also gettered back to the emitter. In Fig. 4-20, the 2D DL+GB and 2D GB Fokker-Planck Models predict slight precipitate nucleation and thus a decrease in average size during cooling. In the Ham's Law Models, this change in precipitates is sometimes seen as a subtle increase in average precipitate size.

It is important to note that the  $[\text{Fe}_i]$  reduction due to annealing (as in the PD+Anneal and Peak+PD+Anneal profiles) is almost completely reversed during firing. Thus, the reduction in  $[\text{Fe}_i]$  after P-diffusion can be erased [136, 141]. Firing time-temperature profiles with lower peak temperatures and a slower cool from the peak as suggested in [141] can reduce  $[\text{Fe}_i]$ . Overall, the simulations match the experimental data in Michl et al [136] fairly well (excluding the 2D GB Models for the higher  $[\text{Fe}_0]$ ). For the  $[\text{Fe}_0] = 3.5 \times 10^{13} \text{ cm}^{-3}$  the Model predictions for the Peak+PD+Anneal are almost exactly the same as the experimental results while for the other profiles, the Model predictions are slightly lower than the experimental results by no more than a factor of two. For  $[\text{Fe}_0] = 2 \times 10^{14} \text{ cm}^{-3}$  the experimental data for the PD and Peak+PD profiles lie within the range predicted by simulation. The experimental data for the profiles with an Anneal are at or above the predicted values (excluding the 2D GB Models) with the Ham's law values being more accurate than the Fokker-Planck values.

## 4.4 Conclusions

Process simulation has accelerated optimization of semiconductor processing for the last couple of decades, but with many different Models available, it can be difficult to discern the key differences and similarities between the models and the essential physics occurring during processing. To address both of these needs, we combine Model Elements of three existing solar cell Process Simulation tools into one software environment. We combine four different structural defect distributions and two sets of iron precipitation equations to create eight distinct processing Models, and we analyze how the iron distribution evolves at different stages of device processing: crystal growth, thermal annealing, phosphorus diffusion, and contact-metallization firing.

We define a useful classifying framework of *solubility-limited* and *diffusivity-limited* impurity behavior. The slow cooldown of crystallization is *solubility-limited* and the  $[\text{Fe}_i]$  depends strongly on the structural defect distribution. Heating at low and moderate temperatures is *diffusivity-limited* and depends primarily on structural defect distribution and secondarily on precipitation Model differences while at higher temperatures it is *solubility-limited* and there are few differences between the Models. Phosphorus diffusion gettering involves both *diffusivity-* and *solubility-limited* aspects, depending on the total iron concentration, time-temperature profile, structural defect distribution, and precipitation models. For the profiles analyzed here, the Model predictions of post-gettering  $[\text{Fe}_i]$  were overall quite similar. Finally, the rapid temperature spike of contact metallization firing is a strongly *diffusivity-limited* process that increases  $[\text{Fe}_i]$  uniformly across the Models.

The framework defined here can inform the extension of kinetic defect modeling to other impurities in silicon based on their known solubilities and diffusivities in semiconductor materials, including *n*-type silicon. It is expected that at high temperatures, impurity kinetics for *n*- and *p*-type Si are similar because the material becomes intrinsic. Kinetics at lower temperatures may differ because of Fermi-level effects.

This analysis enables the PV industry to better understand how Si materials with different structural defect distributions, including CZ (0D/1D), mono-like and epitaxially-grown Si (DL only), standard mc-Si (DL+GB), and high-performance mc-Si (approximated by GB only) respond to processing and therefore what processing is necessary for each of these materials to achieve high-performance devices. The appropriate and necessary simulation Model can also be matched to the material of interest.

A key figure of merit for any Simulation tool is the required computation time. The 0D/1D Models can be orders of magnitude faster than the 2D Models, and the Ham’s Law Models are typically faster than the Fokker-Planck Models. This rigorous analysis quantitatively illustrates when the Models are similar, when they are different, and to what degree. When rapid optimization is paramount, the 0D/1D Models may be the most appropriate for defining a small parameter space of interest while a combination of experiment and 2D Modeling may be more appropriate for fine-tuning. The Fokker-Planck Models are necessary when the precipitate size distribution [157, 158], nucleation, and full dissolution are important factors such as in crystallization. 2D modeling is needed when analyzing inherently multi-dimensional phenomena such as lateral diffusion of point defects and the effect of grain size.

This rigorous Model comparison and analysis provides new physical intuition that assists with future material, process, and Process Simulation development, and enables scientists and engineers to choose the appropriate level of model complexity (simulation run time) based on material characteristics and processing conditions.

## 4.5 Detailed description of precipitation equations

### Model Element

*Ham’s Law* [110] describes all the precipitates as spheres with a single average number of atoms/precipitate  $n_{\text{avg}}$ . The input parameter is the precipitate density,  $N_p$ . The time evolution of the precipitated iron concentration,  $[Fe_p]$ , depends on  $g(n_{\text{avg}})$

and  $d(n_{\text{avg}})$ , the precipitate size-dependent precipitate growth and dissolution rates respectively.  $C_{\text{Fe}}$  is the interstitial iron concentration and  $D_{\text{Fe}}$  is the iron diffusivity.  $r_c$  is the size-dependent capture radius of the precipitates. The capture radius determines how close to the center of the precipitates the dissolved iron atoms need to be in order to attach to the iron precipitate. The capture radius and local equilibrium iron concentration are defined differently in the two precipitation approaches. For the Ham's Law Model, the equilibrium iron concentration,  $C_{\text{Eq}}$ , is the solid solubility of iron,  $C_{\text{S}}$ , as defined in [111]. The precipitates are modeled as spheres with the volume of a unit cell containing a single iron atom in a  $\beta$ -FeSi<sub>2</sub> precipitate,  $V_{\text{p}} = 3.91 \times 10^{-23}$  cm<sup>3</sup>. These equations are summarized in the left-hand column of Table 4.1.

The *Fokker-Planck equation-based* precipitation Model analyses precipitates with a distribution of sizes and assigns a different spatial density for each size [103, 159]. The input parameter is the density of precipitation sites,  $N_{\text{prec}}$ . The density of precipitates with  $n$  atoms is  $f(n)$ , and the total density of precipitates is  $N_{\text{p}} = \int_1^{n_{\text{max}}=10^{10}} f(n)dn$ , where  $n_{\text{max}}$  is the maximum precipitate size. The time evolution of the precipitate distribution,  $f(n)$ , is described by the Fokker-Planck equations [103], and it is numerically solved with Cooper and Chang's method [160]. The factor  $A(n, t) = g(n, t) - d(n, t)$  is the net growth rate of the precipitates, and the factor  $B(n, t) = \frac{1}{2}[g(n, t) + d(n, t)]$  describes random fluctuations in the precipitate size. The boundary conditions,  $f(n = n_{\text{max}}, t)$  and  $f(n = 1, t)$ , are defined in Table 4.1,  $p_1 = 1 \times 10^4$  is a fitting parameter and  $f(n = 0, t)$  is the density of empty precipitation sites.  $f(n = 1, t)$  describes which fraction of these sites contain an iron atom, *i.e.* where nucleation occurs. The Gibbs free energy of a precipitate with  $n$  atoms is  $\Delta G(n)$  [161], where  $E_{\text{a}}$  is an energy parameter that accounts for all changes in surface energy and strain caused by the growth and dissolution of precipitates. It has been assumed to be independent of  $n$  and has been estimated in [162]. Assuming that precipitation is *diffusivity-limited*, the equilibrium concentration in the proximity of a precipitate is the dissolved iron concentration for which the change in Gibbs free energy is zero. The precipitate size-dependent equilibrium iron concentration,  $C_{\text{Eq}}$ , depends on the solid solubility of iron,  $C_{\text{S}}$ , and the factor in the exponential captures

the fact that iron has a higher chemical potential in a small cluster than in a large cluster [103]. Precipitates are modeled as flat disks [161] with thickness  $a = 20$  nm, and the capture radius of the precipitation site is explicitly accounted for [163]. Due to the inclusion of the size of the precipitation site, the Fokker-Planck equation model predicts higher capture radii at small precipitate sizes, and due to the faster expansion of 2D disks compared to 3D spheres, the growth of the capture radius remains faster at large precipitate sizes. These equations are summarized in the right-hand column of Table 4.1.

Note that for large precipitate sizes ( $n \gg 1$ ),  $C_{\text{Eq}} \approx C_{\text{S}}$  and the two precipitation models predict similar equilibrium concentrations. However, when modeling small precipitates, the models differ. The expression for the Gibbs free energy predicts a temperature and dissolved iron concentration dependent critical size  $n_{\text{crit}}$ , defined as the size that maximizes  $\Delta G(n)$ . Thermodynamics dictates that precipitates smaller than  $n_{\text{crit}}$  tend to dissolve, whereas precipitates larger than  $n_{\text{crit}}$  tend to grow. The energy needed for the precipitates to cross from the dissolution favoring regime into the growth regime is defined as the nucleation barrier. In the Fokker-Planck equations precipitation model, a certain level of local supersaturation is needed for nucleation to occur; however, in the Ham's law model, there is no nucleation barrier.

Table 4.1: Equations for Precipitation Behavior Model Element

Ham's Law	Fokker-Planck Equation
Evolution of precipitated iron over time	
<p>1 Average Time-Dependent Size</p> $\frac{\partial [Fe_p]}{\partial t} = [g(n_{\text{avg}}) - d(n_{\text{avg}})]N_p$	<p>Time-dependent density and size distribution <math>f(n, t)</math></p> $\frac{\partial f(n, t)}{\partial t} = \frac{\partial}{\partial n} [-A(n, t)f(n, t) + B(n, t)\frac{\partial f(n, t)}{\partial n}]$ $A(n, t) = g(n, t) - d(n, t)$ $B(n, t) = \frac{1}{2}[g(n, t) + d(n, t)]$ <p>Boundary Conditions</p> $f(n = 1, t) = f(0, t)p_1 \exp\left[\frac{-\Delta G(1)}{kT}\right]$ $f(n = 0, t) = N_{\text{prec}} - \int_1^{n_{\text{max}}} f(n, t) dn$ $f(n = n_{\text{max}}, t) = 0$ $\Delta G(n) = -nkT \ln \frac{C_{\text{Fe}}}{C_{\text{S}}} + 2E_a n^{\frac{1}{2}}$
Precipitate growth and dissolution rates	
$g(n_{\text{avg}}, t) = 4\pi r_c(n_{\text{avg}})D_{\text{Fe}}C_{\text{Fe}}$ $d(n_{\text{avg}}, t) = 4\pi r_c(n_{\text{avg}})D_{\text{Fe}}C_{\text{Eq}}$	$g(n, t) = 4\pi r_c(n)D_{\text{Fe}}C_{\text{Fe}}$ $d(n, t) = 4\pi r_c(n)D_{\text{Fe}}C_{\text{Eq}}(n)$ $C_{\text{Eq}}(n) = C_{\text{S}} \exp\left(\frac{E_a}{kTn^{\frac{1}{2}}}\right)$ $E_a = \begin{cases} 1.015 \times T \times 10^{-4} + 0.8003 & \text{if } T < 773 \text{ K} \\ 6.038 \times T \times 10^{-4} & \text{if } T \leq 773 \text{ K} \end{cases}$
Precipitate shape and size	
<p>Spherical precipitates with capture radius <math>r_c</math></p> $r_c(n_{\text{avg}}) = \left(\frac{3V_{\text{P}}}{4\pi}n_{\text{avg}}\right)^{\frac{1}{3}}$	<p>Flat disk-shaped precipitates with capture radius <math>r_c^{\text{FPE}}</math></p> $r_c(n) = \begin{cases} 15 \text{ nm} + 0.051 \text{ nm} \times n^{\frac{1}{2}} & \text{if } n < 5.42 \times 10^4 \text{ atoms} \\ 15 \text{ nm} + \frac{(\frac{nV_{\text{P}}}{\pi a})^{\frac{1}{2}} \pi}{\ln [16(\frac{nV_{\text{P}}}{\pi a^3})^{\frac{1}{2}}]} & \text{if } n \geq 5.42 \times 10^4 \text{ atoms} \end{cases}$



## Chapter 5

# Synchrotron-based investigation of transition-metal getterability in *n*-type multicrystalline silicon

The material in this Chapter is adapted from [164].

Solar cells based on *n*-type multicrystalline silicon (mc-Si) wafers are a promising path to reduce the cost per kWh of photovoltaics; however, the full potential of the material and how to optimally process it is still unknown. Modeling and process optimization require knowledge of the response of the metal-silicide precipitate distribution to processing, which has yet to be directly measured and quantified. To supply this missing piece, we use synchrotron-based micro-X-ray fluorescence ( $\mu$ -XRF) to quantitatively map  $>250$  metal-rich particles in *n*-type mc-Si wafers before and after phosphorus diffusion gettering (PDG) performed over a wide range of temperatures. We find that a low-temperature 820°C PDG is sufficient to remove precipitates of fast-diffusing impurities and that a high-temperature 920°C PDG can eliminate precipitated iron to below the detection limit of the technique. Thus, the evolution of precipitated metal impurities during gettering is observed to be similar for *n*- and *p*-type mc-Si, an observation consistent with calculations of the driving forces for precipitate dissolution and segregation gettering. Measurements of the minority-carrier lifetime improvement after each of the gettering processes show that lifetime

increases with increasing precipitate dissolution from 820°C to 880°C and the lifetime after PDG at 920°C lies between those of the two lower temperatures.

## 5.1 Overview of Impurity Gettering and Process Simulations for *n*- and *p*-type mc-Si

For photovoltaics, *n*-type multicrystalline silicon (mc-Si) wafers are an attractive alternative to *p*-type mc-Si wafers. One advantage is that some common metal point defects, notably interstitial iron, are less recombination active in *n*-type than in *p*-type Si [39, 106, 142]. It has been shown that phosphorus diffusion gettering (PDG) can increase the lifetime of *n*-type mc-Si, including in low-lifetime ingot border regions [44, 61, 165, 166], and that industrially-relevant efficiencies are achievable [167, 168]. For *p*-type mc-Si, simulation of the redistribution of metal impurities during PDG and the resulting lifetime impact has enabled development of PDG processes that improve yield and extract higher performance, especially in border regions and the top of the ingot [94, 104, 136, 169–171]. For *n*-type mc-Si, lifetime models for point defects [39] and iron-silicide precipitates [98] have been developed. The precipitated metal distribution for a range of PDG temperatures has yet to be measured and quantified, hampering the development of modeling and processing that is co-optimized for manufacturing throughput and high performance. In this contribution, we mapped the precipitated metal distributions in *n*-type mc-Si wafers before and after several different processes. We also report spatially-resolved lifetime improvement associated with each process.

## 5.2 Samples, Gettering Processes, and Impurity and Lifetime Characterization Methods

Three nearly vertically-adjacent wafers with thickness  $205 \pm 5$   $\mu\text{m}$  and resistivity of 2  $\Omega\text{-cm}$  were selected from the middle height of a corner brick of a 6N's purity compen-

sated *n*-type upgraded metallurgical grade (UMG) industrially-produced Generation 5 cast mc-Si ingot. The low-lifetime “red zone” region formed near the crucible walls during casting was identified with microwave photoconductance decay using a *Semilab WT-2000*. All samples were CP4 etched to a thickness of 190  $\mu\text{m}$  to remove saw damage.

From each wafer, several different samples were selected for characterization and processing. To quantify the total concentrations of metal impurities in the as-grown wafers, 1 g samples from the red zone were selected from two of the wafers for inductively coupled plasma mass spectroscopy (ICP-MS). To map the precipitated impurity distribution before and after PDG, a  $1\times 1\text{ cm}^2$  sample was selected from the red zone of each wafer for synchrotron-based micro-X-ray fluorescence spectroscopy ( $\mu$ -XRF) measurements. For photoconductance-calibrated photoluminescence imaging (PC-PL),  $4\times 5\text{ cm}^2$  lifetime samples adjacent to each  $\mu$ -XRF sample were cut.

The  $\mu$ -XRF and electrical characterization samples were phosphorus-diffused in a Tystar Titan 3800 tube furnace at 820, 880, and 920°C for 60 min followed by a slow cool at  $\sim 4\text{ }^\circ\text{C}/\text{min}$  to 600°C, at which point they were unloaded from the furnace. The time-temperature profiles and their respective sheet resistances measured on a *p*-type Cz-Si control sample processed at the same time are shown in Fig. 5-1. The same region on each sample was measured before and after PDG. To test the effect of the time spent at diffusion temperature on the precipitated metal distribution,  $\mu$ -XRF was also measured on a sample that was diffused at 820°C for only 30 min followed by the same slow cool (S820°C).

$\mu$ -XRF was measured at Argonne National Laboratory’s Advanced Photon Source Beamline 2-ID-D using an incident X-ray energy of 10 keV with data mapped in step-by-step scanning mode. A  $\Sigma 33$  grain boundary that is present in all three  $\mu$ -XRF samples was identified with electron backscatter diffraction (EBSD).  $\mu$ -XRF maps were measured along the grain boundary in 220 nm steps with a spot size of 209 nm at full width half maximum. To be considered a detected particle, a given pixel had to have a metal loading above both of the following noise floors. The statistical detection limit (SDL) was set at four standard deviations above the mean of the noise [31].

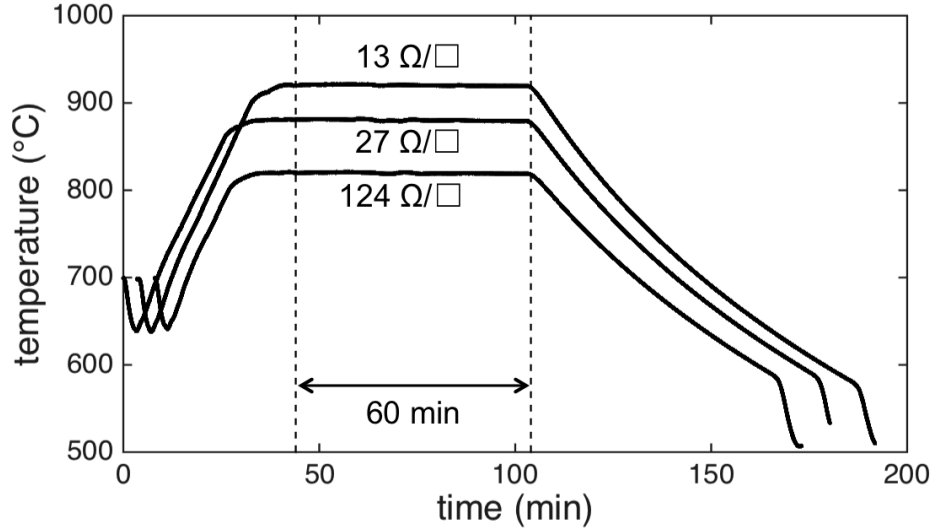


Figure 5-1: PDG time-temperature profiles used in this study. A 60 min plateau was followed by an in-furnace cool to below 600°C. Sheet resistances were measured on a *p*-type Cz-Si control sample processed at the same time.

The theoretical minimum detection limit (MDL) was calculated from measurements of NIST standards 1832 and 1833 measured in the same experimental configuration as the respective sample. We assume that the detected Fe in these mc-Si wafers is in  $\beta$ -FeSi<sub>2</sub> precipitates [172] in which  $3.76 \times 10^{-23}$  cm<sup>3</sup> is the effective volume of one Fe atom [173]. We further assume that the precipitates are spherical and that for size calculations they are all at the surface of the sample as in Refs. [31, 50, 59, 171]. Further details are available in Refs. [50, 171].

The PC-PL images were captured using the same experimental setup as in Jensen *et al.* [31] and originally described in Herlufsen *et al.* [174]. Surface passivation is the same as in Jensen *et al.* [31].

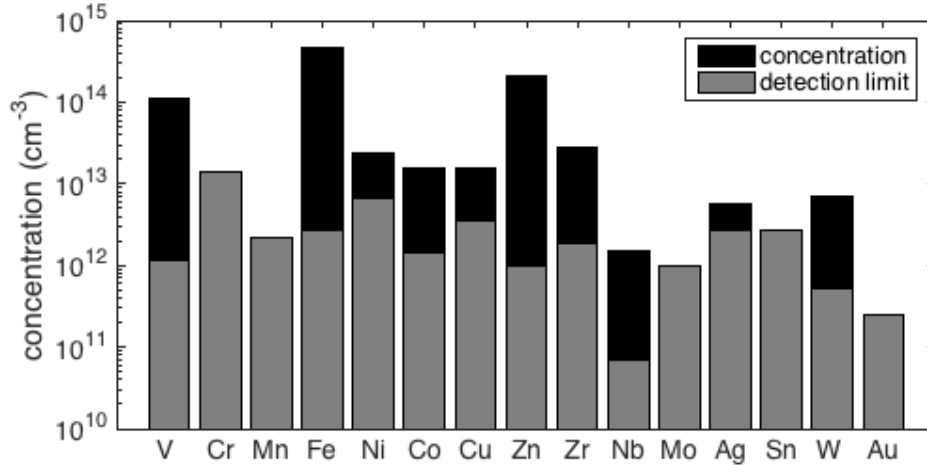


Figure 5-2: ICP-MS of 15 transition metals from red zone of as-grown *n*-type UMG mc-Si. The gray bars indicate the detection limit of the measurement for each element. Fe is  $4.7 \times 10^{14} \text{ cm}^{-3}$  while Ni, Co, and Cu are at concentrations of  $2.4 \times 10^{13} \text{ cm}^{-3}$ ,  $1.6 \times 10^{13} \text{ cm}^{-3}$ , and  $1.6 \times 10^{13} \text{ cm}^{-3}$ , respectively

### 5.3 $\mu$ -XRF Maps of Metals and Calibrated Lifetime Maps Before and After a Wide Range of PDG Temperatures

The ICP-MS results (Fig. 5-2) reveal V, Fe, Ni, Co, Cu, Zn, Zr, Nb, Ag, and W in the red zone. The concentration of Fe is  $4.7 \times 10^{14} \text{ cm}^{-3}$  while Ni, Co, and Cu are at concentrations of  $2.4 \times 10^{13} \text{ cm}^{-3}$ ,  $1.6 \times 10^{13} \text{ cm}^{-3}$ , and  $1.6 \times 10^{13} \text{ cm}^{-3}$ , respectively. Consistent with the high concentrations identified by ICP-MS, the as-grown  $\mu$ -XRF measurements revealed Fe-, Co-, Ni-, and Cu-containing particles co-located along the  $\Sigma 33$  grain boundary (Fig. 5-4). Zr, Nb, Mo, Ag, Sn, W, and Au are not detected in the as-grown  $\mu$ -XRF measurements because their  $K\alpha$  binding energies are greater than the 10 keV incident energy [175]. We hypothesize that any Zn particles are too small to detect because Zn diffuses relatively slowly in silicon and thus may be found in a high spatial density of small precipitates [29]. V, Cr, and Mn were also not detected in quantities above the noise floor of the  $\mu$ -XRF measurements. ICP-MS was measured on two red zone and two bulk samples from the same wafers. The full results are shown in Fig. 5-3.

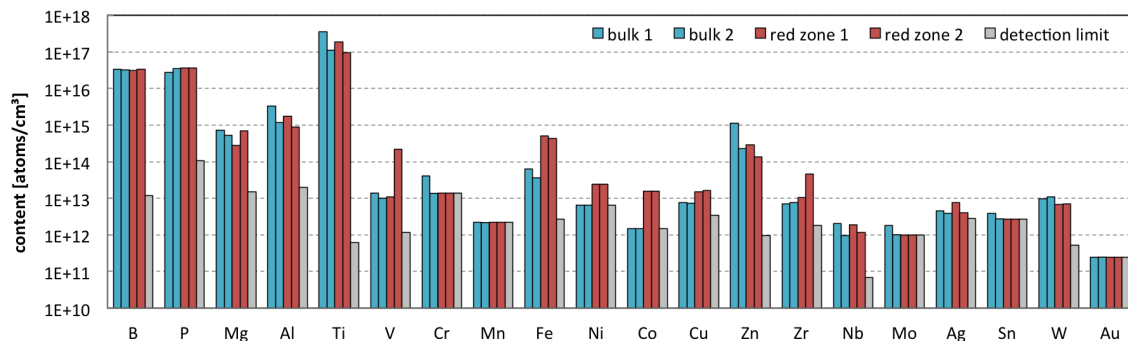


Figure 5-3: ICP-MS of 20 elements from two nearly vertically adjacent samples from the bulk (blue bars) and two nearly vertically adjacent samples from the red zone (red bars) of as-grown *n*-type UMG mc-Si. The gray bars indicate the detection limit of the measurement for each element.

After all of the PDG processes studied, Fe is the only metal that persists at detectable levels in the  $\mu$ -XRF measurements. Shown in Fig. 5-6 are the Fe channel of quantified  $\mu$ -XRF maps of a  $\sim 50$   $\mu\text{m}$ -wide portion of the grain boundary before and after each 60 min PDG process. Bright yellow pixels have high Fe loading, likely along the plane of the grain boundary. PDG at 820°C reduced the number of Fe particles from 39 to 28, a 28% removal. PDG at 880°C reduced the number of Fe particles from 58 to 36, a 38% removal. Finally, PDG at 920°C removed all 60 Fe particles, to within the detection limit, a 100% removal. The post-gettering  $\mu$ -XRF maps for the S820°C and 820°C processes are shown in Fig. 5-5.

The Fe maps of Fig. 5-6 were further analyzed to quantify the particle size distribution before and after gettering. Fig. 5-8 shows the number of Fe atoms per particle and the corresponding calculated precipitate radius before and after each process. As-grown, Fe-rich particles ranging in size from 8 to 30 nm were identified. After gettering at 820°C, the mean precipitate size is similar, and the median precipitate size increases compared to the as-grown state. After gettering at 880°C, the mean and median precipitate size decrease noticeably from the as-grown state. After the 920°C gettering, even though the noise floor of the  $\mu$ -XRF measurement after gettering was lower than that of the as-grown measurement, no particles were detected. To directly compare the effect of PDG at 820 and 880°C, histograms of the precipitate size distributions are plotted in Fig. 5-9a and b. After PDG at 820°C, the relative

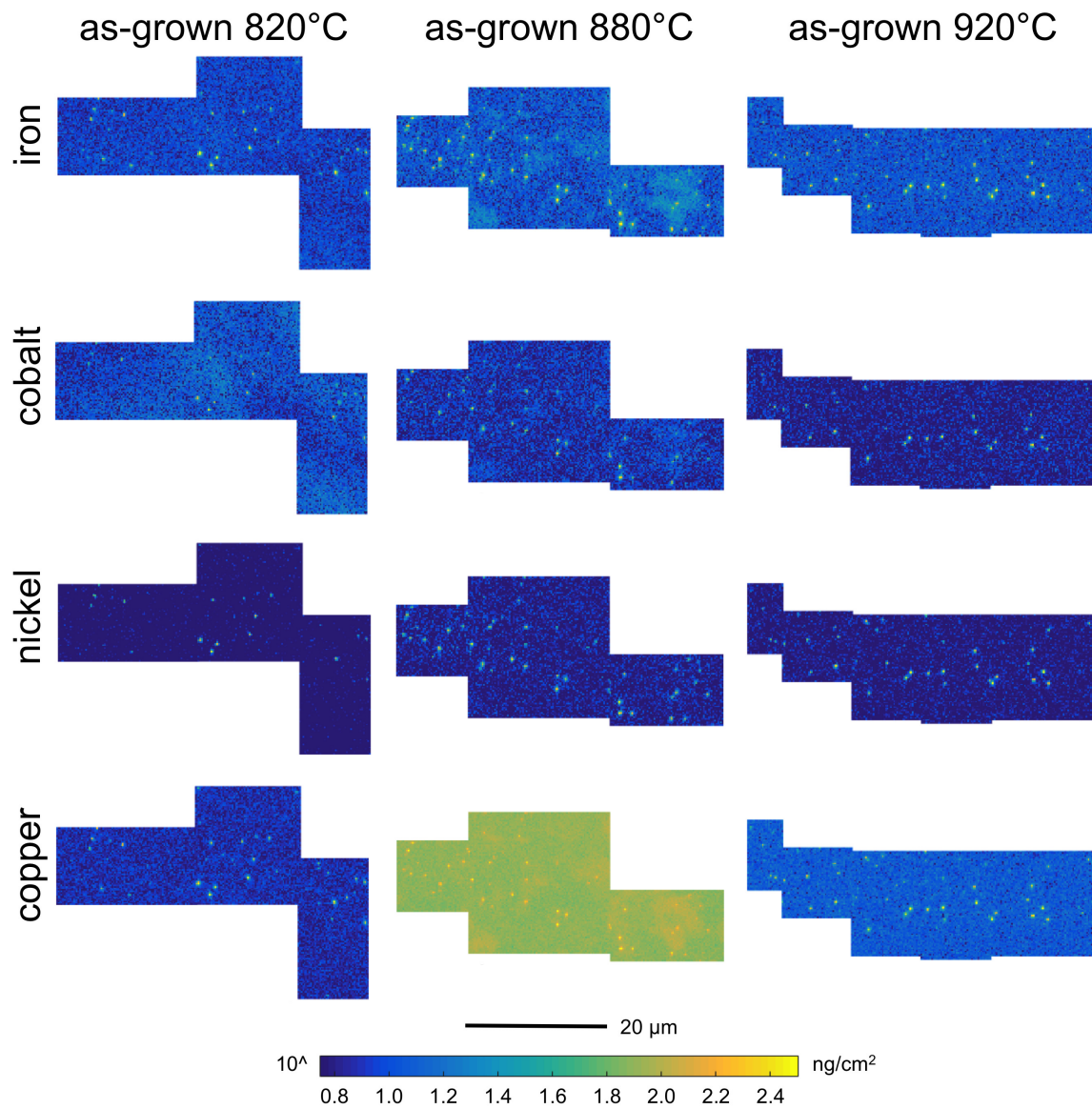


Figure 5-4:  $\mu$ -XRF maps of Fe (row 1), Co (row 2), Ni (row 3), and Cu (row 4) precipitates in the three samples as-grown (each column). Particles are found co-located along a  $\Sigma$ 33 grain boundary.

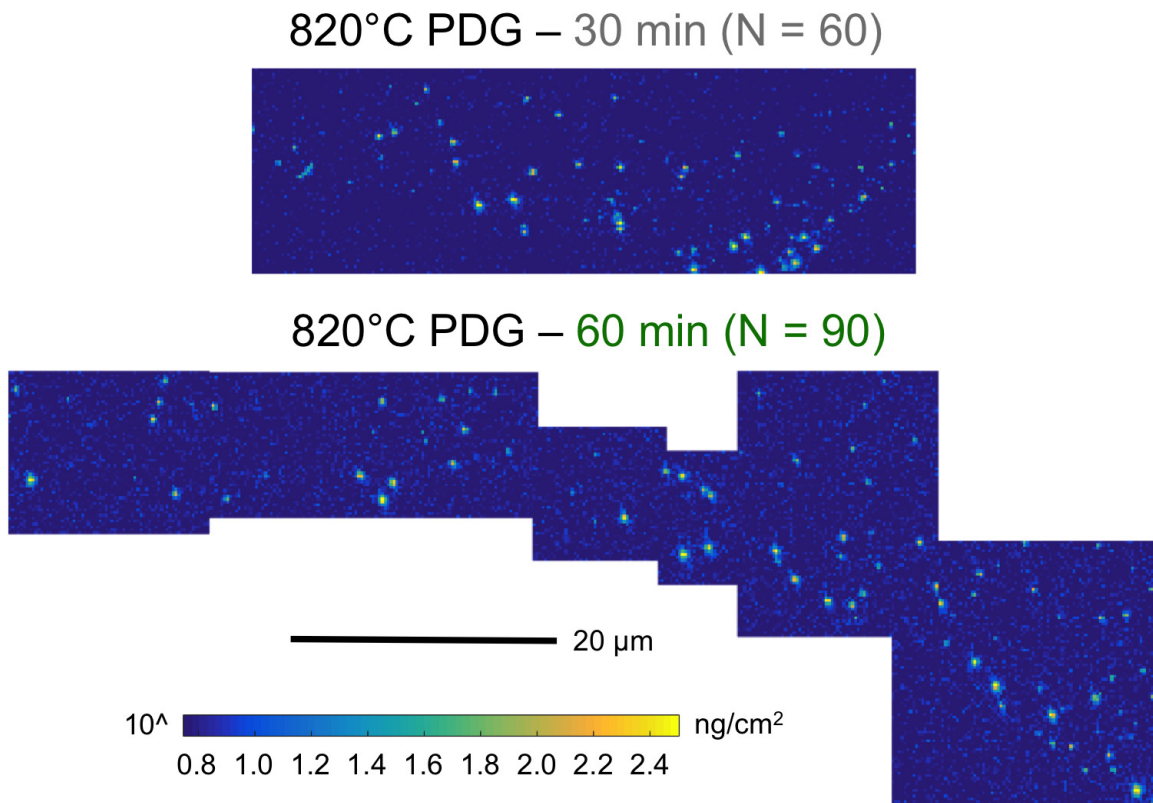


Figure 5-5: The Fe channel of  $\mu$ -XRF maps at 820°C for 30 min (S820°C) and 60 min. Histograms of the Fe particles shown in these  $\mu$ -XRF maps are shown in Fig. 5-7. Quantified precipitate size distributions for each of these maps are shown in Fig. 5-11.

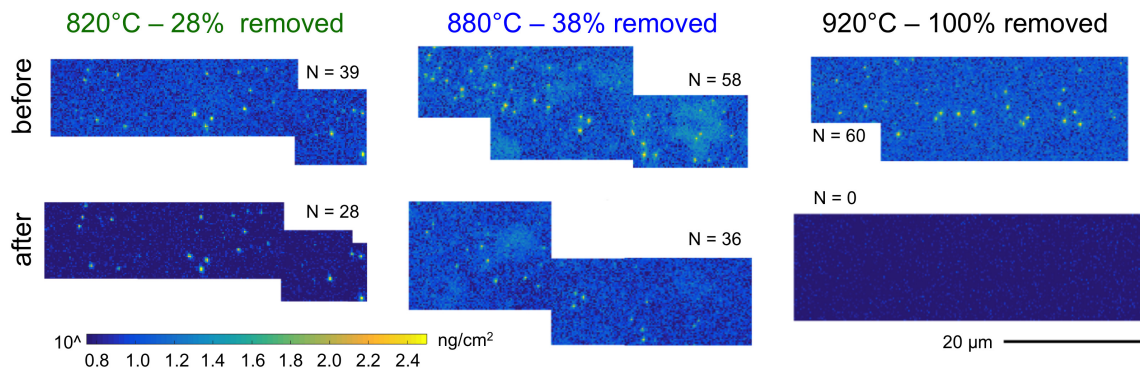


Figure 5-6:  $\mu$ -XRF maps of the Fe channel for  $\sim 50 \mu\text{m}$  of a  $\Sigma 33$  grain boundary in three nearly vertically-adjacent *n*-type mc-Si samples before (*top row*) and after (*bottom row*) PDG at 820°C (*left*), 880°C (*center*), and 920°C (*right*). Bright yellow pixels have high Fe loading, measured in  $\text{ng}/\text{cm}^2$ . The number of Fe particles identified,  $N$ , in each map is indicated. As the PDG temperature increases, Fe particles are more readily dissolved. 920°C PDG reduced Fe to undetectable levels.



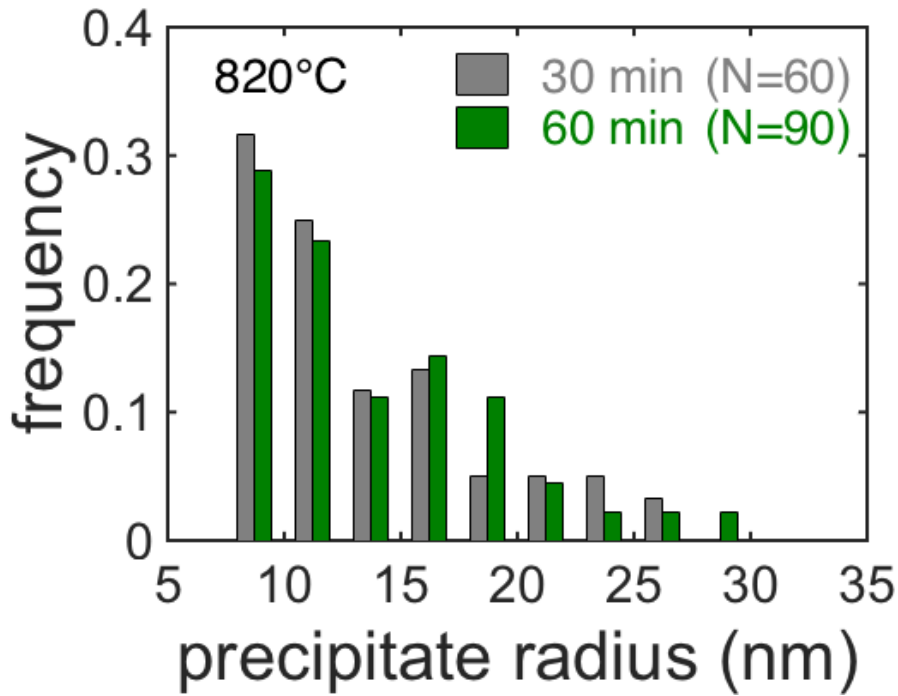


Figure 5-7: Histograms of the Fe precipitate distribution measured by  $\mu$ -XRF (maps in Fig. 5-5) for 820°C for 30 min (S820°C) and 60 min.

frequency of many, but not all, of the precipitate sizes decreases. In contrast, PDG at 880°C noticeably shifts the precipitate size distribution to smaller precipitates. A histogram of the precipitate sizes after gettering for the S820°C and 820°C process show very similar distributions (Fig. 5-7).

To quantify the effect on an individual precipitate basis, for Fe particles identifiable before and after gettering in the maps of Fig. 5-6, the percent reduction in the number of Fe atoms per precipitate was calculated for each particle, and the resulting frequency distribution of the size reduction for each process is shown in Fig. 5-9c. For PDG at 820°C, the peak of the size reduction distribution is 45% reduction. For PDG at 880°C, the peak of the size reduction distribution is higher at 65% reduction.

The total sample area scanned after gettering was larger than and included the areas scanned before processing to ensure that all regions measured as-grown would be measured after gettering. The trends in precipitate size the subset of the data shown in Figs. 5-6 – 5-9 are the same as those of the full data set. The full Fe  $\mu$ -XRF maps are shown in Fig. 5-10. The quantified Fe precipitate sizes for all of the regions

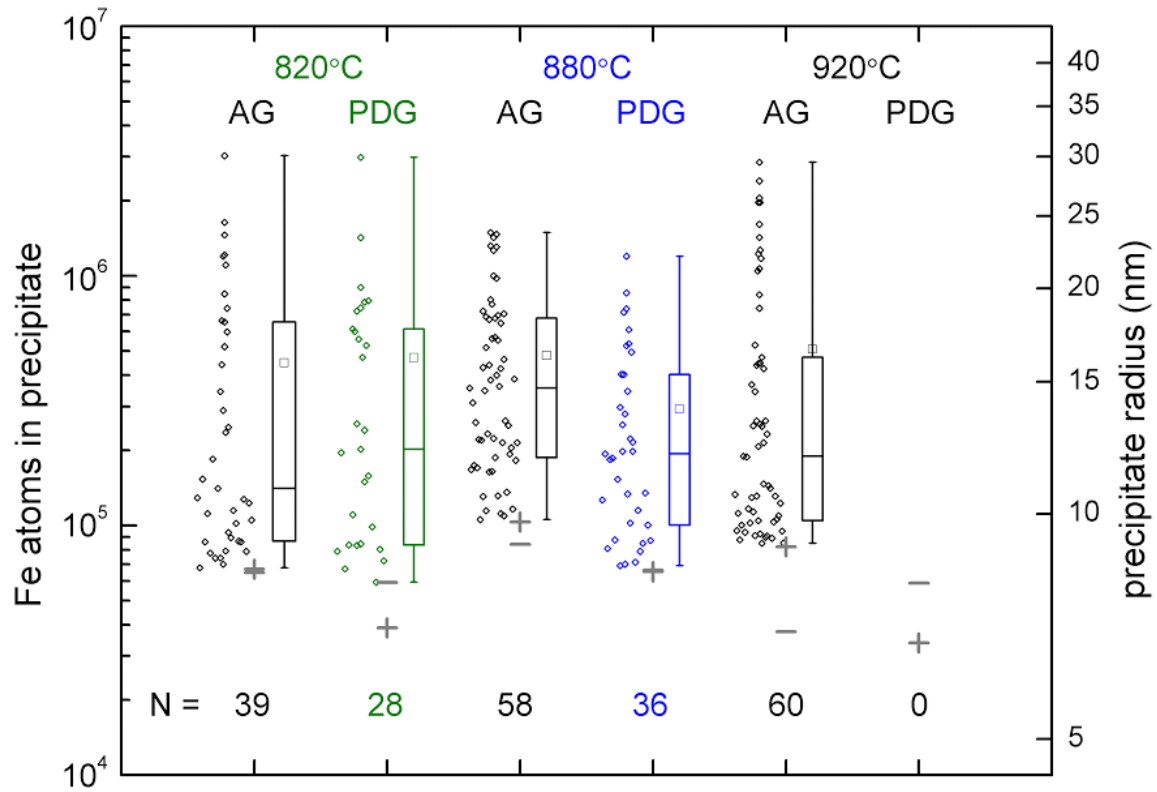


Figure 5-8: Quantified Fe precipitate size distribution before (AG) and after three different PDG processes for the  $\mu$ -XRF maps shown in Fig. 5-6. The box plots to the right of each data set show the minimum, maximum, and quartiles of the distribution. The arithmetic average is indicated by the open square.  $N$  is the number of Fe particles identified in each map. The “-” indicates the MDL. The “+” indicates SDL.

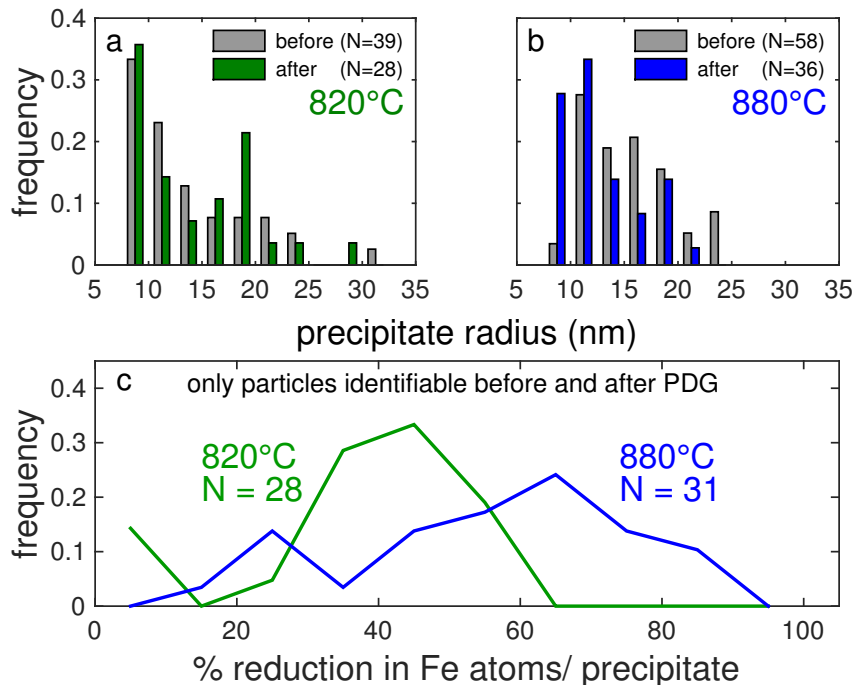


Figure 5-9: Fe precipitate size distributions for particles in the maps of Fig. 5-6 before and after PDG at 820°C (a) and 880°C (b). (c) Histogram of reduction in size of individual precipitates for Fe-rich particles identifiable before and after gettinger. PDG at 820°C has a peak reduction of 45%. PDG at 880°C has a peak reduction of 65%. PDG at 920°C removes 100% of Fe particles to below the detection limit.  $N$  is the number of Fe particles included in each analysis.

mapped (shown in Fig. 5-5 and 5-10) are shown in Fig. 5-11.

To quantify the improvement in lifetime after each process, the spatially-resolved ratio of post- to pre-gettering PC-PL lifetime was calculated. Then, for each pixel, the lifetime improvement ratio in was plotted as a function of the as-grown lifetime (Fig. 5-12). PC-PL lifetime images at an average injection level of  $1.4 \times 10^{14} \text{ cm}^{-3}$  before and after PDG and their ratio are shown in Fig. 5-13. As-grown, the samples had similar lifetimes with a harmonic mean of 23  $\mu\text{s}$ . After processing, the lifetimes increase for all processes by over an order of magnitude. The post-gettering harmonic mean lifetimes were 500, 575, and 520  $\mu\text{s}$  for PDG at 820, 880, and 920°C, respectively.

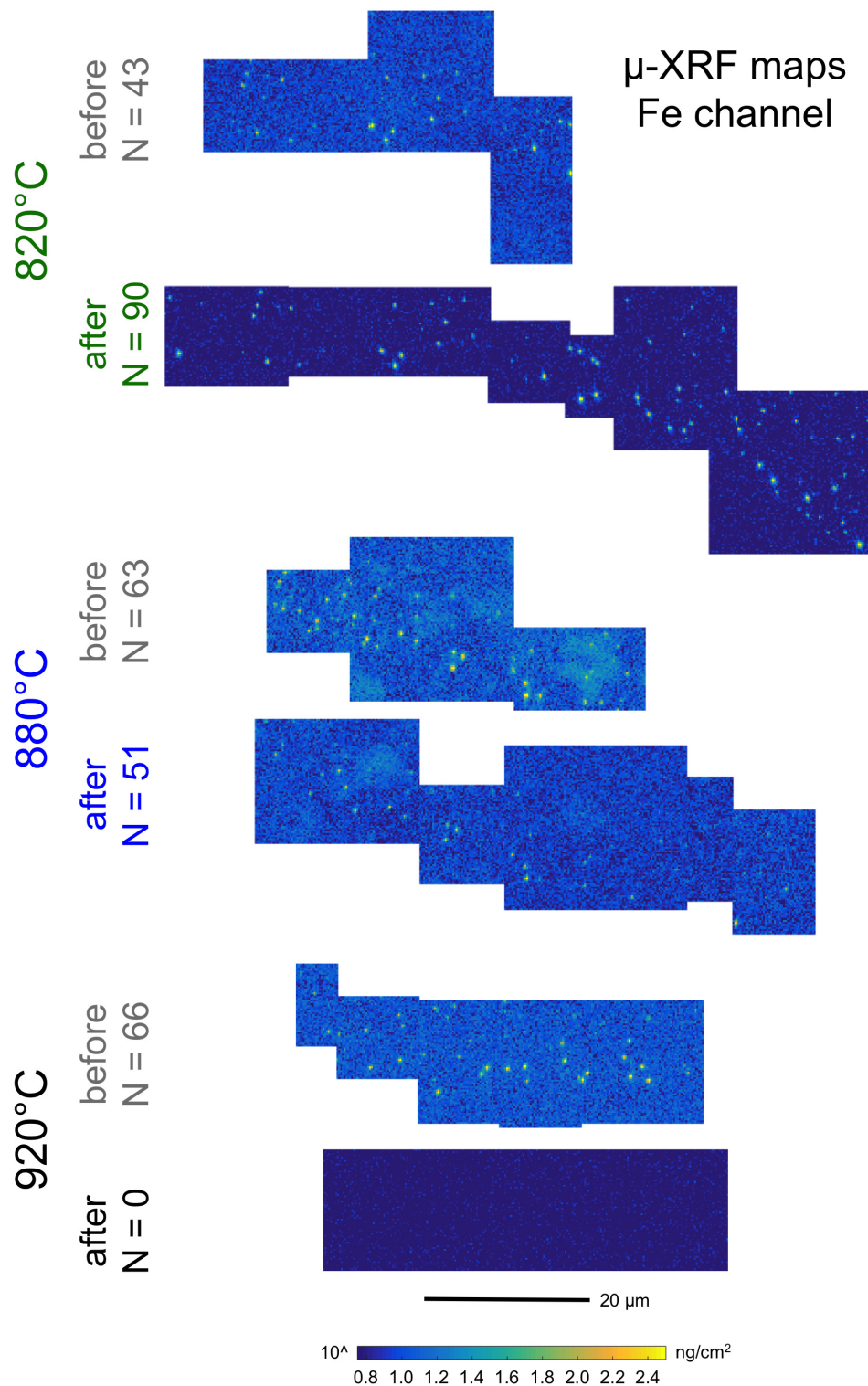


Figure 5-10: The Fe channel of  $\mu$ -XRF maps measured before and after PDG for 60 min at 820, 880, and 920°C. Bright yellow pixels are Fe-rich particles. A larger total area was measured after PDG to ensure that all regions measured as-grown would be captured after gettinger.  $N$  is the number of particles identified in each  $\mu$ -XRF map. Quantified precipitate size distributions for each of these maps are shown in Fig. 5-11.

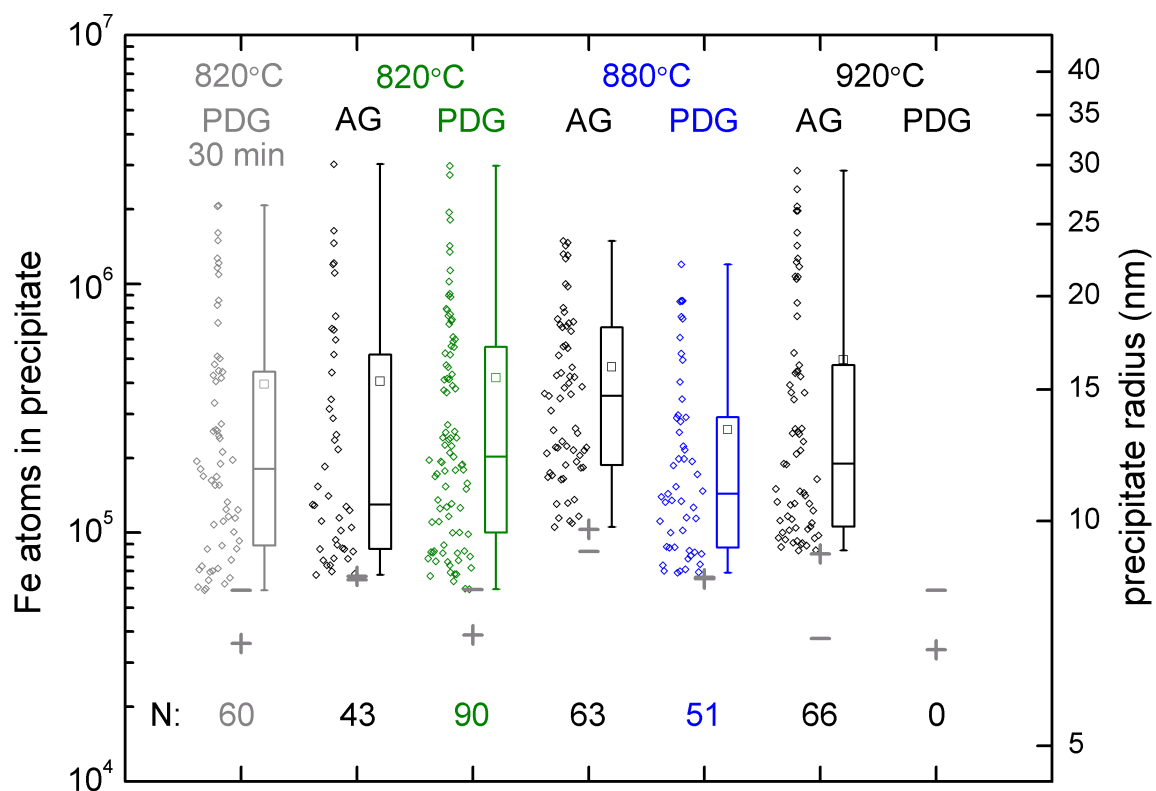


Figure 5-11: Synchrotron-based  $\mu$ -XRF measurements of Fe particle size before and after four different PDG processes (S820, 820, 880, and 920°C) for all of the data collected (maps in Fig. 5-10). As-grown, particles range in size from 8 to 30 nm radius. After PDG at 820°C, the distribution appears to be similar. After PDG at 880°C, the size distribution shifts to smaller precipitates. After PDG at 920°C, no precipitates are identified above the noise floor. The “-” indicates the MDL. The “+” indicates SDL. The box plots highlight the minimum, maximum, 1st, 2nd, and 3rd quartiles, and the arithmetic average.

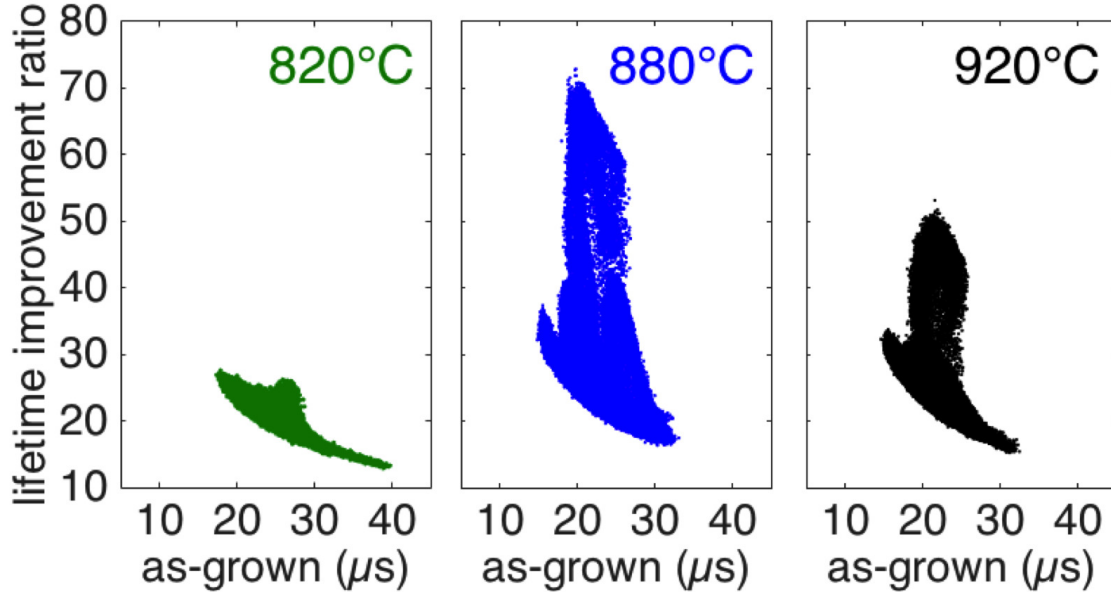


Figure 5-12: Plots of the lifetime improvement ratio (PDG/ as-grown lifetime) as a function of the as-grown lifetime for each process. All processes increase lifetime. PDG at 880°C is the most effective, followed by PDG at 920°C. PDG at 820°C is the least effective. Each data point is a pixel from the images shown in Fig. 5-13.

## 5.4 Discussion: metal redistribution is similar in *n*-type and *p*-type mc-Si during phosphorus diffusion gettering

Our results support the hypothesis that the redistribution of metals during PDG is similar in *p*-type and *n*-type mc-Si.  $\mu$ -XRF measurements of as-grown *p*-type mc-Si wafers with a very similar total Fe concentration of  $4.4 \times 10^{14} \text{ cm}^{-3}$  revealed a similar precipitate size distribution of up to 30 nm radius particles [50]. After gettering at 870°C, precipitates of fast-diffusing species, specifically Cu, are readily removed from *p*-type mc-Si, but Fe precipitates persisted at a reduced level [171]. For *p*-type mc-Si with a total Fe concentration of  $\sim 10^{15} \text{ cm}^{-3}$ , the median reduction in precipitate size of Fe-rich precipitates identifiable both before and after gettering increased as the gettering temperature increased [171]. The median reduction after 820°C, 870°C, and 920°C PDG was 84.1%, 85.3%, and 91.5%, respectively [171]. For the highest temperature 920°C PDG, we hypothesize that the Fe precipitates

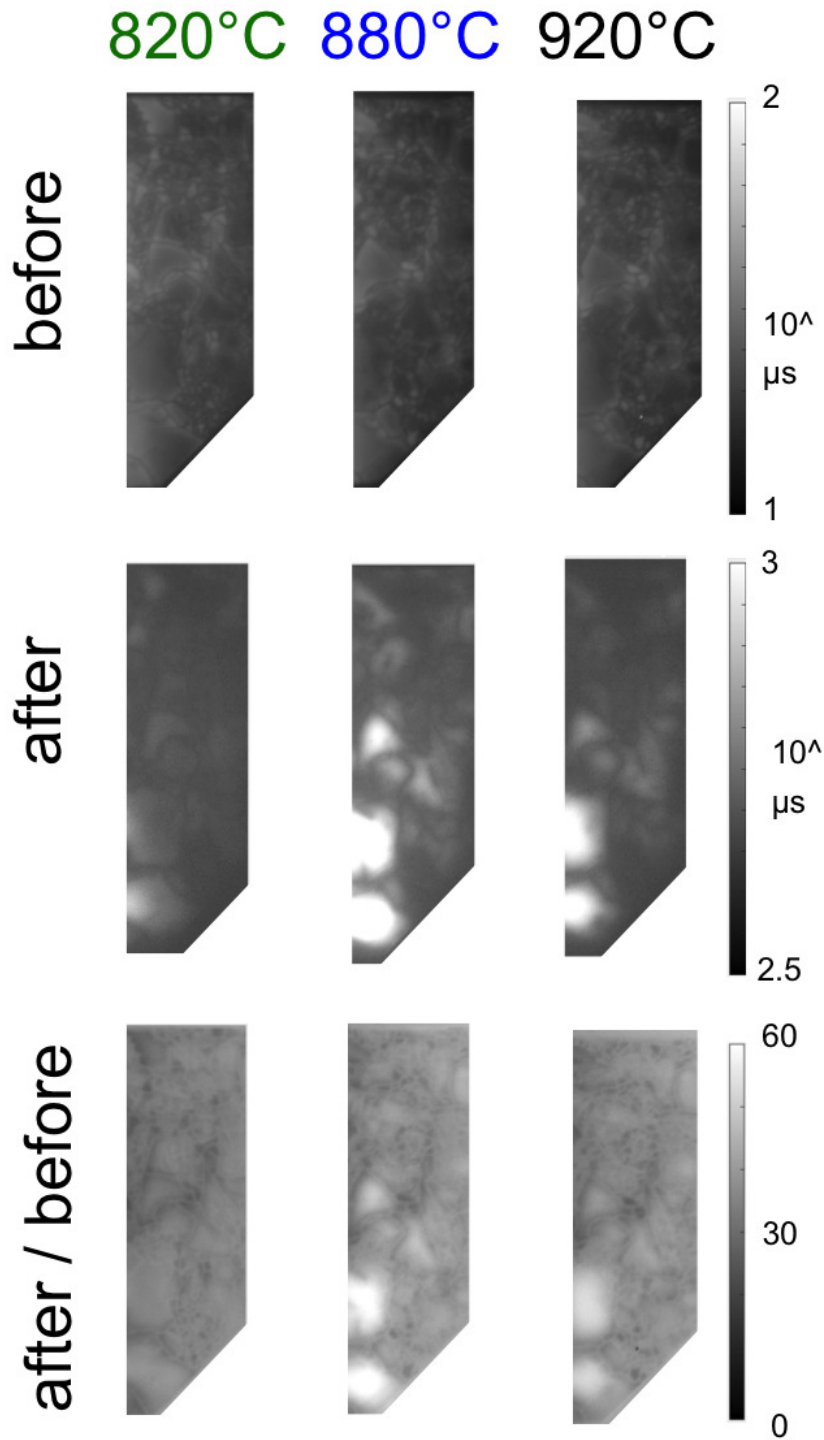


Figure 5-13: PC-PL images of samples from the red zone in *n*-type mc-Si wafers before (top row) and after (middle row) PDG at 820, 880, and 920°C. The spatially-resolved ratio of gettered to as-grown lifetime was also calculated (bottom). The average injection level was  $1.4 \times 10^{14} \text{ cm}^{-3}$ . PDG at 880°C most effectively improves lifetime.

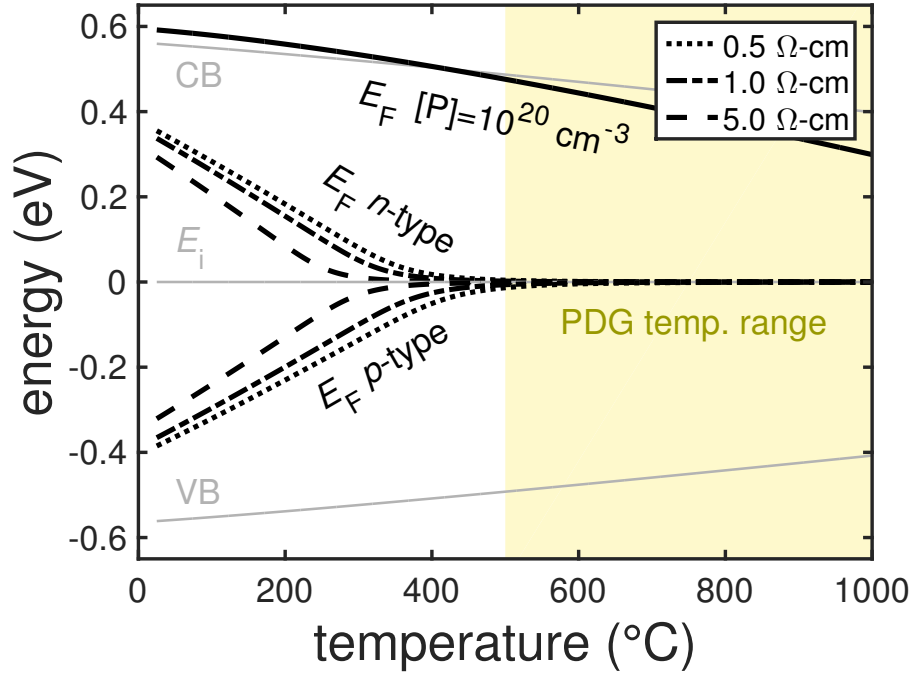


Figure 5-14: Energy band diagram of doped Si as a function of temperature. The Fermi level,  $E_F$ , in the phosphorus in-diffused region (solid black line) for a representative phosphorus concentration of  $10^{20} \text{ cm}^{-3}$  is far above midgap for the whole temperature range shown. The  $E_F$  curves for phosphorus-doped and boron-doped wafers with resistivities of 0.5, 1.0, and 5.0  $\Omega\text{-cm}$  approach and then equal the intrinsic Fermi level,  $E_i$ , above 500°C. The yellow region highlights temperature  $>500^\circ\text{C}$ , the range of temperatures of interest for PDG processing.  $E_F$ -dependent physical phenomena driving the redistribution of Fe during PDG are thus similar in  $n$ -type and  $p$ -type mc-Si during PDG.

were reduced to below the detection limit in the  $n$ -type material because the total Fe concentration of  $4.7 \times 10^{14} \text{ cm}^{-3}$  is only slightly higher than the solid solubility of Fe at  $920^\circ\text{C}$  [176], making it likely that in the bulk full dissolution was achieved at guttering temperature. The reported percent reductions in precipitate size after the  $820^\circ\text{C}$  and  $880^\circ\text{C}$  PDG were higher than those observed in this study. We attribute this difference to differences in the initial Fe distribution, time-temperature profiles, and differing noise limits of the measurements. Thus, the temperature-dependence of metal redistribution in  $p$ -type mc-Si and the  $n$ -type mc-Si studied herein is similar and for simulation and modeling purposes can be assumed to be the same.

We observe similar precipitate-dissolution behavior during gettering in both  $n$ -



and *p*-type silicon, suggesting similar governing physics. Our calculations indicate that at phosphorus diffusion gettering temperatures, the Fermi energy is close to or at midgap for both *n*- and *p*-type silicon. Fig. 5-14 shows the evolution of the energy band diagram of crystalline silicon as a function of temperature for phosphorus-doped and boron-doped silicon for three different resistivity levels relevant to photovoltaics. At temperatures relevant for PDG  $>500^\circ$ , both *p*- and *n*-type Si, the intrinsic carrier concentration is high enough that the Fermi levels of the doped material approach the intrinsic Fermi level. This has important implications for transition-metal diffusion and segregation. The physics underlying PDG are the nucleation and subsequent growth or dissolution of precipitates, the solid solubility, and the diffusivity of metal point defects [32]. This study provides evidence that the trends in these physical driving forces are similar in *n*- and *p*-type silicon at PDG process temperature for deep level defects. The nucleation and subsequent growth or dissolution of precipitates does not depend on the base doping type when nucleation occurs at high temperature [177], but rather on the local temperature-dependent solid solubility, the local dissolved species concentration, the precipitate size, the surface energy, lattice strain, and the morphology of the precipitate [161, 178–181]. The solid solubility of doped Si is enhanced compared to that of intrinsic Si, but the enhancement is similar for Fermi levels that are equidistant from midgap [57, 176, 182]. Finally, the diffusivity of metals in Si depends on the relative concentrations of charged and neutral species. For a wide range of parameters, including doping type and varying relative concentrations of charged and neutral Fe, the diffusivity of Fe in Si can be relatively well described with a single straight line fit [176]. At higher temperatures, the majority of the Fe is neutral because the Fermi level is at or close to midgap as discussed above [176].

Modeling indicates that the lifetimes measured after PDG in this 6N's UMG *n*-type mc-Si,  $>500 \mu\text{s}$ , are long enough to support high-efficiency solar cells [166, 183]. The lifetime trends are also similar to those in a similar study of *p*-type mc-Si that was gettered at  $820^\circ\text{C}$ ,  $870^\circ\text{C}$ , and  $920^\circ\text{C}$  [171]. For both materials, the average lifetimes increased by over an order of magnitude, and the lifetime was longest after gettering at the intermediate temperature.

Our results are consistent with the hypothesis that, as with *p*-type mc-Si [60], removal of both precipitated and point defect impurities is likely important for maximizing lifetime in *n*-type mc-Si. The 820°C gettering leaves much of the iron in precipitates, limiting the lifetime. The 920°C process removes precipitates, but the cooling time is inadequate for external gettering of the resulting high Fe point defect concentration. The 880°C balances the two lifetime-limiting factors because it reduces the concentration of precipitated Fe, and the cooling time is sufficient to remove much of the resulting Fe point defects. Further comparative investigation, including the effect of hydrogen passivation [184–186] on structural defect recombination activity, measurements of the recombination activity of individual metal-rich precipitates, and further perturbations of the time-temperature profile parameters, is needed to clarify the role of the metal impurity distribution in the performance of *n*-type mc-Si and thus how to process it to extract its full performance potential.

## 5.5 Conclusions

In summary, using a combination of synchrotron-based  $\mu$ -XRF mapping of >250 metal-rich particles and PC-PL lifetime imaging, we show that metal impurities in industrially-grown *n*-type UMG mc-Si are getterable and that PDG improves minority carrier lifetime by over an order of magnitude. PDG at temperatures as low as 820°C fully removed Cu-, Ni-, and Co-rich particles to below detection limits. We achieved partial removal of Fe with PDG at 880°C and a 920°C process removed all precipitated transition metals to below detection limits. Gettering at 820°C for 30 min and 60 min resulted in similar precipitated iron distributions, indicating that precipitate dissolution may saturate after 30 min or less and pointing to an opportunity to shorten processing without sacrificing precipitate remediation. Our results are consistent with calculations showing that the physical mechanisms underlying the redistribution of metals during PDG are similar for *n*-type and *p*-type mc-Si.

## Chapter 6

# Direct measurement of Iron Content and Lifetime of individual Fe-rich precipitates in *n*-type crystalline silicon using $\mu$ -XRF in on-the-fly scanning mode and $\mu$ -photoluminescence

To directly quantify the recombination activity of iron-rich precipitates in *n*-type crystalline silicon, an essential component of minority carrier lifetime modeling, micro-X-ray fluorescence ( $\mu$ -XRF) and micro-photoluminescence ( $\mu$ -PL) were used to quantitatively map an intentionally iron-contaminated wafer-bonded dislocation network sample of the type described in [40]. This carefully designed structure has proven to be a useful model system for studying transition metals in crystalline Si because metals readily precipitate out in the well-defined plane of the dislocation network. The  $\mu$ -XRF was measured and the areal density of metals was quantified at Beamline 2-ID-D, and the  $\mu$ -PL was measured and quantified by Friedemann Heinz at Fraun-

hofer ISE by the group of Martin Schubert. Details of the  $\mu$ -PL measurement are provided in Refs. [187–189]. The data were further quantified and analyzed in collaboration with Hannu Laine of the Electron Physics Group headed by Hele Savin at Aalto University.

## 6.1 Development of Flyscan Capability at Advanced Photon Source’s Synchrotron Beamline 2-ID-D

The material in this Section is adapted from [190].

Synchrotron-based  $\mu$ -XRF is a powerful tool to measure elemental distributions non-destructively with high spatial resolution ( $<200$  nm) and excellent sensitivity (typically  $\sim 10^{14}$  atoms/cm<sup>2</sup>). Recently, on-the-fly data collection (flyscan) was implemented at Beamline 2-ID-D at the Advanced Photon Source at Argonne National Laboratory, making data acquisition faster than 300 ms per pixel practical. Flyscan mode at Beamline 2-ID-D enables (a) traditional elemental maps to be completed twenty times more quickly while maintaining reasonably high sensitivity, and (b) practical studies of materials with an order of magnitude lower total impurity concentration and sparser spatial density of impurities. Opportunities for flyscan to enable qualitatively new forms of microscopy, leveraging the accelerated data-acquisition rate for mapping are highlighted.

### 6.1.1 $\mu$ -XRF at Beamline 2-ID-D: Step-by-Step and On-the-Fly Scanning Modes

Synchrotron-based micro-X-ray fluorescence spectroscopy ( $\mu$ -XRF) is a spatially resolved, non-destructive, and relatively sensitive and large-area spectroscopy technique that can be used to map elemental distributions in materials. This technique has been used to characterize and develop improved impurity-gettering processes for multiple detrimental metal species in several different PV-Si materials [31, 45, 109]. Given a specified time spent collecting fluorescence in a given pixel (dwell time), the local

concentration of an element must be high enough to be detected, and particles must be at a high enough spatial density so a particle can be detected within a practical scan area. For this work, a typical high-resolution  $\mu$ -XRF scan is defined as having a 1000 ms dwell time, a 220 nm step size, and taking 8 hours to complete.

During  $\mu$ -XRF acquisition, a sample is mounted on an  $x$ - $y$  sample stage. One of two data-collection modes is used: step-by-step (stepscan) or on-the-fly (flyscan) [191]. Stepscan mode involves settling time at each pixel, which increases measurement overhead. During flyscan, the motors move continuously and time intervals define the bounds of each pixel. In stepscan mode at Argonne National Laboratory's Advanced Photon Source Beamline 2-ID-D, the typical overhead time is 300 ms per pixel. Flyscans avoid this overhead time, enabling practical use of dwell times shorter than 300 ms. This time saving translates into faster scanning of typical samples compared to a typical 1000 ms dwell time, 30% larger map sizes within the same scan time without sacrificing sensitivity, or orders of magnitude larger map sizes if sensitivity or step size requirements can be relaxed. This increase in efficiency is critical to faster cycles of learning and increased productivity of limited, expensive, complex user facility resources, where a typical user has access to the tool for only a few days a year.

An open question with this new flyscan capability is the tradeoff between dwell time and sensitivity. Scanning larger areas more quickly is beneficial, but it is essential to maintain adequate sensitivity to the element distribution of interest. In multicrystalline silicon, recombination-active metal impurities in parts per billion are found in point defect and precipitated forms [36, 37, 67, 93, 192], so both types of defect must be controlled during solar cell processing to maximize cell performance. In this benchmarking study, using five different dwell times, we measure the same region of a previously well-characterized  $n$ -type multicrystalline silicon sample containing trace amounts of iron, and we quantify the decrease in sensitivity as dwell time is reduced. Additionally, using results from a published simulation tool [32], we show that with flyscans, it is practical to measure silicon with lower total impurity concentrations and a lower density of impurity particles using  $\mu$ -XRF in flyscan mode.

### 6.1.2 Benchmarking Flyscan Mode

Multicrystalline *n*-type, 2  $\Omega$ -cm silicon wafers were obtained from an industrial directionally solidified Generation 5 ingot. A  $1 \times 1$  cm<sup>2</sup> sample containing a  $\Sigma 33$  grain boundary identified by electron backscatter diffraction was selected from the low-lifetime border region of a wafer from a corner brick. To reduce Ni, Cu, and Co to below their detection limits, leaving only Fe particles, the sample was saw damage etched and subjected to a phosphorus diffusion gettering at 820°C for 60 min followed by a slow in-furnace cool to 600°C before removal from the furnace.  $\mu$ -XRF was performed at the Advanced Photon Source beamline 2-ID-D [193]. A 209 nm spot size at full width at half maximum and an incident photon energy of 10 keV were used to map a  $16.5 \times 15$   $\mu\text{m}^2$  region with 220 nm step size. Five different effective dwell times were used: 50, 100, 250, 500, and 1000 ms. No other experimental parameters were changed when the dwell time was changed. The maps were measured sequentially within a single eight-hour period. The effective information depth in this experimental setup for outgoing Fe  $K\alpha$  fluorescence was 8.8  $\mu\text{m}$ . All data were quantified using NIST 1832 and 1833 standards. From measurements of the standards, the theoretical minimum detection limit (MDL) for iron in the experimental setup, which is the smallest theoretically detectable elemental content, was calculated for each dwell time. The MDL is proportional to (dwell time)<sup>-1/2</sup>. A second measure of the noise limit, the statistical detection limit (SDL), is defined as  $\mu + 4\sigma$ , where  $\mu$  and  $\sigma$  are the mean and standard deviation, respectively, of a truncated Gaussian fit to the lowest 99% of measured pixel values. See reference [31] for more details.

Quantified synchrotron-based  $\mu$ -XRF maps of the Fe  $K\alpha$  fluorescence of the same sample region are shown (Fig. 6-1, top row) for dwell times of 50, 250, and 1000 ms. Pixels with high Fe  $K\alpha$  fluorescence loading are black. From the maps, it is evident that for the range of dwell times studied, as the dwell time increases, more particles are detected. Additionally, many of the particles detected at all three dwell times become more prominent as the dwell time increases.

The MDL and SDL were then applied to these three maps to separate the particles

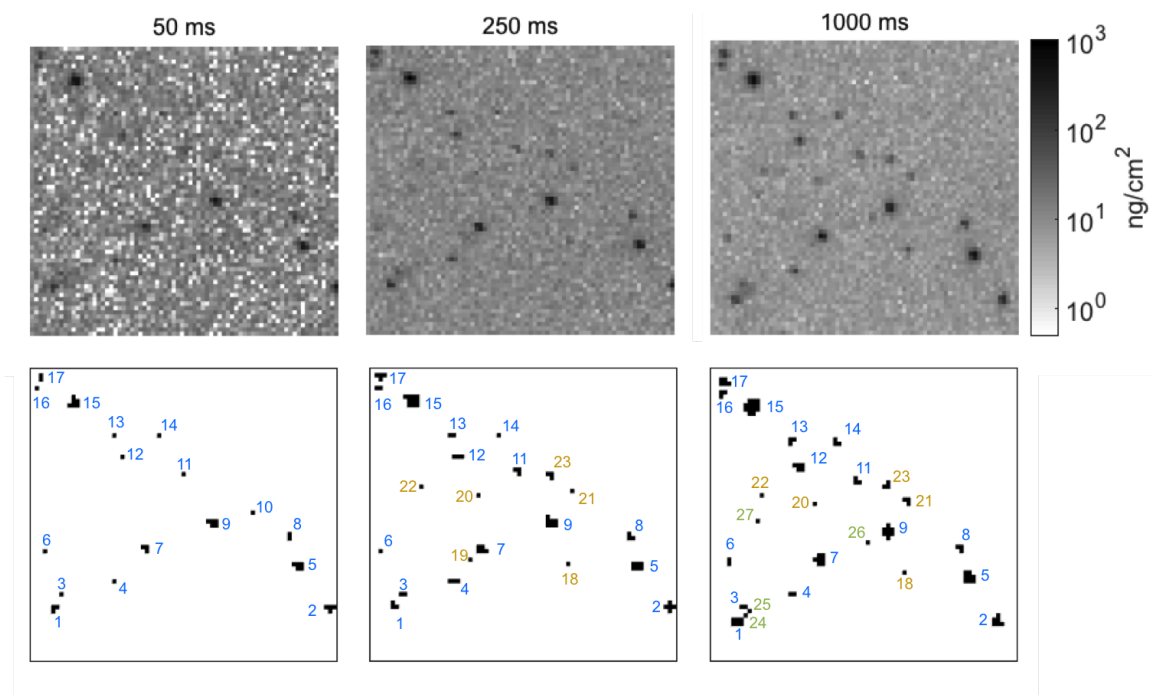


Figure 6-1: Flyscan mode  $\mu$ -XRF maps of Fe  $K_{\alpha}$  fluorescence for dwell times of 50, 250, and 1000 ms. Top row: maps of fitted, quantified area density of mass of Fe. Bottom row: binary maps highlight detected Fe particles at each dwell time that are above the minimum size limits determined by MDL and SDL. Particles are numbered, with different colors indicating detection at one (green), two (yellow), or all three (blue) dwell times. In all maps, black is high Fe loading, and white is low Fe loading.

from noise, and the maps were re-plotted with the detected particles in black and the noise in white (Fig. 6-1, bottom row). At 50 ms, 17 Fe-rich particles are identified. At 1000 ms dwell, 27 particles are identified, a 59% increase in the number of detected particles.

To quantify the sensitivity as a function of dwell time, the MDL, SDL, and sizes (in number of Fe atoms) of the detected Fe precipitates that are equal to or larger than the respective MDL were plotted for all five dwell times (Fig. 6-2). At longer dwell times, the two detection limits diverge, with the SDL decreasing at a slower rate as the dwell time increases. The MDL decreases from  $2.2 \times 10^5$  Fe atoms/particle at a dwell time of 50 ms to  $4.9 \times 10^4$  Fe atoms/particle at a dwell time of 1000 ms. The SDL decreases from  $2.3 \times 10^5$  Fe atoms/particle at a dwell time of 50 ms to  $8.6 \times 10^4$  Fe atoms/particle at a dwell time of 1000 ms. Particles detected with a 1000 ms dwell

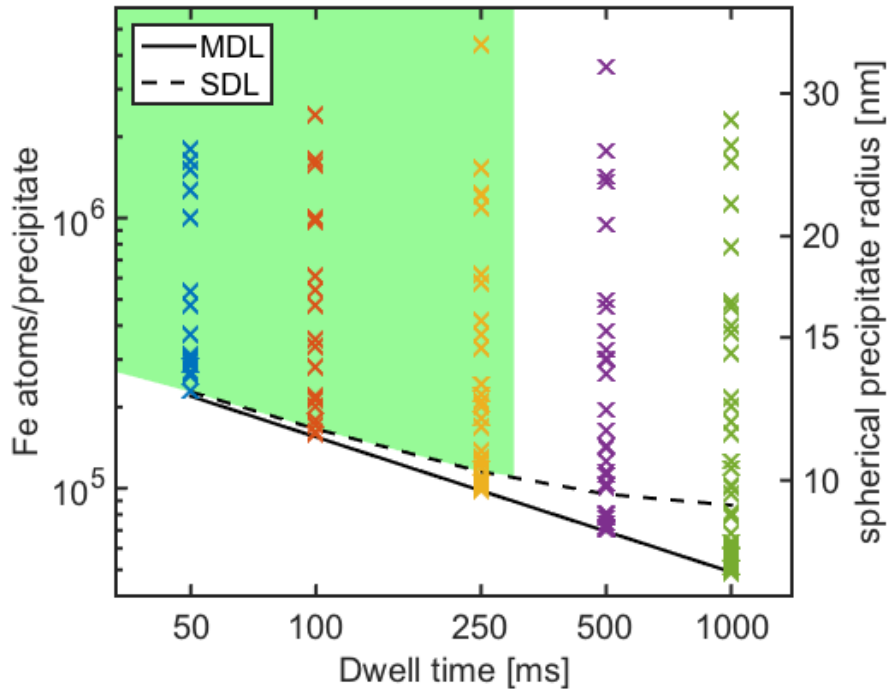


Figure 6-2: The sizes of the detected precipitates compared to the MDL and the SDL at each dwell time. The green region highlights parameter space made practical by flyscans. Each x is one measured Fe particle.

time,  $20\times$  longer than 50 ms dwell time, resulted in a decrease in the SDL of 63%.

The particles above both detection limits range between  $2\times 10^5$  and  $2\times 10^6$  Fe atoms/ precipitate for the 50 ms dwell time and range between  $9\times 10^4$  and  $2.5\times 10^6$  Fe atoms/ precipitate for the 1000 ms dwell time. In this experimental configuration, the 1000 ms dwell enables detection of small particles with radius between 9 and 12 nm, which the 50 ms dwell is not sensitive enough to detect.

Finally, to illustrate the new parameter space that the flyscan can access, simulated the as-grown precipitated iron distribution for typical mc-Si with a total iron concentration of  $5\times 10^{13} \text{ cm}^{-3}$  and  $10^{13} \text{ cm}^{-3}$  was simulated. See [32] for further details about simulation parameters and methods. Fig. 6-3 shows the simulated precipitate sizes as a function of the spatial distribution of precipitates at grain boundaries and within grains. The gray area is the parameter space that was possible to scan using flyscans with 1000 ms dwell with 220 nm step size for an 8-hour scan. Highlighted in green is a region of much sparser spacing of precipitates that 50 ms dwell flyscans



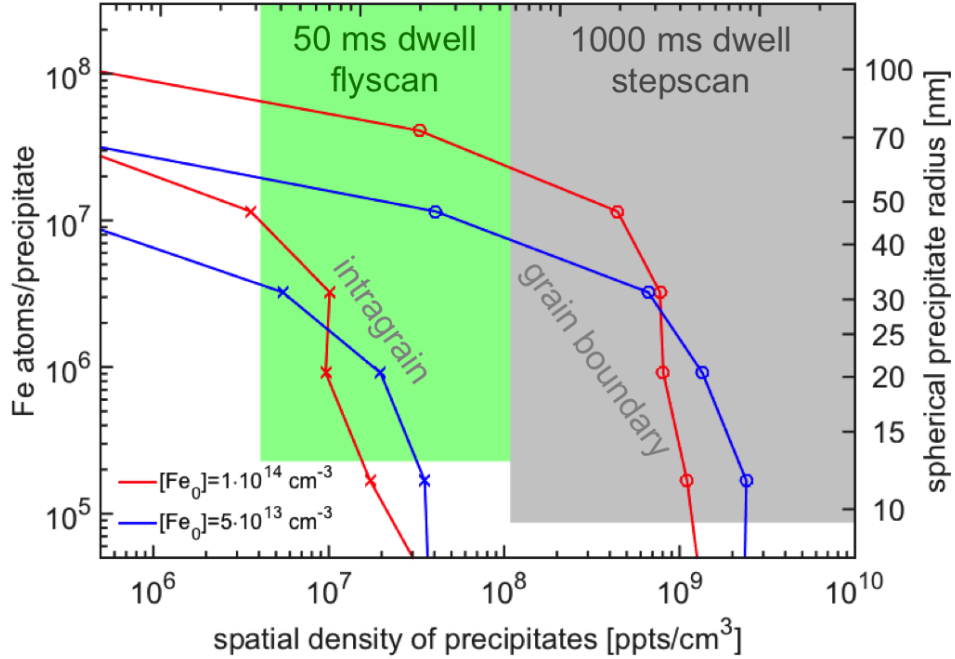


Figure 6-3: New parameter space made practical with 50 ms flyscans. Simulated precipitate size vs. precipitate spatial density at grain boundaries (o's) and within grains (x's) for as-grown impurity concentrations of  $10^{14} \text{ cm}^{-3}$  (red) and  $5 \times 10^{13} \text{ cm}^{-3}$  (blue).

also with 220 nm step size for an 8-hour scan enable. Physically, this spacing of precipitates is typical of intragranular regions of multicrystalline silicon. To detect these precipitates that are more spread out, a larger region must be scanned. Compared to a 1000 ms dwell and with minor penalty on the sensitivity, 50 ms flyscans enable this larger-area scanning in the same amount of time.

These simulations show what has been born out by experience that past observations with typical 1000 ms step scans were limited to highly-decorated grain boundaries and small clusters of intragranular dislocations. With 50 ms flyscans, while still maintaining reasonable sensitivity limits, it is now practical to map at sub-micron resolution over half a million pixels in eight hours. At a step size of 220 nm, the area that could be mapped can encompass hundreds of intragranular structural defects, which are highly detrimental to solar cell performance [194].

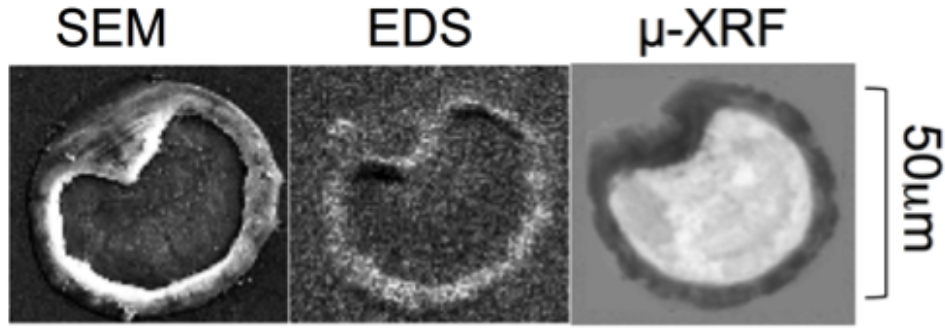


Figure 6-4: Large-area correlative microscopy enabled by flyscan: titanium concentration assessment at a laser-fired contact. Sample courtesy of U. Delaware and IPG Laser.

### 6.1.3 Impact and Applications of Flyscan Mode

Our results indicate that for the  $\mu$ -XRF experimental conditions used at APS beamline 2-ID-D, if particles are larger than  $2 \times 10^5$  Fe atoms, 50 ms dwell time flyscans can improve productivity by 20-fold. Either 20 times the area could be measured in a given amount of time, or one twentieth of the time would be required to map a given area. However, longer dwell times are essential for detecting smaller particles.

For precipitated impurities in mc-Si for PV, in typical material, the peak of the as-grown precipitate size distribution is around  $10^4$  Fe atoms/precipitate, and after a typical phosphorus diffusion, it is around  $5 \times 10^5$  Fe atoms/precipitate [84]. To detect particles smaller than  $10^5$  atoms per precipitate, dwell times of 250 ms and higher are required while for  $5 \times 10^5$  Fe atoms/precipitate, a 50 ms dwell time may be adequate.

Lastly, the faster data acquisition rate of flyscan has the potential to enable truly multi-dimensional scanning, enabling qualitatively new forms of microscopy. Examples include temperature-dependent measurements with a novel in-situ sample stage [195], or large-area maps to enable correlative microscopy. One example appears in Fig. 6-4, where the elemental distribution of titanium in a 50  $\mu$ m-diameter laser-fired contact is assessed by flyscan  $\mu$ -XRF in just 90 minutes; these data are correlated with scanning electron microscopy. The flyscan mode was leveraged for the direct measurement of the recombination activity associated with Fe-rich precipitates in *n*-type crystalline silicon.

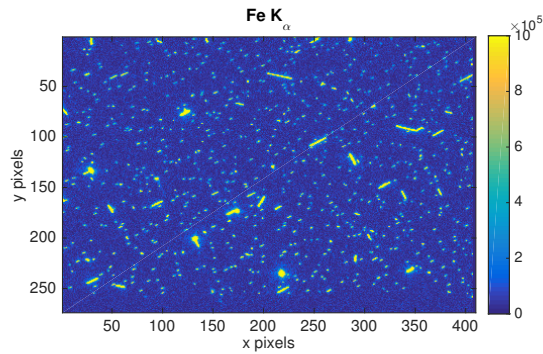
## 6.2 Analysis of $\mu$ -XRF and $\mu$ -PL maps of Fe-rich particles in $n$ -type crystalline silicon

Figure 6-5 shows the full, quantified  $\mu$ -XRF and  $\mu$ -PL maps. The dimensions of the maps are as follows:  $\mu$ -XRF is  $60\ \mu\text{m} \times 90\ \mu\text{m}$  and  $\mu$ -PL is  $150\ \mu\text{m} \times 240\ \mu\text{m}$ . The pixel size in the  $\mu$ -XRF is 220 nm, and in the  $\mu$ -PL it is 500 nm.

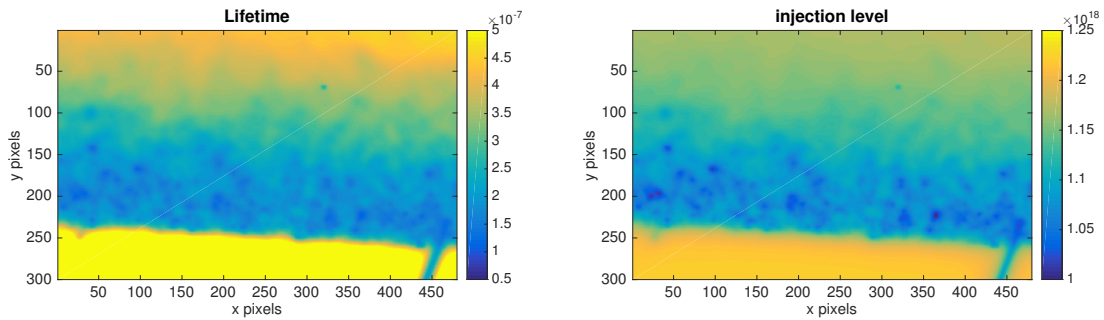
The maps were then put transformed to the same resolution, cropped, and masked to enable a particle-by-particle analysis of the recombination strength. First, they were each cropped so that they contained only the regions where both  $\mu$ -XRF and  $\mu$ -PL were measured (Fig. 6-6). Next, the higher-resolution  $\mu$ -XRF was decreased to the resolution of the  $\mu$ -PL using MATLAB's *imresize* function, and the inverse of the lifetime map was taken to view the recombination strength, a quantity proportional to the recombination rate rather than the lifetime (Fig. 6-7). To enable pixel-by-pixel comparison, this pair of maps was then registered using MATLAB's *imregister* function using a similarity transformation. Then, the maps were further cropped on the right and the bottom to remove regions that were not measured by  $\mu$ -XRF and that were below the border between the top and bottom bonded wafers, respectively. The noise was removed from the  $\mu$ -XRF map, where noise is defined as pixels containing less than the mean of the noise plus four standard deviations above the noise. Additionally, because the recombination strength is much more blurred than the Fe elemental map, each particle was required to be comprised of at least 4 pixels (Fig. 6-8). Fe particles were then identified and numbered in white text to the bottom right of each identified particle (Fig. 6-9). The final map size is  $47.5\ \mu\text{m} \times 62.5\ \mu\text{m}$ .

## 6.3 Modeling the Recombination Strength of Fe-rich Particles in $n$ -type Crystalline Silicon

For each of the 83 identified particles, a circle was drawn around the particle with the diameter determined by the largest dimension of the particle that is visible in



(a)  $\mu$ -XRF Fe channel map. Yellow pixels have high Fe loading measured in  $\text{ng}/\text{cm}^2$ .



(b)  $\mu$ -PL-based minority carrier lifetime. Yellow pixels are high lifetime (sec).

(c)  $\mu$ -PL-based injection level. Yellow pixels are high injection level in  $\text{carriers}/\text{cm}^3$ .

Figure 6-5: Full measured  $\mu$ -XRF ( $60 \mu\text{m} \times 90 \mu\text{m}$ ) and  $\mu$ -PL ( $150 \mu\text{m} \times 240 \mu\text{m}$ ) maps of an intentionally Fe-contaminated wafer-bonded dislocation network  $n$ -type crystalline silicon wafer sample.

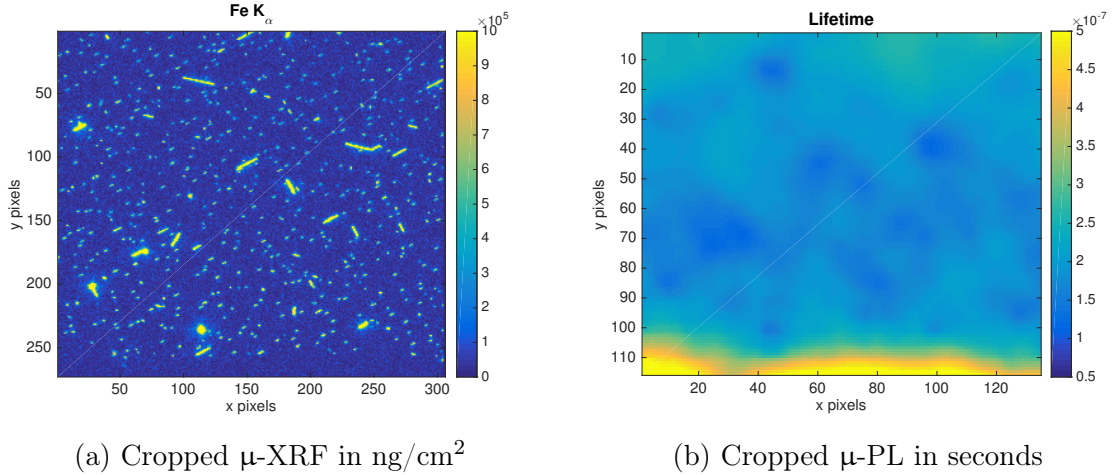
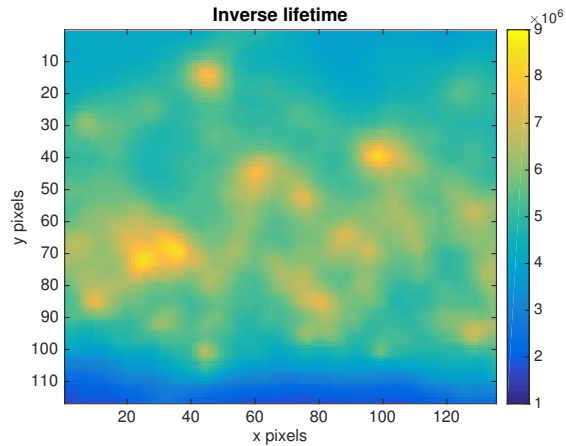


Figure 6-6:  $\mu$ -XRF and  $\mu$ -PL maps of an intentionally Fe-contaminated wafer-bonded dislocation network *n*-type crystalline silicon wafer sample. Maps cropped to region where both measurements were taken. There is a noticeable correlation between locations of high iron content and low lifetime.

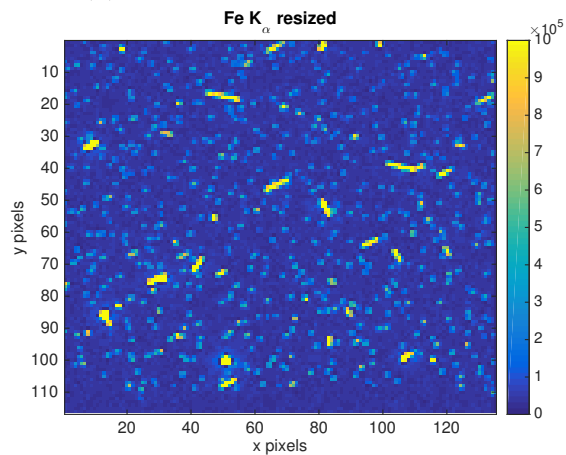
the 2D map. The diameter was defined as the larger dimension of a bounding box enclosing the particle. A circle was chosen because the lifetime maps show that the recombination active area seems to be circular in shape, even for the long particles as mentioned in [68, 196]. These circles were then used to mask both the Fe and the lifetime maps (Fig. 6-10). Any pixels outside of the circles were excluded from the analysis.

The Fe loading in the connected Fe-containing pixels that form each particle were summed, defining the total Fe content of each particle. The inverse lifetime was summed in each circle to define the total recombination activity of that given particle. For each particle, the recombination strength was plotted as a function of the iron content (Fig. 6-11). This type of plot was generated for copper in [197] and for both copper and iron in [40]. It should be noted that the plot contained herein is the first to have quantified lifetime values and quantified metal contents, and more particles were analyzed than in previous studies.

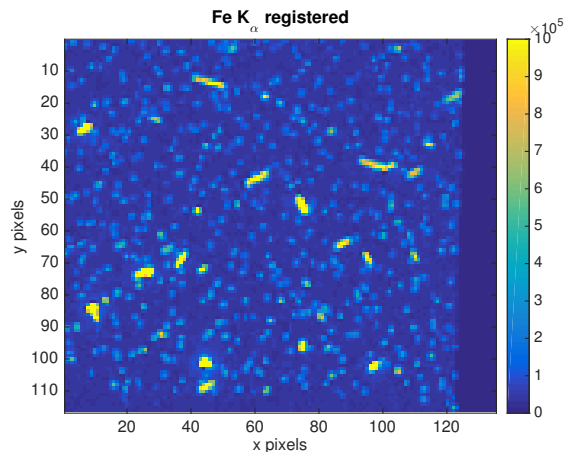
All of the data were then fit with a power function with a power of 0.73. The resulting  $R^2$  of the fit was 0.73. Assuming that only the surface of the precipitates ( $\text{FeSi}_2/\text{Si}$  interface) is recombination active, the surface area of different geometries can be expressed as a function of the number of Fe particles in the precipitate. For a



(a) Inverse of  $\mu$ -PL lifetime in  $s^{-1}$

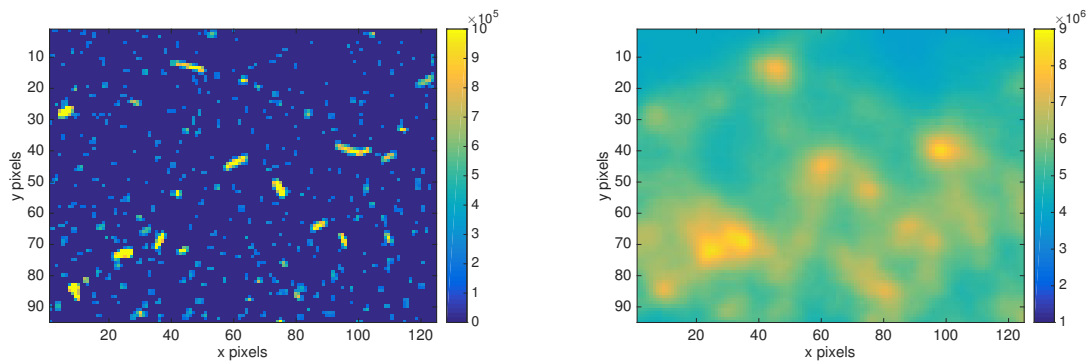


(b)  $\mu$ -XRF map resized to resolution of  $\mu$ -PL map



(c)  $\mu$ -XRF resized and registered to  $\mu$ -PL map

Figure 6-7:  $\mu$ -XRF and  $\mu$ -PL maps of an intentionally Fe-contaminated wafer-bonded dislocation network  $n$ -type crystalline silicon wafer sample.  $\mu$ -XRF map resized and registered to  $\mu$ -PL map. The registration required a translation and slight rotation. There is a noticeable correlation between locations of high iron content and high inverse lifetime, or recombination strength.



(a) Final size  $\mu$ -XRF map in  $\text{ng}/\text{cm}^2$

(b) Final size  $\mu$ -PL map in  $\text{s}^{-1}$

Figure 6-8:  $\mu$ -XRF and  $\mu$ -PL maps of an intentionally Fe-contaminated wafer-bonded dislocation network *n*-type crystalline silicon wafer sample.  $\mu$ -XRF and  $\mu$ -PL maps further cropped to exclude bottom and right side regions that did not contain Fe particles but were used to register the images. Maps are  $47.5 \mu\text{m} \times 62.5 \mu\text{m}$ .

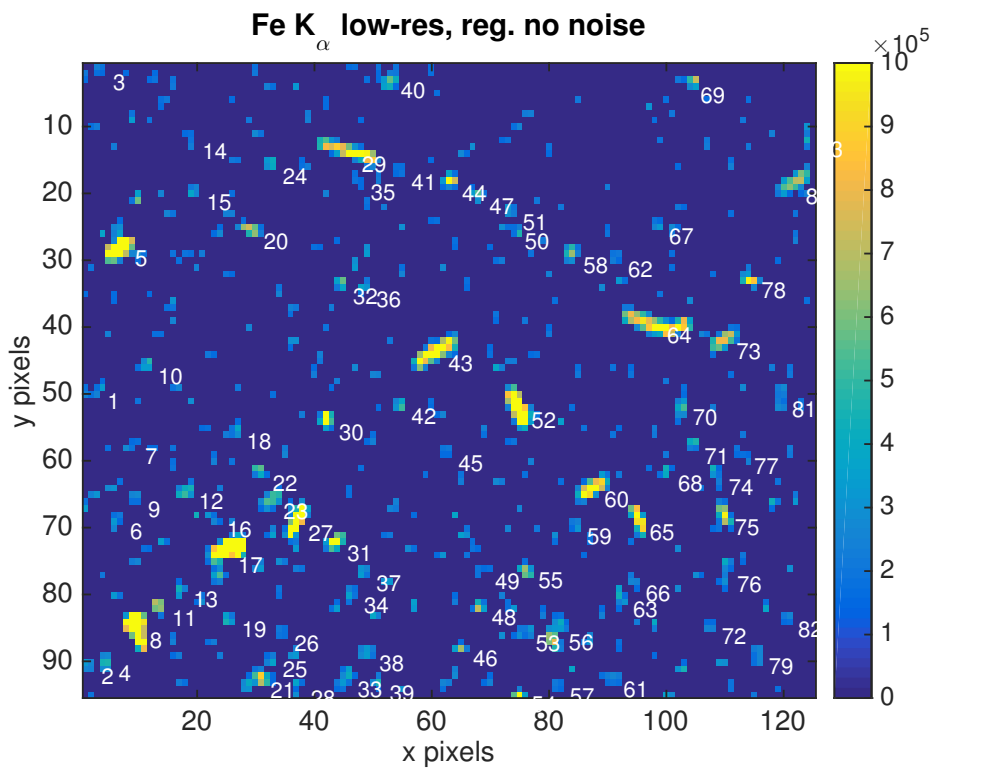
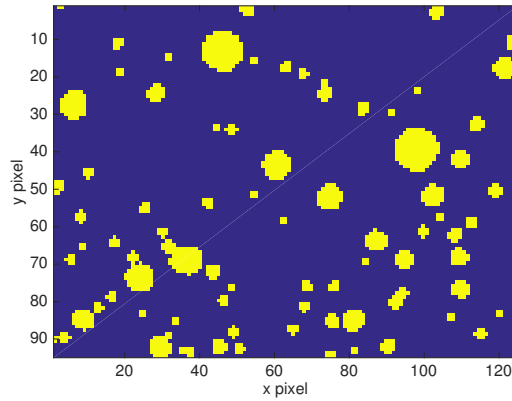
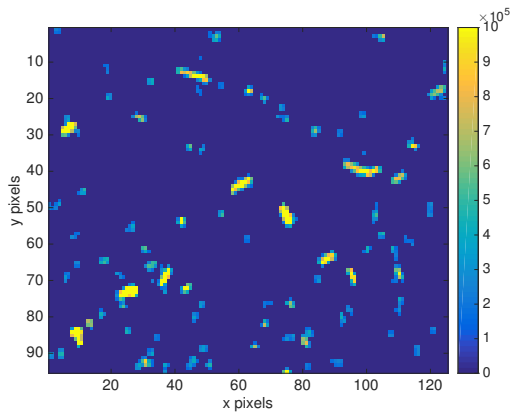


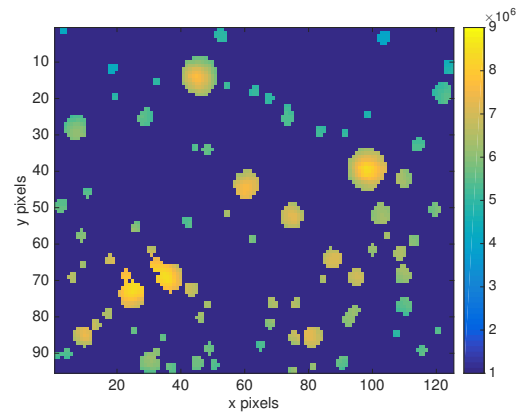
Figure 6-9:  $\mu$ -XRF with individual precipitates identified and numbered.



(a) Mask of circles with diameter defined by largest dimension of Fe particles.



(b)  $\mu$ -XRF ( $\text{ng}/\text{cm}^2$ ) masked



(c)  $\mu$ -PL ( $\text{s}^{-1}$ ) masked

Figure 6-10:  $\mu$ -XRF and  $\mu$ -PL of an intentionally Fe-contaminated wafer-bonded crystalline silicon wafer sample. Masked maps with circles defined by largest dimension of the box bounding Fe particles in  $\mu$ -XRF maps.



sphere, surface area depends on the number of Fe atoms to the power of 0.67. For a rod the power is 1, and for a platelet it is 0.5. Detailed calculations of these powers are shown in Table 6.1.  $S$  is the surface area,  $r$  is the precipitate radius,  $l$  is the platelet or rod length,  $n$  is the number of Fe atoms in the precipitate,  $V_{Fe}$  is the volume of one iron atom in a  $-FeSi_2$  precipitate, and  $V$  is the volume of the precipitate. Consistent with the shapes of the clusters that are observed in the  $\mu$ -XRF maps, the power of 0.73 dependence is between that of a sphere and a platelet.

Table 6.1: surface area of different shape precipitates as a function of the number of Fe atoms in the precipitate

sphere	platelet	rod
$S = 4\pi r^2$	$S = 2\pi r l$	$S = 2\pi r l$
$r = \text{constant}$	$l = \text{constant}$	$r = \text{constant}$
need $r(n)$	need $r(n)$	need $l(n)$
$V = \frac{4}{3}\pi r^3 = nV_{Fe}$	$V = \pi r^2 l = nV_{Fe}$	$V = \pi r^2 l = nV_{Fe}$
$r \sim n^{1/3}$	$r \sim n^{1/2}$	$l \sim n^1$
$S \sim n^{1/3}$	$S \sim n^{1/2}$	$S \sim n^1$

Other factors that affect the recombination activity of individual precipitates include proximity to large, highly recombination-active particles, recombination due to a background of other recombination-active centers, presumably including point defects, other impurities, and possibly lattice strain due to such a high concentration of Fe introduced. From the  $\mu$ -XRF maps (not shown), we also identify Cu contamination co-located with the intentionally introduced Fe at a level of 10% by mass.

It should be noted that the level of Fe contamination in the sample analyze herein is much higher than a typical wafer for PV, so care must be taken when extrapolating to lower contamination levels. Additionally, the  $\mu$ -PL was measured at an injection level of  $\sim 10^{18} \text{ cm}^{-3}$ , which is approximately four orders of magnitude higher than typical operating injection level in crystalline silicon solar cells. These measurements clearly demonstrate that Fe-rich particles can be strongly recombination-active in

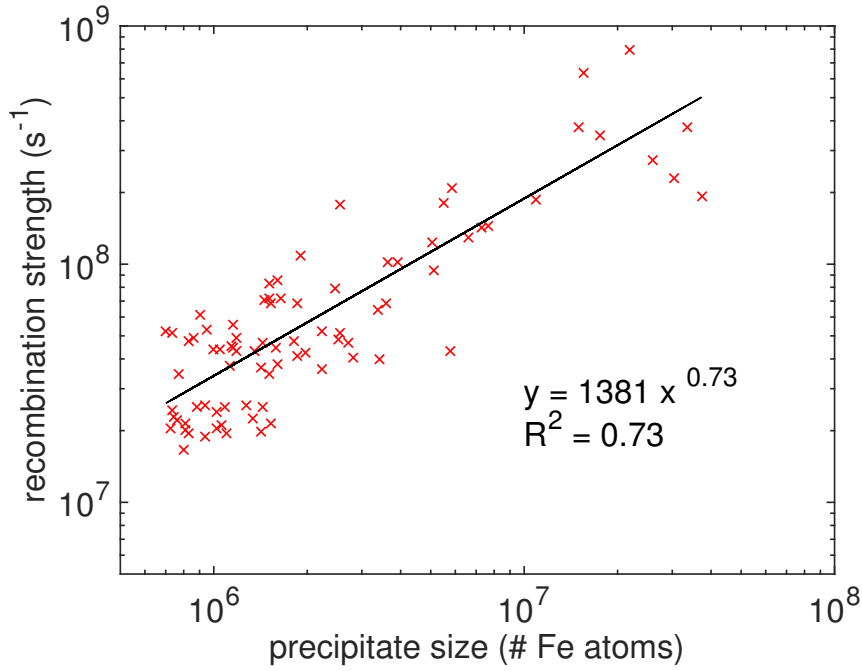


Figure 6-11: Recombination strength (1/s) vs. Fe content (Fe atoms/ precipitate) with a power function fit.

*n*-type crystalline silicon, consistent with predictions from lifetime modeling [68]. This observation is also consistent with the hypothesis that metal contamination, especially in the form of precipitates, may limit the lifetime of *n*-type mc-Si before and after solar cell processing. Thus, high-temperature processing that dissolves Fe-rich particles may be an essential component of maximizing the lifetime of *n*-type mc-Si for PV.

This is the first fully quantified, high-resolution, direct measurement of the recombination activity of Fe precipitates in *n*-type crystalline silicon. Additionally, many more precipitates were analyzed compared to previous studies, increasing confidence in the results.

# Chapter 7

## A Comparative Predictive Simulation Tool for *n*-type and *p*-type Crystalline Silicon for Photovoltaics

### 7.1 Tool Description

To increase the speed of learning and to understand how the Fe-related injection-dependent electrical quality of *n*-type and *p*-type mc-Si differ, a comparative simulation and lifetime calculator was developed. The tool has two different coupled components: (1) a simulation of the location and redistribution of metals in response to temperature and the presence or absence of phosphorus, (2) a calculation of the electrical impact of the metal distribution captured by the injection-dependent lifetime due to metal point defects and precipitated metals, and (3) lifetime- and injection level-dependent solar cell efficiency. Currently, the tool accounts only for iron explicitly in point defect form and in precipitates.

Supported by the experimental results of the *n*-type mc-Si  $\mu$ -XRF study, we assume that the redistribution of metals in *n*-type and *p*-type mc-Si for PV at high temperatures, for example, during phosphorus diffusion gettering is the same for modeling purposes. we use the simulation tool developed earlier to describe this

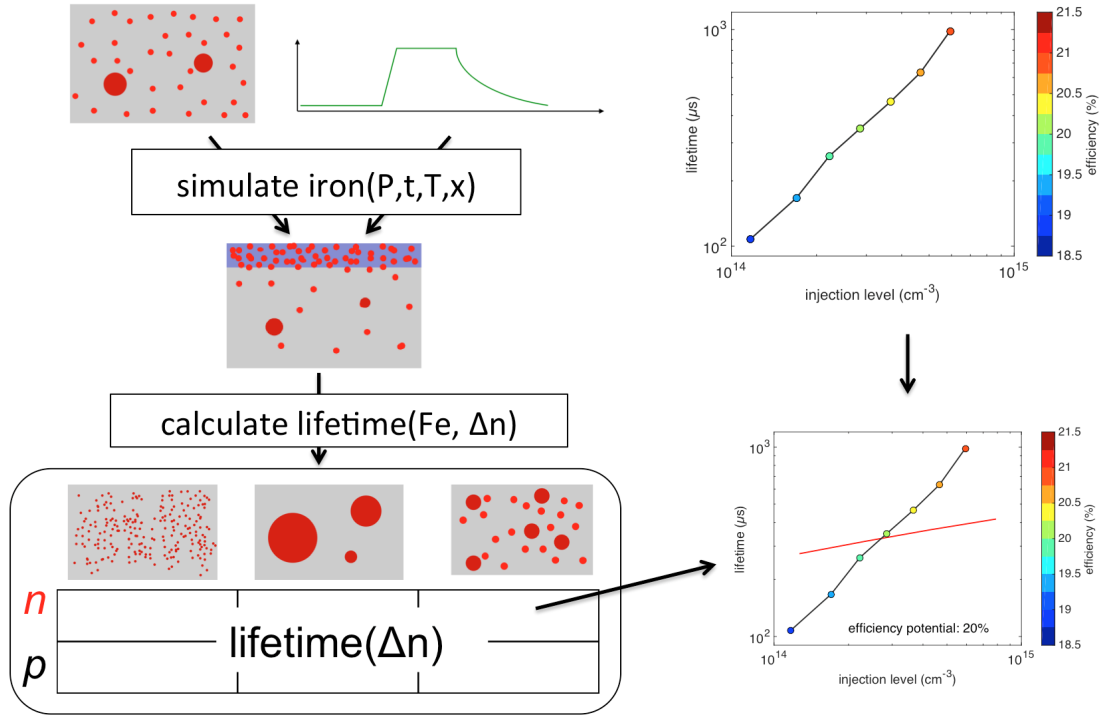


Figure 7-1: Comparative predictive simulation tool for  $n$ -type and  $p$ -type crystalline silicon. The inputs are the phosphorus time-temperature profile, the as-grown total iron concentration, and a model for the injection level- and lifetime-dependent solar cell efficiency. The tool calculates the redistribution of iron, the injection level-dependent minority carrier lifetime associated with point defects, precipitates, and the total iron distribution for  $n$ - and  $p$ -type Si, and the solar cell efficiency potential of the gettered wafer.

metal redistribution. Specifically, we used the one-dimensional Fokker-Planck Equation model from [32] because it is a relatively simple model that is relatively fast computationally and still simulates a distribution of precipitate sizes.

The Shockley-Read-Hall lifetime formulation with accepted capture cross-section and energy level values is used for iron point defects. The model of Kwapil *et al.* [68] is used for calculating the effect of precipitated iron. A parameterized version of Kwapil's model was made publicly available in Microsoft Excel, and it was coded in MATLAB for this work by Erin Looney, a member of the MIT PVLab.

Figure 7-1 is a flowchart that describes the essential pieces of the model. The tool can be used either coupled or de-coupled, depending on the desired analysis.

variable	range
Total initial Fe	$10^{12} - 10^{15} \text{ cm}^{-3}$
Fraction Fe point defects	1–99%
Precipitate size	5 or 20 nm
Total # of scenarios	40

Figure 7-2: Tested Fe distributions for building intuition of lifetime impact of Fe in *p*-type and *n*-type mc-Si.

## 7.2 Quantifying the Electrical Impact of Iron Point Defects and Precipitates in *n*-type and *p*-type mc-Si

To reveal the patterns of lifetime for different Fe distributions that are found in mc-Si, a wide range of Fe distributions was defined, and the point defect-related, precipitate-related, and total Fe-related injection-dependent minority carrier diffusion lengths were calculated using the combined lifetime calculator. The Fe distributions that were tested are summarized in Fig. 7-2.

The injection-dependent lifetime and diffusion lengths for *p*-type and *n*-type mc-Si for each of the simulated distributions are shown in Fig. 7-3 – 7-6. The total iron scales the magnitudes of the diffusion lengths, but the trends and shape of the diffusion length curves are maintained over this range of iron concentrations. All of the diffusion lengths increase as the injection level increases. For a given injection level, the smaller 5 nm precipitate size results in lower diffusion lengths than the larger 20 nm precipitate size because there is more surface area exposed when a given amount of Fe is spread among a larger quantity of smaller precipitates. For these parameters, the injection level at which the precipitate-related diffusion lengths are equal in the two materials is lower than the injection level at which the point defect-related diffusion lengths are equal, so as the point defect concentration increases, the injection level at which the *p*-type Si achieves the same diffusion length at the *n*-type Si increases. Another consistent pattern is that the shortest diffusion lengths

for the  $n$ -type Si are for the smaller fraction of point defects while the  $p$ -type Si has the shortest diffusion length when the fraction of point defects is largest. This is a result of the large asymmetry in the capture cross sections of Fe for electrons and holes in silicon. As the fraction of point defects increases, the diffusion lengths are limited by precipitates initially and then eventually by point defects. For  $p$ -type, the point defects start to dominate at approximately 10% point defect concentration. For  $n$ -type, the point defects dominate somewhere between 50% and 90% point defect concentration for the small precipitate case and somewhere between 10% and 50% point defect concentration for the larger precipitate case. Overall, at low injection,  $n$ -type outperforms the  $p$ -type, but at high injection,  $p$ -type Si has higher calculated diffusion lengths because both the precipitate and point defect diffusion lengths are longer for  $p$ -type than for  $n$ -type at high injection.

### 7.2.1 Comparing Injection-Dependent and Injection-Independent Lifetime Models

The injection-dependent diffusion lengths due to precipitates were also compared for reference to the injection-independent and doping-type-independent diffusion length described by [59, 198]. The value of the injection-independent model is marked with the open triangles on Figs. 7-3 – 7-6 at the injection level where the two models are equal. The injection-independent model matches well at low injection levels. For the 5 nm precipitate size, the models match at an injection level of  $10^{12}$   $\text{cm}^{-3}$  while for the 20 nm precipitate size, the models match at an injection level of  $\sim 2 \times 10^{13}$   $\text{cm}^{-3}$ . The injection- and doping-type- independent model overestimates the diffusion lengths at lower injection and underestimates them at higher injection. Typical crystalline silicon solar cells operating at maximum power point under standard test conditions in the mid- $10^{13}$   $\text{cm}^{-3}$  injection level, so in many cases, the simple model may be appropriate to use.

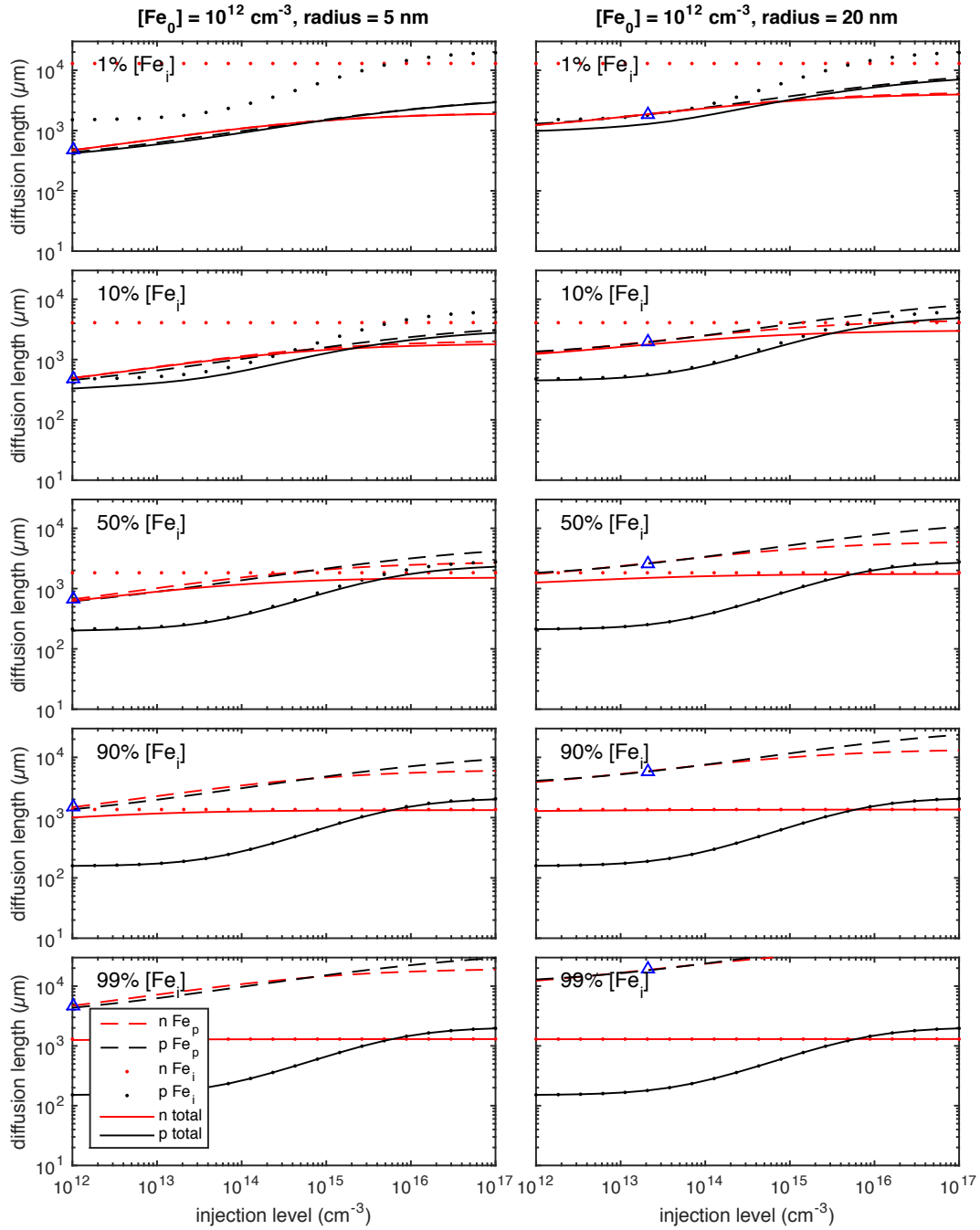


Figure 7-3: Minority carrier diffusion lengths due to Fe point defects (dotted lines), Fe precipitates (dashed lines), and the total Fe distribution (solid lines) in *p*-type (black) and *n*-type (red) mc-Si. The blue open triangle is the injection- and doping-independent lifetime model. Total initial Fe concentration of  $10^{12} \text{ cm}^{-3}$ .

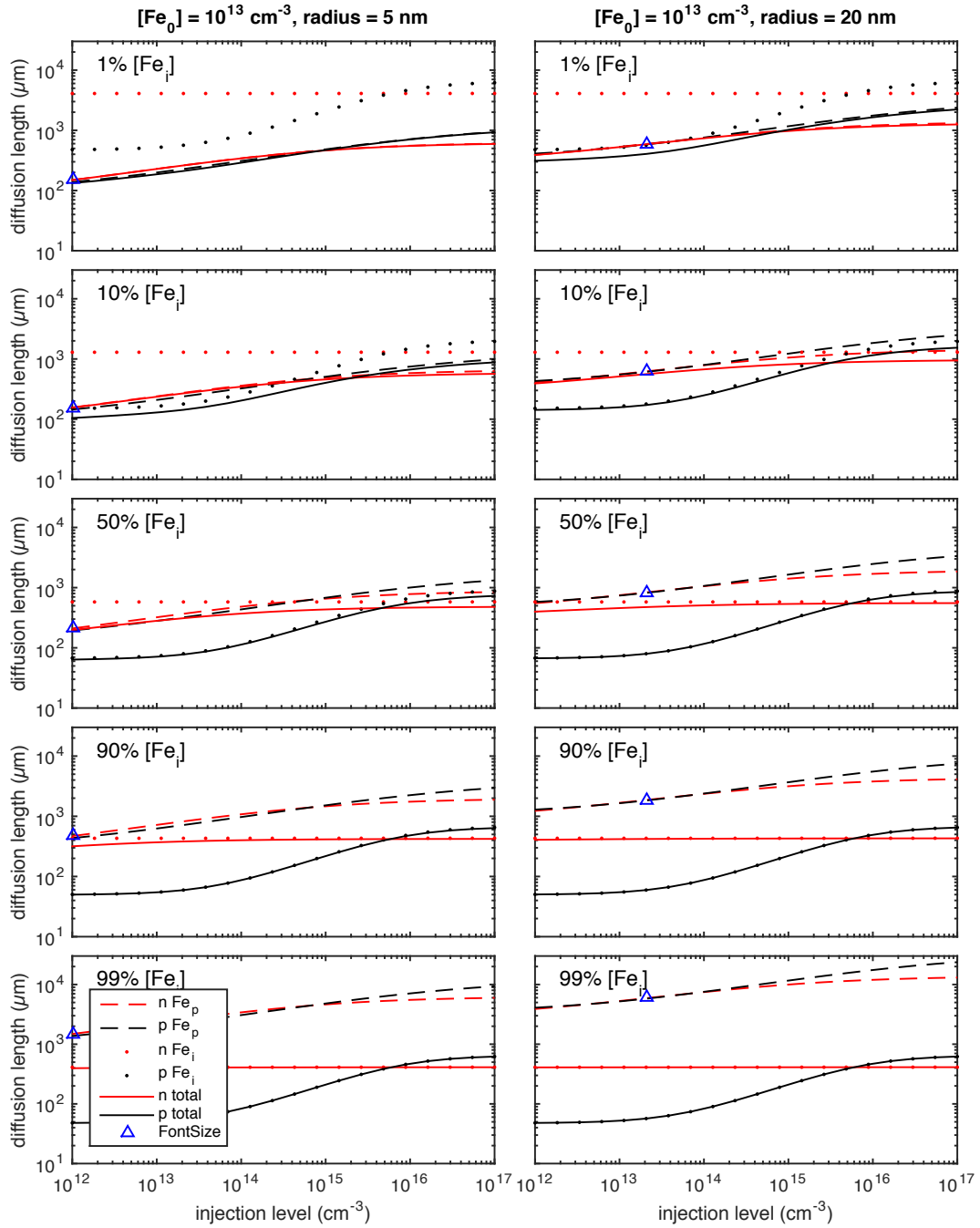


Figure 7-4: Minority carrier diffusion lengths due to Fe point defects (dotted lines), Fe precipitates (dashed lines), and the total Fe distribution (solid lines) in *p*-type (black) and *n*-type (red) mc-Si. The blue open triangle is the injection- and doping-independent lifetime model. Total initial Fe concentration of  $10^{13} \text{ cm}^{-3}$ .



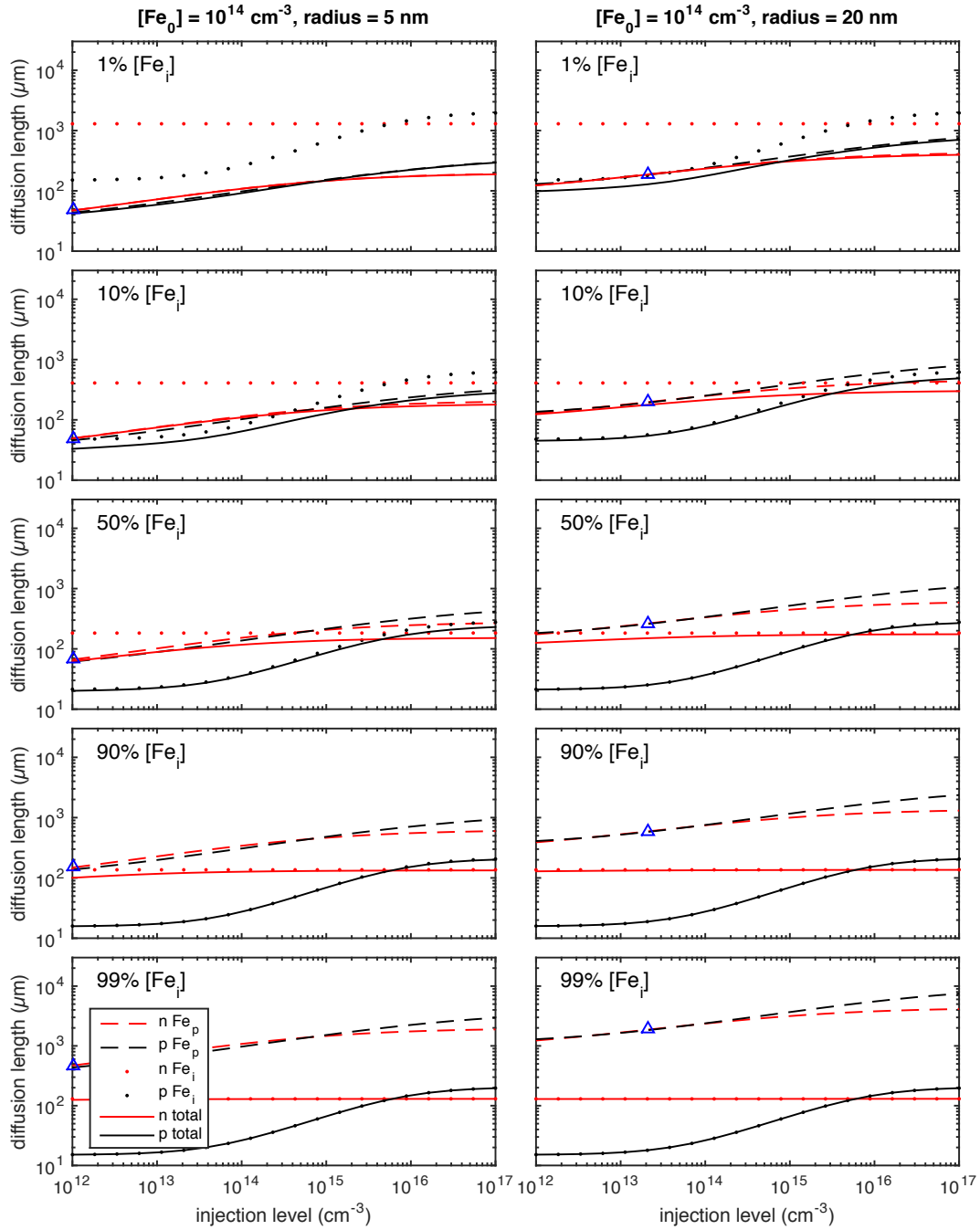


Figure 7-5: Minority carrier diffusion lengths due to Fe point defects (dotted lines), Fe precipitates (dashed lines), and the total Fe distribution (solid lines) in *p*-type (black) and *n*-type (red) mc-Si. The blue open triangle is the injection- and doping-independent lifetime model. Total initial Fe concentration of  $10^{14} \text{ cm}^{-3}$ .

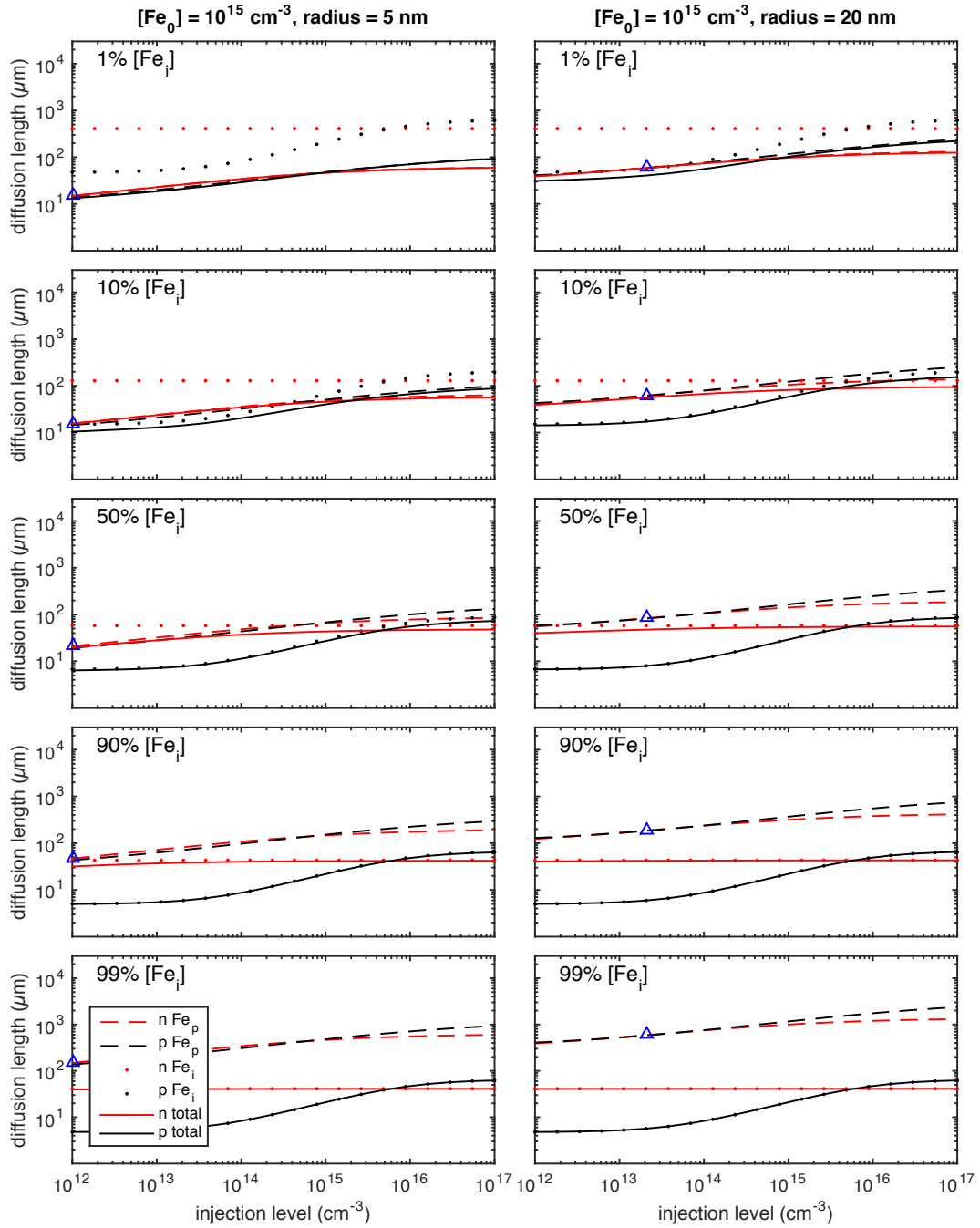


Figure 7-6: Minority carrier diffusion lengths due to Fe point defects (dotted lines), Fe precipitates (dashed lines), and the total Fe distribution (solid lines) in *p*-type (black) and *n*-type (red) mc-Si. The blue open triangle is the injection- and doping-independent lifetime model. Total initial Fe concentration of  $10^{15} \text{ cm}^{-3}$ .

## 7.2.2 Quantifying the Relative Impact of Iron Point Defects and Precipitates in *n*- and *p*-type mc-Si

The relative effect of precipitates and point defects as a function of injection level was quantified in two different ways (Fig. 7-7 and 7-8). The percent difference in injection level calculated as the precipitated diffusion length minus the point defect diffusion length divided by the point defect diffusion length was plotted in Fig. 7-7. The blue horizontal line delineates equal contributions from precipitates and point defects. Below the blue line, the effective diffusion length is limited by precipitated Fe. Above the blue line, point defects limit the diffusion length. Secondly, the percent of the diffusion length attributable to precipitates was calculated as the difference between the point defect-related and precipitate related diffusion lengths normalized by the point-defect related diffusion length in Fig. 7-8. Note that for all four total iron concentrations, these relative diffusion length plots are the same. These plots clearly demonstrate that for a wide range of injection levels and iron distributions, *n*-type mc-Si is more heavily precipitate-limited than *p*-type mc-Si. As lower injection levels, this difference is more pronounced than at higher injection levels

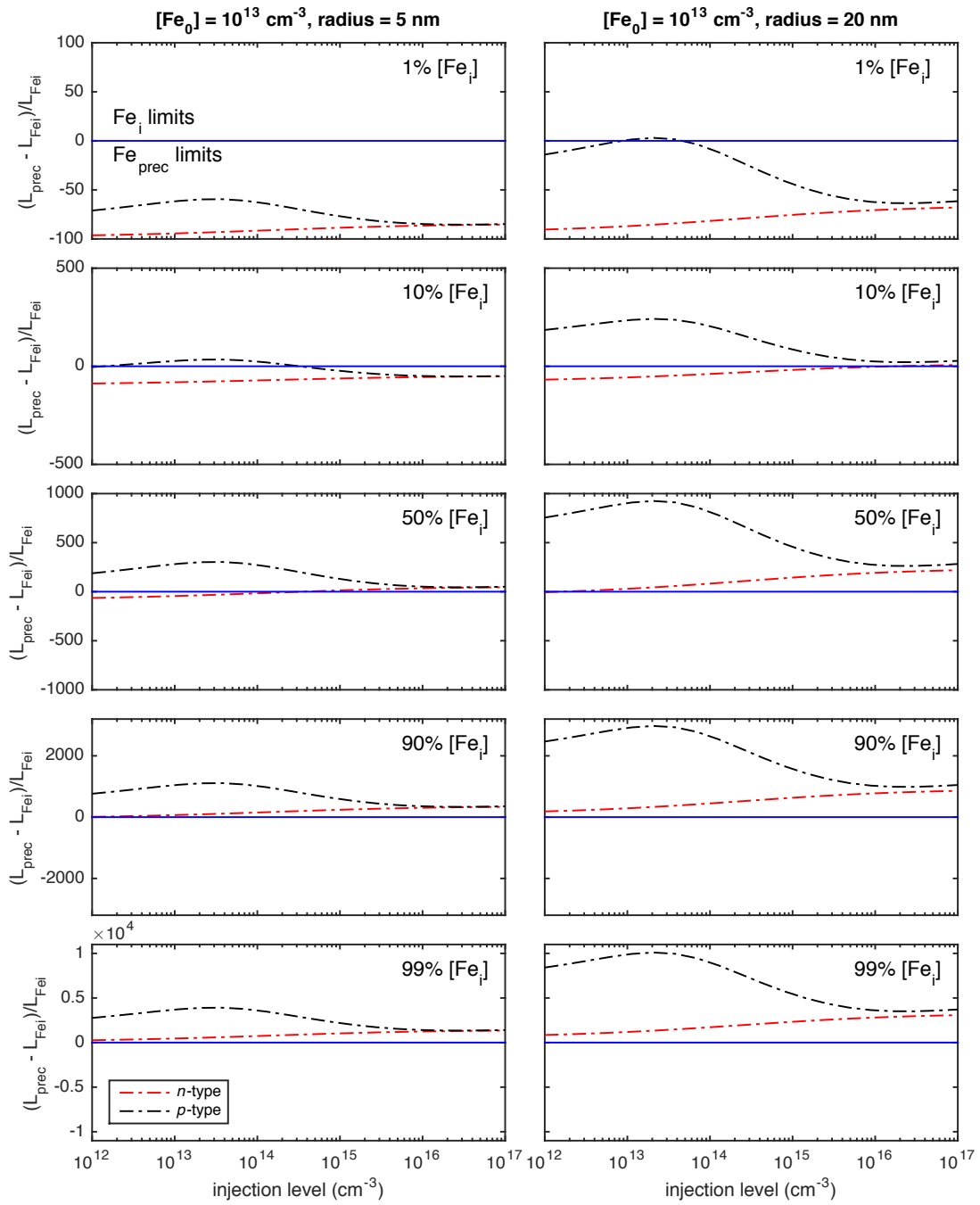


Figure 7-7: Percent difference in diffusion lengths due to point defects and precipitates in *p*-type and *n*-type mc-Si.

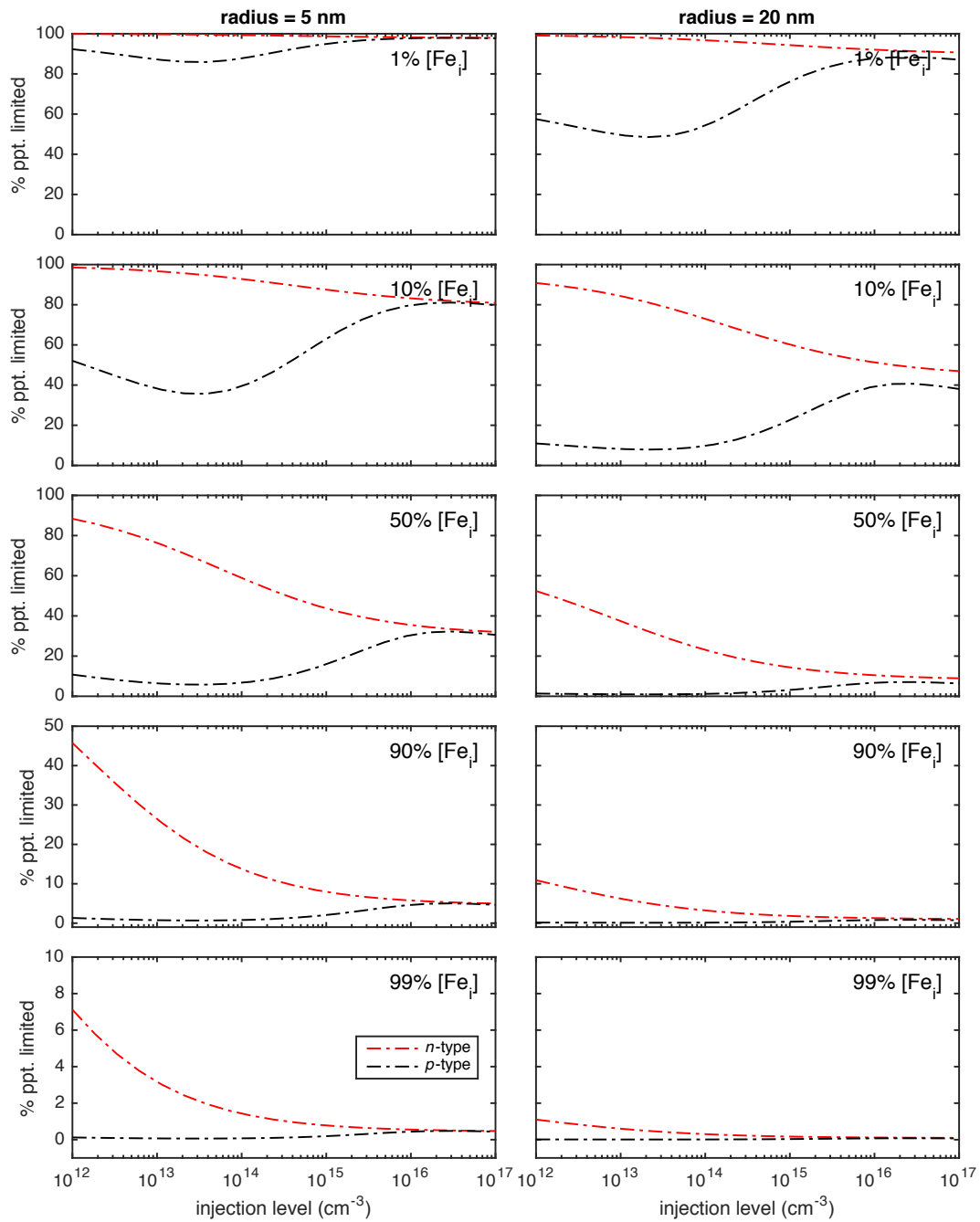


Figure 7-8: Percent of diffusion lengths limited by precipitates in *p*-type and *n*-type mc-Si.

## 7.3 Comparing Simulation Predictions and Experimental Results for *n*-type mc-Si

To quantify to what degree the coupled lifetime and gettering tool captures the redistribution of metals and the electrical impact of actual crystalline silicon material, the *n*-type mc-Si phosphorus diffusion gettering results of Chapter 5 were simulated.

Ideally, the points of comparison between simulation and experiment include the interstitial iron concentration, the precipitated iron distribution, and the injection-dependent lifetime as-grown and after gettering. In *n*-type Si, in which there are not any known metastable defects to leverage for lifetime measurements such as Fe-B in *p*-type Si [54], it is not currently practical to measure the low concentrations of bulk interstitial iron present in typical *n*-type mc-Si wafers. The  $\mu$ -XRF measurements capture the precipitate distribution that is along the grain boundaries, which tend to be the larger and more closely-spaced precipitates. The injection-dependent diffusion lengths averaged over the thickness and area of the wafer can be directly compared.

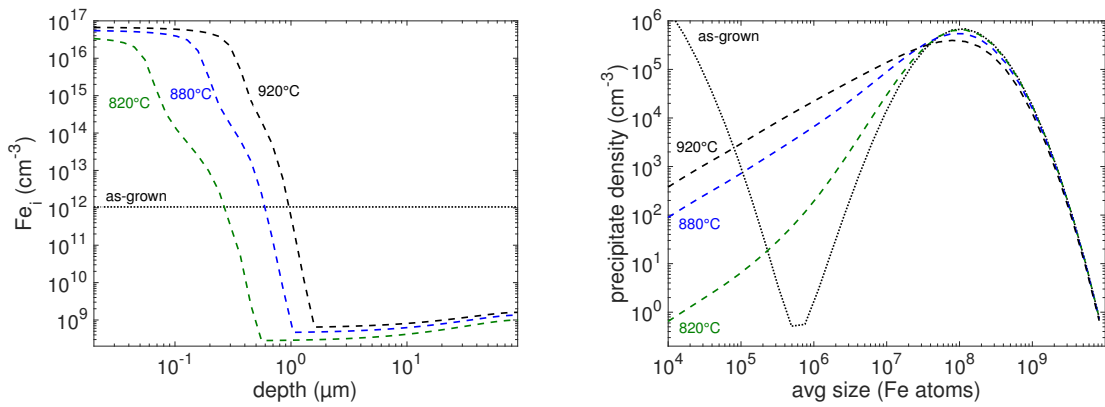
The total iron concentration at the wafer level measured with ICP-MS was  $4.7 \times 10^{14} \text{ cm}^{-3}$ , and the crystallization process was simulated as a decrease from 1100°C to 200°C at 1.35°C/min as in [32]. The phosphorus diffusion time-temperature profiles were defined as starting at 750°C, ramping up to the plateau temperature at 7°C/min, holding at the plateau temperature with phosphorus present for 60 minutes, then cooling to 550°C at a rate of 3.5°C/min. See Figure 5-1 for the measured time-temperature profiles.

The as-grown and post-PDG iron distributions are shown in Fig. 7-9. The simulations predict an as-grown  $[\text{Fe}_i]$  of just over  $10^{12} \text{ cm}^{-3}$ . After gettering, there is strong segregation of point defects to the surface where phosphorus is being in-diffused, resulting in a significantly decreased bulk point defect concentration of approximately  $10^9 \text{ cm}^{-3}$ . As the plateau temperature increases, the bulk interstitial iron concentration increases slightly, and the concentration that is segregated to the phosphorus-rich region also increases slightly. This overall increase in point defect concentration throughout the thickness is due to enhanced precipitate dissolution due to the higher

plateau temperature.

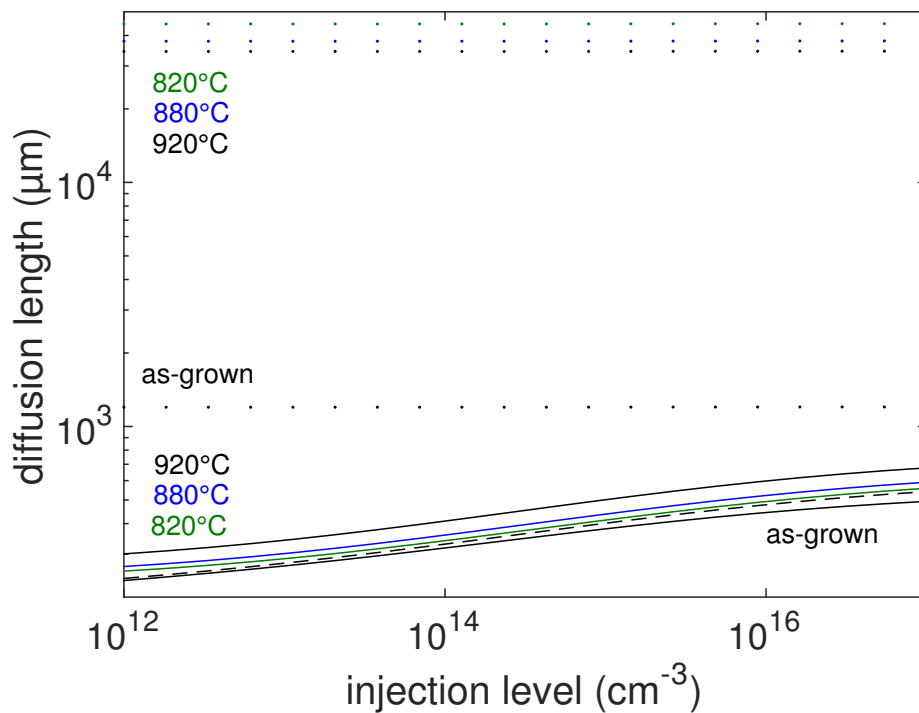
Consistent with the simulated changes in interstitial iron, compared to the as-grown state, gettering significantly reduces occurrence of the small precipitates. As the diffusion temperature increases, the precipitate distribution shifts to smaller precipitate sizes and a lower spatial density of precipitates overall. This trend is consistent with that observed in the  $\mu$ -XRF precipitate distribution measurements, but the simulations do not capture the dramatic full removal of precipitates to below the detection limit observed with  $\mu$ -XRF after 920°C gettering. Additionally the simulated precipitate sizes are about an order of magnitude larger than those that were measured.

The injection-dependent diffusion lengths after crystallization and after each gettering step are shown in Figure 7-9. The as-grown diffusion length in low injection is equivalent to  $\sim 40$   $\mu$ s lifetime, which is higher than the measured as-grown lifetime, indicating that perhaps iron alone does not limit the lifetime. All of the lettering processes are predicted to be strongly precipitate limited across the whole injection level range, and the diffusion lengths increase monotonically from  $\sim 210$   $\mu$ m to  $\sim 280$   $\mu$ m in low injection. The lifetimes still remain relatively low,  $< 80$   $\mu$ s. This precipitate-limited simulated lifetime is much lower than the measured lifetimes of  $> 500$   $\mu$ s. Additionally, the experimentally measured lifetimes reveal a slight drop in lifetime after the highest 920°C process compared to the medium temperature process of 880°C.



(a) Simulated interstitial iron concentration as a function of depth into the wafer as-grown and after three different temperature gettering processes.

(b) Simulated precipitated iron distribution, precipitate spatial density vs. average precipitate size, as-grown and after three different temperature gettering processes.



(c) Simulated minority carrier diffusion length as a function of injection level associated with point defects (dotted line), precipitates (dashed lines), and the total iron distribution (solid lines) as-grown and after three different temperature gettering processes. For 820°C and 880°C, the precipitated and total iron lines overlap.

Figure 7-9: Simulated post-gettering Fe-related diffusion lengths for the initial iron concentration of experiments of Chapter 5. Equivalent injection-dependent diffusion lengths associated with point defects, precipitates, and all iron total for *n*-type mc-Si are shown.



### 7.3.1 Accounting for Enhanced Precipitation due to Co-Location of Multiple Metals

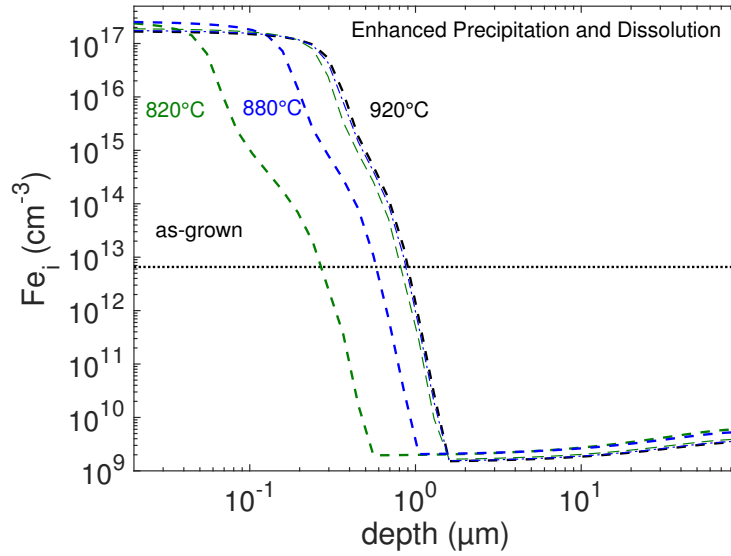
Given the overestimation of precipitate size and the underestimation of the precipitate dissolution and the lifetime, which is precipitate-limited, it is hypothesized that the model underestimates precipitate growth and dissolution rates compared to the observed measurements. The ICP-MS revealed high concentrations of Fe, Ni, Cu, and Co in the as-grown red zone of the wafers. The  $\mu$ -XRF revealed that the Fe-, Ni-, Cu-, and Co are co-located. It is hypothesized that co-location of metals can result in enhanced precipitation and precipitate dissolution [45].

To test the hypothesis of enhanced precipitation due to co-location of metals, the simulated crystallization rate was increased from  $1.35^{\circ}\text{C}/\text{min}$  to  $10^{\circ}\text{C}/\text{min}$  as suggested by [84]. The simulation results are shown in Figure 7-10 and 7-11. The simulated as-grown iron point defect concentration in the bulk was  $\sim 6.5 \times 10^{12} \text{ cm}^{-3}$ . The simulated post-gettering iron point defect concentration in the bulk was  $\sim 10^9 \text{ cm}^{-3}$ . The simulated iron precipitate distribution peaks at  $\sim 5 \times 10^6$  Fe atoms, more consistent with the observed precipitate sizes at the grain boundary (Fig. 5-11). The diffusion lengths are slightly lower than the previous case with crystallization at  $1.35^{\circ}\text{C}/\text{min}$  due to the higher concentration of smaller precipitates.

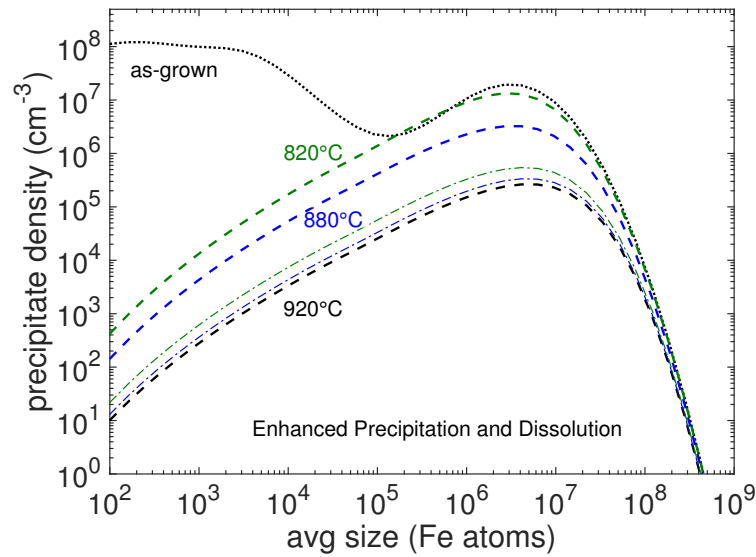
To test the hypothesized enhanced precipitation and dissolution due to co-location of multiple metals, the simulated plateau temperatures were increased until the diffusion lengths were close to the values of the measured diffusion lengths. The simulation results are shown in Figure 7-10 and 7-11. The  $820^{\circ}\text{C}$  was increased to  $911^{\circ}\text{C}$ , and the  $880^{\circ}\text{C}$  was increased to  $917^{\circ}\text{C}$ . The  $920^{\circ}\text{C}$  was left as-is because the model does not capture the observed decrease in lifetime relative to the  $880^{\circ}\text{C}$  process.

While the simulations with enhanced precipitate growth and dissolution rates match reasonably well for the  $820^{\circ}\text{C}$  and  $880^{\circ}\text{C}$  phosphorus diffusion processes, the decrease in lifetime after  $920^{\circ}\text{C}$  compared to the  $880^{\circ}\text{C}$  is still not well explained, and the full disappearance to below the detection limit of the  $\mu$ -XRF is not clearly captured either. It is hypothesized that somewhere above  $880^{\circ}\text{C}$ , another defect is

activated and limits the lifetime of the material. It is difficult to know if Fe limits the as-grown lifetime of the material because it contains many impurities other than iron. The simulations support the hypothesis that after 820°C and 880°C the material may be limited by precipitated Fe as was concluded by [44].

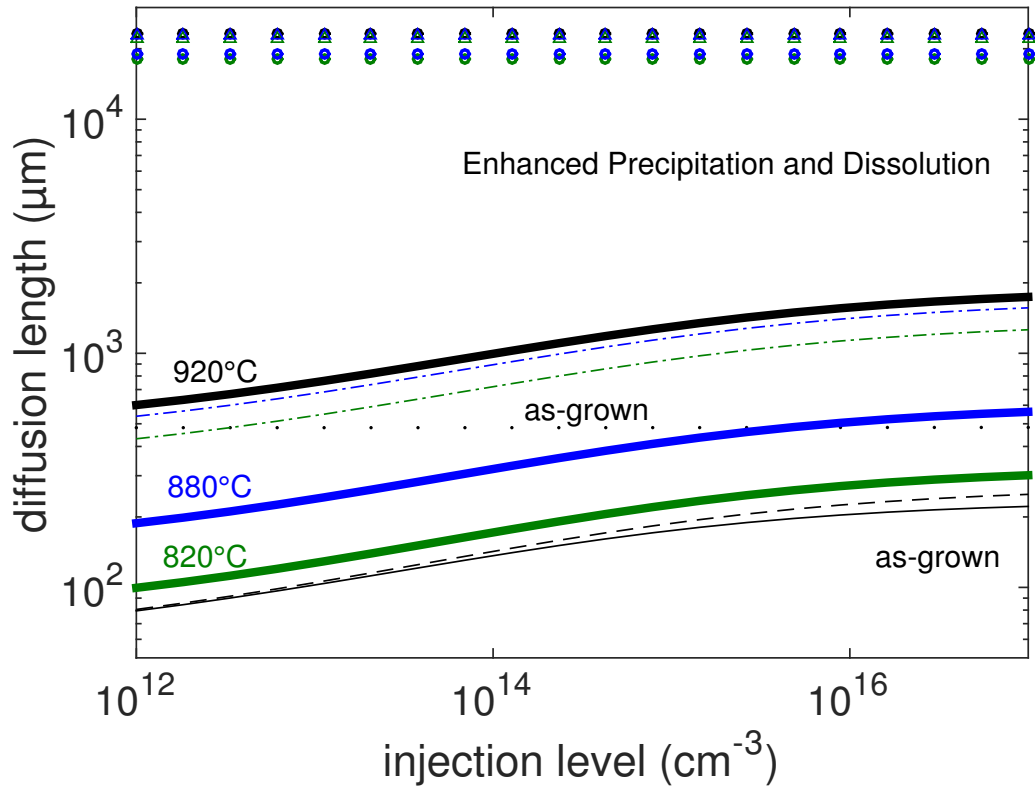


(a) Interstitial iron concentration as a function of depth into the wafer as-grown and after three different temperature gettering processes. Simulation with enhanced precipitation (thick dashed lines) and enhanced precipitation and dissolution (thin dashed lines).



(b) Precipitated iron distribution (precipitate spatial density vs. average precipitate size) as-grown and after three different temperature gettering processes. Simulation with enhanced precipitation (thick dashed lines) and enhanced precipitation and dissolution (thin dashed lines).

Figure 7-10: Simulating enhanced precipitation and dissolution: iron distribution for experiments of Chapter 5.



(a) Minority carrier diffusion lengths as a function of injection level as-grown and after three different temperatures of gettering assuming enhanced precipitation and precipitate dissolution. As-grown lifetime due to: point defects (black dotted line), precipitated Fe (thin dashed black line), and both point defects and precipitates (thin solid black line). Post-gettering lifetime due to: point defects assuming enhanced precipitation (open circles) and assuming enhanced precipitation and dissolution (open triangles); precipitates assuming enhanced precipitation (thick solid lines); total iron distribution assuming enhanced precipitation and precipitate dissolution (dashed-dotted lines). For the enhanced precipitation and precipitate dissolution, for 820°C and 880°C, the precipitated and total iron lines overlap.

Figure 7-11: Simulating enhanced precipitation and dissolution: injection-dependent diffusion lengths for experiments of Chapter 5.

# Chapter 8

## Sensitivity analysis to guide PDG processing for *n*-type mc-Si and *p*-type mc-Si

To understand the relative effect of processing on *n*- and *p*-type mc-Si, a sensitivity analysis was performed using the coupled gettering and lifetime simulation tool described in Chapter 7.

### 8.1 Defining Test Processes and Initial Total Iron Concentrations

A base case of a phosphorus diffusion time-temperature profile was defined and then the time-temperature profile was perturbed, either lengthening it by 15 minutes or shortening it by 15 minutes. The factors that were perturbed include the plateau temperature, the plateau time, the cooling rate, and the unload temperature. For example, to shorten the profile, either the plateau temperature was decreased, or the plateau time was shortened, or the cooling rate was increased, or the unload temperature was increased.

The time-temperature profiles of the processes that were tested are shown in Fig.

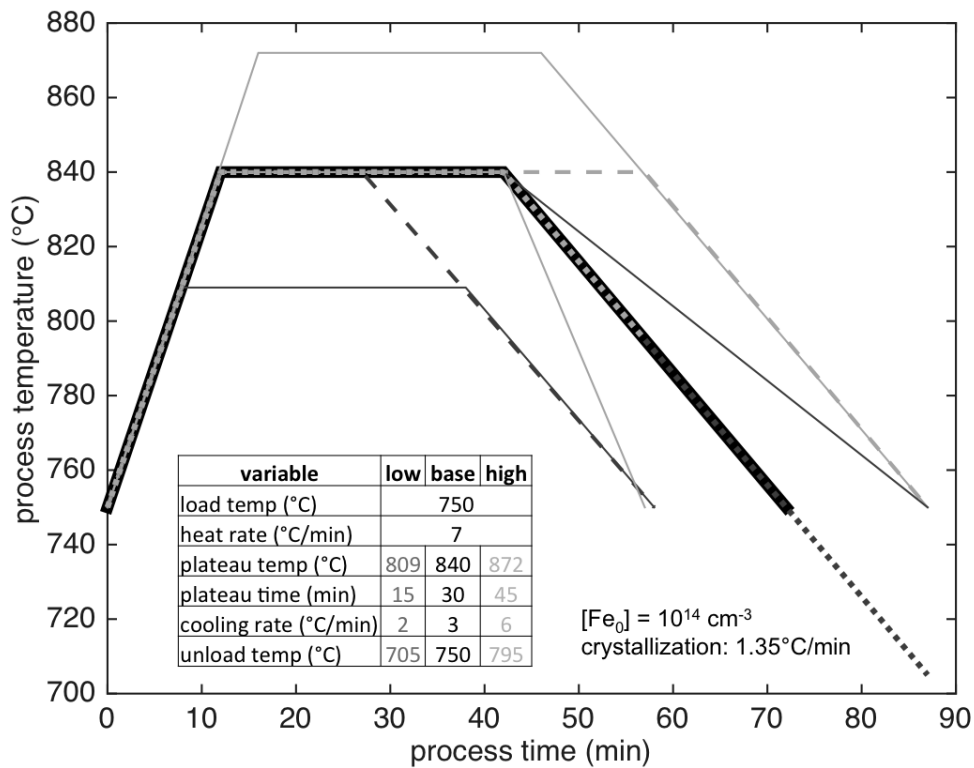


Figure 8-1: Time-temperature profiles used in sensitivity study.

8-1. Phosphorus in-diffusion starts at the beginning of the isothermal plateau step. Three different total initial iron concentrations —  $10^{13}$ ,  $10^{14}$ , and  $10^{15}$  cm<sup>-3</sup> — were simulated to account for the wide range of iron concentrations found in as-grown mc-Si. The crystallization step was the same in all cases and was modeled as a linear cooling from 1100°C to 200°C at 1.35°C/min as in Chapter 4. Additionally, the load temperature of 750°C and heating rate of 7°C/min were kept constant. The electrical quality of wafers was found to be quite insensitive to these two parameters in [60]. The effect of load temperature and the heating rate are captured in the plateau temperature and time.

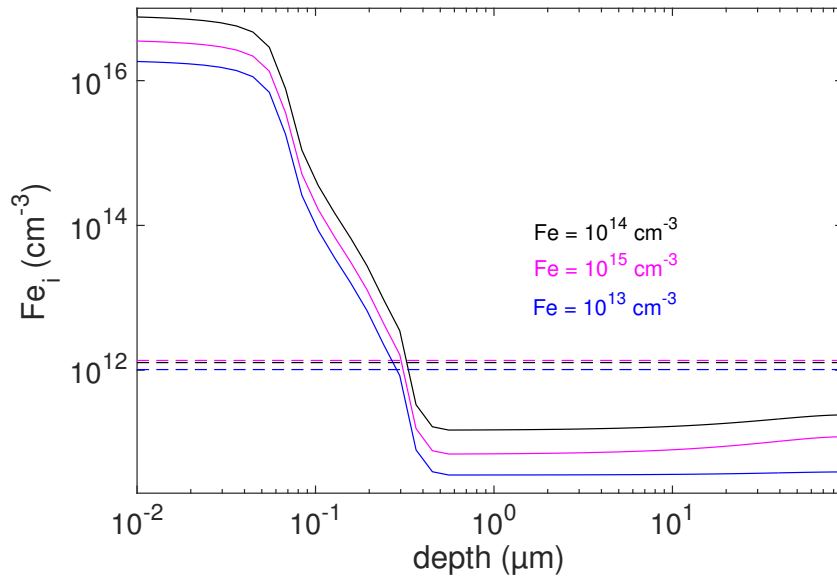
## 8.2 Base Cases: Iron Distributions and Injection-Dependent Minority Carrier Diffusion Lengths

For the base case time-temperature profile and for each of the initial iron concentrations, the iron distributions and injection-dependent bulk minority carrier diffusion lengths were simulated. The iron distributions are plotted in Fig. 11-1 and the diffusion lengths are plotted in Fig. 8-3.

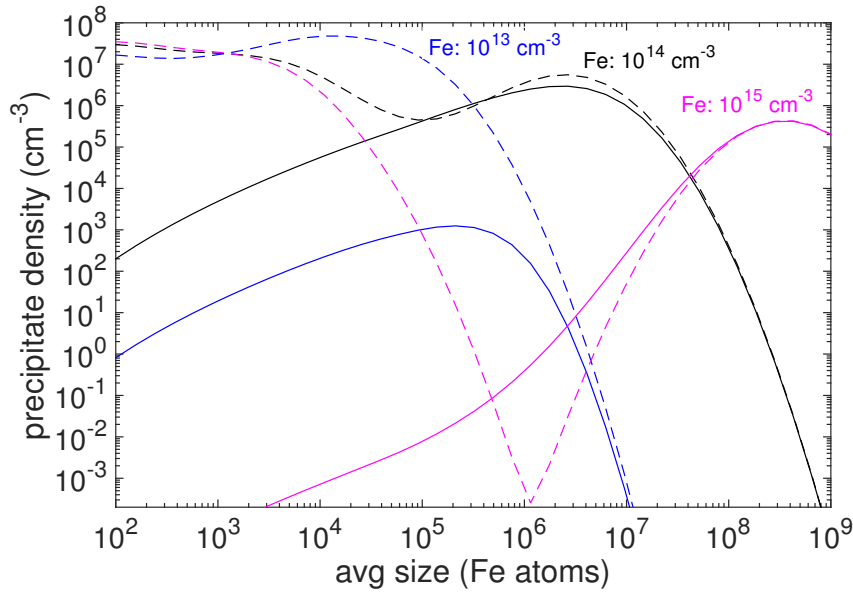
Fig. 8-2a shows the interstitial iron concentration as a function of depth into the wafer before and after gettering. As-grown, for all three initial iron concentrations, the interstitial iron concentration is  $\sim 10^{12} \text{ cm}^{-3}$  with higher initial iron concentration corresponding with slightly higher interstitial iron concentration. After gettering, the interstitial iron profiles are the same shape because the wafers were all simulated with the same base case process. The effect of external gettering to the phosphorus-rich layer at the surface is clearly evident here, leaving a much lower interstitial iron concentration in the bulk compared to the as-grown state. For the base case, the initial iron concentration of  $10^{14} \text{ cm}^{-3}$  has the highest bulk interstitial concentration, and the lowest initial contamination of  $10^{13} \text{ cm}^{-3}$  has the lowest bulk interstitial iron concentration.

Fig. 8-2b shows the precipitated iron distribution before and after the base case process for all three initial iron concentrations. As-grown, as the total iron concentration increases, the precipitated iron distribution shifts from many small precipitates to sparser larger precipitates to a bimodal distribution of small and large precipitates both in large quantities. After gettering, some precipitates disappear, especially the small ones, indicated by the decrease in precipitate density. For the initial iron concentration of  $10^{13} \text{ cm}^{-3}$ , there is an especially dramatic reduction probably due to full or nearly full dissolution during gettering and external gettering that is sufficient to lower the resulting interstitial iron concentration as shown in Fig. 8-2a.

The injection-dependent diffusion lengths before and after the base case process for all three simulated total iron concentrations are shown in Fig. 8-3. The diffusion lengths assuming *p*-type material are in the left column and the values assuming *n*-



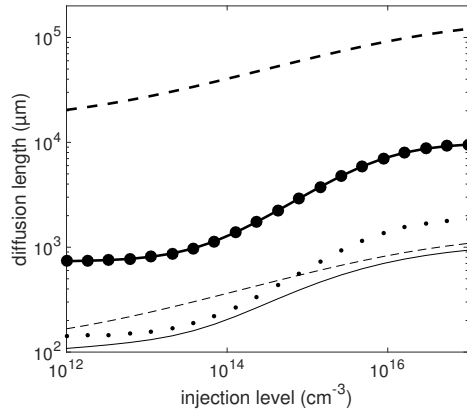
(a) base cases:  $[Fe_i]$  vs. depth before and after gettingting



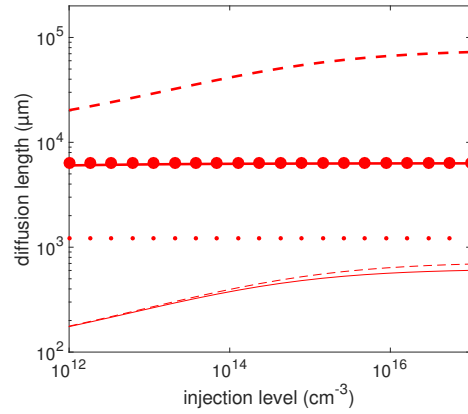
(b) base cases: precipitated Fe distribution before and after gettingting

Figure 8-2: Base Case Iron Distributions for Total Fe of  $10^{13}$  (blue),  $10^{14}$  (black), and  $10^{15}$  (magenta)  $\text{cm}^{-3}$ . 8-2a shows the interstitial iron concentration as a function of depth into the wafer before (dashed lines) and after (solid lines) the base case gettingting profile. 8-2b shows the precipitated iron distribution before (dashed lines) and after (solid lines) the base case gettingting profile.

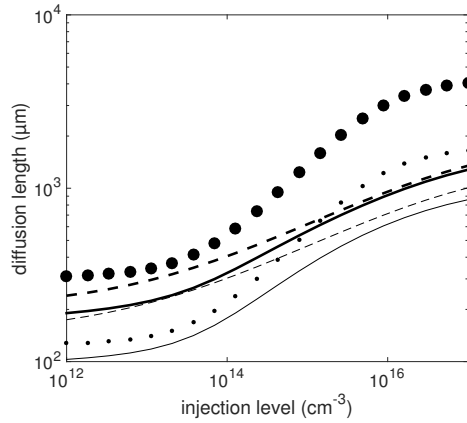




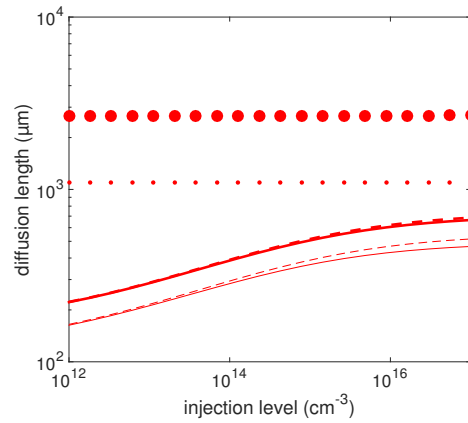
(a) base case,  $10^{13} \text{ cm}^{-3}$ , *p*-type



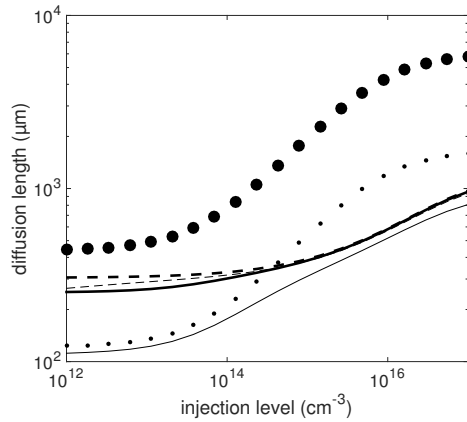
(b) base case,  $10^{13} \text{ cm}^{-3}$ , *n*-type



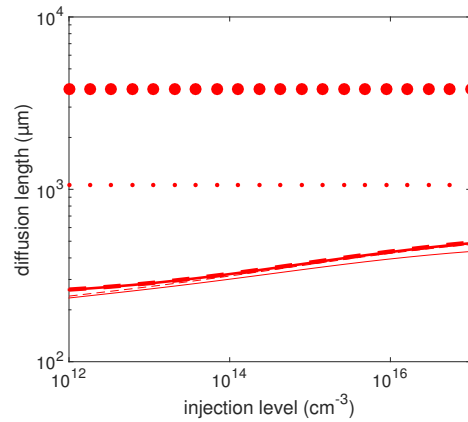
(c) base case,  $10^{14} \text{ cm}^{-3}$ , *p*-type



(d) base case,  $10^{14} \text{ cm}^{-3}$ , *n*-type



(e) base case,  $10^{15} \text{ cm}^{-3}$ , *p*-type



(f) base case,  $10^{15} \text{ cm}^{-3}$ , *n*-type

Figure 8-3: Base case Fe distributions for total Fe of  $10^{13}$  (top row),  $10^{14}$  (middle row), and  $10^{15}$  (bottom row)  $\text{cm}^{-3}$  for *p*-type (left column) and *n*-type (right column) Si. The dots are the point defects. Dashed lines are the precipitates. Solid lines are the effective diffusion length due to both point defects and precipitates. Thin lines and small dots are as-grown. Thick lines and small dots are post-gettering.

type material are in the right column. The plots indicate that the  $p$ -type material is more strongly injection-dependent than the  $n$ -type material. The injection dependence of the  $n$ -type material is due to the injection dependence of the precipitate-related diffusion lengths. The injection dependence of the  $p$ -type material is due to both precipitates and precipitates with the point defects being a stronger effect.

For the initial iron concentration of  $10^{13} \text{ cm}^{-3}$ , as-grown the  $n$ -type Si is limited by precipitates, and after gettering, it is limited defects. For the  $p$ -type Si, as-grown the material is limited by point defects at low injection level and by precipitates at high injection level. After the base case gettering,  $p$ -type is limited by point defects. Thus, a longer cooling or low-temperature anneal could increase the minority carrier diffusion lengths for both doping types at this iron contamination level.

For the initial iron concentration of  $10^{14} \text{ cm}^{-3}$ , as-grown and after the base case gettering, the  $n$ -type Si is limited by precipitates. For the  $p$ -type Si, as-grown the material is limited by point defects at low injection level and by precipitates at high injection level. After the base case gettering,  $p$ -type is more strongly limited by precipitates. Thus, for  $n$ -type, a higher temperature or longer plateau would increase the diffusion length. For the  $p$ -type Si, a longer cool down and a higher temperature plateau would increase the diffusion length.

For the initial iron concentration of  $10^{15} \text{ cm}^{-3}$ , as-grown and after the base case gettering, the  $n$ -type Si is limited by precipitates. The effective lifetimes are only slightly increased by the base case gettering. For the  $p$ -type Si, as-grown the material is limited by point defects at low injection level and by precipitates at high injection level. After the base case gettering,  $p$ -type is more strongly limited by precipitates. Thus, for  $n$ -type, a higher temperature or longer plateau would increase the diffusion length. For the  $p$ -type Si, a longer cool down and a higher temperature plateau would increase the diffusion length.

## 8.3 Minority Carrier Diffusion Length Sensitivity Plots for *n*- and *p*-type Si

The sensitivity plots of the diffusion lengths at an injection level of  $7 \times 10^{13} \text{ cm}^{-3}$  are shown for an initial total iron concentration of  $10^{13} \text{ cm}^{-3}$  (Fig. 8-4),  $10^{14} \text{ cm}^{-3}$  (Fig. 8-5),  $10^{15} \text{ cm}^{-3}$  (Fig. 8-6). It should be noted that the magnitudes of this sensitivity analysis vary with injection level, but the trends shown in these figures apply to a wide range of injection levels under which typical solar cells operate. For injection levels above  $\sim 10^{15} \text{ cm}^{-3}$ , this analysis should be re-run.

The sensitivity results for initial total iron concentration of  $10^{13} \text{ cm}^{-3}$  are in Fig. 8-4. The base case diffusion lengths of *n*-type are  $>5 \times$  those of *p*-type mc-Si. Material of both doping types is strongly limited by  $\text{Fe}_i$ , so the effective sensitivity plots are very similar to the  $\text{Fe}_i$  sensitivity plots. The *p*-type lower unload temperature profile that is 87-minute long results in a shorter diffusion length than even the 30 minute shorter *n*-type 57-minute long low-temperature plateau process. Thus, *n*-type mc-Si for this iron distribution may be especially beneficial over *p*-type mc-Si.

The sensitivity results for initial total iron concentration of  $10^{14} \text{ cm}^{-3}$  are in Fig. 8-5. The base case diffusion length of the *n*-type mc-Si is 365  $\mu\text{m}$  while that of the *p*-type mc-Si is 300  $\mu\text{m}$ . The *p*-type mc-Si is about equally limited by precipitates and interstitials at this injection level, so its effective lifetime pattern reflects the importance of the unload temperature, which affects the point defects, and the plateau temperature, which affects the precipitates. The *n*-type mc-Si is severely limited by the precipitates, so its effective diffusion length pattern is nearly identical to that of the precipitates. The *p*-type higher plateau temperature profile that is 87-minute long results in a similar diffusion length to that of the base case *n*-type 72-minute long process. Thus, *n*-type mc-Si for this iron distribution may enable shorter processing compared to *p*-type mc-Si.

The sensitivity results for initial total iron concentration of  $10^{15} \text{ cm}^{-3}$  are in Fig. 8-6. The base case diffusion length of the *n*-type mc-Si is 315  $\mu\text{m}$  while that of the *p*-type mc-Si is 292  $\mu\text{m}$ . The *p*-type mc-Si is more strongly limited by precipitates,

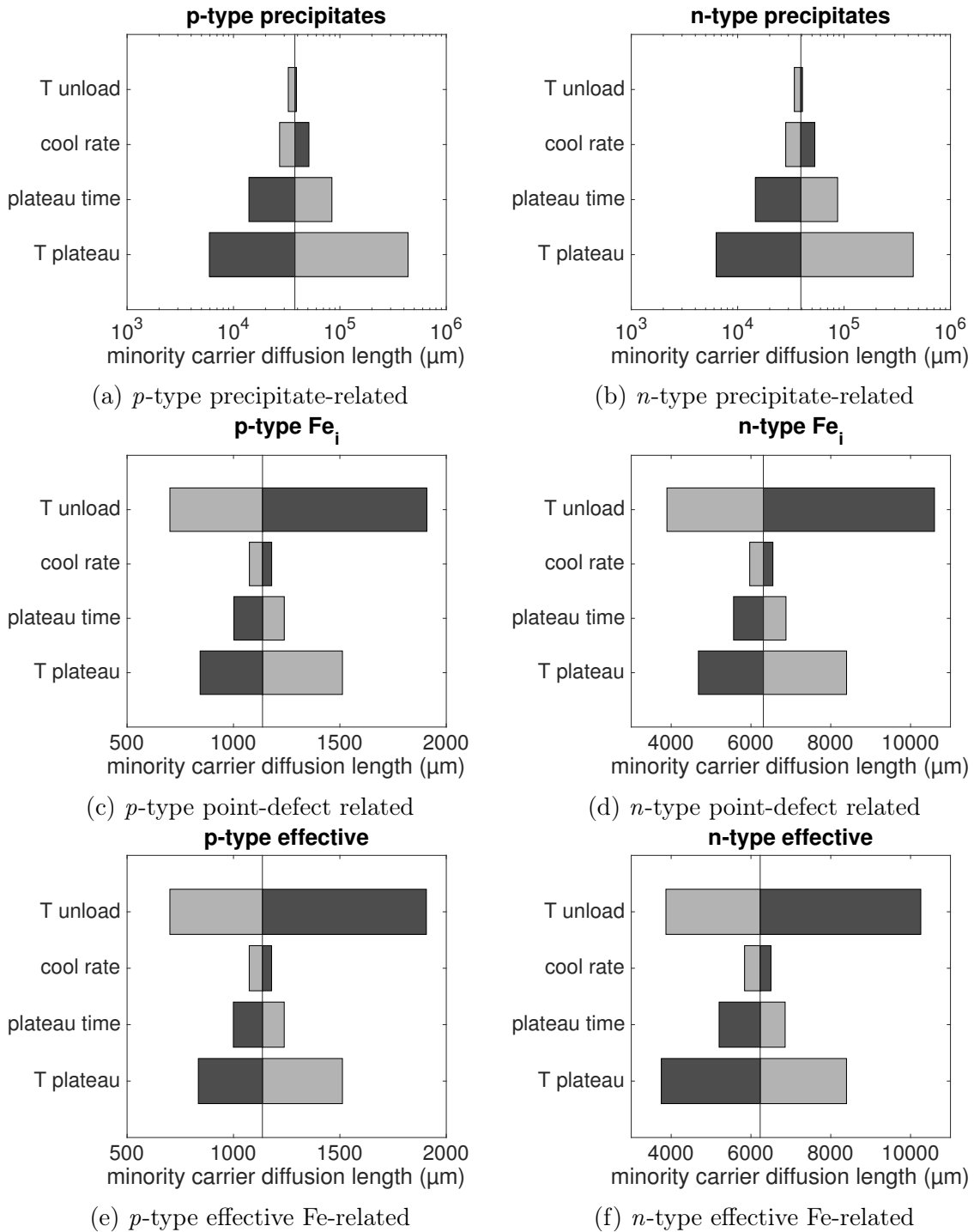


Figure 8-4: Sensitivity of diffusion length to PDG time-temperature profile parameters for initial total iron concentration of  $10^{13} \text{ cm}^{-3}$ . Light bars are a lower value of the given parameter. Dark bars are a higher value of the given parameter. The injection level is just below  $10^{14} \text{ cm}^{-3}$ .

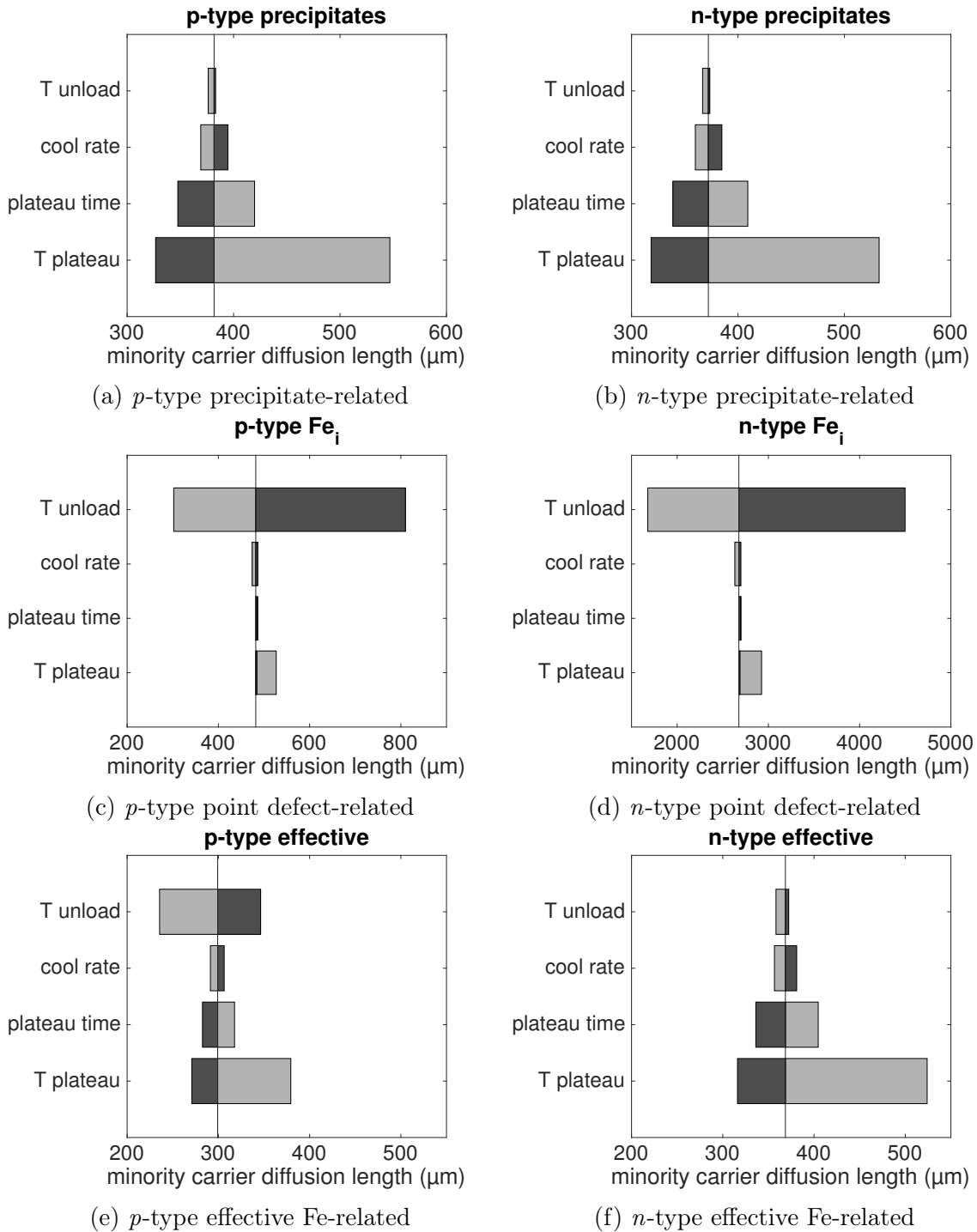


Figure 8-5: Sensitivity of diffusion length to PDG time-temperature profile parameters for initial total iron concentration of  $10^{14} \text{ cm}^{-3}$ . Light bars are a lower value of the given parameter. Dark bars are a higher value of the given parameter. The injection level is just below  $10^{14} \text{ cm}^{-3}$ .

but the most significant change to the base diffusion length that can be achieved in 15 minutes is through point defect control, so the effective diffusion length is most sensitive to the unload temperature. The  $n$ -type mc-Si is severely limited by the precipitates, and the simulations indicate that any 15-minute change in the time-temperature profile make little difference in the diffusion length at this injection level. The  $p$ -type lower unload temperature profile that is 87-minute long results in a similar diffusion length to that of the  $n$ -type PDG processes. Thus,  $n$ -type mc-Si for this iron distribution may enable shorter processing compared to  $p$ -type mc-Si.

In summary, after the total iron concentration, the phosphorus diffusion time-temperature profile is an important lever on the minority carrier diffusion lengths of  $n$ - and  $p$ -type mc-Si material. The performance of both  $n$ - and  $p$ -type Si can be limited by either precipitated or point defect form iron, depending on the relative quantities of each and the injection level of interest. For both materials, the unload temperature determines the concentration and thus the electrical impact of point defects while the plateau temperature and, to a lesser degree, the plateau time control the precipitated iron concentration and electrical impact. For all the situations considered herein, the minority carrier diffusion length was more sensitive to the unload temperature and the plateau temperature, due to the exponential dependencies on temperature, than to the cool rate or the plateau time. At the low total iron level of  $10^{13} \text{ cm}^{-3}$ , both materials are limited by point defects. At a medium level of  $10^{14} \text{ cm}^{-3}$ ,  $p$ -type material is limited by both precipitate and point defects while  $n$ -type material is limited by precipitates. Finally, at a very high level of  $10^{15} \text{ cm}^{-3}$ , which exceeds the concentration in most “red zone” border material, precipitates severely limit the minority carrier diffusion lengths of both materials, and it is very difficult to change the diffusion length. The  $n$ -type material is only slightly improved by gettering compared to the as-grown state, and the  $p$ -type material is improved after gettering mostly due to point defect removal.

In general,  $n$ -type mc-Si can be processed to the same or a higher minority carrier diffusion length than  $p$ -type mc-Si can using a shorter process because precipitates are more often limiting  $n$ -type mc-Si, and they can be remedied by increasing plateau

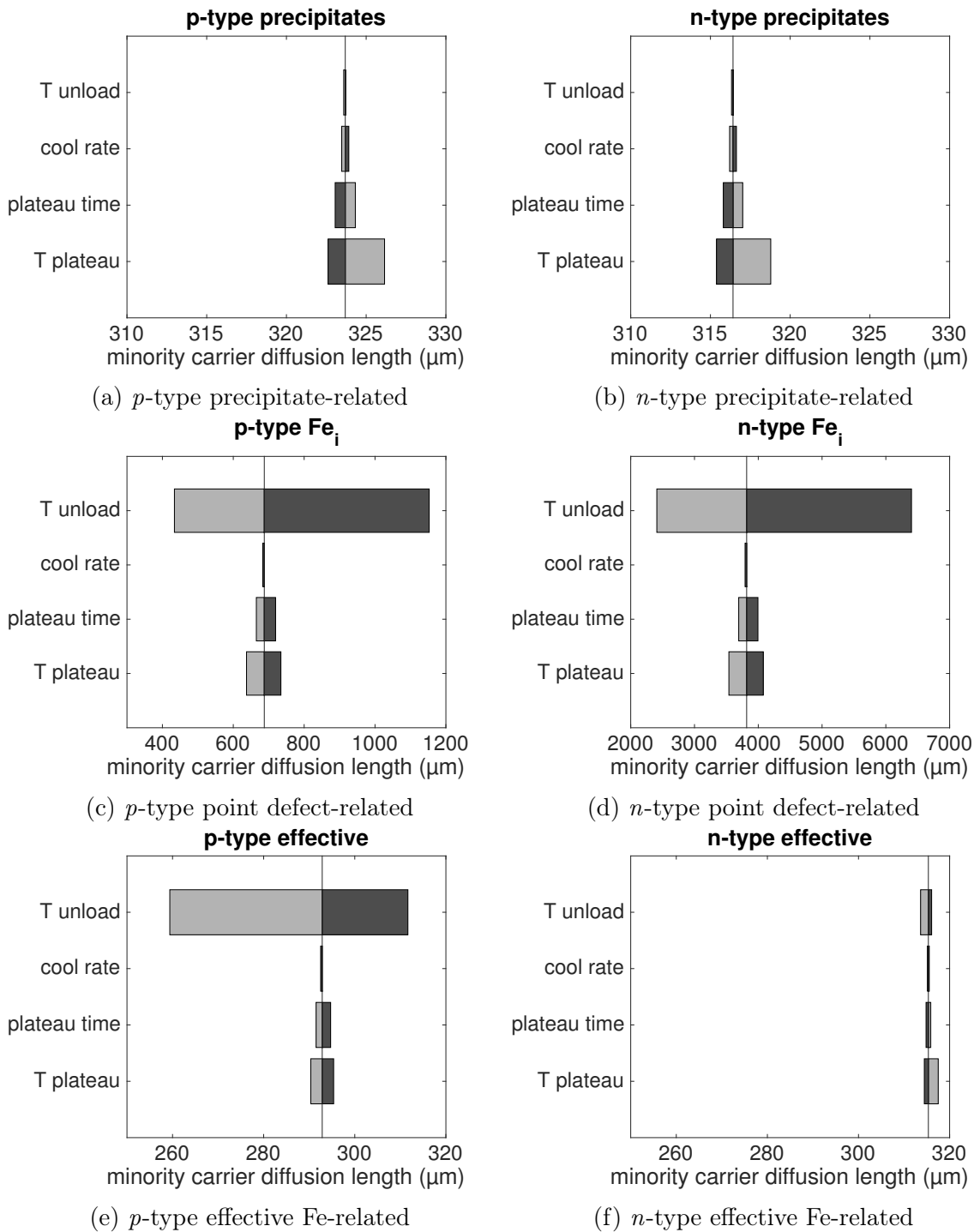


Figure 8-6: Sensitivity of diffusion length to PDG time-temperature profile parameters for initial total iron concentration of  $10^{15} \text{ cm}^{-3}$ . Light bars are a lower value of the given parameter. Dark bars are a higher value of the given parameter. The injection level is just below  $10^{14} \text{ cm}^{-3}$ .

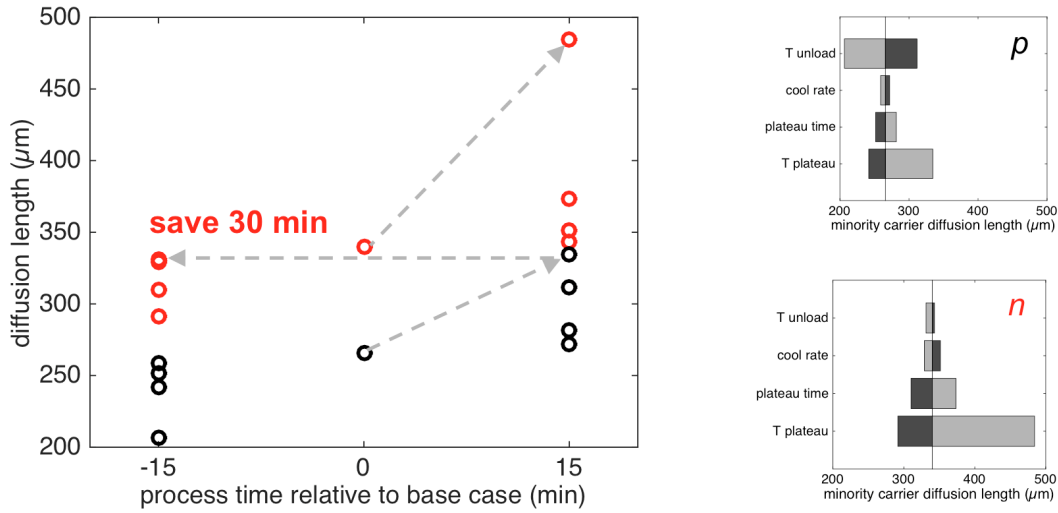


Figure 8-7: Manufacturing benefits of *n*-type Si. On the right side, plots of sensitivity of the effective minority carrier diffusion lengths for *p*-type (top) and *n*-type (bottom) Si with initial total Fe concentration of  $10^{14} \text{ cm}^{-3}$  for an injection level of  $4 \times 10^{13} \text{ cm}^{-3}$ . On the left side, the minority carrier diffusion lengths shown in the sensitivity plots of the right side as a function of process time relative to the base case PDG time-temperature profile. Red open circles are *n*-type and black open circles are *p*-type.

temperature, which adds less time than adding an extended cool. This potential manufacturing benefit is illustrated in Figure 8-7. For a given process time, *n*-type has a longer diffusion length. *n*-type enables saving of 30 mins for the same diffusion length. In the same amount of time, *n*-type can be improved more than *p*-type. Of course, in some *n*-type architectures, the phosphorus diffusion gettering is a sacrificial gettering and is thus an extra step. Nonetheless, especially for architectures such as the PERT device that includes phosphorus and boron diffusion, this is an important implication for manufacturing throughput and thus cost.



# Chapter 9

## Injection-Dependent Efficiency

## Entitlement of Various $n$ -type Si Materials

### 9.1 Efficiency Depends on Lifetime and Injection Level

Solar cells operate at a certain injection level, depending on the illumination conditions, doping type, doping level, wafer thickness, and injection-dependent electrical performance of the wafer, among other factors.

To directly compare the performance of  $p$ -type and  $n$ -type wafers, Schindler *et al.* simulated a  $p$ -type-based PERC-type and an  $n$ -type-based PERC-type device that had equivalent performance assuming no bulk recombination [166]. They simulated both doping types and resistivity values of 1  $\Omega$ -cm and 3  $\Omega$ -cm and plotted the simulated solar cell efficiency as a function of the minority carrier lifetime for standard illumination conditions. See Figure 9-1. One can measure the minority carrier lifetime of a wafer in the  $10^{13} - 10^{15} \text{ cm}^{-3}$  range and identify the corresponding efficiency assuming that the device is only bulk lifetime limited, but the variation in efficiency as a function of injection level can change rapidly, making this only an approximate estimate of efficiency entitlement.

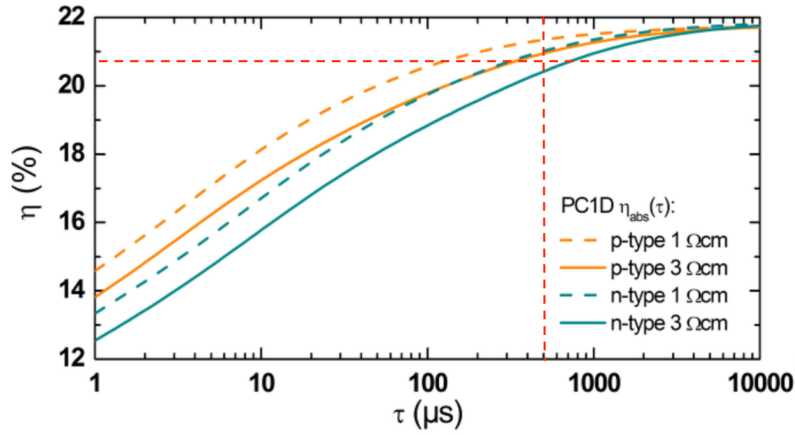


Figure 9-1: Efficiency as a Function of Lifetime for  $n$ - and  $p$ -type Si. The red dashed lines indicate the approximate efficiency entitlement of 500  $\mu\text{s}$   $n$ -type Si material. Adapted from [166].

## 9.2 Efficiency entitlement of $n$ -type materials

Florian Schindler shared the PC1D parameter files with me, enabling the adaptation of these efficiency as a function of lifetime curves to the type of injection-dependent visualization of efficiency entitlement developed and explained in [183]. For each of the simulations shown in Fig. 9-1, I identified the voltage at maximum power point, swept the simulation from -0.8 V to that voltage and then output the simulated injection level halfway through the wafer thickness. I then plotted the lifetime as a function of injection level and used color to indicate the simulated solar cell efficiency. All four curves are shown together in Fig. 9-2, and they are shown in pairs in Fig. 9-3 for clearer comparison.

These plots highlight several key trends. As the bulk lifetime increases, the solar cell efficiency increases, and at just over 21% efficiency, the improvement with lifetime slows. The highest efficiency value plotted is 21.8% with a bulk lifetime of 10 ms. For the parameters plotted here, achieving efficiencies greater than 22% requires very long bulk lifetimes, in excess of 10 ms. All four devices theoretically can achieve higher

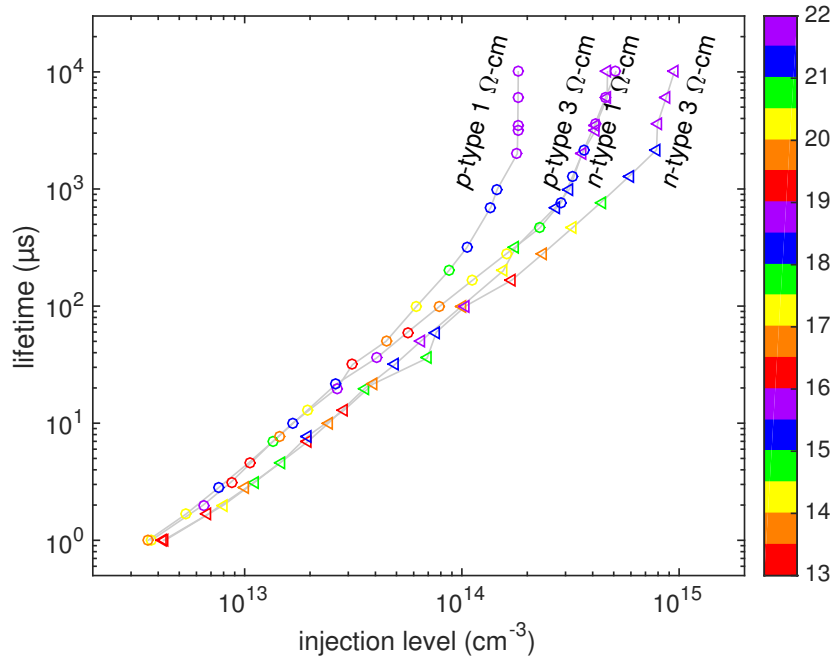
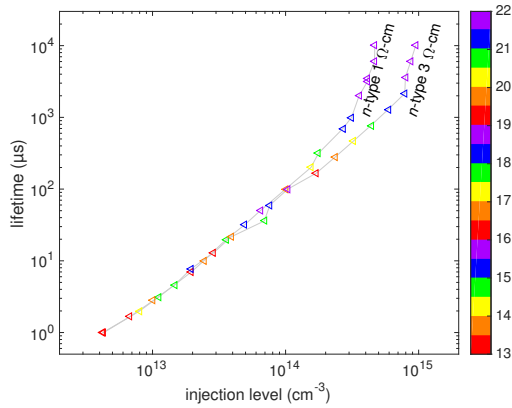


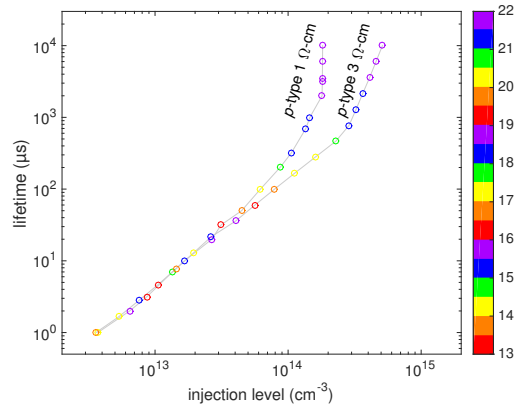
Figure 9-2: Efficiency as a Function of Lifetime and Injection Level at Maximum Power Point for  $n$ - and  $p$ -type Si with bulk resistivity of 1 and 3  $\Omega$ -cm. Simulations in PC1D. Data provided by and adapted from [166].

than 21% efficiency given longer than 1 millisecond lifetimes. At above 21%, all of the cells operate at an average injection level of over  $10^{14} \text{ cm}^{-3}$ . For a given lifetime, the higher resistivity (lower doping level) cells operate at higher injection level than the lower resistivity cells. Also for a given lifetime, the  $n$ -type cells operate at higher injection than the  $p$ -type cells.

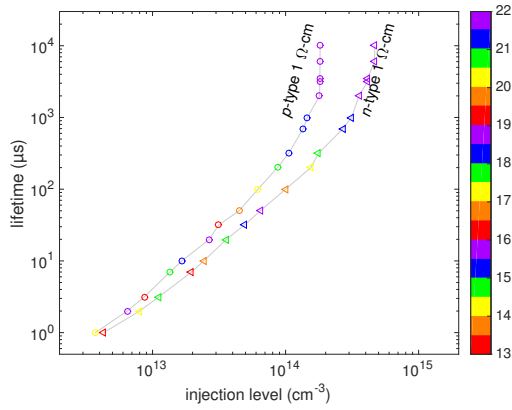
To estimate the efficiency entitlement of wafer materials from their injection-dependent lifetime curves, one can overlay the minority carrier lifetime curve on the efficiency entitlement curves. For reference, the record  $n$ -type wafer heterojunction cell is from Panasonic at 25.6% efficient. The record large-area single crystal non-heterostructure is Sunpower's 25% rear junction cell also on  $n$ -type Si [6]. Crystal Solar and imec have reported 22.5% full-size nPERT cells using epitaxially-grown kerfless wafers with grown-in  $p$ - $n$  junctions. Finally, Trina Solar holds the record for high-performance  $p$ -type mc-Si at 21.25%. Schindler *et al.* [167] reported 19.3% on  $n$ -type high-performance mc-Si. Fig. 9-4 shows the  $n$ -type efficiency plot with several different injection-dependent lifetime curves overlaid, including simulated and



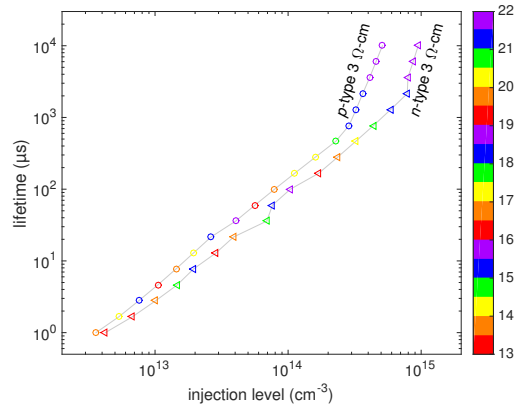
(a) *n*-type for 1 and 3  $\Omega$ -cm resistivity



(b) *p*-type for 1 and 3  $\Omega$ -cm resistivity



(c) 1  $\Omega$ -cm resistivity for *n*- and *p*-type



(d) 3  $\Omega$ -cm resistivity for *n*- and *p*-type

Figure 9-3: Efficiency as a Function of Lifetime and Injection Level at Maximum Power Point for *n*- and *p*-type Si with bulk resistivity of 1 and 3  $\Omega$ -cm. Simulations in PC1D. Data provided by and adapted from [166].

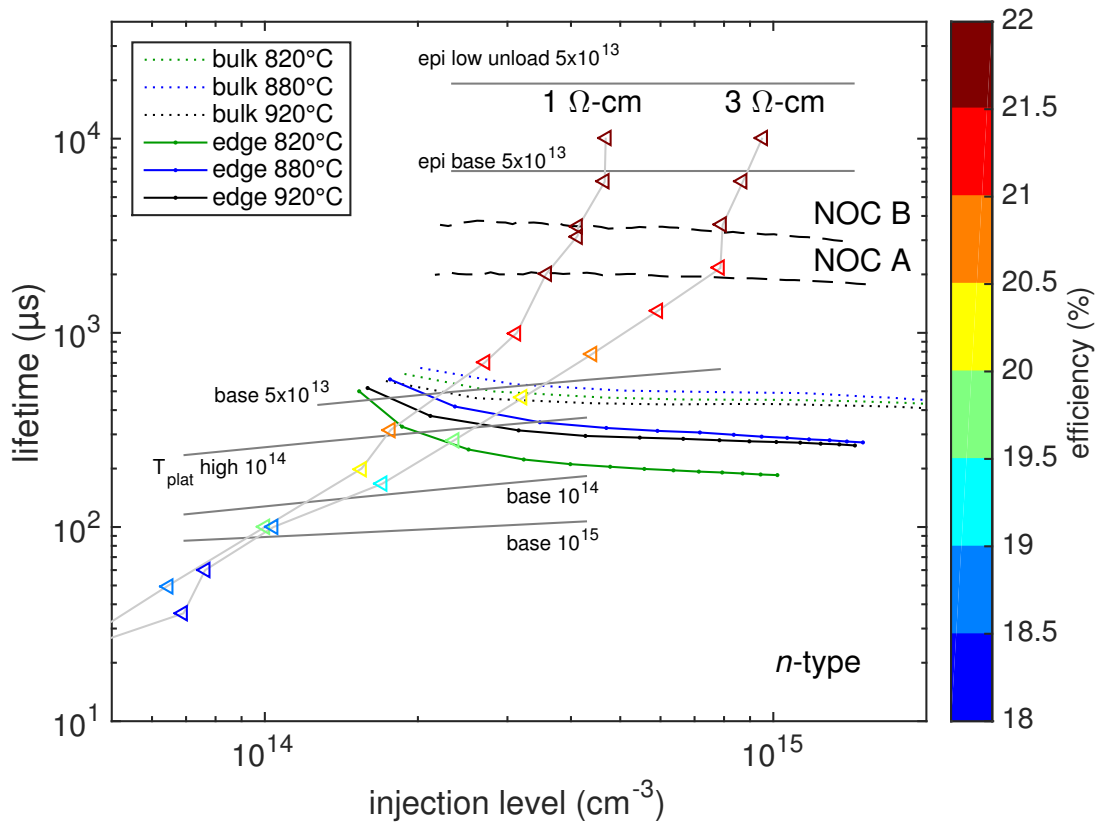


Figure 9-4: Efficiency as a Function of Lifetime and Injection Level at Maximum Power Point for *n*-type Si with bulk resistivity of 1 and 3  $\Omega$ -cm. Simulations in PC1D. Overlaid are experimentally measured injection-level-dependent lifetime curves to. The intersection of the lifetime curves and the efficiency curves are the efficiency entitlement for the material. Data provided by and adapted from [166].

experimentally measured curves.

The experimentally measured overlaid curves include ones for the *n*-type upgraded metallurgical grade mc-Si material discussed in Chapter 5 and a new cast monocrystalline material called non-contact crucible material from the laboratory of Kazuo Nakajima. The curves labelled “NOC A” and “NOC B” are this non contact crucible material after phosphorus diffusion gettering, and A and B refer to two different impurity levels [199]. The efficiency entitlement is estimated to be at or over 21.5%, depending on the bulk resistivity. For the material of Chapter 5, the post-gettering harmonic means of the photoconductance-calibrated photoluminescence images for material from the bulk of the wafers and from the poorer-quality border region are

shown. The dotted lines are measurements of the bulk material while the solid lines are the “red zone” border region. This upgraded metallurgical grade 6N’s purity material has a bulk resistivity of 1–2  $\Omega$ -cm. The material is estimated to have an efficiency entitlement of about 20.5%. The high-performance *n*-type mc-Si wafers of Schindler *et al.* [166] have a measured minority carrier diffusion length of 550  $\mu\text{m}$  after phosphorus diffusion gettering, which is equivalent to  $\sim 260$   $\mu\text{s}$  lifetime, or an efficiency entitlement of  $\sim 19.5\%$  in the cell architecture simulated here. They demonstrated 19.3% efficiency in an advanced architecture featuring a full area passivated rear contact [167].

The simulated overlaid curves of *n*-type Si material are the medium solid gray lines running roughly horizontally. All six curves are simulated using the simulator described in Chapter 7. The curves include: the base case PDG defined in Chapter 8 for  $10^{15}$ ,  $10^{14}$ , and  $5 \times 10^{13}$   $\text{cm}^{-3}$  initial total iron, the high-temperature plateau case also defined in Chapter 8 for  $10^{14}$   $\text{cm}^{-3}$  initial total iron, and the base and low unload temperature PDG processes approximating epitaxially-grown silicon with a wafer crystallization rate of  $60^\circ\text{C}/\text{min}$ , much faster than the typical  $1.35^\circ\text{C}/\text{min}$  for mc-Si. As was shown in the sensitivity analysis of Chapter 8, it is difficult to improve the quality of highly contaminated material, and this efficiency entitlement plot shows that standard processing of material with more than  $10^{14}$   $\text{cm}^{-3}$  of iron cannot exceed 20%, depending on the resistivity level. Processing material with  $10^{14}$   $\text{cm}^{-3}$  of iron with a high-temperature plateau increases the efficiency potential to 19.5% to 20.5% with the penalty of longer and more energy-intensive processing. Lower as-grown iron concentrations of  $5 \times 10^{13}$   $\text{cm}^{-3}$  enable greater than 20.5% efficiency.  $10^{13}$   $\text{cm}^{-3}$  (not shown) of iron enables greater than 21.5% efficiency. Finally, simulated epitaxially-grown *n*-type Si with an estimated wafer cooling rate of  $60^\circ\text{C}/\text{min}$  can enable efficiencies at or exceeding 21.5% because of the high as-grown point defect concentration that is readily externally gettered.

These efficiency entitlement plots indicate that, in principle, for *n*-type Si cooled at rates typical of mc-Si ingot growth, achieving 19% efficiency is readily accessible. Achieving just 1% higher absolute, 20% requires relatively clean as-grown material

that is no dirtier than  $10^{14} \text{ cm}^{-3}$  of iron. Achieving 21% requires nearly an order of magnitude reduction in impurities or alternative wafer growth methods that reduce the precipitated iron concentration in the as-grown wafers. It should be noted that this plot is one of efficiency *entitlement* meaning that these are the maximum predicted efficiencies if the cell performance is limited only by the bulk lifetime. It is an achievement to come close to these entitlement values and thus achieving efficiencies higher than 20%, depending on the material, is an active area of strong competition in industry. This plot by itself implies that the way forward for photovoltaics is cleaner, higher efficiency materials; however, it neglects the very important factor of cost. The costs of capital, manufacturing, and silicon, and the difficulty of developing incrementally better technology that is repeatable on a massive scale are important and fluctuating factors that have led to the propagation of both mono crystalline and multicrystalline materials in the PV industry. With the development of new cell architectures can come unexpected setbacks. One example for the development of passivated emitter and rear (PERC) devices is discussed in the next Chapter.





# Chapter 10

## Root-Cause Analysis of Light-Induced Degradation in *p*-type Multicrystalline Silicon PERC Modules

### 10.1 Overview of *p*-type mc-Si PERC LID

Passivated emitter and rear cells (PERC) offer theoretical cost advantages relative to ubiquitous aluminum back-surface field (Al-BSF) devices [200]. However, PERC devices incorporating certain types of *p*-type multicrystalline silicon (mc-Si) wafers exhibit light-induced degradation (LID), in severe cases reducing power output at the maximum power point (MPP) by more than 10% relative. Developing engineering solutions and identifying the root causes for this LID may accelerate industrial adoption of PERC, with projected manufacturing cost savings (\$/W).

Ramspeck *et al.* [201] observed LID in *p*-type mc-Si PERC, exacerbated by elevated temperatures between 50 and 95°C. The authors ruled out boron-oxygen (B-O) and iron-boron ( $\text{Fe}_i\text{-B}_s$ ) point defects as root causes for this LID by replacing boron doping with gallium and observing the persistence of the LID. A material dependence

was observed: LID was most pronounced in mc-Si, less pronounced in seeded cast monocrystalline Si (although significant variation between different cast monocrystalline Si was observed), and least pronounced in monocrystalline silicon grown by the Czochralski method (Cz-Si).

Fertig *et al.* [202] and Krauß *et al.* [203] quantified the power loss due to LID in PERC, metal wrap-through (MWT) [204], and Al-BSF devices. They found that degradation was most pronounced for PERC, weaker for MWT, and weakest for Al-BSF. The authors hypothesized that the observed LID was due to degradation of the alumina ( $\text{AlO}_x$ ) surface passivation quality. Further, Krauß *et al.* [203] noted that local degradation appeared stronger in areas of high dislocation density.

Kersten *et al.* [205] observed stronger LID in *p*-type mc-Si PERC devices than in both mc-Si and Cz-Si Al-BSF devices as well as *p*-type Cz-Si PERC. They also noted larger power loss when light soaking at higher temperatures. Regarding root cause, they observed no clear correlation between LID and interstitial oxygen concentration, contrary to previous observations of the B-O defect. The maximum degradation and the degradation rate were also inconsistent with dissociation of  $\text{Fe}_i\text{-B}_s$  pairs. In contrast to the hypothesis from Fertig *et al.* and Krauß *et al.*, they observed similar degradation of minority-carrier lifetime for both  $\text{AlO}_x$ /silicon nitride ( $\text{SiN}_x$ ) stacks and  $\text{SiN}_x$  alone, suggesting a degradation of bulk lifetime instead of surface passivation. They were light-soaked at different conditions, corresponding (from low to high) to short-circuit current, MPP, and open-circuit voltage conditions, and observed increased degradation with increasing injection level. They further observed similar degradation for devices illuminated at MPP and devices held in the dark and injected with current equivalent to MPP. Thus, excess electron density – and not a property unique to light – was implicated as the key to activating the degradation. The authors also observed a regeneration of the defect after extended exposure to illumination and elevated temperature. Finally, they noted that with “defect engineering,” they were able to reduce the degradation to <1% (relative) over 1000 hours of illumination at elevated temperature.

In summary, several researchers have reported LID in *p*-type mc-Si PERC during

the last year that exhibit the following similarities: (1) module power loss to LID in  $p$ -type PERC is more severe for mc-Si substrates than Cz, and (2) time constants across several papers are distinct from well-known  $\text{Fe}_i$ - $\text{B}_s$  and B-O defect kinetics. The LID reported by different researchers may have similar or different origins, as there are likely uncontrolled variations in mc-Si wafer quality, cell processing conditions, device architectures, and LID generation conditions.

When untreated, light-induced degradation (LID) of  $p$ -type multicrystalline silicon-based PERC modules can reduce power output by up to 10% relative during the first fifty-six days of sun soaking under open-circuit conditions. Herein are presented new observations of similar LID in industrial mc-Si PERC modules and cells. In this contribution, it is determined that LID in test modules has a strong bulk component, which spatially resolved lifetime measurements indicate is ubiquitously distributed across the wafer. Injection-dependent lifetime spectroscopy is applied to elucidate the underlying root cause of LID in  $p$ -type mc-Si PERC, and the analysis indicates that the recombination-active state has an electron-to-hole capture cross section ratio of  $\sim 28.5$ . This is evidence for a deep-level donor defect, including Ti, Mo, W, and charged nanoprecipitates.

## 10.2 Root-cause analysis for PERC LID

### 10.2.1 The case for a ubiquitous, bulk point defect

Microwave photoconductivity decay ( $\mu$ -PCD, 905 nm laser, 300 K, 1 mm step size,  $\sim 10^{16}$  carriers/cm<sup>3</sup>/s) lifetime maps of semifabricates at several different steps in the process reveal that the lifetime degradation appears to occur fairly ubiquitously, supporting the hypothesis that a bulk point defect that is spread relatively homogeneously throughout the wafer is responsible for the LID.

## 10.2.2 Defect Identification Using Injection-Dependent Lifetime Spectroscopy

It is hypothesized that this LID defect can be identified by lifetime spectroscopy. Murphy *et al.* [69] proposed a parameterized Shockley-Read-Hall [36, 37] recombination model for defects in silicon that enables the extraction of electron to hole capture cross-section ratio,  $k$ , as a function of defect energy,  $E$ , from injection-dependent lifetime data.

Here, this lifetime spectroscopy method is applied to identify which defect(s) might be causing the LID observed in wafers that were fired at high temperature and subsequently degraded after light- or sun-soaking. The method is applied to undegraded and degraded wafers with the emitter and dielectrics that were present during firing still intact. The injection-dependent quasi-steady-state photoconductivity (QSSPC) lifetime, alternatively known as injection-dependent lifetime spectroscopy (IDLS), is measured. The SRH (bulk) lifetime as a function of injection level is estimated by removing the emitter recombination using the  $J_{0e}$  approach described by Cuevas [206] and removing the contribution of the intrinsic recombination (radiative and Auger) using Richter's model [70]. The undegraded wafer shows a  $J_{0e} = 5.75 \times 10^{-14}$  A/cm<sup>2</sup> and the degraded wafer had a  $J_{0e} = 4.76 \times 10^{-14}$  A/cm<sup>2</sup>.

In Fig. 10-1, the extracted SRH lifetime is shown as a function of the parameter,  $X$ , which is the ratio of electrons to holes at each injection level [69]. The curve clearly shows a non-linear behavior, indicating the presence of more than one lifetime-limiting defect. Fitting for two defects (the sum of two lines) produces a good fit in both samples. Note that these fits are not unique because one lifetime curve at a single doping level and temperature was fit. Additionally, it is possible to fit an arbitrary number of defects. The lifetime as a function of  $X$  for each state is shown for the two defects, and the reciprocal combination of the two defects is also shown. The reciprocal combination (solid line) fits the SRH lifetime (blue open circles) data well. The mean squared error is  $2.54 \mu\text{s}^2$  for the degraded wafer,  $4.59 \times 10^{-3} \mu\text{s}^2$  for the undegraded wafer. In both wafers there seems to be a dominant defect (dashed) that

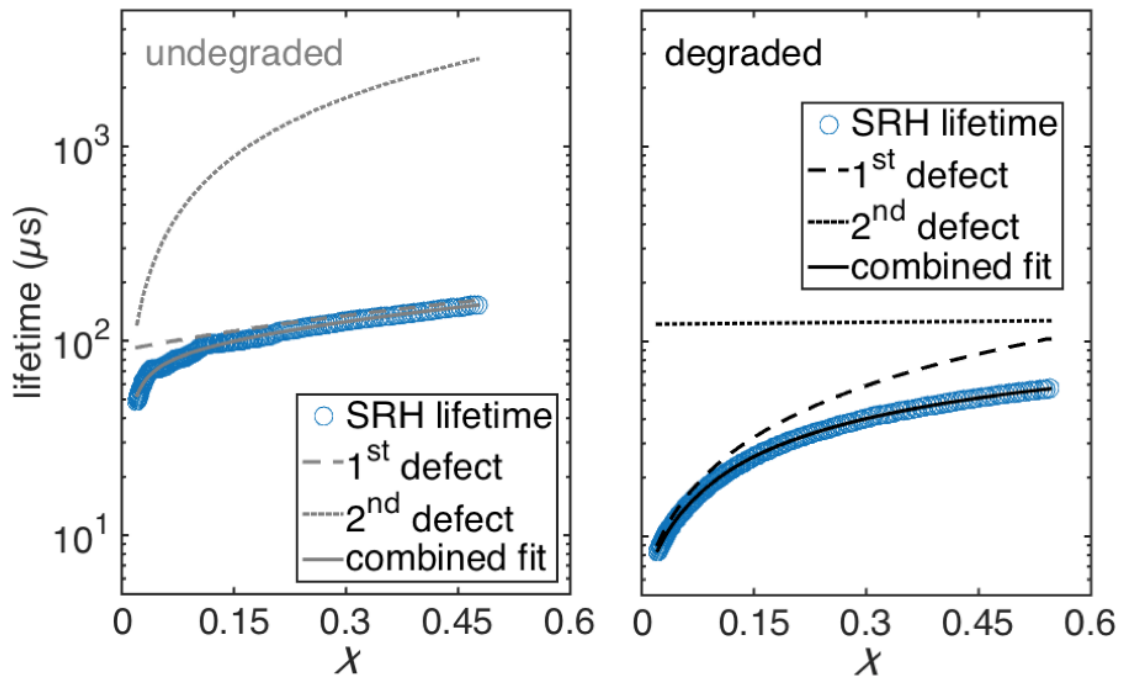


Figure 10-1: SRH lifetime data (blue open circles) for wafers fired at  $950^{\circ}\text{C}$  with emitter and dielectrics intact. Parameterized fits assuming two defects for the undegraded (left) and degraded (right) states are shown. The dominant defects (dashed) and secondary defects (dotted) and their reciprocal combination (solid) are shown for each state. The locations of the regions measured with QSSPC are marked on the  $\mu$ -PCD maps shown in Fig. 10-1.

closely follows the SRH lifetime data and a secondary (dotted) defect that together limit the lifetime. There appear to be at least three distinct defects: (1) the secondary defect in the undegraded state, (2) the primary defect in the degraded state, and (3) the primary defect in the undegraded state, which may be the same defect as the secondary defect in the degraded state.

For the dominant defect curve (dashed line) in each state,  $k$  as a function of  $E$  is calculated by solving the parameterized SRH equations [69] with known inputs including the equilibrium carrier concentrations, carrier thermal velocities, and the densities of states for the conduction and valence bands. The resulting curves are shown in Figure 10-2. Defects with values of  $k$  and  $E$  available in the literature [33, 93, 207–214] are plotted with the curves. Other defects with parameters available in the literature that lie outside the bounds of the axes in Fig. 10-2 do not lie near the calculated curves and are thus excluded. Defects that are close to the degraded curve are labeled with black text.

This analysis indicates that in the undegraded state, the dominant defect either has electron and hole capture cross sections that are symmetric ( $k \sim 1.4$ ) or is very close to the valence band. Conversely, the dominant defect characterized in the degraded sample has a ratio of electron to hole capture cross-sections  $\sim 28.5$ . Some candidates for lifetime-limiting impurities in the degraded state include the Ti double donor, the Mo donor, and the W donor. In addition, charged nanoprecipitates [215] and extended defects, including dislocations [216], have also been known to exhibit similarly large  $k$  values.

### 10.3 Discussion

The extrinsic impurity atoms identified in the IDLS analysis ( $k \sim 28.5$ , *i.e.*,  $\text{Ti}_i$ ,  $\text{Mo}_i$ ,  $\text{W}_s$ ) diffuse slowly in silicon especially at temperatures between 60–200°C. Therefore, it is unlikely that the defect that causes LID involves significant diffusion of these species — although they may still be involved as mostly static atoms. In light of this information and to inspire further experiments, possible root causes of LID that

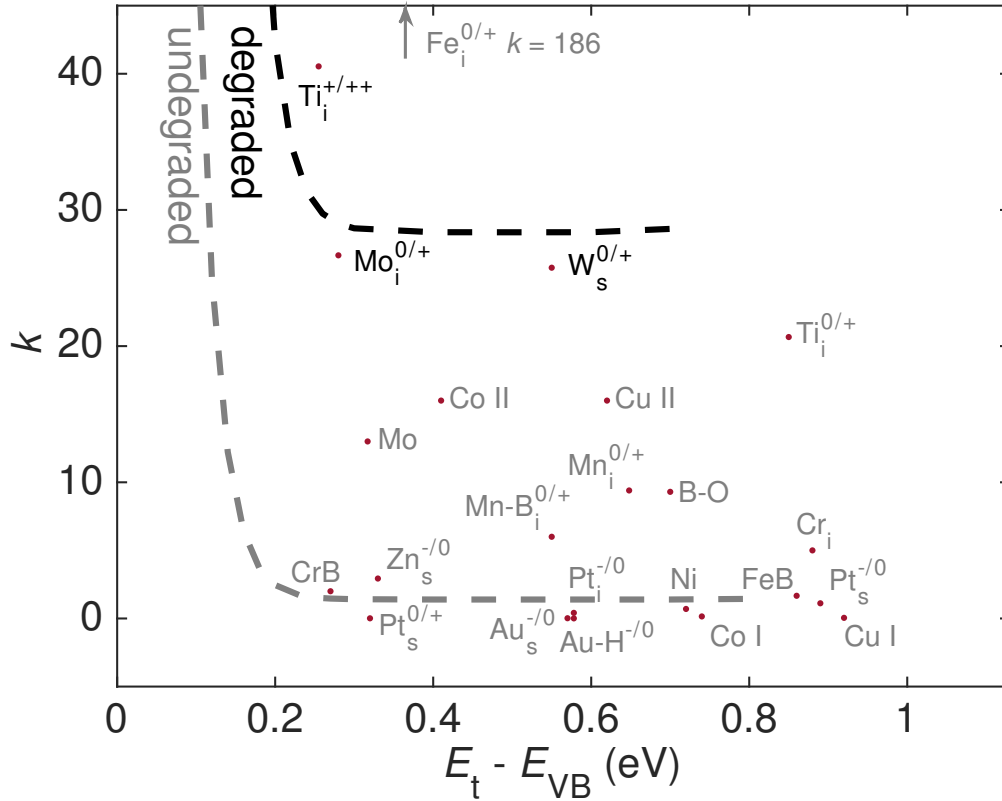


Figure 10-2: Capture cross-section ratio,  $k$ , as a function of energy level above the valence band for the dominant defects in the 950°C firing condition in the undegraded and degraded states. For energy levels between 0.3 and 0.8 eV above the valence band, the undegraded state has a  $k \sim 1.4$  while the degraded state has a  $k \sim 28.5$ . Defects with parameters from literature are plotted with red dots and labeled in either gray or black. Black labeled defects are possible candidates for the root cause of the LID observed in this work.

appear to be consistent with experimental observations are discussed.

### 10.3.1 The case for a metastable deep-level donor

To review the principal observations from previous sections, the PERC LID observed in our study appears to have a strong bulk component.  $\mu$ -PCD lifetime mapping reveals uniform lifetime degradation during LID, suggesting a ubiquitous defect consistent with a point defect. SRH lifetime spectroscopy analysis indicates the best fit for the dominant defect in the degraded state has a  $k \sim 28.5$ .

This high  $k$  value suggests a positively charged defect (*e.g.*, ionized donor or charged nanoprecipitate), to which negatively charged minority carriers in  $p$ -type silicon experience a Coulombic attraction. If an impurity is involved, the electrically active impurity concentration in the finished device would depend on the as-grown impurity concentration in the wafer, and the effectiveness of gettering, firing, and passivation.

### 10.3.2 Possible root causes for LID

While it is not possible to confidently pinpoint the defect responsible for LID with the available data, the analysis constrains the range of possible solutions based on our observations, especially the  $k$ - $E_t$  relationships shown in Figure 10-2.

The range of possible root causes of  $p$ -type mc-Si PERC LID in our samples are constrained, based on the observations, especially the  $k$ - $E_t$  relationships shown in Figure 10-2. One possible working hypothesis that is consistent with these experimental data is presented. First, it is observed that the electron quasi Fermi energy (*i.e.*, excess electron density) is higher at the open-circuit condition in a PERC than in an Al-BSF cell, thus deep-level donor states have a higher probability of being occupied, *i.e.*, in a neutral charge state. The point defects identified in Figure 10-2 are too slowly diffusing to move at temperatures below 100°C, during sun- or light-soaking. However, after metallization firing, hydrogen is released from the SiNx layer into the bulk. Hydrogen is known to passivate bulk defects, shifting their defect levels and



reducing their capture cross sections. One possible hypothesis for LID, is that as the electron quasi Fermi energy approaches the conduction band at illuminated open-circuit condition in a PERC, the charge state of one or more of the atoms involved in this passivated complex changes, resulting in the hydrogen dissociating from the deep-level defect reducing defect passivation. If this model holds, then LID can be minimized by increasing wafer purity, or by increasing the amount of hydrogen released into the wafer (lower metallization firing temperatures). Note that in certain defect-rich regions (e.g., dislocation clusters in Figure 1), LID is observed, consistent with a weaker hydrogenation effect in these regions. It is conceivable that further experiments involving intentional contamination, hydrogen passivation, or complete lack thereof, and temperature-dependent lifetime spectroscopy are likely to identify not one, but a family of related PERC LID defects with similar underlying mechanisms. The role of the higher injection level (excess electron density) in PERC relative to Al-BSF cells at MPP and open-circuit voltage is likely to play a role.

In the following, two working hypotheses (conjectures) that are consistent with the experimental data are presented. Both possibilities rely on the fact that the electron quasi Fermi energy (*i.e.*, excess electron density) is higher at the open-circuit condition in a PERC than in an Al-BSF cell [64], thus deep-level donor states have a higher probability of being occupied, *i.e.*, in a neutral charge state. When the sample is held in the dark at open-circuit, the electron quasi Fermi energy level moves toward midgap, and deep-level donor point defects have a higher probability of being in a positive charge state. Annealing at 200°C provides the thermal activation energy necessary for diffusion and/or configurational changes to occur reversibly.

## 10.4 Conclusions

To elucidate the root cause(s) of PERC LID, experiments with semifabricates and light-soaking are conducted. The solution space is constrained based on the observations. In the degraded state, injection-dependent lifetime spectroscopy identifies an asymmetry of electron and hole capture cross sections of  $k \sim 28.5$  for the dominant

defect. These data are consistent with deep-level donor point defects, charged nanoprecipitates [215], or charged structural defects, such as dislocations [216]. Higher injection levels at the open-circuit condition in PERC relative to Al-BSF may help explain the larger LID in mc-Si PERC. As device architectures improve and wafer thicknesses decrease, higher injection levels are expected, suggesting that a continuously improving LID mitigation strategy may be advised.

# Chapter 11

## Outlook and Implications: Vertically-Integrated Defect Engineering in Crystalline Silicon PV

To significantly contribute to reducing anthropogenic carbon emissions, the cost of photovoltaics needs to continue decreasing. Progress requires a balance between high-efficiency devices and low-cost materials, processing, and capital expenditures. Extensive research enabled the development of metal defect process simulations and engineering guidelines for *p*-type mc-Si, pushing the material performance close to its intrinsic limit. However, the industry is investigating alternative wafer materials that offer a higher efficiency-to-cost ratio. *n*-type mc-Si is one “drop-in” replacement candidate that has the potential to meet these criteria.

The material characterization techniques, processing approaches, and simulation tools that enabled the dominance of *p*-type mc-Si were applied to the investigation of *n*-type mc-Si. The similarities and differences in the gettering of metals and their electrical impact in *n*- and *p*-type Si were identified and quantified. A combined solar cell process and lifetime simulation tool for *n*- and *p*-type Si was developed. The key contributions of this research include:

- Deepening understanding of the effect of as-grown impurity distribution and

solar cell processing parameters on metal impurity redistribution. A 2D tool in Sentaurus TCAD software enables visualization of the metal distribution after processing and the corresponding recombination activity through the wafer cross section.

- A review of the state-of-the-art of crystalline silicon solar cell process simulation tools. A single tool that organized and combined the features of already-published models was constructed. Leveraging the combined simulation tool, the side-by-side solar cell process simulation analysis elucidated the key physics of impurity gettering during solar cell processing and enabled guidelines for efficient, yet accurate, solar cell process simulation.
- Directly showing that redistribution of metal impurities during phosphorus diffusion gettering is similar in *n*- and *p*-type mc-Si. Direct measurement of precipitated metals at a grain boundary in *n*-type mc-Si using  $\mu$ -XRF mapping showed that precipitates of fast-diffusing species such as copper, nickel, and cobalt are readily removed by gettering and that full removal of Fe-rich precipitates requires and can be achieved with higher-temperature processing. Additionally, the enhanced growth and dissolution of metal-rich precipitates observed in *p*-type mc-Si was observed in and modeled for *n*-type mc-Si. Temperature-dependent Fermi-level analysis shows that the fundamental driving force of these phenomena are similar at high process temperature because *n*- and *p*-type Si with doping levels relevant to PV are both electrically intrinsic at gettering temperature. This study confirmed that the kinetics simulation tools and processing guidelines developed for *p*-type mc-Si are directly applicable to *n*-type mc-Si.
- Quantifying the recombination activity of individual iron-rich precipitates in *n*-type crystalline silicon. The iron content and recombination strength of over eighty individual Fe-rich precipitates in an *n*-type crystalline silicon sample were quantitatively mapped. To enable this study, a new high-throughput synchrotron-based data collection mode called on-the-fly scanning was bench-

marked and used to generate a  $\mu$ -XRF map of a large sample region. Iron-containing precipitates were found to be highly recombination active in  $n$ -type Si, and the recombination strength is positively correlated with its size.

- A simulation tool for both  $p$ - and  $n$ -type Si that calculates the redistribution of iron throughout the solar cell process and the resulting injection-dependent minority carrier lifetime.
- Processing guidelines for  $n$ - and  $p$ -type Si solar cells. Injection-dependent sensitivity analysis revealed that, unlike in  $p$ -type mc-Si, controlling Fe-rich precipitates by dissolving them during high temperature processing is often required to maximize the performance of  $n$ -type mc-Si. Efficiency entitlement curves predict that  $n$ -type mc-Si can support 20% efficient solar cells.
- Quantified recombination parameters for defect responsible for light-induced degradation in  $p$ -type mc-Si PERC modules. The understanding of defects developed for Si wafers was applied to analysis of PV modules. Leveraging the injection-dependent lifetime signature of impurities in Si wafers, the recombination parameters, including the energy level and capture cross-section ratio of the root-cause defect complex were extracted and quantified.

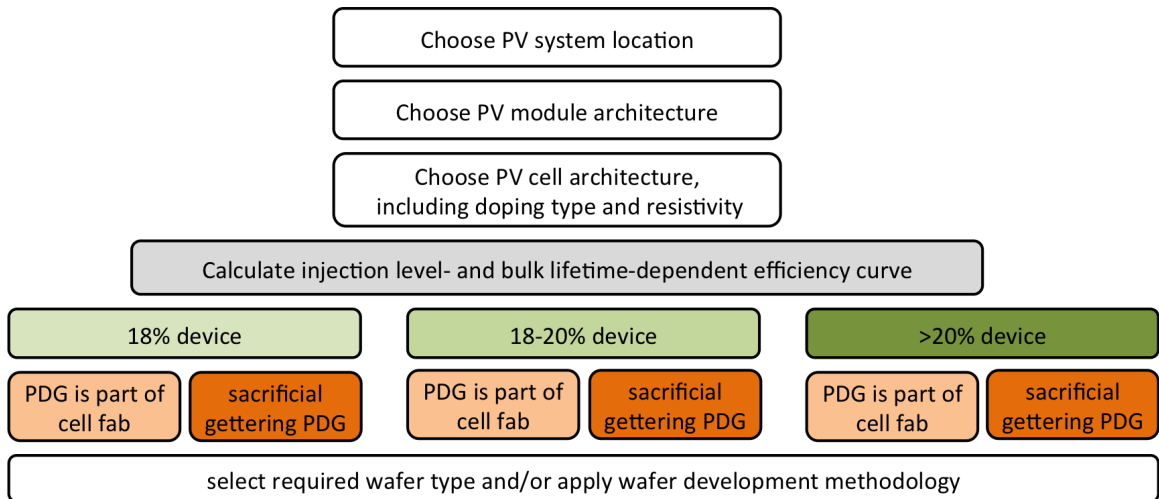
This thesis further develops the defect engineering framework developed for  $p$ -type crystalline silicon materials for PV and extends it to  $n$ -type Si. It explicitly addresses the importance of injection level and defects related to light-induced degradation. Figs. 11-1a and 11-1b illustrate a vertically-integrated approach to photovoltaics system design with emphasis on wafer-level defect management.

Defect considerations start at the system level and propagate all the way down to the nanoscale of impurity precipitates and crystal defects. The PV system level flowchart is in Fig. 11-1a. After PV has been identified as the appropriate energy generation technology, a PV system location or application is chosen, an appropriate module architecture must be selected. Next, an applicable cell architecture, including the doping type ( $n$  or  $p$ ) and level (resistivity) should be defined and the corresponding

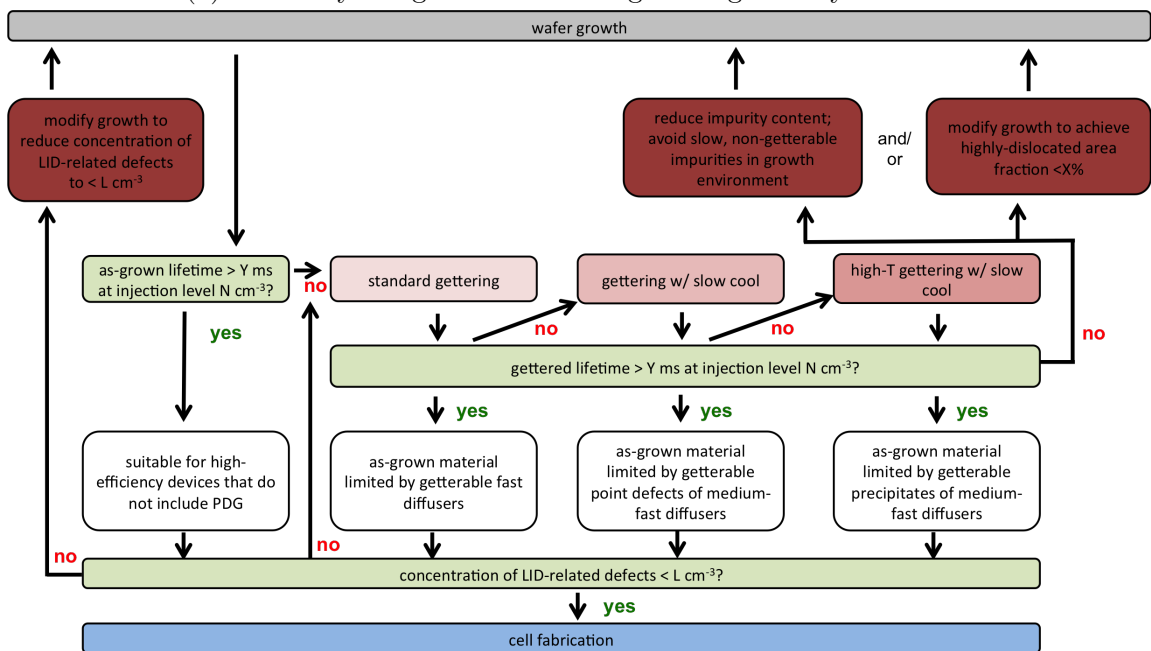
efficiency entitlement curve (as shown in Chapters 2 and 9 and first developed in [217]) should be calculated. The target efficiency, informed by cost targets, should be chosen, thus defining the minimum injection-dependent lifetime. Then, depending on whether or not gettering is an inherent part of the cell process, the wafer can be specified and either purchased or designed using the wafer development methodology illustrated in Fig. 11-1a.

At the wafer level, for a given combination of module operation conditions, solar cell architecture, and desired efficiency, a wafer must be designed that has a concentration of LID-related defects less than a critical value  $L \text{ cm}^{-3}$  and a minority carrier lifetime in the target injection range  $N \text{ cm}^{-3}$ . To fulfill these two requirements, material that meets these specifications can be grown, or material can be engineered through, for example, phosphorus diffusion gettering of various degrees. The impurity species, concentrations, and spatial and chemical distribution are important as is the interacting factor of dislocations. Overlaid but not explicitly accounted for in this flowchart is the constraint of cost. For example, higher quality growth environments and extended gettering can be effective and essential ways to achieve high-quality wafers, but these advanced processes also add expense.

This thesis focused on the spatial and chemical distribution, electrical impact, and phosphorus diffusion gettering of iron impurities in  $n$ - and  $p$ -type Si. While iron is often initially the limiting defect in mc-Si, there is much more to the picture. There are many important areas of future work. Continuing the comparison between the two doping types, quantifying the effect of hydrogenation on various defects in silicon materials is essential for maximizing lifetimes and also possibly limiting light-induced degradation. In addition to iron, other metals, including copper, nickel, cobalt, zinc, and titanium in either point defect or precipitated form likely impact efficiencies. In  $p$ -type Si, the boron-oxygen complex is an important well-studied non-metal defect. Further investigation into non-metal defects may be important to realizing the full potential of especially  $n$ -type mc-Si. In addition to impurities, structural defects are an important part of the picture especially in their interaction with impurities. All of the considerations above may also need to be revisited as new cell architectures and



(a) Vertically Integrated Defect Engineering: PV System Level



(b) Vertically Integrated Defect Engineering: Wafer Level. Flowchart guiding wafer development methodology. Flowchart inspired by [217].

Figure 11-1: Vertically Integrated Defect Engineering: from macro to nano

processes are developed.

Photovoltaics have an important role to play in the pursuit of a reduced-carbon energy supply. The dominant crystalline silicon is a proven, reliable technology that so far has best balanced cost and performance. Progress in the field continues from ever-increasing efficiencies in mass production to improvements in our understanding of the material at the atomic level. New promising Si wafer technologies are being proven at the cell level, including direct-from-melt and epitaxially-grown Si. *p*-type mc-Si, the workhorse of the PV industry, continues to steadily improve. The duration and share of the market enjoyed by *p*-type mc-Si and possible replacements, including *n*-type monocrystalline and multicrystalline silicon and *p*-type monocrystalline silicon is difficult to predict. This thesis provides tools and analysis that enable the assessment and processing of both improved and new crystalline silicon materials. The exact path the industry will take depends on timely proofs-of-concept from research laboratories; adoption and scaling by manufacturers; the cost of capital, raw materials, processing, and installation; the policy climate; and the economics of a renewables-rich electricity grid. It is an exciting and dynamic time for PV and for the energy sector as a whole.



# Bibliography

- [1] Oliver Morton. Solar energy: A new day dawning?: Silicon Valley sunrise. *Nature*, 443(7107):19–22, 2006.
- [2] Trends 2013 in Photovoltaic Applications Report IEA-PVPS T1-23:2013. Technical report, April 2014.
- [3] International Technology Roadmap for Photovoltaic (ITRPV) 2015 Results. pages 1–54, March 2016.
- [4] William Shockley and Hans J Queisser. Detailed Balance Limit of Efficiency of p-n Junction Solar Cells. *Journal of Applied Physics*, 32(3):510–10, 1961.
- [5] Vladimir Alekseenko and Alexey Alekseenko. Journal of Geochemical Exploration. *Journal of Geochemical Exploration*, 147(PB):245–249, December 2014.
- [6] Martin A Green, Keith Emery, Yoshihiro Hishikawa, Wilhelm Warta, and Ewan D Dunlop. Solar cell efficiency tables (Version 45). *Progress in Photovoltaics: Research and Applications*, 23(1):1–9, December 2014.
- [7] Fraunhofer Insititute for Solar Energy Systems. Photovoltaics Report. Technical report, March 2016.
- [8] A A Istratov, H Hieslmair, and E R Weber. Iron contamination in silicon technology. *Applied Physics A: Materials Science & Processing*, 70(5):489–534, 2000.
- [9] International Technology Roadmap for Photovoltaic (ITRPV) 2014 Results. pages 1–38, July 2015.
- [10] U.S. Energy Information Administration. Energy in brief: How much of our electricity is generated from renewable energy?, May 2013.
- [11] U.S. Energy Information Administration. Annual energy review table 10.1 renewable energy production and consumption by primary energy source, 1949-2011.
- [12] SunShot Vision Study. pages 1–320, February 2012.

- [13] Douglas M Powell, Mark T Winkler, Alan Goodrich, and Tonio Buonassisi. Modeling the Cost and Minimum Sustainable Price of Crystalline Silicon Photovoltaic Manufacturing in the United States. *IEEE Journal of Photovoltaics*, 3(2):662–668.
- [14] J E Cotter, J H Guo, P J Cousins, M D Abbott, F W Chen, and K C Fisher. P-Type Versus n-Type Silicon Wafers: Prospects for High-Efficiency Commercial Silicon Solar Cells. *Ieee Transactions on Electron Devices*, 53(8):1893–1901.
- [15] International Technology Roadmap for Photovoltaic (ITRPV) 2013 Results. pages 1–37, March 2014.
- [16] International Technology Roadmap for Photovoltaic (ITRPV) 2012 Results. pages 1–34, March 2013.
- [17] International Technology Roadmap for Photovoltaics (ITRPV) 2011 Results. pages 1–20, February 2013.
- [18] Douglas M Powell, Ran Fu, Kelsey Horowitz, Paul A Basore, Michael Woodhouse, and Tonio Buonassisi. Energy & Environmental Science. *Energy & Environmental Science*, 8:3395–3408, November 2015.
- [19] Y M Yang, A Yu, B Hsu, W C Hsu, A Yang, and C W Lan. Development of high-performance multicrystalline silicon for photovoltaic industry. *Progress in Photovoltaics: Research and Applications*, 23(3):340–351, October 2013.
- [20] Martin A Green, Keith Emery, Yoshihiro Hishikawa, Wilhelm Warta, and Ewan D Dunlop. Solar cell efficiency tables (version 43). *Progress in Photovoltaics: Research and Applications*, 22(1):1–9, December 2013.
- [21] G Coletti, R Kvande, V D Mihailetchi, L J Geerligs, L Arnberg, and E J Ovrelid. Effect of iron in silicon feedstock on p- and n-type multicrystalline silicon solar cells. *Journal of Applied Physics*, 104(10):104913, 2008.
- [22] A Cuevas, S Riepe, M J Kerr, D H Macdonald, G Coletti, and F Ferrazza. N-type multicrystalline silicon: a stable, high lifetime material. In *Photovoltaic Energy Conversion, 2003. Proceedings of 3rd World Conference on*, pages 1312–1315, 2003.
- [23] Tonio Buonassisi, Andrei A Istratov, Matthias Heuer, Matthew A Marcus, Ralf Jonczyk, Joerg Isenberg, Barry Lai, Zhonghou Cai, Steven Heald, Wilhelm Warta, Roland Schindler, Gerhard Willeke, and Eicke R Weber. Synchrotron-based investigations of the nature and impact of iron contamination in multicrystalline silicon solar cells. *Journal of Applied Physics*, 97(7):074901, 2005.
- [24] T Buonassisi, A A Istratov, M D Pickett, J P Rakotoniaina, O Breitenstein, M A Marcus, S M Heald, and E R Weber. Transition metals in photovoltaic-grade ingot-cast multicrystalline silicon: Assessing the role of impurities in silicon

- nitride crucible lining material. *Journal of Crystal Growth*, 287(2):402–407, January 2006.
- [25] Worth B Henley and Deepak A Ramappa. Iron precipitation in float zone grown silicon. *Journal of Applied Physics*, 82(2):589, 1997.
- [26] Erich Scheil. Bemerkungen zur schichtkristallbildung. *Zeitschrift für Metallkunde*, 34(3):70–72, 1942.
- [27] GH Gulliver. The quantitative effect of rapid cooling upon the constitution of binary alloys. *J. Inst. Met*, 9(1):120–157, 1913.
- [28] Daniel Macdonald, Andrés Cuevas, A Kinomura, Y Nakano, and L J Geerligs. Transition-metal profiles in a multicrystalline silicon ingot. *Journal of Applied Physics*, 97(3):033523, 2005.
- [29] Eicke R Weber. Transition metals in silicon. *Applied Physics A: Materials Science & Processing*, 30(1):1–22, 1983.
- [30] R Kvande, L J Geerligs, G Coletti, L Arnberg, M Di Sabatino, E J Ovrelid, and C C Swanson. Distribution of iron in multicrystalline silicon ingots. *Journal of Applied Physics*, 104(6):064905, 2008.
- [31] Mallory Ann Jensen, Jasmin Hofstetter, Ashley E Morishige, Gianluca Coletti, Barry Lai, David P Fenning, and Tonio Buonassisi. Synchrotron-based analysis of chromium distributions in multicrystalline silicon for solar cells. *Applied Physics Letters*, 106(20):202104, May 2015.
- [32] Ashley E Morishige, Hannu S Laine, Jonas Schön, Antti Haarahiltunen, Jasmin Hofstetter, Carlos del Cañizo, Martin C Schubert, Hele Savin, and Tonio Buonassisi. Building intuition of iron evolution during solar cell processing through analysis of different process models. *Applied Physics A: Materials Science & Processing*, 120(4):1357–1373, July 2015.
- [33] Jan Schmidt, Bianca Lim, Dominic Walter, Karsten Bothe, Sebastian Gatz, Thorsten Dullweber, and Pietro P Altermatt. Impurity-Related Limitations of Next-Generation Industrial Silicon Solar Cells. *IEEE Journal of Photovoltaics*, 3(1):114–118.
- [34] H J Queisser and E E Haller. Defects in semiconductors: some fatal, some vital. *Science*, 1998.
- [35] Martin A Green. *Solar cells. operating principles, technology, and system applications*. Prentice Hall, 1982.
- [36] W Shockley and W T Read, Jr. Statistics of the recombinations of holes and electrons. *Physical Review*, 1952.
- [37] R N Hall. Electron-hole recombination in germanium. *Physical Review*, 1952.

- [38] S Rein, T Rehr, W Warta, and S W Glunz. Lifetime spectroscopy for defect characterization: Systematic analysis of the possibilities and restrictions. *Journal of Applied Physics*, 91(4):2059, 2002.
- [39] Daniel Macdonald and L J Geerligs. Recombination activity of interstitial iron and other transition metal point defects in p- and n-type crystalline silicon. *Applied Physics Letters*, 85(18):4061, 2004.
- [40] Paul Gundel, Martin C Schubert, Friedemann D Heinz, Wolfram Kwapil, Wilhelm Warta, Gema Martinez-Criado, Manfred Reiche, and Eicke R Weber. Impact of stress on the recombination at metal precipitates in silicon. *Journal of Applied Physics*, 108(10):103707, 2010.
- [41] S Martinuzzi, O Palais, and S Ostapenko. Scanning techniques applied to the characterisation of P and N type multicrystalline silicon. *Materials Science in Semiconductor Processing*, 9(1-3):230–235, February 2006.
- [42] Martin Kittler, Winfried Seifert, and Klaus Knobloch. Influence of contamination on the electrical activity of crystal defects in silicon. *Microelectronic Engineering*, 66(1-4):281–288, April 2003.
- [43] L J Geerligs, Y Komatsu, I Röver, K Wambach, I Yamaga, and T Saitoh. Precipitates and hydrogen passivation at crystal defects in n- and p-type multicrystalline silicon. *Journal of Applied Physics*, 102(9):093702, 2007.
- [44] J Schön, F Schindler, W Kwapil, M Knörlein, P Krenckel, S Riepe, W Warta, and M C Schubert. Solar Energy Materials & Solar Cells. *Solar Energy Materials and Solar Cells*, pages 1–9, July 2015.
- [45] D P Fenning, A S Zuschlag, M I Bertoni, B Lai, G Hahn, and T Buonassisi. Improved iron gettering of contaminated multicrystalline silicon by high-temperature phosphorus diffusion. *Journal of Applied Physics*, 113(21):214504–214504, 2013.
- [46] Scott A McHugo. Release of metal impurities from structural defects in polycrystalline silicon. *Applied Physics Letters*, 71(14):1984, 1997.
- [47] Tonio Buonassisi, Matthew A Marcus, Andrei A Istratov, Matthias Heuer, Theodore F Ciszek, Barry Lai, Zhonghou Cai, and Eicke R Weber. Analysis of copper-rich precipitates in silicon: Chemical state, gettering, and impact on multicrystalline silicon solar cell material. *Journal of Applied Physics*, 97(6):063503, 2005.
- [48] T Buonassisi, A A Istratov, S Peters, C Ballif, J Isenberg, S Riepe, W Warta, R Schindler, G Willeke, Z Cai, B Lai, and E R Weber. Impact of metal silicide precipitate dissolution during rapid thermal processing of multicrystalline silicon solar cells. *Applied Physics Letters*, 87(12):121918, 2005.

- [49] T Buonassisi, A A Istratov, M A Marcus, Matthias Heuer, Matthew D Pickett, Barry Lai, Zhonghou Cai, Steven M Heald, and Eicke R Weber. Local measurements of diffusion length and chemical character of metal clusters in multicrystalline silicon. *Solid State Phenomena*, 108-109:577–584, 2005.
- [50] D P Fenning, J Hofstetter, M I Bertoni, G Coletti, B Lai, C del Cañizo, and T Buonassisi. Precipitated iron: A limit on gettering efficacy in multicrystalline silicon. *Journal of Applied Physics*, 113(4):044521, 2013.
- [51] Ronald A Sinton and Andrés Cuevas. Contactless determination of current–voltage characteristics and minority-carrier lifetimes in semiconductors from quasi-steady-state photoconductance data. *Applied Physics Letters*, 69(17):2510, 1996.
- [52] Steven W Johnston, Nathan J Call, Bill Phan, and Richard K Ahrenkiel. Applications of imaging techniques for solar cell characterization. In *34th IEEE Photovoltaic Specialists Conference*, pages 000276–000281. IEEE, 2009.
- [53] O Breitenstein, J Bauer, M Kittler, T Arguirov, and W Seifert. EBIC and luminescence studies of defects in solar cells. *Scanning*, 30(4):331–338, January 2008.
- [54] Martin C Schubert, Holger Habenicht, and Wilhelm Warta. Imaging of Metastable Defects in Silicon. *IEEE Journal of Photovoltaics*, 1(2):168–173, April 2011.
- [55] G Zoth and W Bergholz. A fast, preparation-free method to detect iron in silicon. *Journal of Applied Physics*, 67(11):6764–6771, 1990.
- [56] A A Istratov, H Hieslmair, and E R Weber. Iron and its complexes in silicon. *Applied Physics A: Materials Science & Processing*, 69(1):13–44, 1999.
- [57] Dominique Gilles, W Schröter, and W Bergholz. Impact of the Electronic-Structure on the Solubility and Diffusion of 3d Transition-Elements in Silicon. *Physical Review B*, 41(9):5770–5782, 1990.
- [58] A Haarahiltunen, H Savin, M Yli-Koski, H Talvitie, and J Sinkkonen. Modeling phosphorus diffusion gettering of iron in single crystal silicon. *Journal of Applied Physics*, 105(2):023510, 2009.
- [59] J Hofstetter, D P Fenning, M I Bertoni, J F Lelièvre, C del Cañizo, and T Buonassisi. Impurity-to-efficiency simulator: predictive simulation of silicon solar cell performance based on iron content and distribution. *Progress in Photovoltaics: Research and Applications*, 19(4):487–497, 2011.
- [60] David P Fenning, Jasmin Hofstetter, Ashley E Morishige, Douglas M Powell, Annika Zuschlag, Giso Hahn, and Tonio Buonassisi. Darwin at High Temperature: Advancing Solar Cell Material Design Using Defect Kinetics Simulations

- and Evolutionary Optimization. *Advanced Energy Materials*, 4(13):1400459, May 2014.
- [61] Ville Vähänissi, Marko Yli-Koski, Antti Haarahiltunen, Heli Talvitie, Yameng Bao, and Hele Savin. Solar Energy Materials & Solar Cells. *Solar Energy Materials and Solar Cells*, 114(C):54–58, July 2013.
- [62] S M Myers, M Seibt, and W Schröter. Mechanisms of transition-metal gettering in silicon. *Journal of Applied Physics*, 88(7):3795, 2000.
- [63] Martin A Green. Solar Energy Materials & Solar Cells. *Solar Energy Materials and Solar Cells*, 143(C):190–197, December 2015.
- [64] Jasmin Hofstetter, Carlos del Cañizo, Hannes Wagner, Sergio Castellanos, and Tonio Buonassisi. Material requirements for the adoption of unconventional silicon crystal and wafer growth techniques for high-efficiency solar cells. *Progress in Photovoltaics: Research and Applications*, 24(1):122–132, October 2015.
- [65] S Gatz, K Bothe, J Müller, T Dullweber, and R Brendel. Analysis of local Al-doped back surface fields for high efficiency screen-printed solar cells. *Energy Procedia*, 2011.
- [66] Pietro P Altermatt. Models for numerical device simulations of crystalline silicon solar cells—a review. *Journal of Computational Electronics*, 10(3):314–330, July 2011.
- [67] Wolfram Kwapil, Jonas Schön, Florian Schindler, Wilhelm Warta, and Martin C Schubert. Impact of Iron Precipitates on Carrier Lifetime in As-Grown and Phosphorus-Gettered Multicrystalline Silicon Wafers in Model and Experiment. *IEEE Journal of Photovoltaics*, 4(3):791–798.
- [68] Wolfram Kwapil, Jonas Schön, Wilhelm Warta, and Martin C Schubert. Carrier Recombination at Metallic Precipitates in p-and n-Type Silicon. *IEEE Journal of Photovoltaics*, 5(5):1285–1292.
- [69] J D Murphy, K Bothe, R Krain, V V Voronkov, and R J Falster. Parameterisation of injection-dependent lifetime measurements in semiconductors in terms of Shockley-Read-Hall statistics: An application to oxide precipitates in silicon. *Journal of Applied Physics*, 111(11):113709, 2012.
- [70] A Richter, F Werner, A Cuevas, J Schmidt, and S W Glunz. Improved Parameterization of Auger Recombination in Silicon. *Energy Procedia*, 27:88–94, January 2012.
- [71] Ashley E Morishige, Hannes Wagner, Jasmin Hofstetter, Ibrahim Avci, Carlos del Cañizo, and Tonio Buonassisi. ScienceDirect. *Energy Procedia*, 77:119–128, August 2015.

- [72] Thorsten Trupke, Jørgen Nyhus, and Jonas Haunschild. Luminescence imaging for inline characterisation in silicon photovoltaics. *physica status solidi (RRL) - Rapid Research Letters*, 5(4):131–137, February 2011.
- [73] Jonas Haunschild, Isolde E Reis, Teodora Chipei, Matthias Demant, Benjamin Thaidigsmann, Michael Linse, and Stefan Rein. Solar Energy Materials & Solar Cells. *Solar Energy Materials and Solar Cells*, 106(C):71–75, November 2012.
- [74] Ronald A Sinton, Jonas Haunschild, Matthias Demant, and Stefan Rein. Comparing lifetime and photoluminescence imaging pattern recognition methodologies for predicting solar cell results based on as-cut wafer properties. *Progress in Photovoltaics: Research and Applications*, 21(8):1634–1639, July 2012.
- [75] H Wagner, M Müller, G Fischer, and P P Altermatt. A simple criterion for predicting multicrystalline Si solar cell performance from lifetime images of wafers prior to cell production. *Journal of Applied Physics*, 114(5):054501, 2013.
- [76] O Schultz, S W Glunz, S Riepe, and G P Willeke. High-efficiency solar cells on phosphorus gettered multicrystalline silicon substrates. *Progress in Photovoltaics: Research and Applications*, 14(8):711–719, 2006.
- [77] Y M Yang, A Yu, B Hsu, W C Hsu, A Yang, and C W Lan. Development of high-performance multicrystalline silicon for photovoltaic industry. *Progress in Photovoltaics: Research and Applications*, 23(3):340–351, October 2013.
- [78] Jasmin Hofstetter, David P Fenning, Douglas M Powell, Ashley E Morishige, Hannes Wagner, and Tonio Buonassisi. Sorting Metrics for Customized Phosphorus Diffusion Gettering. *IEEE Journal of Photovoltaics*, 4(6):1421–1428, April 2014.
- [79] P Pichler. Intrinsic Point Defects. *Intrinsic Point Defects*, 2004.
- [80] Synopsys, Inc. Sentaurus Process User Guide. *Sentaurus Process User Guide*, pages 1–1038, November 2010.
- [81] Synopsys, Inc. Sentaurus Device User Guide. *Sentaurus Device User Guide*, pages 1–1284, October 2010.
- [82] Hannes Wagner, Tobias Ohrdes, Amir Dastgheib-Shirazi, Binesh Puthen-Veetil, Dirk König, and Pietro P Altermatt. A numerical simulation study of gallium-phosphide/silicon heterojunction passivated emitter and rear solar cells. *Journal of Applied Physics*, 115(4):044508, January 2014.
- [83] A Bentzen, A Holt, R Kopecek, G Stokkan, J S Christensen, and B G Svensson. Gettering of transition metal impurities during phosphorus emitter diffusion in multicrystalline silicon solar cell processing. *Journal of Applied Physics*, 99(9):093509, 2006.

- [84] Jonas Schön, A Haarahiltunen, H Savin, D P Fenning, T Buonassisi, W Warta, and M C Schubert. Analyses of the Evolution of Iron-Silicide Precipitates in Multicrystalline Silicon During Solar Cell Processing. *IEEE Journal of Photovoltaics*, 3(1):131–137, April 2013.
- [85] D Macdonald, T Roth, P N K Deenapanray, T Trupke, and R A Bardos. Doping dependence of the carrier lifetime crossover point upon dissociation of iron-boron pairs in crystalline silicon. *Applied Physics Letters*, 89(14):142107, 2006.
- [86] D Macdonald, J Tan, and T Trupke. Imaging interstitial iron concentrations in boron-doped crystalline silicon using photoluminescence. *Journal of Applied Physics*, 103(7):073710, 2008.
- [87] Jasmin Hofstetter, Jean-François Lelièvre, David P Fenning, Mariana I Bertoni, Tonio Buonassisi, Antonio Luque, and Carlos del Cañizo. Enhanced iron gettering by short, optimized low-temperature annealing after phosphorus emitter diffusion for industrial silicon solar cell processing. *physica status solidi (c)*, 8(3):759–762, January 2011.
- [88] Silvaco, Inc. Atlas User’s Manual. *Atlas User’s Manual*, November 2014.
- [89] D A Clugston and P A Basore. PC1D version 5: 32-bit solar cell modeling on personal computers. In *Proceedings of the 26th IEEE PVSC*, pages 207–210, Anaheim, 1997.
- [90] P A Basore and K Cabanas-Holmen. PC2D: A Circular-Reference Spreadsheet Solar Cell Device Simulator. *IEEE Journal of Photovoltaics*, 1(1):72–77, 2011.
- [91] Yiming Liu, D Heinzl, and A Rockett. A revised version of the AMPS simulation code. In *Proceedings of the 35th IEEE PVSC*, pages 001943–001947, Honolulu, June 2010.
- [92] Marc Burgelman, Johan Verschraegen, Stefaan Degraeve, and Peter Nollet. Modeling thin-film PV devices. *Progress in Photovoltaics: Research and Applications*, 12(23):143–153, March 2004.
- [93] Gianluca Coletti. Sensitivity of state-of-the-art and high efficiency crystalline silicon solar cells to metal impurities. *Progress in Photovoltaics: Research and Applications*, 21:1163–1170, 2013.
- [94] A A Istratov, T Buonassisi, R J McDonald, A R Smith, R Schindler, J A Rand, J P Kalejs, and E R Weber. Metal content of multicrystalline silicon for solar cells and its impact on minority carrier diffusion length. *Journal of Applied Physics*, 94(10):6552, 2003.
- [95] T Buonassisi, A A Istratov, M D Pickett, M Heuer, J P Kalejs, G Hahn, M A Marcus, B Lai, Z Cai, S M Heald, T F Cizek, R F Clark, D W Cunningham,



- A M Gabor, R Jonczyk, S Narayanan, E Sauar, and E R Weber. Chemical natures and distributions of metal impurities in multicrystalline silicon materials. *Progress in Photovoltaics: Research and Applications*, 14(6):513–531, 2006.
- [96] S A McHugo, H Hieslmair, and E R Weber. Gettering of metallic impurities in photovoltaic silicon. *Applied Physics A: Materials Science & Processing*, 64(2):127–137, January 1997.
- [97] J Tan, D Macdonald, N Bennett, D Kong, A Cuevas, and I Romijn. Dissolution of metal precipitates in multicrystalline silicon during annealing and the protective effect of phosphorus emitters. *Applied Physics Letters*, 91(4):043505, 2007.
- [98] Wolfram Kwapil, Jonas Schön, Florian Schindler, Wilhelm Warta, and Martin C Schubert. Impact of Iron Precipitates on Carrier Lifetime in As-Grown and Phosphorus-Gettered Multicrystalline Silicon Wafers in Model and Experiment. *IEEE Journal of Photovoltaics*, 4(3):791–798, February 2014.
- [99] M Seibt, H Hedemann, Andrei A Istratov, F Riedel, A Sattler, and W Schröter. Structural and Electrical Properties of Metal Silicide Precipitates in Silicon. *physica status solidi (a)*, 171:301–310, January 1999.
- [100] Carlos del Cañizo and Antonio Luque. A Comprehensive Model for the Gettering of Lifetime-Killing Impurities in Silicon. *Journal of The Electrochemical Society*, 147(7):2685, 2000.
- [101] H Hieslmair, S Balasubramanian, A A Istratov, and E R Weber. Gettering simulator: physical basis and algorithm. *Semiconductor science and technology*, 16(7):567, 2001.
- [102] A L Smith, K Wada, and L C Kimerling. Modeling of Transition Metal Redistribution to Enable Wafer Design for Gettering. *Journal of The Electrochemical Society*, 147(3):1154, 2000.
- [103] A Haarahiltunen, H Savin, M Yli-Koski, H Talvitie, M I Asghar, and J Sinkkonen. As-grown iron precipitates and gettering in multicrystalline silicon. *Materials Science and Engineering: B*, 159-160:248–252, March 2009.
- [104] J Schön, H Habenicht, M C Schubert, and W Warta. Understanding the distribution of iron in multicrystalline silicon after emitter formation: Theoretical model and experiments. *Journal of Applied Physics*, 109(6):063717, 2011.
- [105] Renyu Chen, Bart Trzynadlowski, and Scott T Dunham. Phosphorus vacancy cluster model for phosphorus diffusion gettering of metals in Si. *Journal of Applied Physics*, 115(5):054906–054906, 2014.
- [106] Jan Schmidt, Bianca Lim, Dominic Walter, Karsten Bothe, Sebastian Gatz, Thorsten Dullweber, and Pietro P Altermatt. Impurity-Related Limitations of

- Next-Generation Industrial Silicon Solar Cells. *IEEE Journal of Photovoltaics*, 3(1):114–118, May 2013.
- [107] M Kittler, J Lärz, W Seifert, M Seibt, and W Schröter. Recombination properties of structurally well defined NiSi<sub>2</sub> precipitates in silicon. *Applied Physics Letters*, 58(9):911, 1991.
- [108] Yohan Yoon, Bijaya Paudyal, Jinwoo Kim, Young-Woo Ok, Prashant Kulshreshtha, Steve Johnston, and George Rozgonyi. Effect of nickel contamination on high carrier lifetime n-type crystalline silicon. *Journal of Applied Physics*, 111(3):033702, 2012.
- [109] A E Morishige, D P Fenning, J Hofstetter, M Ann Jensen, S Ramanathan, C Wang, B Lai, and T Buonassisi. Elucidating and engineering recombination-active metal-rich precipitates in n-type multicrystalline silicon. In *Proceedings of the 40th IEEE PVSC*, pages 3004–3007, Denver, 2014.
- [110] Frank S Ham. Theory of diffusion-limited precipitation. *Journal of Physics and Chemistry of Solids*, 6(4):335–351, 1958.
- [111] Masaki Aoki, Akito Hara, and Akira Ohsawa. Fundamental properties of intrinsic gettering of iron in a silicon wafer. *Journal of Applied Physics*, 72(3):895, 1992.
- [112] M Seibt, D Abdelbarey, V Kveder, C Rudolf, P Saring, L Stolze, and O Voß. Interaction of metal impurities with extended defects in crystalline silicon and its implications for gettering techniques used in photovoltaics. *Materials Science and Engineering: B*, 159-160:264–268, March 2009.
- [113] H Hieslmair, A A Istratov, T Heiser, and E R Weber. Evaluation of precipitate densities and capture radii from the analysis of precipitation kinetics. *Journal of Applied Physics*, 84(2):713, 1998.
- [114] J D Murphy and R J Falster. The relaxation behaviour of supersaturated iron in single-crystal silicon at 500 to 750 Å°C. *Journal of Applied Physics*, 112(11):113506, 2012.
- [115] A Bentzen, A Holt, J S Christensen, and B G Svensson. High concentration in-diffusion of phosphorus in Si from a spray-on source. *Journal of Applied Physics*, 99(6):064502, 2006.
- [116] T Y Tan, P S Plekhanov, S Joshi, R Gafiteanu, and U M Gösele. Physics of Impurity Gettering in PV Silicon. In *Eighth Workshop on Crystalline Silicon Solar Cell Materials and Process*, pages 42–49, Copper Mountain, CO, August 1998.
- [117] Horng-Ming You, Ulrich M Gösele, and Teh Y Tan. Simulation of the transient indiffusion-segregation process of triply negatively charged Ga vacancies

- in GaAs and AlAs/GaAs superlattices. *Journal of Applied Physics*, 74(4):2461, 1993.
- [118] Peng Zhang, Hele Väinölä, Andrei A Istratov, and Eicke R Weber. The thermal stability of iron precipitates in silicon after internal gettering. *Physica B: Condensed Matter*, 340-342:1051–1055, December 2003.
- [119] Katy Hartman, Mariana Bertoni, James Serdy, and Tonio Buonassisi. Dislocation density reduction in multicrystalline silicon solar cell material by high temperature annealing. *Applied Physics Letters*, 93(12):122108, 2008.
- [120] Daniel McDonald and Andrés Cuevas. The trade-off between phosphorus gettering and thermal degradation in multicrystalline silicon. *16th European Photovoltaic Solar Energy Conference*, May 2000.
- [121] D Franke. Rise of dislocation density in crystalline silicon wafers during diffusion processing. In *Photovoltaic Energy Conversion, 2003. Proceedings of 3rd World Conference on*, pages 1344–1347, 2003.
- [122] Bei Wu, Nathan Stoddard, Ronghui Ma, and Roger Clark. Bulk multicrystalline silicon growth for photovoltaic (PV) application. *Journal of Crystal Growth*, 310(7-9):2178–2184, April 2008.
- [123] Anis Jouini, Damien Ponthenier, Hélène Lignier, Nicolas Enjalbert, Benoit Marie, Béatrice Drevet, Etienne Pihan, Cyril Cayron, Tamzin Lafford, and Denis Camel. Improved multicrystalline silicon ingot crystal quality through seed growth for high efficiency solar cells. *Progress in Photovoltaics: Research and Applications*, 20(6):735–746, December 2011.
- [124] Torunn Ervik, Gaute Stokkan, Tonio Buonassisi, Øyvind Mjøs, and Otto Lohne. Dislocation formation in seeds for quasi-monocrystalline silicon for solar cells. *Acta Materialia*, 67(C):199–206, April 2014.
- [125] M G Tsoutsouva, V A Oliveira, D Camel, T N Tran Thi, J Baruchel, B Marie, and T A Lafford. Journal of Crystal Growth. *Journal of Crystal Growth*, 401(C):397–403, September 2014.
- [126] Longfei Gong, Fengzhen Wang, Qing Cai, Da You, and Bing Dai. Solar Energy Materials & Solar Cells. *Solar Energy Materials and Solar Cells*, 120(PA):289–294, January 2014.
- [127] Ismael Guerrero, Vicente Parra, Teresa Carballo, Andrés Black, Miguel Miranda, David Cancillo, Benito Moralejo, Juan Jiménez, Jean-François Lelièvre, and Carlos del Cañizo. About the origin of low wafer performance and crystal defect generation on seed-cast growth of industrial mono-like-silicon ingots. *Progress in Photovoltaics: Research and Applications*, 22(8):923–932, December 2012.

- [128] Kyu-Min Han, Hi-deok Lee, Jun-Sik Cho, Sang-Hyun Park, Jae-Ho Yun, Kyung-Hoon Yoon, and Jin-Su Yoo. Fabrication and characterization of monocrystalline-like silicon solar cells. *Journal of the Korean Physical Society*, 61(8):1279–1282, November 2012.
- [129] Xin Gu, Xuegong Yu, Kuanxin Guo, Lin Chen, Dong Wang, and Deren Yang. Solar Energy Materials & Solar Cells. *Solar Energy Materials and Solar Cells*, 101(C):95–101, June 2012.
- [130] R B Bergmann. Crystalline Si thin-film solar cells: a review. *Applied physics A*, 69(2):187–194, 1999.
- [131] D M Powell, J Hofstetter, D P Fenning, R Hao, T S Ravi, and T Buonassisi. Effective lifetimes exceeding 300  $\mu$ s in gettered p-type epitaxial kerfless silicon for photovoltaics. *Applied Physics Letters*, 103(26):263902, December 2013.
- [132] Martin Keller, Stefan Reber, Norbert Schillinger, David Pocza, and Martin Arnold. In-Line Silicon Epitaxy for Photovoltaics Using a Continuous Chemical Vapour Deposition Reactor. *Journal of nanoscience and nanotechnology*, 11(9):8024–8029, 2011.
- [133] Howard M Branz, Charles W Teplin, Manuel J Romero, Ina T Martin, Qi Wang, Kirstin Alberi, David L Young, and Paul Stradins. Thin Solid Films. *Thin Solid Films*, 519(14):4545–4550, May 2011.
- [134] G Hahn and A Schönecker. New crystalline silicon ribbon materials for photovoltaics. *Journal of Physics: Condensed Matter*, 16(50):R1615–R1648, December 2004.
- [135] A Schönecker, L J Geerligs, and A Müller. Casting Technologies for Solar Silicon Wafers: Block Casting and Ribbon-Growth-on Substrate. *Solid State Phenomena*, 95-96:149–158, December 2004.
- [136] B Michl, Jonas Schön, W Warta, and M C Schubert. The Impact of Different Diffusion Temperature Profiles on Iron Concentrations and Carrier Lifetimes in Multicrystalline Silicon Wafers. *IEEE Journal of Photovoltaics*, 3(2):635–640, February 2013.
- [137] Scott A McHugo, A C Thompson, G Lamble, C Flink, and E R Weber. Metal impurity precipitates in silicon: chemical state and stability. *Physica B: Condensed Matter*, 273-274:371–374, December 1999.
- [138] Stephan Riepe, Isolde E Reis, Wolfram Kwapil, Marie Aylin Falkenberg, Jonas Schön, Herfried Behnken, Jan Bauer, Denise Krefner-Kiel, Winfried Seifert, and Wolfgang Koch. Research on efficiency limiting defects and defect engineering in silicon solar cells - results of the German research cluster SolarFocus. *physica status solidi (c)*, 8(3):733–738, December 2010.

- [139] Mohammed M'Hamdi. Thermo-Mechanical Analysis of Multicrystalline Silicon Ingot Casting. Technical report, January 2007.
- [140] Jasmin Hofstetter, David P Fenning, Jean-François Lelièvre, Carlos del Cañizo, and Tonio Buonassisi. Engineering metal precipitate size distributions to enhance gettering in multicrystalline silicon. *physica status solidi (a)*, 209(10):1861–1865, August 2012.
- [141] J F Lelièvre, J Hofstetter, A Peral, I Hoces, F Recart, and C del Cañizo. Dissolution and gettering of iron during contact co-firing. *Energy Procedia*, 8:257–262, 2011.
- [142] G Coletti, R Kvande, V D Mihailetchi, L J Geerligts, L Arnberg, and E J Ovrelid. Effect of iron in silicon feedstock on p- and n-type multicrystalline silicon solar cells. *Journal of Applied Physics*, 104(10):104913, 2008.
- [143] Maulid Kivambe, Douglas M Powell, Sergio Castellanos, Mallory Ann Jensen, Ashley E Morishige, Kazuo Nakajima, Kohei Morishita, Ryota Murai, and Tonio Buonassisi. Journal of Crystal Growth. *Journal of Crystal Growth*, 407(C):31–36, December 2014.
- [144] Yuguo Tao, Young-Woo Ok, Francesco Zimbardi, Ajay D Upadhyaya, Jiun-Hong Lai, Steven Ning, Vijaykumar D Upadhyaya, and Ajeet Rohatgi. Fully Ion-Implanted and Screen-Printed 20.2Junction Silicon Cells on 239 cm<sup>2</sup> n-Type CZ Substrate. *IEEE Journal of Photovoltaics*, 4(1):58–63, April 2014.
- [145] Philip Rothhardt, Sebastian Meier, Stefan Maier, Kaiyun Jiang, Andreas Wolf, and Daniel Biro. Characterization of POCl<sub>3</sub>-Based Codiffusion Processes for Bifacial N-Type Solar Cells. *IEEE Journal of Photovoltaics*, 4(3):827–833, April 2014.
- [146] Antonio Luque and Steven Hegedus. *Handbook of Photovoltaic Science and Engineering*. John Wiley & Sons, March 2011.
- [147] Klaus Graff. *Metal Impurities in Silicon-Device Fabrication*. Springer, October 2012.
- [148] Mohammad B Shabani, T Yamashita, and E Morita. Study of gettering mechanisms in silicon: competitive gettering between phosphorus diffusion gettering and other gettering sites. *Solid State Phenomena*, 131:399–404, 2008.
- [149] Matthew D Pickett and Tonio Buonassisi. Iron point defect reduction in multicrystalline silicon solar cells. *Applied Physics Letters*, 92(12):122103, 2008.
- [150] Markus Rinio, Arthit Yodyunyong, Sinje Keipert-Colberg, Yves Patrick Botchak Mouafi, Dietmar Borchert, and Amada Montesdeoca-Santana. Improvement of multicrystalline silicon solar cells by a low temperature anneal after emitter diffusion. *Progress in Photovoltaics: Research and Applications*, 19(2):165–169, July 2010.

- [151] Rafael Krain, Sandra Herlufsen, and Jan Schmidt. Internal gettering of iron in multicrystalline silicon at low temperature. *Applied Physics Letters*, 93(15):152108, 2008.
- [152] D P Fenning, J Hofstetter, M I Bertoni, S Hudelson, M Rinio, J F Lelièvre, B Lai, C del Cañizo, and T Buonassisi. Iron distribution in silicon after solar cell processing: Synchrotron analysis and predictive modeling. *Applied Physics Letters*, 98(16):162103, 2011.
- [153] S Martinuzzi. Hydrogen passivation of defects in multicrystalline silicon solar cells. *Solar Energy Materials and Solar Cells*, 80(3):343–353, November 2003.
- [154] D Abdelbarey, V Kveder, W Schröter, and M Seibt. Aluminum gettering of iron in silicon as a problem of the ternary phase diagram. *Applied Physics Letters*, 94(6):061912, 2009.
- [155] M Loghmarti, R Stuck, J C Muller, D Sayah, and P Siffert. Strong improvement of diffusion length by phosphorus and aluminum gettering. *Applied Physics Letters*, 62(9):979, 1993.
- [156] D Macdonald, A Cheung, and A Cuevas. Gettering and poisoning of silicon wafers by phosphorus diffused layers. In *Photovoltaic Energy Conversion, 2003. Proceedings of 3rd World Conference on*, pages 1336–1339, 2003.
- [157] Ville Vähänissi, Antti Haarahiltunen, Marko Yli-Koski, and Hele Savin. Gettering of Iron in Silicon Solar Cells With Implanted Emitters. *IEEE Journal of Photovoltaics*, 4(1):142–147, January 2014.
- [158] David P Fenning, V Vähänissi, J Hofstetter, A E Morishige, H S Laine, Antti Haarahiltunen, Sergio Castellanos, Mallory Ann Jensen, Barry Lai, and Hele Savin. Iron precipitation upon gettering in phosphorus-implanted Czochralski silicon and its impact on solar cell performance. In *Proceedings of the 40th IEEE PVSC*, Denver, 2014.
- [159] M C Schubert, J Schön, B Michl, A Abdollahinia, and W Warta. Modeling distribution and impact of efficiency limiting metallic impurities in silicon solar cells. In *Proceedings of the 38th IEEE PVSC*, pages 000286–000291, Austin, 2012.
- [160] J S Chang and G Cooper. A practical difference scheme for Fokker-Planck equations. *Journal of Computational Physics*, 6(1):1–16, January 1970.
- [161] Scott T Dunham. Growth kinetics of disk-shaped extended defects with constant thickness. *Applied Physics Letters*, 63(4):464, 1993.
- [162] A Haarahiltunen, H Väinölä, O Anttila, M Yli-Koski, and J Sinkkonen. Experimental and theoretical study of heterogeneous iron precipitation in silicon. *Journal of Applied Physics*, 101(4):043507, 2007.

- [163] A Haarahiltunen, H Talvitie, H Savin, O Anttila, M Yli-Koski, M I Asghar, and J Sinkkonen. Gettering of iron in silicon by boron implantation. *Journal of Materials Science: Materials in Electronics*, 19(S1):41–45, February 2008.
- [164] Ashley E Morishige, Mallory A Jensen, Jasmin Hofstetter, Patricia X T Yen, Chenlei Wang, Barry Lai, David P Fenning, and Tonio Buonassisi. Synchrotron-based investigation of transition-metal getterability in n-type multicrystalline silicon. *Applied Physics Letters*, 108(20):202104, May 2016.
- [165] A Cuevas, S Riepe, M J Kerr, D H Macdonald, G Coletti, and F Ferrazza. N-type multicrystalline silicon: a stable, high lifetime material. In *Photovoltaic Energy Conversion, 2003. Proceedings of 3rd World Conference on*, pages 1312–1315 Vol.2. IEEE, 2003.
- [166] Florian Schindler, Bernhard Michl, Andreas Kleiber, Heiko Steinkemper, Jonas Schön, Wolfram Kwapil, Patricia Krenckel, Stephan Riepe, Wilhelm Warta, and Martin C Schubert. Potential Gain in Multicrystalline Silicon Solar Cell Efficiency by n-Type Doping. *IEEE Journal of Photovoltaics*, 5(2):499–506.
- [167] F Schindler, B Michl, P Krenckel, S Riepe, and F Feldmann. Efficiency potential of p- and n-type high performance multicrystalline silicon. *Energy Procedia*, 2015.
- [168] S Martinuzzi, O Palais, M Pasquinelli, and F Ferrazza. N-type multicrystalline silicon wafers and rear junction solar cells. *The European Physical Journal Applied Physics*, 32(3):187–192, November 2005.
- [169] Jasmin Hofstetter, Jean-François Lelièvre, David P Fenning, Mariana I Bertoni, Tonio Buonassisi, and Carlos del Cañizo. Towards the Tailoring of P Diffusion Gettering to As-Grown Silicon Material Properties. *Solid State Phenomena*, 178-179:158–165, August 2011.
- [170] Jasmin Hofstetter, David P Fenning, Douglas M Powell, Ashley E Morishige, Hannes Wagner, and Tonio Buonassisi. Sorting Metrics for Customized Phosphorus Diffusion Gettering. *IEEE Journal of Photovoltaics*, 4(6):1421–1428.
- [171] D P Fenning, A S Zuschlag, M I Bertoni, B Lai, G Hahn, and T Buonassisi. Improved iron gettering of contaminated multicrystalline silicon by high-temperature phosphorus diffusion. *Journal of Applied Physics*, 113(21):214504, 2013.
- [172] T Buonassisi, M Heuer, O F Vyvenko, A A Istratov, E R Weber, Z Cai, B Lai, T F Ciszek, and R Schindler. Applications of synchrotron radiation X-ray techniques on the analysis of the behavior of transition metals in solar cells and single-crystalline silicon with extended defects. *Physica B: Condensed Matter*, 340-342:1137–1141, December 2003.

- [173] Y Dusausoy, J Protas, R Wandji, and B Roques. Structure Cristalline du Disiliciure de fer, FeSi<sub>2</sub>B. *Acta Cryst*, pages 1–10, June 1971.
- [174] Sandra Herlufsen, Jan Schmidt, David Hinken, Karsten Bothe, and Rolf Brendel. Photoconductance-calibrated photoluminescence lifetime imaging of crystalline silicon. *physica status solidi (RRL) - Rapid Research Letters*, 2(6):245–247, December 2008.
- [175] X-Ray Data Booklet. *Lawrence Berkeley National Laboratory*, pages 1–176, April 2009.
- [176] A A Istratov, H Hieslmair, and E R Weber. Iron and its complexes in silicon. *Applied Physics A: Materials Science & Processing*, 69(1):13–44, 1999.
- [177] Hsiu-Wu Guo and Scott T Dunham. Accurate modeling of copper precipitation kinetics including Fermi level dependence. *Applied Physics Letters*, 89(18):182106, 2006.
- [178] A Haarahiltunen, H Väinölä, O Anttila, E Saarnilehto, M Yli-Koski, J Storgårds, and J Sinkkonen. Modeling of heterogeneous precipitation of iron in silicon. *Applied Physics Letters*, 87(15):151908, 2005.
- [179] H Takahashi and H Yamada-Kaneta. Iron gettering controlled by size and density of oxygen precipitates in Czochralski-grown silicon. *Japanese journal of . . .*, 1998.
- [180] Scott A McHugo, E R Weber, M Mizuno, and F G Kirscht. A study of gettering efficiency and stability in Czochralski silicon. *Applied Physics Letters*, 66(21):2840, 1995.
- [181] A Mesli, T Heiser, N Amroun, and P Siffert. Charge-state-dependent iron precipitation in silicon. *Applied Physics Letters*, 57(18):1898, 1990.
- [182] S A McHugo, R J McDonald, A R Smith, D L Hurley, and E R Weber. Iron solubility in highly boron-doped silicon. *Applied Physics Letters*, 73(10):1424, 1998.
- [183] Jasmin Hofstetter, Carlos del Cañizo, Hannes Wagner, Sergio Castellanos, and Tonio Buonassisi. Material requirements for the adoption of unconventional silicon crystal and wafer growth techniques for high-efficiency solar cells. *Progress in Photovoltaics: Research and Applications*, 24(1):122–132, October 2015.
- [184] Chang Sun, Fiacre E Rougieux, and Daniel Macdonald. A unified approach to modelling the charge state of monatomic hydrogen and other defects in crystalline silicon. *Journal of Applied Physics*, 117(4):045702, January 2015.
- [185] S Wilking, A Herguth, and G Hahn. Influence of hydrogen on the regeneration of boron-oxygen related defects in crystalline silicon. *Journal of Applied Physics*, 113(19):194503, 2013.



- [186] Brett J Hallam, Phill G Hamer, Stuart R Wenham, Malcolm D Abbott, Adeline Sugianto, Alison M Wenham, Catherine E Chan, GuangQi Xu, Jed Kraiem, Julien Degoulange, and Roland Einhaus. Advanced Bulk Defect Passivation for Silicon Solar Cells. *IEEE Journal of Photovoltaics*, 4(1):88–95.
- [187] Friedemann D Heinz, Laura E Mundt, Wilhelm Warta, and Martin C Schubert. A combined transient and steady state approach for robust lifetime spectroscopy with micrometer resolution. *physica status solidi (RRL) - Rapid Research Letters*, 9(12):697–700, October 2015.
- [188] Friedemann D Heinz, Martin Kasemann, Wilhelm Warta, and Martin C Schubert. Microscopic charge carrier lifetime in silicon from a transient approach. *Applied Physics Letters*, 107(12):122101, September 2015.
- [189] Friedemann D Heinz, Johannes Giesecke, Laura E Mundt, Martin Kasemann, Wilhelm Warta, and Martin C Schubert. On the implication of spatial carrier density non-uniformity on lifetime determination in silicon. *Journal of Applied Physics*, 118(10):105706, September 2015.
- [190] Ashley E Morishige, Hannu S Laine, Mallory A Jensen, Patricia X T Yen, Erin E Looney, Stefan Vogt, Barry Lai, Hele Savin, and Tonio Buonassisi. Accelerating Synchrotron-Based Characterization of Solar Materials: Development of Flyscan Capability. In *Proceedings of the 43rd IEEE Photovoltaic Specialists Conference*, May 2016.
- [191] L M Murphy, B R Dobson, M Neu, C A Ramsdale, R W Strange, and S S Hasnain. Quick Fluorescence-EXAFS: an Improved Method for Collection of Conventional XAFS Data, an Improved Method for Collection of Conventional XAFS Data and for Studying Reaction Intermediates in Dilute Systems. *Journal of Synchrotron Radiation*, 2(1):64–69, January 1995.
- [192] P S Plekhanov and T Y Tan. Schottky effect model of electrical activity of metallic precipitates in silicon. *Applied Physics Letters*, 76(25):3777–3779, 2000.
- [193] Z Cai. A hard x-ray scanning microprobe for fluorescence imaging and microdiffraction at the advanced photon source. In *Sixth international conference on x-ray microscopy (XRM99)*, pages 472–477. AIP.
- [194] Jan Bauer, Angelika Hahnel, Peter Werner, Nikolai Zakharov, Horst Blumtritt, Annika Zuschlag, and Otwin Breitenstein. Recombination at Lomer Dislocations in Multicrystalline Silicon for Solar Cells. *IEEE Journal of Photovoltaics*, 6(1):100–110.
- [195] R Chakraborty, J Serdy, B West, M Stuckelberger, B Lai, J Maser, M I Bertoni, M L Culpepper, and T Buonassisi. Development of an in situ temperature stage for synchrotron X-ray spectromicroscopy. *Review of Scientific Instruments*, 86(11):113705, November 2015.

- [196] C Donolato. The space-charge region around a metallic platelet in a semiconductor. *Semiconductor science and technology*, 1993.
- [197] O F Vyvenko, T Buonassisi, A A Istratov, and E R Weber. X-ray beam induced current/microprobe x-ray fluorescence: synchrotron radiation based x-ray microprobe techniques for analysis of the recombination activity and chemical nature of metal impurities in silicon. *Journal of Physics: Condensed Matter*, 16(2):S141–S151, December 2003.
- [198] J M Hwang and D K Schroder. Recombination properties of oxygen-precipitated silicon. *Journal of Applied Physics*, 59(7):2476, 1986.
- [199] Sergio Castellanos, Maulid M Kivambe, Mallory A Jensen, Douglas M Powell, Kazuo Nakajima, Kohei Morishita, Ryota Murai, and Tonio Buonassisi. Exceeding 3 ms Minority Carrier Lifetime in n-type Non-Contact Crucible Silicon. *Energy Procedia*, pages 1–6, March 2016.
- [200] Paul A Basore. Understanding Manufacturing Cost Influence on Future Trends in Silicon Photovoltaics. *IEEE Journal of Photovoltaics*, 4(6):1477–1482.
- [201] K Ramspeck, S Zimmermann, H Nagel, A Metz, Y Gassenbauer, B Birkmann, and A Seidl. *Light induced degradation of rear passivated mc-Si solar cells*. Proceedings of the 27th European Photovoltaic Solar Energy Conference, 2012.
- [202] Fabian Fertig, Karin Krauss, and Stefan Rein. Light-induced degradation of PECVD aluminium oxide passivated silicon solar cells. *physica status solidi (RRL) - Rapid Research Letters*, 9(1):41–46, December 2014.
- [203] Karin Krauss, Fabian Fertig, Dorothee Menzel, and Stefan Rein. ScienceDirect. *Energy Procedia*, 77:599–606, August 2015.
- [204] Fabian Fertig, Johannes Greulich, Karin Krauss, Florian Clement, Daniel Biro, Ralf Preu, and Stefan Rein. The BOSCO Solar Cell: Simulation and Experiment. *IEEE Journal of Photovoltaics*, 4(5):1243–1251.
- [205] Friederike Kersten, Peter Engelhart, Hans-Christoph Ploigt, Andrey Stekolnikov, Thomas Lindner, Florian Stenzel, Matthias Bartzsch, Andy Szpeth, Kai Petter, Johannes Heitmann, and Jörg W Müller. Solar Energy Materials & Solar Cells. *Solar Energy Materials and Solar Cells*, 142(C):83–86, November 2015.
- [206] A Cuevas. The effect of emitter recombination on the effective lifetime of silicon wafers. *Solar Energy Materials and Solar Cells*, 1999.
- [207] Daniel Macdonald and L J Geerligs. Recombination activity of interstitial iron and other transition metal point defects in p- and n-type crystalline silicon. *Applied Physics Letters*, 85(18):4061, 2004.

- [208] Dan A Iordache, Paul E Sterian, and Ionel Tunaru. Charge Coupled Devices as Particle Detectors. *Advances in High Energy Physics*, 2013(1):1–12, 2013.
- [209] P Deixler, J Terry, I D Hawkins, J H Evans-Freeman, A R Peaker, L Rubaldo, D K Maude, J C Portal, L Dobaczewski, K Bonde Nielsen, A Nylandsted Larsen, and A Mesli. Laplace-transform deep-level transient spectroscopy studies of the G4 gold–hydrogen complex in silicon. *Applied Physics Letters*, 73(21):3126, 1998.
- [210] S Boughaba and D Mathiot. Deep level transient spectroscopy characterization of tungsten-related deep levels in silicon. *Journal of Applied Physics*, 69(1):278, 1991.
- [211] T Roth, P Rosenits, S Diez, S W Glunz, D Macdonald, S Beljakowa, and G Pensl. Electronic properties and dopant pairing behavior of manganese in boron-doped silicon. *Journal of Applied Physics*, 102(10):103716, 2007.
- [212] Stefan Rein. *Lifetime Spectroscopy. A Method of Defect Characterization in Silicon for Photovoltaic Applications*. Springer Science & Business Media, March 2006.
- [213] Klaus Graff. *Metal Impurities in Silicon-Device Fabrication*. Springer Science & Business Media, March 2013.
- [214] S Rein and S W Glunz. Electronic properties of the metastable defect in boron-doped Czochralski silicon: Unambiguous determination by advanced lifetime spectroscopy. *Applied Physics Letters*, 82(7):1054, 2003.
- [215] A R Peaker, B Hamilton, S Leonard, V P Markevich, K Youssef, and George Rozgonyi. Recombination via nano-precipitates... a new mechanism for efficiency loss in solar silicon? *40th IEEE Photovoltaic Specialists Conference*, 2014.
- [216] Michael Seibt, Reda Khalil, Vitaly Kveder, and Wolfgang Schröter. Electronic states at dislocations and metal silicide precipitates in crystalline silicon and their role in solar cell materials. *Applied Physics A: Materials Science & Processing*, 96(1):235–253, December 2008.
- [217] Jasmin Hofstetter, Carlos del Cañizo, Hannes Wagner, Sergio Castellanos, and Tonio Buonassisi. Material requirements for the adoption of unconventional silicon crystal and wafer growth techniques for high-efficiency solar cells. *Progress in Photovoltaics: Research and Applications*, 24(1):122–132, October 2015.